IntechOpen

Volcanoes

Geological and Geophysical Setting, Theoretical Aspects and Numerical Modeling, Applications to Industry and Their Impact on the Human Health

Edited by Gemma Aiello

VOLCANOES - GEOLOGICAL AND GEOPHYSICAL SETTING, THEORETICAL ASPECTS AND NUMERICAL MODELING, APPLICATIONS TO INDUSTRY AND THEIR IMPACT ON THE HUMAN HEA

Edited by **Gemma Aiello**

Volcanoes - Geological and Geophysical Setting, Theoretical Aspects and Numerical Modeling, Applications to Industry and Their Impact on the Human Health
http://dx.doi.org/10.5772/intechopen.68230
Edited by Gemma Aiello

Contributors

Pier Luigi Bragato, J. Magdalena Santana-Casiano, Melchor González-Dávila, Eugenio Fraile-Nuez, Masao Ban, Shin Sato, Seiko Yamasaki, Teruki Oikawa, Yuki Nishi, Irina Zhulanova, Victor Sharapov, Yury Perepechko, Konstantin Sorokin, Anna Vladlenovna Mikheeva, Timothy Masterlark, Sui Tung, Alexander Simakin, Ahmad Ghassemi, Eko Hariyono, Liliasari S, Aref Al-Swaidani, Enrique Rodríguez-Castellón, Patricia Sierra-Vargas, Claudia Vargas-Domínguez, Karen Bobadilla-Lozoya, Octavio Gamaliel Aztatzi-Aguilar, Gemma Aiello

Notice

First published in London, United Kingdom, 2018 by IntechOpen
eBook (PDF) Published by IntechOpen, 2019
IntechOpen is the global imprint of INTECHOPEN LIMITED, registered in England and Wales, registration number: 11086078, The Shard, 25th floor, 32 London Bridge Street
London, SE19SG – United Kingdom
Printed in Croatia

British Library Cataloguing-in-Publication Data
A catalogue record for this book is available from the British Library

Additional hard and PDF copies can be obtained from orders@intechopen.com

Volcanoes - Geological and Geophysical Setting, Theoretical Aspects and Numerical Modeling, Applications to Industry and Their Impact on the Human Health
Edited by Gemma Aiello

p. cm.

Print ISBN 978-1-78923-348-3

Online ISBN 978-1-78923-349-0

eBook (PDF) ISBN 978-1-83881-290-4

Meet the editor

Dr. Gemma Aiello was born in Aversa (CE), Italy, on October 24, 1964. In 1989, she graduated in Geological Sciences from the University of Naples "Federico II." In 1993, she received her PhD degree in Sedimentary Geology from the University of Naples "Federico II," Department of Earth Sciences, Faculty of Geological Sciences. She completed a 2-year postdoctoral fellowship at the University of Naples "Federico II," a CNR-CEE fellowship, and several contracts at the Research Institute "Geomare Sud," CNR, Naples, Italy. Since 1998, she has been a full-time researcher at the Italian CNR. She has a 25-year experience in the field of sedimentary geology, marine geology, and geophysics, participating in different research projects of the Italian National Research Council.

Contents

Preface

This book contains 12 chapters dealing with the studies on volcanoes, their geological and geophysical setting, the theoretical aspects and the numerical modeling on volcanoes, the applications of volcanoes to the industry, and the impact of volcanoes on the human health, in different geological settings and using several techniques and methods, including the volcanology, the seismology, the statistical methods to assess the correlation between seismic and volcanic activity (modified Ripley's K-function to regional seismicity), the field geological survey of volcanic successions, the analytical methods of petrologic analysis, the petrography of the volcanic rocks with the individuation of the modal compositions of volcanic rocks and their comparison with major elements and trace elements in variation diagrams, and the argon isotopic measurements performed through the peak height comparison (unspiked) method. The oceanographic methods have also been applied to case studies of submarine volcanic edifices located in the Canary Islands (Atlantic Ocean), including the sampling of the water column with a conductivity-temperature-depth (CTD) sensor rosette with 24 Niskin bottles, in order to determinate key physical and chemical parameters, such as the total-scale pH, the total dissolved inorganic carbon (C), the total alkalinity (A), the temperature, the salinity, and the dissolved oxygen. Problems of volcanic risk mitigation have also been treated, regarding the eruption disasters in Indonesia, a country where a high number of people live next to the volcanoes, and characterized by the lack of public awareness of the eruption disasters. Petrographic methods have been successfully applied to the study of the Cretaceous magmatism of the layered gabbroids of the Chukotka region (Pekulney Ridge, Russia), and geodynamic implications have been successfully established through geological and petrographic studies. The relationships among the mantle wedge, the convective heat and mass transfer, the infiltration metasomatism, the zoning, and the mathematical models have been applied to the comprehension of complex volcanic areas through the theoretical aspects of volcanic studies on magmatic chambers coupled with numerical modeling, including finite element models (FEMs) in the individuation of volcanic deformations. Book chapters are separated into five main sections: (i) "Introduction," (ii) "Geological and Geophysical Setting of Volcanoes," (iii) "Theoretical Aspects and Numerical Modeling of Volcanoes," (iv) "Applications of Volcanoes to Industry," and (v) "Impact of Volcanoes on the Human Health." There is one chapter in the first section on the "Introduction," the "Introductory Chapter." In the second section, there are five chapters, dealing with the correlation between seismic and volcanic activity at the Vesuvius volcano, with the exploration of the base of the Zao stratovolcano in the northeastern Japan, with the volcanic emissions of the Tagoro submarine volcano in the Canary Islands and their impact on the physical and chemical properties of the oceanic waters, with the characteristics of the volcanic eruptions in Indonesia and the problems of risk mitigation of volcanic disasters, and, finally, with the geological and petrographic study of Cretaceous volcanites of the Pekulney

Ridge (Russia) and corresponding geodynamic implications. In the third section, there are three chapters, the first one dealing with the dynamics of convective heating of the mantle and crustal rocks in the seismic focal zone of the Kamchatka region and the genetically related volcanic arcs, characterized by the occurrence of compressive stresses and by the compaction of the heterophase medium; the second one regarding the numerical methods of volcanic deformation through InSAR methods, showing a systematic approach to the quantitative simulation of geodetic data with finite element models (FEMs) in the general framework of a protocol for the modeling of deformations in volcanic areas; and the third one showing the mechanics of the magmatic chambers under the volcanoes, referring to the Yellowstone caldera, which, due to its large volume, owes the critical overpressure necessary to start the volcanic eruption, requiring large volumes of magmas and fluids. In the fourth section, there are two chapters, the first one dealing with the use of volcanic scoriae in the cement replacement, a common practice in the construction industry, as concrete mixes, showing the chemical and mineralogical composition of the scoria samples coming from 36 different countries and calculating some equations of estimated depending on the analyzed data and the second one regarding the use of volcanic glasses or obsidians as absorbents, highlighting that the volcanic glasses represent amorphous phyllosilicates formed through a rapid magmatic cooling and that the macroporosity of the volcanic glasses allows to host biomolecules, tensioactives, and dyes.

Introduction

The first chapter "Introductory Chapter—Volcanoes: From Their Geological and Geophysical Setting to Their Impact on the Human Health" by Gemma Aiello introduces the concepts of the geological and geophysical setting of volcanoes, of the theoretical aspects and numerical modeling of volcanoes, of the application of volcanoes to the industry, and of the impact of the volcanoes of the human health. Volcanoes represent geological structures, which form on the earth's surface in the areas where the emission of magma verifies, namely, a volcanic eruption. They can have different shapes and dimensions, which are strictly related to the type of eruptive activity. Examples of important stratovolcanoes have been mentioned, including the Etna and the Vesuvius volcanoes in Italy and the Fujiyama volcano in Japan. The volcanological problems related with the Zao volcano have been introduced, being a complex stratovolcano, composed of several volcanic edifices. The volcanological problems linked with the ones in Indonesia have been shortly discussed, due to the fact that this active volcanic region, one of the most important volcanic regions of the world together with the ones in Japan, hosts 147 volcanoes. The volcanoes studied in this book are located in different places of the world: Southern Italy (Vesuvius volcano), northeastern Japan (Zao volcano), Canary Islands (Tagoro volcano), Indonesia (Indonesian volcanoes), and northeastern Russia (Pekulney Ridge volcanic complex). Some theoretical aspects on volcanoes, coupled with their numerical modeling, have been briefly discussed, including the convective heat transfer, the heat and mass transfer in volcanic systems, the heat release and the carbon dioxide degassing, and the amount of energy released from volcanic and hydrothermal systems. The new methods of analysis of the volcanic deformation through InSAR measurements have also been introduced. The applications of volcanoes to the industry have been discussed. Before the Industrial Age, the volcanic deposits and rocks have been used for a wide range of purposes in the industrial field. Their prehistoric uses have been numerous, while the modern uses range from the mining of volcanogenic minerals for manufacturing to the artistic purposes in gardens and monuments. Finally, the impact of volca-

noes on the human health has been discussed, referring to the volcanic emissions. In fact, volcanic and geothermal regions are densely populated and often closely located next to major towns, threatening the local people.

Geological and Geophysical Setting of Volcanoes

The second chapter, "Correlation between Seismic and Volcanic Activity at a Large Spatial Scale in Italy: Examples from the Neapolitan Volcanic District, Vesuvius Volcano, Southern Italy," by Pier Luigi Bragato has presented the time correlation between the Vesuvius eruptions and the Italian earthquakes based on the new catalogues. The correlation is statistically significant, involving the earthquakes, which are located far away from the volcanic edifice. A transient of accelerated volcanic and seismic activity has been found between 1600 and 1900 at the Somma-Vesuvius volcanic edifice. A similar correlation between the seismicity and the uplift episodes has been found at the Phlegrean Fields caldera during the last 70 years. Two volcanic and seismic cycles have been recognized, the first one ranging from 1970 to 1980 and the second one including strong and recent earthquakes (earthquake of L'Aquila, 2009; Emilia-Romagna earthquake, 2012; and Central Italy earthquake, 2016). Such a close time correlation accounts for climatic processes, which have controlled both the volcanic and the seismotectonic phases to a regional scale. These climatic processes may include the global surface temperature and the extension of the glaciers in the northwestern Europe, representing possible key parameters in controlling both the volcanism and the seismicity.

The third chapter, "Exploring the Base of the Volcano: A Case Study of an Active Stratovolcano, Mt. Zao, NE Japan," by Shin Sato, Masao Ban, Teiruki Oikawa, Seiko Yamasaki, and Yuki Nishi shows the results of a volcanological, petrographic, and geochemical study of the basal volcanic products of the Zao volcano, including K-Ar age dating. The active Zao stratovolcano is located in the northeastern Japan and, in particular, in the northern Honshu volcanic district, being the most active volcanic edifice. In particular, the Zao volcano is composed of several stratovolcanoes, which divide the Pacific Ocean from the Sea of Japan. The older parts of the volcanic edifice are represented by the Ryuzan volcano, located in the western sector of the volcanic district, and by the Byobu and Fubo volcanoes, which are located in the southern sector of the volcanic district. A newly discovered volcanic edifice, namely, the Hiyamizuyama volcano, has been revealed by the field geological survey in the southern part of the volcanic district. Its volcanic products consist of andesitic lavas grading into dacitic lavas and cropping out at the top of the volcanic edifice. A detailed petrological analysis has been carried out revealing the petrographic features of the volcanic rocks of the Hiyamizuyama volcano, which are represented by quartz-bearing clinopyroxene-orthopyroxene andesites and dacites. The total volume of phenocrysts (15%) has been compared with that one of the rocks of the Zao volcano, having a more than 20% phenocrystic modal composition and resulted to be particularly low. K-Ar dating has suggested an obtained age of 1.45–0.03 for the samples of the newly discovered volcanic edifice. This age seems to be very old, suggesting an emplacement of the volcanic edifice older than the first stage of the Zao eruptive activity, starting about 450 ky later.

Chapter 4, "The Emissions of the Tagoro Submarine Volcano, Canary Islands, Atlantic Ocean: Effects on the Physical and Chemical Properties of the Seawater," by Juana Magdalena Santana-Casiano, Melchor Gonzalez-Davila, and Eugenio Fraile-Nuez deals with the application of the oceanographic methods.

The oceanographic methods have also been applied to case studies of submarine volcanic edifices located in the Canary Islands (Atlantic Ocean), including the sampling of the water column with a conductivity-temperature-depth (CTD) sensor rosette with 24 Niskin bottles, in order to determinate key physical and chemical parameters, such as the total-scale pH, the total dissolved inorganic carbon (C), the total alkalinity (A), the temperature, the salinity, and the dissolved oxygen. In this chapter, a new submarine volcano, growth at water depths of 300 m in the island of El Hierro, located in the NE Atlantic Ocean, has been described. Bathymetric and hydrographic surveys have been performed in order to monitor the variations both of the sea bottom topography after the growth of the volcanic edifice and of the physical and chemical parameters of the water column. The top of the volcanic edifice has been found at increasing shallower water depths, reaching up to 88 m in February 2012. The emission of fluids due to the volcanic eruption has allowed for the emplacement of a plume in the water column, modified during the time by the volcanic dynamics and by the oceanographic parameters. Based on the main conclusions of this chapter, the inputs of CO_2 along different sampled sections (tow-yo) have allowed for the evaluation of a CO_2 flux mainly transported toward southwest. Global volcanic flux has also been estimated.

Chapter 5, "The Characteristics of Volcanic Eruption in Indonesia," by Eko Hariyono and S. Liliasari has discussed the characteristics of the volcanic eruptions in Indonesia, unique in the world, with respect to the geological processes of volcanic formation, volcanic eruption, and consequent volcanic disasters and related volcanic hazard. Even if the Indonesian volcanoes are mainly stratovolcanoes, the resulting eruptions are not always explosive and have different durations. The Semeru volcano has a daily effusive activity; the Sinabung volcano erupts with a very short period; and the Merapi and Kelud volcanoes have short eruptions. Volcanic eruptions are strongly controlled by the earthquakes affecting the area. The volcanic behavior in Indonesia is strongly changing during the geological time. The patterns of the volcanic eruptions are strongly different before and after the earthquakes. In the first case, the time interval of the volcanic eruption is larger, while in the second case, the time interval is shorter and the frequency of the volcanic eruption is larger.

Chapter 6, "Layered Gabbroids of the Pekulney Ridge, Chukotka, Northeastern Russia: Geology, Petrography, Age, and Geodynamics," by Irina L'vovna Zhulanova has examined the geological and geodynamic setting of the layered gabbroids cropping out in the Pekulney Ridge, a complex volcanic structure located in the northeastern Russia. The adopted methodologies include the field geological survey and the petrographic analysis. The Svetlorechensky gabbro complex has been distinguished and studied in detail, reconstructing a wide intrusive massif, namely, the Svetlorechensky layered pluton, having homologous volcanic rocks cropping out in other sectors of the Pekulney Ridge. Four groups of rocks have been distinguished in the hornblende-rich gabbro, including the amphibole microgabbronorites, whose structure and composition have been correlated with the basic crystalline schists of the granulite facies; the amphibole gabbro, which does not differ from the pyroxene-amphibole ones; the biotite-amphibole gabbro; and the leucogabbro.

Theoretical Aspects and Numerical Modeling of Volcanoes

Chapter 7, "Dynamics of Convective Heat and Mass Transfer in Permeable Parts of Seismofocal Zones of the Kamchatka Region and Conjugated Volcanic Arcs," by Yury Perepechko, Victor Sharapov, Konstantin Sorokin, and Anna Mikheeva has examined some theoretical aspects of volcanoes dealing with the convective heat and mass transfer. Numerical model-

ing has also been applied in order to highlight novel theoretical aspects. In the Kamchatka region, the morphologic analysis of the volcanic structures has revealed the occurrence of linear volcanic ridges, crossing the structural elements from the continental shelf margin to the oceanic settings. These ridges often cut tectonic terraces located on the continental slope and are located in correspondence with significant normal faults. These faults have also controlled the emplacement of onshore volcanoes, located in southern and eastern Kamchatka. The distribution of extensional and compressional regions on the continental slope in the seismic focal region of the Kamchatka has revealed the occurrence of vertical and inclined destruction zones of rocks pertaining to the mantle. Moreover, in the upper mantle, the perovskite transition has been identified. The equations relative to the two-velocity hydrodynamics of a heterophase medium have been calculated, taking into account the relative physical laws.

Chapter 8, "Finite Element Models of Elastic Volcano Deformation," by Timothy Masterlak and Sui Tung has applied the finite element model (FEM) method to the physical study of the elastic deformations in volcanic settings. To this aim, geodetic, GPS, and InSAR data have been studied, coupled with seismic data for the construction of tomographic models of volcanoes through the data geophysical inversion. The auxiliary data consisted of topography and bathymetry since in deformational studies, the volcanic land is considered as a stress-free surface by assuming that the shear resistance is zero and the normal stress variations are quite small. Governing equations of the physical behavior of the volcanic system have also been calculated. The FEM volcanic model has been discussed, calibrated, and validated.

Chapter 9, "Mechanics of Magma Chamber with the Implication of the Effect of CO_2 Fluxing," by Alexander Simakin and Ghassemi Ahmad has examined the mechanical stability of large magmatic chambers in the case history of the Yellowstone magmatic chamber. The large volume of this magmatic chamber has influenced the critical overpressure, which is necessary to trigger the volcanic eruption, requiring large volumes of magmas and fluids. The mechanical models of the magma chambers allow for the prediction/localization of the chamber roofs and volcanic cones, for the localization of the magmatic transport through volcanic dykes, and for the simulation of the geological processes occurring during a volcanic eruption. The obtained results have shown that large magmatic chambers, such as the Yellowstone caldera, are located in areas where a high rate of magma generation occurred, coupled with a high CO_2 inflow, significantly affecting the mechanical stability of the magmatic chamber. The analysis of the melt inclusions has allowed to estimate the current integrated mass flux of CO_2 in the order of 0.1–0.3 of the total mass melt. The modeling of the deformations in the Yellowstone magmatic chamber has shown that a deep CO_2 fluxing occurred.

Applications of Volcanoes to Industry

Chapter 10, "Volcanic Scoria as Cement Replacement," by Aref M. al-Swaidani has examined the use of the volcanic scoriae in the cement replacement and, as a general rule, for the industrial aims. Volcanic scoriae belong to the tephra and, as a general rule, to the volcanic ejecta represented by fragments. During modern times, the volcanic scoriae have been used in creating concrete prefabricate parts for buildings and several other uses and developments. The chemical and mineralogical analysis of volcanic scoriae has shown that they are often relatively rich in silica and alumina, while the most detected minerals are represented by plagioclase, olivine, pyroxene, and clinopyroxene. Moreover, the properties of the VS-based cement paste, herein analyzed, include the setting times, the heat of hydration, and

the microstructure, while the concrete properties include the compressive and flexural strength, the drying shrinkage, the sulfate attack, and the acidic attack. Equations have been derived in order to estimate the investigated concrete properties, incorporating the effects both of the curing time and of the replacement level of volcanic scoriae. In this way, the concrete properties may be predicted with accuracy.

Chapter 11, "Volcanic Glass and Its Uses as Adsorbent," by Juan Antonio Cecilia, Miguel Armando Autie-Pérez, Juan Manuel Labadie-Suarez, Enrique Rodriguez-Castellon, and Antonia Infantes-Molina has discussed the use of the volcanic glasses as adsorbents and, as a general rule, for commercial and industrial purposes. The volcanic glasses or obsidians are represented by black and glassy rocks, often displaying conchoidal fractures and having a rhyolitic composition. More in detail, the perlite is a glassy devitrified rock having a trachytic composition, widely used as adsorbent and insulator. Due to their suitable physical properties, the volcanic rocks have been used in the processes of manufacture as insulators and adsorbents, more than as abrasives. In this chapter, the use of the volcanic glasses as adsorbents has been discussed. The chemical composition of the volcanic scoriae has been studied. Moreover, the volcanic glasses appear to be located in America, Europe, Africa, Asia, and Oceania: their location has been mapped. Based on the performed studies, the obsidians are highly sensitive to the selective adsorption of several biomolecules, while the perlite can host molecules having a different behavior and dimensions.

Impact of Volcanoes on the Human Health

Chapter 12, "Health Impact on Volcanic Emissions," by Martha Patricia Sierra-Vargas, Claudia Vargas-Dominguez, Karen Bobadilla-Lozoya, and Octavio Gamaliel Aztatzi-Aguilar has examined the influence of the volcanic emissions on the human health. In this chapter, it is clarified that the volcanic emissions influence, in particular, the respiratory tract, the gastrointestinal tract, and the contact of the skin. Among them, the respiratory system is highly sensitive. Different factors act as control factors: the heavy metals, the metal oxides, the inorganic carbons, the silicates, the plastics, and the organics. One of the main conclusions is that the effects of the volcanic emissions of the human health depend mainly on the physical and chemical characteristics of the volcanic emissions and on the related toxicological properties. If the volcanic particles are inhaled, the related health effects may be acute or chronic.

I thank Mr. Slobodan Momcilovic and Mr. Edi Lipovic, Author Service Manager of InTech—Open Science, Open Minds—who have contributed on the book project on volcanoes with competence and patience, following day after day the editorial activities and making possible the publication of this book.

Dr. Gemma Aiello, PhD
Full-Time Researcher
National Research Council (CNR) of Italy
Institute of Marine and Coastal Environment (IAMC)
Naples, Italy

Introduction

Chapter 1

Introductory Chapter: Volcanoes - From Their Geological and Geophysical Setting to Their Impact on Human Health

Gemma Aiello

Additional information is available at the end of the chapter

http://dx.doi.org/10.5772/intechopen.78541

1. Introduction

This is the introductory chapter of the book "Volcanoes: Geological and Geophysical Setting, Theoretical Aspects and Numerical Modelling, Applications to Industry and Their Impact on the Human Health". In this chapter, the research themes studied in this book have been introduced referring to the geological and geophysical setting of volcanoes, pertaining, in particular, to the correlation between seismic and volcanic activity in volcanic edifices of Southern Italy (Somma-Vesuvius) carried out on a regional scale, the volcanic emissions of the submarine edifice of the Tagoro volcano (Canary Islands, Atlantic Ocean) and the corresponding implications on the chemical and physical properties of the oceanic water, the volcanological studies on the base of the volcanoes and the discovery of a new volcanic edifice, namely the Hiyamizuyama volcano, allowing to evaluate the long-term variations of volcanic and magmatic processes in Northeastern Japan, the volcanic eruptions in Indonesia, a land hosting 147 volcanoes (76 active volcanoes) spreading along the islands of Java, Lesser Sunda, Sumatra and Celebes and mostly characterised by stratovolcanoes and finally, the geologic, petrographic and geodynamic study of the layered gabbroids of Pekulney Ridge, a complex volcanic structure located in Northeastern Russia. Moreover, in this book, significant theoretical aspects and numerical modelling of volcanoes have been addressed, including, in particular, the volcanic dynamics of the convective heat and of the mass transfer in the seismo-focal areas of the Kamchatka Region, including the related volcanic arcs, the modelling of the elastic deformation of volcanoes through the development of computational tools for inverse analyses of geodetic data, which have evidenced the mechanical complexity of the volcanic systems, and finally, the mechanical aspects of the magmatic chambers and their

relationships with the fluxing of CO_2, referring to the Yellowstone magmatic chamber, whose large volume has required additional large volumes of magmas and fluids in order to trigger volcanic eruption. In this book, significant applications of volcanic studies to the industry have also been presented, focusing, in particular, on the use of volcanic scorias (VS) and natural pozzolans as cement replacement in the construction industry based on the concrete mixes by analysing their setting times, the compressive strength, water permeability and chloride penetrability and, moreover, on the use of volcanic glasses as adsorbents for industrial aims and scopes, being materials displaying a low thermal conductivity, a low density and a high resistance to fire and perlite aggregate plasters. The volcanic glasses have also been often used as starting materials in the synthesis of clay minerals, as smectites and zeolites. The impact of volcanoes on human health is significant, referring to both the volcanic deposits and to volcanic emissions. In this book, the impact of volcanic emissions on human health has been mainly examined, highlighting that exposure to volcanic emissions can influence the health of people living in the surroundings of the volcano in many ways (dermal and ocular irritation, cardiologic and pulmonary exacerbations and cancer). Moreover, volcanic ashes which have been deposited in a subaqueous environment may produce significant variations in the chemistry of the surface waters and may increase the risk of exposure to metals by drinking that water.

Volcanoes represent geological structures forming on the Earth's surface in the zones where an emission of magma verifies, that is, a volcanic eruption [1]. Many volcanoes have an outer shape of a conical mountain, constructed through the superimposition of the erupted products. The inner part of the cone is crossed by one or more volcanic conduits, representing the last tract of magma uprising. These conduits open outward through the craters. When the magma uprising happens for a long time along the same conduit, the products of different volcanic eruptions accumulate around the same, forming a central volcano. After that the volcanic eruption terminates and the volcanic conduit remains empty; the volcanic crater occurs as a deep cavity. Along the central conduit the uprising of new magma may become very difficult in a high volcano or having the conduit filled by solidified magma. The magma tends to accumulate and pushes along the walls of the volcano up to fracture them. The fractures and faults represent one way out on the flanks or at the base of the volcanic cone, where parasitic vents consequently form.

Volcanoes may have different shapes and dimensions, strictly related to the type of eruptive activity. The effusive eruptions tend to grow a volcano through the accumulation of superimposed lava flows. The explosive eruptions may, on the contrary, remove whole parts of volcanoes. A stratovolcano is typically formed by the superimposition of volcanic products erupted by both explosive and effusive eruptions. The flanks of these volcanoes have steep slopes. Remnants of previous craters, partially destroyed by the strongest explosive phases, have often been individuated. The dimensions of the stratovolcanoes are often relevant but smaller than the ones of shield volcanoes. Important examples of stratovolcanoes in Italy are represented by the Etna [2–4] and Vesuvius [5–7] volcanoes, while between the largest volcanoes of the world there is the Fujiyama volcano (Japan) [8–10].

The Neapolitan volcanic district is composed of the Phlegraean Fields volcanic complex, by the Somma-Vesuvius volcanic complex and by the Ischia Island volcanic complex. In this

book, geophysical studies on the Somma-Vesuvius have been presented, referring, in particular, to the correlation between the volcanic activity and the seismic activity. The geological and geophysical setting of these volcanic districts will be discussed in dedicated sections of this chapter.

Important studies of this book deal with the Tagoro submarine volcano, located in the Canary Islands (Atlantic Ocean), and with the effects of the volcanic eruptions on the physical and chemical composition of the oceanic water. The Tagoro submarine volcano is a deeply studied site up to recent times. Significant results have been obtained on the submarine volcanic eruptions of El Hierro Island, referring to the physical and chemical perturbation and to the biological activity [11].

In 2017, Danovaro et al. [12] have recently studied the same volcano, publishing an article in Nature Ecology and Evolution, establishing that a submarine volcanic eruption leads to a novel microbial habitat. Near the top of the volcanic cone, marine exploration has revealed the occurrence of massive mats of white filaments. Microscopic and molecular analyses have revealed that these filaments are made of bacterial trichomes colonised by epibiotic bacteria. Surrounding biology suggests that these microorganisms can drive the restart of biological systems after submarine volcanic eruptions.

In this book, the exploration of the base of a Japanese volcano will be presented, the active stratovolcano of Mt. Zao, located in Northeastern Japan. More than 100 active volcanoes occur in Japan, representing about 10% of volcanoes of the world. They are located in correspondence with the so-called Pacific Ring of Fire, whose occurrence is controlled by important geological processes of subduction among plates. The Japanese region is located at the junction of the Pacific, Philippine, Eurasian and North American plates. Five main subduction zones occur. The Pacific plate descends under the North American plate forming the Kuril and the Japan trenches and controlling the formation of the Northeast Honshu and Kurile volcanic arcs to the north. On the other side, the Philippine plate undergoes subduction beneath the Eurasian plate, controlling the formation of the Ryukyu and Southwest Honshu volcanic arcs. Contemporaneously, the Pacific plate undergoes subduction beneath the Philippine plate, controlling the formation of the Izu-Bonin-Mariana volcanic arc. An important seismic activity is associated with these geodynamic processes, often triggering large tsunamis.

In particular, the Zao volcano, studied in this book, is located in the Northern Honshu volcanic district and is a complex volcanic edifice, characterised by an eruption style that is mainly explosive (phreatic) [13]. In the Honshu volcanic district, the Zao volcano is the most active volcanic edifice. It is composed of several stratovolcanoes, which divide the Pacific Ocean from the Japanese Sea. The older parts of the volcanic edifice are represented by the Ryuzan volcano in the western sector of the volcanic district and by the Byobu volcano and by the Fubo volcano, which are located in the southern sector of the volcanic district [13].

In this book, the characteristics of volcanic eruptions in Indonesia have also been discussed. The Indonesian region hosts about 147 volcanoes [14]. The archipelago is made up of more than 13,000 islands, spreading over a large area, and represents the country having the greatest number and density of active volcanoes [14]. The most prominent geological structure is represented

by the Sunda Volcanic Arc, resulting from related geological processes of subduction, involving the lithosphere of the Indian Ocean and the Asian Plate. The Andaman Islands, genetically related to the geodynamic and volcanic processes, are characterised by short spreading centres. On the other side, the Banda volcanic arc is formed as a result of the westwards-directed subduction of the Pacific Ocean. Proceeding northwards, the geodynamic setting becomes more and more complex, due to the individuation of multiple subduction zones, N–S trending [14].

In this book, another important research topic is represented by the Pekulney Ridge, located in Northeastern Russia. The Pekulney segment is characterised by a N–S trending portion of the Pekulney-Zolotogorskaya system, which, in its modern tectonic setting, is occupied by the Pekulney Ridge [15]. Its tectonic setting is characterised by several assemblages of the Late Jurassic-Early Cretaceous island arc (Parautochtone), its deformed pre-Late Mesozoic basement and Neoautochtone [15]. The tectonic setting of plagiogranites, coupled with their location, has indicated that they were intruded in the fore arc of the Pekulney segment of the Pekulney-Zolotogorskaya system. This intrusion was contemporaneous with the accretion of the oceanic-volcanic cherty complex and with the subduction and the island arc magmatism during Early Cretaceous times [15].

2. Geological and geophysical settings of volcanoes

In this book, several significant contributions dealing with the geological and geophysical setting of volcanoes have been presented. The study volcanoes are located in several places of the world (Vesuvius volcano, Southern Italy; Zao volcano, Northeastern Japan; Tagoro volcano, Canary Islands, Atlantic Ocean; Indonesian volcanoes, Indonesia; Pekulney Ridge volcanic complex, Northeastern Russia).

The geological and geophysical settings of volcanoes, as a general rule, are important research topics in the volcanological research. It is a broad research topic and many studies have been developed in these research fields, including the determination of the tectonic setting of basic volcanic rocks through the use of trace element analyses [16], the presentation of comprehensive geochemical data sets of recent volcanic rocks from the Mariana Islands, providing volcanological constraints on the timing and the nature of fluxes from the subducting slab [17] and the development of new methods to measure the deformations on volcanoes using interferometric synthetic aperture radar (INSAR) persistent scatterers [18].

The Somma-Vesuvius volcano is one of the most important morphological lineaments occurring in the Naples Bay, typically facing the town of Naples and representing, in some way, its symbol. Studies have been conducted deeply regarding its eruptive events, the recent seismicity involving the surroundings of the volcano, the geochemistry of the volcanic deposits and the volcanic hazard related to the volcano [5–7, 19–23]. The geological setting of the Somma-Vesuvius volcano has been simplified by the stratigraphy of the "Trecase 1" deep exploration well [24]. This well, located on the Vesuvius volcano, has drilled several volcanic complexes, respectively, located below and above the Campanian Ignimbrite deposits, representing an important volcanic marker of the Campania Plain and dating back to 37 ky B.P. In particular,

at the bottom of the well Mesozoic dolomites have been drilled (2068–1885 m), belonging to the paleogeographic unit known as "Piattaforma Campano-Lucana" *Auct.* [25, 26]. These carbonate deposits are overlain by tertiary continental calcareous conglomerates, interlayered with marine sediments. The tertiary deposits are, in turn, overlain by lavas and tuffites of the ancient Somma volcano, Pleistocene in age, alternating with marine deposits. These volcano-sedimentary deposits are overlain by the Campanian Ignimbrite pyroclastic flow deposits. At the top of the well, post-35 ky B.P., subaerial lavas and pyroclastics of Somma and Vesuvius volcanic edifices have been drilled.

3. Theoretical aspects and the numerical modelling of volcanoes

In this book, theoretical aspects of volcanoes have been pointed out through numerical modelling, referring, in particular, to the dynamics of volcanic systems (convective heat and mass transfer) in seismo-focal zones of the Kamchatka Region (Asia), to the analysis of the deformation of volcanic systems through finite element models and to the mechanical aspects referred to the magma chambers and corresponding implications on the flux of the CO_2.

The convective heat transfer is represented by the transfer of heat through the movements of fluids. This mechanism involves an integration between the conduction, represented by the diffusion of the heat, and the advection, represented by the transfer of the heat through the fluid flow.

The heat transfer by convection may be expressed through a basic relationship:

$$Q = hA\left(T_a - T_b\right) \tag{1}$$

In this relationship Q is the transferred heat/unit time, A is the area of the object, h is the coefficient of heat transfer, T_a is the temperature at the surface of the object and T_b is the temperature of the fluid.

The heat and mass transfer in volcanic systems have been deeply investigated. In particular, the chemical mass transfer in magmatic systems has been studied through the elaboration of a thermodynamic model, which takes into account the liquid–solid equilibrium in the volcanic systems, occurring both at elevated temperatures and pressures [27].

The convective heat transfer has been discussed through the mathematical formulation of numerical models, which have been applied to the geothermal systems [28]. The geothermal reservoirs are often characterised by vertical normal faults. The comprehension of the processes of convection to a large scale has been obtained through the idealisation of the reservoir as a porous medium. The thermal anomalies, which are genetically related with the transfer of heat, have been detected through surface manifestations, aerial infrared surveys, geochemical analyses and exploration wells [28].

A tool methodology has been constructed in the case of volcanic and hydrothermal systems in order to estimate the heat release and the carbon dioxide degassing [29]. In the construction

of this methodology, theoretical aspects have been clarified. Referring to the hydrothermal and volcanic emissions, the released energy represents a main component in the balance of energy of quiescent volcanoes. These balances have been often derived calculating the mass balance at crater lakes. They have also been estimated in the volcanic systems without crater lakes (Vulcano, Solfatara, Nisyros, Somma-Vesuvius and Ischia), ranging between 0.23 and 1.39×10^8 W. These estimates were carried out through measurements of CO_2, volcanic and hydrothermal in origin, which has been released through soil diffusion emission.

In this theoretical context the heat flux represents a linear function of the soil thermal gradient, which is proportional to the thermal conductivity [29]. The field and laboratory methods have included the CO_2 soil flux measurements, the temperature measurements along vertical profiles and the samples of fumaroles within the degassing areas. A physical modelling has been applied in order to simulate heat and fluid flow. The used geothermal simulator has accounted for the transport of heat and has been applied also to the degassing of the Solfatara crater at the Phlegraean Fields [30, 31].

The methodology of Chiodini et al. [29] has allowed us to estimate the amount of energy, which is released from volcanic and hydrothermal systems. The use of CO_2 as a tracer of the degassing process has allowed us to find a linear relationship between the fumarolic ratios of the fluids and the ratios of temperature in the shallow part of the soil.

The analysis of deformation in volcanic systems has been deeply studied, taking into account the development of new technologies and methodologies, including INSAR scatterometric measurements.

Hooper et al. [18] have developed a new method, based on the INSAR scatterer in order to analyse the crustal deformation occurring in volcanic systems. This method is based on the spatial correlation of the phases in order to observe the volcanic deformation, representing a geological process varying during geological time. The developed algorithm is based on the removal of the residual topographic component of flat phases of the interferograms and on phase correlation, both spatial and temporal.

The INSAR analysis has been applied also to volcanoes located in Alaska, analysing all available synthetic aperture radar (SAR) images of Okmok acquired during 1997–2008 by three different satellite sensors to investigate inter-eruption deformation patterns [32].

Another tool methodology in studying the deformation of volcanic systems is represented by satellite imagery, allowing for a global coverage of volcanoes, often not systematically surveyed, so providing probabilistic analyses which link the deformation with the volcanic eruption [33]. Taking a sample of 198 volcanoes, which were systematically observed in the last 18 years, 54 volcanoes have undergone a significant deformation and 25 of them erupted [33]. In such a framework the satellite technology applied to the monitoring of deformation in volcanic systems allows for the applications of probabilistic approaches, implying the hazard decisions and strategic development.

Significant studies on the relationships between volcanic activity and seismicity in volcanic settings have been recently furnished based on differential interferometric synthetic aperture

radar co-seismic measurements [34]. These measurements have been collected at Ischia (Southern Italy) and regard, in particular, that the earthquake source model of the Casamicciola earthquake occurred on 21 August 2018 [34]. The integration of geophysical data (seismological data, global positioning system, Sentinel 1 and Cosmo-Skymed) has indicated the occurrence of E–W trending normal faults, dipping southwards and located at depths of 800 m [34].

4. Application of volcanoes to the industry

In this book, the applications of studies on volcanoes to the industry are also presented. In particular, they deal with the use of volcanic scorias as cement replacement and with the volcanic glasses or obsidians and their use as adsorbents.

Volcanic scorias as cement replacement deal with the use of natural pozzolans, representing a common technique in the construction industry and having economic, ecologic and performance benefits. The advantages and the disadvantages of the use of volcanic scoria as cement replacement in concrete mixes in terms of fresh and hardened concrete properties have been shown. The chemical and mineralogical composition of volcanic scoria samples collected from 36 countries has been presented. The effects of using volcanic scoria as cement replacement on some past, mortar and concrete properties, such as the setting times, the heat of hydration, the compressive strength, the water permeability and the chloride penetrability, have been studied. The improvement in resistance against the chemical attack of volcanic scoria-based cement mortar has also been highlighted. Some estimation equations depending on the data available in literature have been derived from the analysed data. The modification of the microstructure of VS-based cement paste has been confirmed, as well.

Volcanic glasses and their use as adsorbents have been studied in detail. The capacity of adsorption of perlite is explained through the occurrence of hydroxyl groups on the surface of the perlite. As a consequence, the silicon atoms maintain their coordination attaching to the monovalent hydroxyl groups; they form silanol groups, whose chemical reactions have been explained. The adsorption of cations and anions has also been explained. The heavy metals represent the most important pollutants harming the aqueous environment and damaging the health of human beings, animals and plants. These metal ions tend to accumulate in the living organisms, provoking different diseases and disorders and having the possibility to be diluted but not destroyed. The ions of heavy metals cause serious health implications on the vital organs of human beings and animals, if they are consumed above certain threshold concentrations. The removal of these toxic metals may be performed through the chemical precipitation, the extraction of solvents, the exchange of ions, the reverse osmosis and nanofiltration. Due to its use as an adsorbent, perlite represents a material having a high potential, due to its low cost and high availability.

The application of volcanoes to the industry are numerous and have been resumed by Dehn and McNutt [35], delineating the use of volcanic materials in commerce and industry. Some key terms need to be clarified in order to improve the understanding of volcanic materials in the industry, as treated in this book, such as the absorbent, representing a material taking up,

assimilating or incorporating liquids through pore interstices, the obsidian, representing a black glassy rock, often of a rhyolitic composition, undergoing a process of devitrification and forming crystal structures, and the pozzolan, a siliceous volcanic ash used to create hydraulic cement [35].

The explosive volcanic products tend to form aggregates, having a low density, and are often vesicular, giving good insulating qualities. Among the industrial processes, the manufacture of perlite is designed to enhance these characteristics. The lava flows and the welded ignimbrites represent cost-effective building materials. Moreover, the concrete constructed from volcanic cinders is a good insulator if compared with the normal concrete, due to the high vesicularity of the cinders used in its manufacture. The vesicles tend to resist the heat's transfer, making it difficult for thermal energy to move through the block [35].

The modern uses of volcanic rocks in the industry range from the mining of volcanogenic minerals for manufacturing and lubricants to their use as construction materials. In the industrial use, the aggregates represent broken pieces of rocks, including the volcanic aggregates, the cinders and the scorias, used for both the construction of roads and the production of building materials. The aggregates may be used as loose aggregates, refractories and absorbents [35].

Perlite represents a volcanic glass, which is highly hydrated and is generally used as a lightweight aggregate. Moreover, perlite has some special uses, as the substitute of sands in lightweight wall plaster and their use in ceramic production, fillers and filters. On the other side, the refractories are materials which are not deformed or damaged by high temperatures. Consequently, they are used to make firebricks, crucibles, insulation and furnace linings. The ingredients of refractories also include the pumices and the clays, while bentonite has been used as a binder during production [35].

The use of volcanic materials in the construction industry is widespread, including the massive stones, providing good building materials, especially lavas and ignimbrites, having high strengths and insulating qualities, the concrete and the cinder blocks, used in creating concrete prefabricated parts for buildings. Moreover, some soft volcanic rocks, such as ignimbrites, have been used for tunnelling, storage and housing (Japan, Ischia, Herculaneum of Pompei and New Guinea) [35].

5. Impact of volcanoes on human health

In this book, the impact of volcanoes on human health has also been considered, dealing, in particular, with the impact of volcanic emissions on human health. As it has been clarified from the authors, the health effects of volcanic emissions depend on their physical and chemical characteristics and by the corresponding toxicological properties, as a consequence of the inhalation of particles directly emitted from the active volcanoes or through the re-suspension of the soil ashes during the cleaning task after the eruption. The effects on human health derived from such an exposure can be classified as acute and chronic.

The health impact of volcanic emissions represents an intriguing research topic and has been studied by different authors. In particular, studies of the respiratory health effects of different

types of volcanic ash have been undertaken only in the last 40 years and mostly since the eruption of Mt. St Helens in 1980. This review of all published clinical, epidemiological and toxicological studies, and other work known to the authors up to and including 2005, highlights the sparseness of studies on acute health effects after the eruptions and the complexity of evaluating the long-term health risk (silicosis, non-specific pneumoconiosis and chronic obstructive pulmonary disease) in populations from prolonged exposure to ash due to persistent eruptive activity [36].

Volcanoes and their eruptions can result in a wide range of health impacts, arguably more varied than in any other kind of natural disaster. At least 500 million people worldwide live within the potential exposure range of a volcano that has been active in recorded history. Many volcanic and geothermal regions are densely populated and several are close to major cities, threatening local populations. Volcanic activity can also affect areas hundreds or thousands of kilometres away, as a result of airborne dispersion of gases and ash or even on a hemispheric to global scale due to impacts on climate. Healthcare workers and physicians responding to the needs of volcanic risk management might therefore find themselves involved in scenarios as varied as disaster planning, epidemiological surveillance, treating the injured or advising on the health hazards associated with long-range transport of volcanic emissions [37].

A health hazard assessment of exposure to soil gases (carbon dioxide and radon) was undertaken in the village of Furnas, located in the caldera of an active volcano. A soil survey to map the area of soil gas flow was undertaken, gas emissions were monitored at fumaroles and in eight houses and a preliminary radon survey of 23 houses in the main anomaly area was performed. Potential volcanic sources of toxic contamination of air, food and water were also investigated, and ambient air quality was evaluated. About one-third (41 ha) of the houses were located in areas of elevated carbon dioxide soil degassing [38].

Millions of people are potentially exposed to volcanic gases worldwide, and exposures may differ from those in anthropogenic air pollution. A systematic literature review found few primary studies relating to health hazards of volcanic gases. SO_2 and acid aerosols from eruptions and degassing events were associated with respiratory morbidity and mortality but not childhood asthma prevalence or lung function decrements. Accumulations of H_2S and CO_2 from volcanic and geothermal sources have caused fatalities from asphyxiation. Chronic exposure to H_2S in geothermal areas was associated with increases in the nervous system and respiratory diseases. Some impacts were on a large scale, affecting several countries (e.g., Laki fissure eruption in Iceland in 1783–4). No studies on health effects of volcanic releases of halogen gases or metal vapours were located. More high-quality collaborative studies involving volcanologists and epidemiologists are recommended [39].

Volcanoes provide a conduit by which magma—the molten rock, gases and water within the Earth—may interact with human biological systems. Because of the range of materials that are ejected during eruptions, the consequent effects on the human health are different. Contact may occur dramatically and immediately for people living close to the vent, such as from pyroclastic density currents or the emission of large projectiles. Alternatively, effects on health may occur slowly or at great distances from the volcano as a result of dispersal of volcanic material such as ash and aerosols [40].

A time-averaged inventory of subaerial volcanic sulphur (S) emissions was compiled primarily for the use of global S and sulphate modellers. This inventory relies upon the 25-year history of S, primarily sulphur dioxide (SO_2), measurements at volcanoes. Subaerial volcanic SO_2 emissions indicate a 13 Tg/a SO_2 time-averaged flux, based from an early 1970s to 1997 time frame. When considering other S species present in volcanic emissions, a time-averaged inventory of subaerial volcanic S fluxes is 10.4 Tg/a S. These time-averaged fluxes are conservative minimum fluxes since they rely upon actual measurements. The temporal, spatial and chemical inhomogeneities inherent to this system gave higher S fluxes in specific years. Despite its relatively small proportion in the atmospheric S cycle, the temporal and spatial distribution of volcanic S emissions provides disproportionate effects at local, regional and global scales [41].

Fluid geochemistry monitoring in the Azores involves the regular sampling and analysis of gas discharges from fumaroles and measurements of CO_2 diffuse soil gas emissions. Main degassing areas under monitoring are associated with hydrothermal systems of active central volcanoes in S. Miguel, Terceira and Graciosa islands. Fumarole discharge analysis since 1991 show that apart from steam these gas emissions are CO_2 dominated with H_2S, H_2, CH_4 and N_2 in minor amounts. Mapping of CO_2 diffuse soil emissions in S. Miguel Island leads to the conclusion that some inhabited areas are located within hazard-zones. At Furnas village, inside Furnas volcano caldera, about 62% of the 896 houses are within the CO_2 anomaly, 5% being in areas of moderate-to-high risk. At Ribeira Seca, on the north flank of Fogo volcano, few family houses were evacuated when CO_2 concentrations in the air reached 8 mol%. To assess and analyse the CO_2 soil flux emissions, continuous monitoring stations were installed in S. Miguel (2), Terceira and Graciosa islands. The statistical analysis of the data showed that some meteorological parameters influence the CO_2 flux. The average of CO_2 flux in S. Miguel stations ranges from 250 g/m^2 /d at Furnas volcano to 530 g/m^2 /d at Fogo volcano. At Terceira Island, it is about 330 g/m^2 /d, and at Graciosa, it is 4400 g/m^2/d [42].

Passive samplers were used to measure the atmospheric concentrations of SO_2 naturally emitted at three volcanoes in Italy (Etna, Vulcano and Stromboli) and of H_2S naturally emitted at three volcanic/geothermal areas in Greece (Milos, Santorini and Nisyros). The measured concentrations and dispersion patterns varied with the strength of the source (open conduits or fumaroles), the meteorological conditions and the area topography. At Etna, Vulcano and Stromboli, SO_2 concentrations reach values that are dangerous to people affected by bronchial asthma or lung diseases (>1000 μg m^{-3}). H_2S values measured at Nisyros also exceed the limit considered safe for the same group of people (>3000 μg m^{-3}). The data obtained using passive samplers represent time-averaged values over periods from a few days up to 1 month, and hence concentrations probably reached much higher peak values that were potentially also dangerous to healthy people. The present study provides evidence of a peculiar volcanic risk associated with tourist exploitation of active volcanic areas. This risk is particularly high at Mt. Etna, where the elderly and people in less-than-perfect health can easily reach areas with dangerous SO_2 concentrations via a cableway and off-road vehicles [43].

Author details

Gemma Aiello

Address all correspondence to: gemma.aiello@iamc.cnr.it

Institute of Marine and Coastal Environment (IAMC), National Research Council of Italy (CNR), Napoli, Italy

References

[1] Simkin T, Siebert DL. Volcanoes of the World. 2nd ed. Tucson, Arizona: Geoscience Press, Inc.; 1994. p. 349. ISBN 0-945005-12-1

[2] Coltelli M, Del Carlo P, Vezzoli L. Discovery of a plinian basaltic eruption of Roman age at Etna volcano, Italy. Geology. 1998;**26**(12):1095-1098

[3] Coltelli M, Del Carlo P, Vezzoli L. Stratigraphic constraints for explosive activity in the past 100 ka at Etna volcano, Italy. International Journal of Earth Sciences. 2000;**89**:665. DOI: 10.1007/s005310000117

[4] Branca S, Coltelli M, Groppelli G, Lentini F. Geological map of Etna volcano, 1:50,000 scale. Italian Journal of Geosciences. 2011;**130**(3):265-291

[5] Cassano E, La Torre P. Geophysics. In: Santacroce R, editor. Somma-Vesuvius. Roma, Italy: CNR, Quaderni De La Ricerca Scientifica; 1987

[6] Santacroce R. Somma-Vesuvius. Roma, Italy: CNR, Quaderni De La Ricerca Scientifica; 1987

[7] Castellano M, Buonocunto C, Capello M, La Rocca M. Seismic surveillance of active volcanoes: The Osservatorio Vesuviano seismic network (OVSN-Southern Italy). Seismology Research Letters. 2002;**73**:177-184

[8] Nakamura K. Volcanoes as possible indicators of tectonic stress orientation—Principle and proposal. Journal of Volcanology and Geothermal Research. 1977;**2**:1-16

[9] Acocella V, Neri M. Dike propagation in volcanic edifices: Overview and possible developments. Tectonophysics. 2009;**471**(1-2):67-77

[10] Togashi S, Terashima S. The behavior of gold in unaltered island arc tholeiitic rocks from Izu-Oshima, Fuji, and Osoreyama volcanic areas, Japan. Geochimica and Cosmochimica Acta. 1997;**61**(3):543-554

[11] Fraile Nuez E, Gonzalez-Dvila M, Santana-Casiano JM, Astergui J, Alonso Gonzalez IJ, Hernandez-Len S, Blanco MJ, Rodriguez-Santana A, Hernandez-Guerra A, Gelado-Caballero MD, Eugenio F, Marcello J, de Armas D, Dominguez-Yanes JF, Montero MF,

Laetsch DR, Vlez-Belch P, Ramos A, Ariza AV, Comas-Rodriguez I, Bentez-Barrios VM. The submarine volcano eruption at the island of el hierro: Physical-chemical perturbation and biological response. Scientific Reports. 2012;**2**(486). DOI: 10.1038/srep00486

[12] Danovaro R, Canals M, Tangherlini M, Dell'Anno A, Gambi C, Galderic L, Amblas D, Sanchez-Vidal A, Frigola J, Calafat AM, Pedrosa R, Rivera J, Rayo X, Corinaldesi C. A submarine volcanic eruption leads to a novel microbial habitat. Nature Ecology and Evolution. 2017;**1**(0144):1-8

[13] https://www.volcanodiscovery.com/zao.html

[14] https://www.volcanodiscovery.com/indonesia.html

[15] Luchitskaya MV, Morozov OL, Palandzhyan SA. Plagiogranite magmatism in the Mesozoic island-arc structure of the Pekulney Ridge, Chukotka Peninsula, NE Russia. Lithos. 2005;**79**(1-2):251-269

[16] Pearce JA, Cann JR. Tectonic setting of basic volcanic rocks determined using trace element analyses. Earth and Planetary Science Letters. 1973;**19**(2):290-300

[17] Elliott T, Plank T, Zindler A, White W, Bourdon B. Element transport from slab to volcanic front at the Mariana arc. Journal of Geophysical Research, Solid Earth. 1997; **102**(B7):14,991-15,019

[18] Hooper A, Zebker H, Segall P, Kampes B. A new method for measuring deformation on volcanoes and other natural terrains using InSAR persistent scatterers. Geophysical Research Letters. 2004;**31**:L23611. DOI: 10.1029/2004GL021737

[19] Esposti Ongaro T, Neri A, Todesco M, Macedonio G. Pyroclastic flow hazard at Vesuvius from numerical modelling II. Analysis of local flow variables. Bulletin of Volcanology. 2002;**64**:178-191

[20] Mastrolorenzo G, Palladino D, Vecchio G, Taddeucci J. The 472 A.D. Pollena eruption at Somma-Vesuvius (Italy) and its environmental impact at the end of Roman Empire. Journal of Volcanology and Geothermal Research. 2002;**113**:19-36

[21] Saccorotti G, Ventura G, Vilardo G. Seismic swarms related to diffusive processes: The case of Somma-Vesuvius volcano, Italy. Geophysics. 2002;**67**:199-203

[22] Scarpa R, Tronca F, Bianco F, Del Pezzo E. High-resolution velocity structure beneath mount Vesuvius from seismic array data. Geophysical Research Letters. 2002;**29**:2040. DOI: 10.1029/2002GL015576

[23] Todesco M, Neri A, Esposti Ongaro T, Papale P, Macedonio R, Santacroce R. Pyroclastic flow hazard at Vesuvius from numerical modeling. Bulletin of Volcanology. 2002;**64**: 155-177

[24] Brocchini F, Principe C, Castradori D, Laurenzi MA, Gorla L. Quaternary evolution of the southern sector of the Campanian plain and early Somma-Vesuvius activity: Insights from the Trecase well. Mineralogy and Petrology. 2001;**73**:67-91

[25] D'Argenio B, Pescatore TS, Scandone P. Schema geologico-strutturale dell'Appennino meridionale (Campania e Lucania). Quaderni dell'Accademia Nazionale dei Lincei, Problemi Attuali di Scienza e Cultura. 1973;**183**:49-72

[26] Bigi G, Cosentino D, Parotto M, Sartori R, Scandone P. Structural Model of Italy. Monografie Progetto Finalizzato Geodinamica. Roma, Italy: CNR; 1992

[27] Ghiorso MS, Sack RO. Chemical mass transfer in magmatic processes IV. A revised and internally consistent thermodynamic model for the interpolation and extrapolation of liquid-solid equilibria in magmatic systems at elevated temperatures and pressures. Contributions to Mineralogy and Petrology. 1995;**119**(2-3):197-212

[28] Cheng P. Heat transfer in geothermal systems. Advances in Heat Transfer. 1979;**14**:1-105

[29] Chiodini G, Granieri D, Avino R, Caliro S, Costa A, Werner C. Carbon dioxide diffuse degassing and estimation of heat release from volcanic and hydrothermal systems. Journal of Geophysical Research. 2005;**110**:B08204

[30] Chiodini G, Todesco M, Caliro S, Del Gaudio C, Macedonio G, Russo M. Magma degassing as a trigger of bradyseismic events: The case of Phlegrean fields, Italy. Geophysical Research Letters. 2003;**30**(8):1434

[31] Todesco M, Chiodini G, Macedonio G. Monitoring and modelling hydrothermal fluid emission at La Solfatara (Phlegrean fields, Italy): An interdisciplinary approach to the study of diffuse degassing. Journal of Volcanology and Geothermal Research. 2003;**125**: 57-79

[32] Lu Z, Dzurisin D, Biggs J, Wicks C Jr, McNutt S. Ground surface deformation patterns, magma supply, and magma storage at Okmok volcano, Alaska, from InSAR analysis: 1. Intereruption deformation, 1997-2008. Journal of Geophysical Research. 2010;**115**:B00B02. DOI: 10.1029/2009JB006969

[33] Biggs J, Ebmeier SK, Aspinall WP, Lu Z, Pritchard ME, Sparks RSJ, Mather TA. Global link between deformation and volcanic eruption quantified by satellite imagery. Nature Communications. 2014;**5**(3471). DOI: 10.1038/ncomms4471

[34] de Novellis V, Carlino S, Castaldo R, Tramelli A, De Luca C, Pino NA, Pepe S, Convertito V, Zinno I, De Martino P, Bonano M, Giudicepietro F, Casu F, Macedonio G, Manunta M, Cardaci C, Manzo M, Di Bucci D, Solaro G, Zeni G, Lanari R, Bianco F, Tizzani P. The 21 August 2017 Ischia (Italy) earthquake source model inferred from seismological, GPS and DInSAR measurements. Geophysical Research Letters. 2018;**45**:2193-2202. DOI: 10.1002/2017GL076336

[35] Dehn J, McNutt SR. Volcanic Materials in Commerce and Industry. Chapter 74, in the Encyclopedia of Volcanoes. Elsevier Science Publishers; 2015. pp. 1285-1294

[36] Horwell CJ, Baxter PJ. The respiratory health hazards of volcanic ash: A review for volcanic risk mitigation. Bulletin of Volcanology. 2006;**69**(1):1-24

[37] Hansell AL, Horwell CJ, Oppenheimer C. The health hazards of volcanoes and geothermal areas. Occupational and Environmental Medicine; **63**(2):149-156. DOI: 10.1136/oem.2005.022459

[38] Baxtera PJ, Baubron JC, Coutinoc R. Health hazards and disaster potential of ground gas emissions at Furnas volcano, Sao Miguel, Azores. Journal of Volcanology and Geothermal Research. 1999;**92**(1-2):95-106

[39] Hansell A, Oppenheimer C. Health hazards from volcanic gases: A systematic literature review. Archives of Environmental Health: An International Journal. 2004;**59**(12):628-639. DOI: 10.1080/00039890409602947

[40] Weinstein P, Horwell CJ, Cook A. Volcanic emissions and health. In: Selinus O. (Ed.) Essentials of Medical Geology. Springer, Dordrecht, 2013

[41] Andres RJ, Kasgnoc AD. A time-averaged inventory of subaerial volcanic sulfur emissions. Journal of Geophysical Research. 1998;**103**(D19):25251-25261. DOI: 10.1029/98JD02091

[42] Ferreira T, Gaspar J, Viveiros F, Marcos M, Faria C, Sousa F. Monitoring of fumaroles discharge and CO_2 soil degassing in the azores: Contribution to volcanic surveillance and public health risk assessment. Annals of Geophysics. 2005;**48**(4-5):787-796

[43] Aiuppa A, Bellomo S, Brusca L, Calabrese S, Kyriakopoulos K, Liotta M, Longo M, D'Alessandro W. Sulphur-gas concentrations in volcanic and geothermal areas in Italy and Greece: Characterising potential human exposures and risks. Journal of Geochemical Exploration. 2013;**131**:1-13

Section 2

Geological and Geophysical Setting of Volcanoes

Chapter 2

Correlation between Seismic and Volcanic Activity at a Large Spatial Scale in Italy: Examples from the Neapolitan Volcanic District (Vesuvius Volcano, Southern Italy)

Pier Luigi Bragato

Additional information is available at the end of the chapter

http://dx.doi.org/10.5772/intechopen.71977

Abstract

The time correlation between the eruptions of Mt Vesuvius and the occurrence of strong earthquakes in Italy has been revised using new and improved catalogs and data made available in the last decade. It has been shown that this correlation is statistically significant and involves also the earthquakes located very far from the volcanic edifice (hundreds of kilometers). In particular, the earthquakes and the Vesuvius' eruptions agree on a transient of accelerated activity between 1600 and 1900. A similar correlation has been found between the seismicity and the uplift episodes at the nearby Campi Flegrei caldera occurred in the last 70 years: there is strict similarity between the two cycles, the first one centered around 1970–1980 and the second one started on 2004 and still continuing and involving recent strong earthquakes (2009 L'Aquila earthquake, 2012 Emilia earthquake and 2016 Central Italy earthquake). The synchronization to such a long distance has suggested the occurrence of large-scale climatic processes controlling both the earthquakes and the volcanism. The comparison with climatic indexes like the global surface temperature and the extension of glaciers in western-central Europe has indicated a possible role of climatic parameters in controlling volcanism and seismicity.

Keywords: Mt Vesuvius, Campi Flegrei caldera, Italian seismicity, event synchronization, Ripley's K-function

1. Introduction

The correlation between the volcanic activity and the earthquakes is a well-known subject of investigation. It commonly refers to two distinct aspects: first, the seismicity in volcanic areas

related to magmatic and hydrothermal movements, which is of interest for predicting the possible volcano unrest [1] and second, discussed in this chapter, the possible triggering of eruptions caused by stress transfer due to strong earthquakes, even located far from the volcano edifice [2]. A recent study carried out to a global scale [3] has shown that this mechanism of triggering is effective for very strong earthquakes (Mw ≥ 7.5) located within 200 km from the volcano. In Italy, the availability of reliable catalogs covering several centuries of earthquake and eruptive observations gives the possibility to explore the long-distance volcanic/seismic relationship with more detail. According to previous studies [4–6], such link is particularly evident for the eruptions of Mt Vesuvius, near Naples, in southern Italy (triangle in **Figure 1**).

The Vesuvius volcano is one of the most studied in the world. Through the centuries, eruptions were described by Neapolitan and foreign scholars. A significant step was performed on 1841, with the institution of the "Osservatorio Vesuviano", the first volcanology observatory in the world. Nowadays, Mt Vesuvius is monitored by a dense network of seismic, geochemical, and GPS stations (http://www.ov.ingv.it/ov/it/vesuvio). Its eruptive history for the last 2000 years is well known through the historical sources and the archaeomagnetic dating of

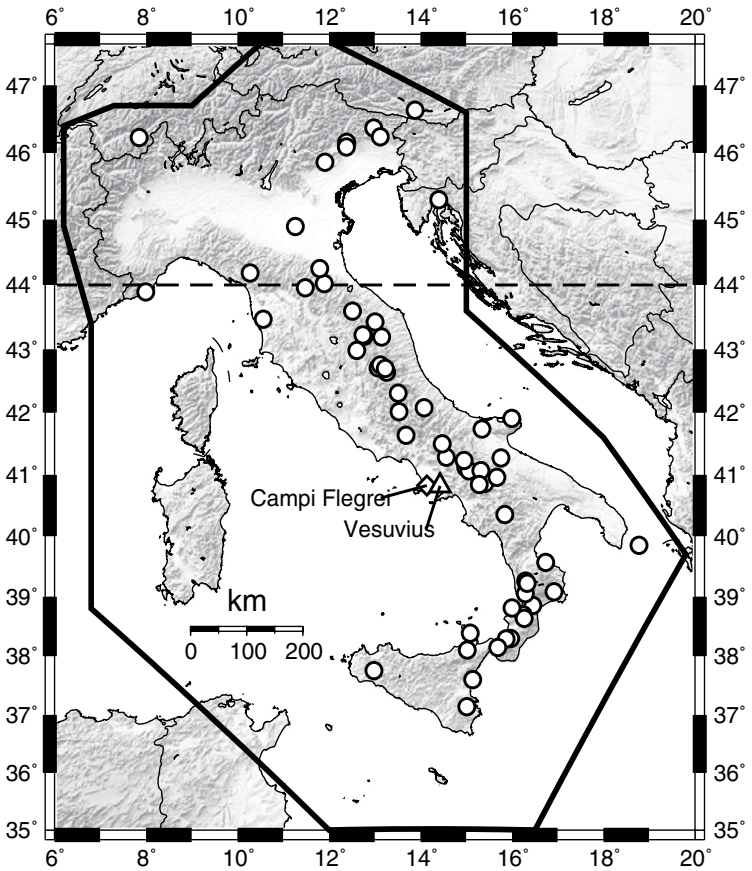

Figure 1. Epicenters of Mw ≥ 6.0 earthquakes occurred in Italy between 1600 and 2016 (declustered catalog).

volcanic deposits [7]. In particular, in the last millennium, after a few centuries of weak activity, the Vesuvius awakened on 1631 and entered in a long period of sustained and almost continuous activity concluded with its last eruption of 1944 [8], followed by the current phase of quiescence.

In the last few decades, geological and geophysical investigations have improved the knowledge about the tectonic setting of Mt Vesuvius as well as its internal structure and magmatic system [4, 9, 10]. Concerning the relationships with far seismicity, [4] has furnished statistical evidence for the time correlation between the eruptions of Mt Vesuvius and moderate-strong earthquakes ($Mw \geq 5.4$) in the Southern Apennines. In [5], such correlation is modeled as the effect of mutual stress transfer working at distances up to 150 km. In [6], it has been observed that the synchronization of eruptions with $Mw \geq 6$ earthquakes occurring throughout the national territory, even hundreds of kilometers far from the volcano and in different tectonic domains. This finding has suggested the occurrence of a common cause at the basis of the two phenomena rather than a direct interaction or mutual triggering.

The investigation of the seismic/volcanic relationship requires two components: statistical methods to assess the existence of the correlation and to estimate its strength and geophysical methods able to furnish realistic models for its occurrence. This chapter is focused on the first aspect and presents an application of the modified Ripley's K-function to countrywide strong seismicity and to the eruptions of Mt Vesuvius since the seventeenth century.

Statistics alone is not able to distinguish between a causal relationship (earthquake triggering eruptions) and the co-causal hypothesis (an external mechanism controlling both earthquakes and eruptions). Elements on this topic can be obtained looking at the bradyseism of the Campi Flegrei caldera (white diamond in **Figure 1**). The caldera and Mt Vesuvius are very near (25 km apart), share a similar regional tectonic environment, and, according to [11], have a common magma chamber. Furthermore, they alternate over time: the caldera was at rest during the intense eruptive period of Mt Vesuvius (1631–1944) and reactivated with an uplift process just after its conclusion (around 1950). Similarly to the eruptions of Mt Vesuvius, the phases of major uplift coincide with accelerated seismic activity in Italy. In a way, the two volcanoes look like twin systems with related behavior. The hypothesis here assumed is that what observed for the sismic/volcanic connection at Campi Flegrei in the last few decades can be reasonably extended to the past activity of Mt Vesuvius. In respect to analyzing rare eruptions, the bradyseism offers more details, thanks to the density of uplift measures in the last 70 years (almost continuous since 2000).

Recent works [6, 12, 13] have pointed out the correspondence between variations in the rate of seismicity throughout Italy and the climatic changes of the last millennium. In particular, the seismic activity accelerated during the most severe period of the Little Ice Age (between 1600 and 1900), while it seems to decrease in the current phase of global warming.

At the end of this chapter, it will be shown that this correspondence can be extended to the eruptive history of Mt Vesuvius. The finding leads to the hypothesis that the climate-related surface processes like glaciation/deglaciation and sea level changes could play a significant role in regulating both the eruptions and the earthquakes.

2. Volcanological and seismological data

The eruptive history of Mt Vesuvius is drawn from the Smithsonian's Global Volcanism Program (GVP) database ([14]; http://www.volcano.si.edu), where each eruption is described by its start date, by its end date, and by the Volcanic Explosivity Index (VEI [15]). An eruption can last from days to decades, and the VEI is attributed based on the strongest, often final, episode. The current analysis has been performed for the eruptions with VEI ≥ 2, assuming that for Mt Vesuvius, the catalog is complete at this level since the year 1600. This is a work hypothesis that seems to be acceptable given the proximity of the volcano to Naples, one of the largest cities in Europe since the Middle Ages. The selected dataset includes 25 eruptions since 1631. The last eruptive cycle started on 1913 and concluded on 1944 (VEI = 3).

The earthquake catalog herein adopted is the same of [13]. Its main characteristics and the processing steps are summarized as it follows. For the years between 1600 and 2014, the seismic events are drawn from the latest revision of the "Catalogo Parametrico dei Terremoti Italiani" (CPTI15, release 1.5 [16]). The dataset extends up to the end of 2016 with the earthquakes reported in the European-Mediterranean Regional Centroid Moment Tensor (RCMT) Catalog [17]. The resulting catalog includes the earthquakes located in Italy and in a narrow surrounding area. Among these events, only the mainshocks have been considered: the clusters of aftershocks have been removed using the algorithm described in [18]. It is important to guarantee that the catalog is complete at the same magnitude level in different time periods to avoid a biased analysis. To this purpose, after considering the completeness analysis carried out in [19], the catalog is assumed to be complete for a moment magnitude Mw larger or equal to 6. The selected dataset contains 60 earthquakes, including the recent destructive earthquake of Central Italy, occurred on August 24, 2016 (Mw 6.2 [17]).

A correlation analysis has been performed for the vertical ground movements at Campi Flegrei. A time history for the period 1905–2017 has been obtained merging the geodetic measurements available from 1905 to 2009 for the benchmark 25A in a leveling line established by the Istituto Geografico Militare (IGM) on 1905 [20], the measurements collected between January 2000 and July 2013 at the GPS station RITE located about 200 m from the benchmark 25A [21], and more recent GPS measurements from the same station (August 2014–April 2017) published in the online monthly bulletins published by the Osservatorio Vesuviano (http://www.ov.ingv.it/ov/campi-flegrei).

3. Time correlation between the eruptions of Mt Vesuvius and strong earthquakes throughout Italy

In this section, the times of occurrence of Vesuvius' eruptions, $V = \{V_1, \ldots, V_{nV}\}$, and those of strong earthquakes in Italy, $E = \{E_1, \ldots, E_{nE}\}$ are compared to assess their time correlation. There are different techniques to perform the task. One possibility, if the number of events sufficiently large, is to compare the histograms representing the time distribution of the events: the period of observation (t_{start}, t_{end}) is subdivided in n_b bins of equal width Δt and the

analysis is performed for the two time series $X = \{X_1, \ldots, X_{nb}\}$ and $Y = \{Y_1, \ldots, Y_{nb}\}$, where X_i and Y_i are the number of eruptions and earthquakes in the ith time bin, respectively. The degree of correlation can be assessed parametrically, using Pearson correlation, which assumes a bivariate normal distribution of data, or non-parametrically, using either Kendall or Spearman rank correlation, which are independent on the type of data distribution. A more flexible way to represent and compare two time distributions of events (useful even in the case they are rare) looks at their smoothed time density obtained by Gaussian kernel estimation [22]. The correlation coefficient (Pearson, Kendall or Spearman) is computed for the two functions

$$\hat{f}(t) = \frac{1}{n_V}\sum_{i=1}^{n_V}\varphi\left(V_i - t; h\right)\hat{g}(t) = \frac{1}{n_E}\sum_{i=1}^{n_E}\varphi\left(E_i - t; h\right) \quad (1)$$

where $\varphi(z;h)$ is the kernel function (zero-mean normal density function in z with standard deviation h), and h is the smoothing parameter (the larger h, the larger the degree of smoothing). Both approaches suffer a common limitation: their results depend on the time resolution adopted for the analysis (i.e., the width of the bin for the histogram, the smoothing parameter for kernel density estimation). In general, a large time window could lead to similar flat distributions and then to a spurious high correlation. A partial solution is to perform a sensitivity analysis, checking how the value of the correlation coefficient varies for different time resolutions. A totally different approach is that based on the bivariate, Ripley's K-function [23] simplified for one dimension [24, 25]. It works directly on the two sets of event times, avoiding any transformation and arbitrary choice of parameters and consequent loss of information. The K-function is a function of time with equation.

$$K_{\mathrm{VE}}(t) = \frac{T}{n_V n_E}\sum_{i=1}^{n_V}\sum_{j=1}^{n_E} I\left(\left|V_i - E_j\right| < t\right), \quad (2)$$

where $I()$ is the identity function (it returns 1 if its argument is true, 0 otherwise) and T is the total period of observation in years. The K-function is transformed to obtain the L-function

$$L_{\mathrm{VE}}(t) = \frac{K_{\mathrm{VE}}(t)}{2} - t \quad (3)$$

The L-function is associated with a 95% confidence envelope computed using N randomizations of V and E (N = 1000 in the present analysis). If, for given t, $L_{VE}(t)$ is larger than the confidence envelope, then the number of couples for which $|V_i - E_j| < t$ is significantly larger than those awaited in a random distribution: it is an indication of synchrony within a time lag t between the two sets of events. Similarly, values of $L_{VE}(t)$ within the confidence envelope indicate independence, while values falling under the confidence envelope indicate asynchrony or repulsion. In the following, the synchronization of events is explored graphically by means of their smoothed time densities, while it is assessed formally examining the L-function. The analysis updates that performed in [12] for an older version of the earthquake catalog.

The eruptive history of Mt Vesuvius between the seventeenth century and the beginning of the twentieth century is illustrated in **Figure 2a**. After a long period of weak activity (6 eruptions since 1100, including a VEI 2 eruption on 1500 and a VEI 1 eruption on 1570), the volcano

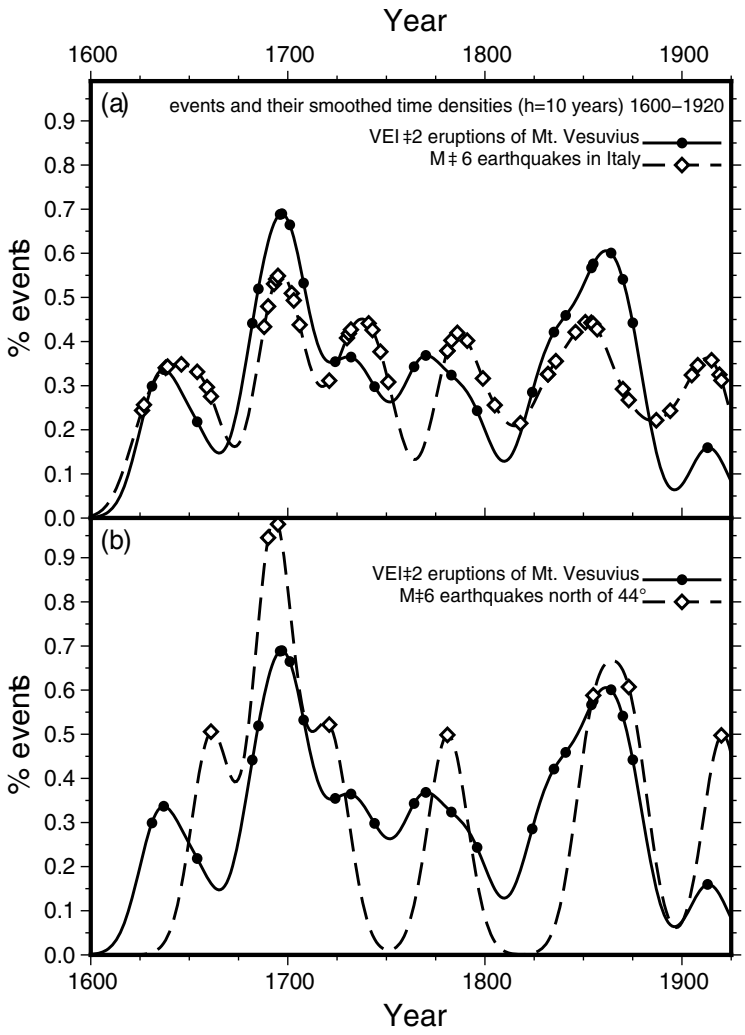

Figure 2. Time distribution of strong earthquakes in Italy compared to Vesuvius' eruptions in the time period 1600–1920: (a) seismicity of the entire territory; (b) earthquakes located north of 44° lat.

reactivated with the strong eruption of 1631 (VEI 5), followed by 24 eruptions (4 with VEI = 2, 19 with VEI = 3, and 1 with VEI = 4). Their smoothed time densities computed for h = 10 years (continuous line in **Figure 2a**) indicate two peaks around 1700 and 1850, as well as an overall oscillatory behavior with a time period of about 50 years. Such trend is very similar to that of the earthquakes (dashed line in **Figure 2a**). Eruptions and earthquakes appear almost synchronous on six regular oscillations. The characteristics of such oscillations were explored graphically in [6]. A more formal test based on Schuster spectrum analysis [26] has been adopted in [13] for the oscillations of seismicity. It demonstrates the statistical significance of the oscillations and refines the estimation of their time period to 46 years. Applied to the set of Vesuvius' eruptions the same test fails, indicating that the oscillations are too weak to gain a

http://dx.doi.org/10.5772/intechopen.71977

statistical significance. Nonetheless, the similarity between the two smoothed time densities is such to suggest a formal test for synchronization. The L-function and the corresponding 95% envelope computed for the two sets of events are traced in **Figure 3a**. The time correlation is significant for the time lags of 3 and 9 years, where the L-function exceed the 95% envelope. **Figures 2b** and **3b** show the same comparison performed for 9 earthquakes located above the 44th parallel north (evidenced with dashed line in **Figure 1**), at more than 400 km from the Vesuvius. Even in this case, the two time densities are similar, with a good correspondence on the two peaks near 1700 and 1850 and less precision on the other local maxima, especially before 1700. The L-function (**Figure 3b**) reflects such deteriorated time correlation: the 95% envelope (dashed line) is just touched for a time lag of 3 years, while there is a widespread time synchronization significant at the 90% confidence level (dotted line) for various time lags up to 25 years, the semi-period of oscillation. Such result indicates that there is some degree of overlapping among the positive part of the oscillations, near the local maxima.

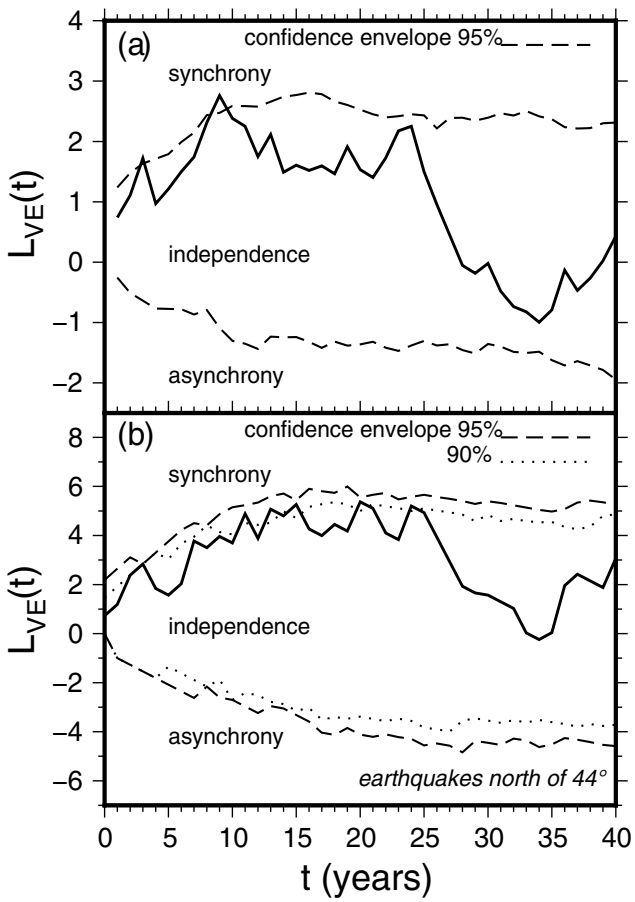

Figure 3. L-function in the modified Ripley's test for synchronization [23–25] applied to the series of strong earthquakes in Italy and Vesuvius' eruptions occurred in the time period 1600–1920: (a) seismicity of the entire territory; (b) earthquakes located north of 44° lat.

4. Further check on the possible volcanic triggering by earthquakes: the case of the Campi Flegrei caldera

After more than three centuries of quiescence, with almost continuous deflating, the Campi Flegrei caldera reactivated around 1950 and, since then, has been subjected to uplift steps of various amplitudes. The vertical movements are documented since 1905 by irregular geodetic levelings and indirect measurements [20], as well as, since 2000, by continuous GPS data [21]. Such a time series, its correlation with strong seismicity and the complementarity with the eruptions of Mt Vesuvius are shown in **Figure 4**. The last eruptive phase of Vesuvius (1913–1944) coincides with the largest seismic oscillation of the last century (peak around 1920), with the Campi Flegrei slowly deflating. Around 1950, the situation is inverted, with the Vesuvius at rest and the caldera that reactivated with two major episodes on 1970 and 1983 almost synchronous with the second (both in amplitude and chronologically) oscillation of seismicity. Around 2004, the caldera started a slower and more reduced uplift phase, currently still active, that coincides with the last, less energetic cycle of seismicity (three earthquakes: 2009, L'Aquila, Mw 6.3; 2012, Emilia, Mw 6.1; and 2016, Central Italy, Mw 6.2).

For the last century, the seismic catalog is complete at a much lower magnitude threshold (Mw 4.8 according to [19]) and the magnitude estimation itself is more reliable. This allows performing a direct comparison between the uplift and the energy radiated by the earthquakes, a quantity which is sampled at a larger number of points than in previous analysis

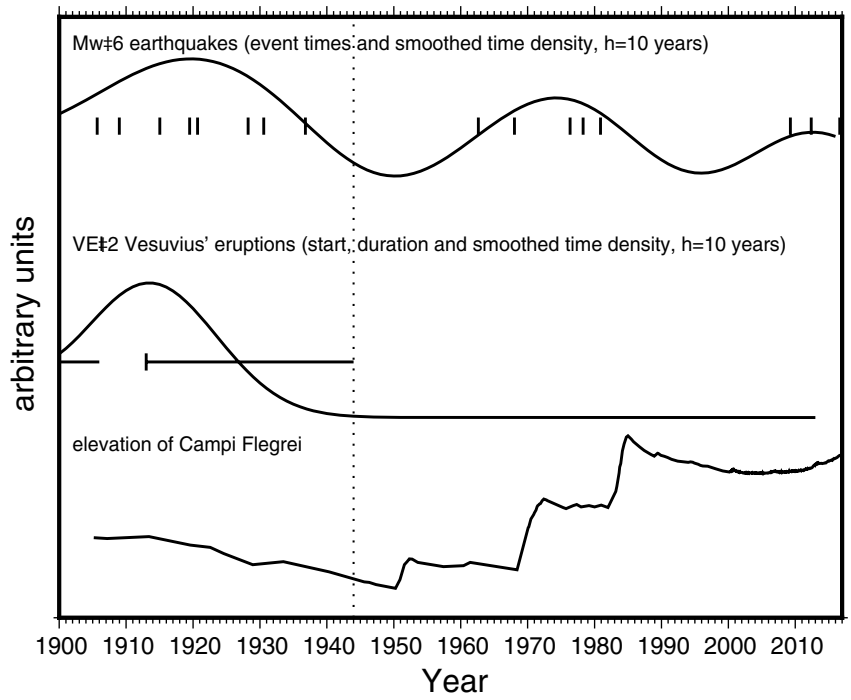

Figure 4. Smoothed time density of Mw ≥ 6.0 earthquakes in Italy since 1900 (top) compared to the smoothed time density of Vesuvius' eruptions (middle) and the elevation of the Campi Flegrei caldera (bottom).

http://dx.doi.org/10.5772/intechopen.71977

(127 mainshocks with Mw ≥ 4.8 since 1950 compared to 8 with Mw ≥ 6). The relationship is illustrated in **Figure 5** for the cumulative uplift (the deflating phases were removed) and the cumulative radiated energy E_S expressed in erg computed from Mw according to the equation

$$\log_{10}(E_S) = 1.5\,M_W + 11.8 \tag{4}$$

drawn from [27]. Since 1950, the vertical movements and the cumulative earthquake energy chase each other, according to an irregular pattern (uplift steps either precede or follow periods of major energy release). Concerning the possible triggering of the uplift by earthquakes, just one step is clearly preceded by a strong earthquake located near the seismo/volcanic coupling zone (SVCZ in the following) delineated in [5]: step S3 in **Figure 5** (1983), preceded by the 1980 Irpinia earthquake (Mw 6.8, located about 95 km east of the caldera). Of the other steps, that of 1952 (S1 in **Figure 5**) has no significant seismicity preceding it; that of 1970 (S2) is preceded by the 1968 Belice earthquake (Mw 6.4), located in Sicily, at more than 300 km from the caldera, while the previous significant earthquake in the SVCZ occurred 8 years before the uplift (1962 Irpinia earthquake, Mw 6.2, located 80 km north-east of the caldera). The more gradual uplift that started on 2004 (S4, shown in detail in **Figure 6**) was preceded on 2002 by two moderate earthquakes, one (Mw 5.9) located externally to the SVCZ in the Tyrrhenian sea (270 km south-east of the caldera) and the other one, with Mw 5.7, located within the SVCZ, 120 km north-east of the caldera (2002 Molise earthquake). After 2004, the uplift goes strictly in parallel with the energy release, with the three strong earthquakes of 2009, 2012, and 2016 located externally to the SVCZ, in central and northern Italy (172, 509, and 221 km north-west of the caldera, respectively). As a consequence, if a triggering effect exists, it is rather fuzzy. In particular, it should involve earthquakes that are external to the SVCZ (e.g., those post-2004) with response times that are not proportional to the distance (e.g., the 1962 earthquake, the nearest to the caldera, which could have triggered an uplift with a delay of 8 years).

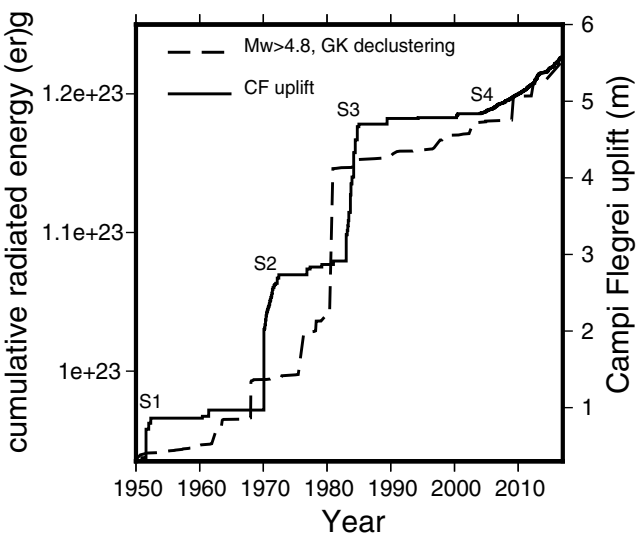

Figure 5. Comparison between the uplift time series of the Campi Flegrei caldera (deflating episodes removed) and the cumulative energy released by earthquakes with Mw ≥ 4.8 occurred in Italy in the time period 1950–2016.

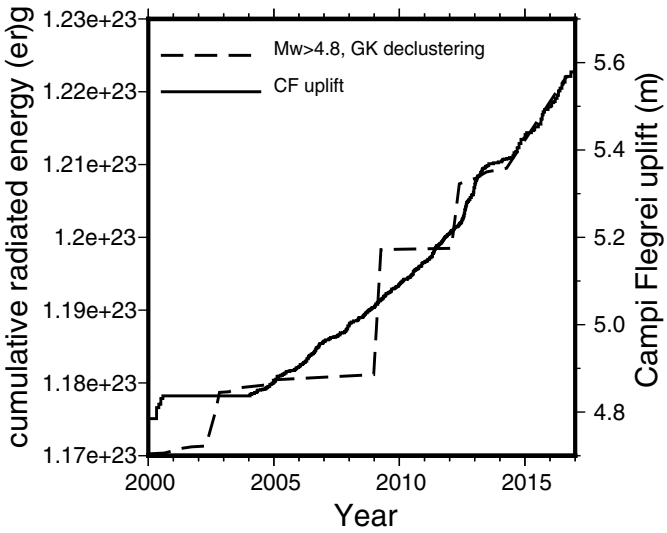

Figure 6. Comparison between the uplift time series of the Campi Flegrei caldera (deflating movements removed) and the cumulative energy radiated by earthquakes with Mw ≥ 4.8 occurred in Italy in the time period 2000–2016.

5. Eruptions, earthquakes, and the climate

The facts described so far suggest that point-to-point elastic stress transfer alone is not sufficient to explain the large-scale seismic/volcanic correlation involving the Neapolitan volcanic district. Perhaps, more general mechanisms should act. Previous works [6, 12, 13] noted the correspondence between the seismic transient that took place between 1600 and 1900 (three time the annual rate of destructive earthquakes in respect to the previous period) and the occurrence of the Little Ice Age (LIA). Furthermore, the current phase of global warming is synchronous with the gradual reduction of seismic activity through the last century (**Figure 4**). Previous works have suggested a possible role of the climate, which could affect both the seismicity and the volcanism through variations of the surface loads (sea level, ice at the poles and glaciers) and consequent changes of the stress field at depth. A similar mechanism is supported by a number of geophysical models and statistical studies available in the literature [28], although most of them (e.g., [29]) refer to the deglaciation and the sea level increase (about 120 m) that followed the last glacial maximum of 21,000 years ago.

What outlined is a promising field of investigation, although very problematic. Just to say, there are a number of climate indexes, most of which are not direct measures but reconstructions obtained by correlation with biological, chemical, and geophysical data. There is no consensus on the beginning of the LIA as well as on its spatial extension (global or restricted to a more limited area, for example, the Euro-Asiatic region) and its temporal evolution. All such complicates the assessment of the time correlation, which is just the first step of the task. The work [6] reports some graphical comparisons between Italian seismicity, the global sea level, and the global sea level rate, since 1700. More robust statistical methods are adopted in [12] to assess the degree of correlation between Italian seismicity of the last millennium and a reconstruction

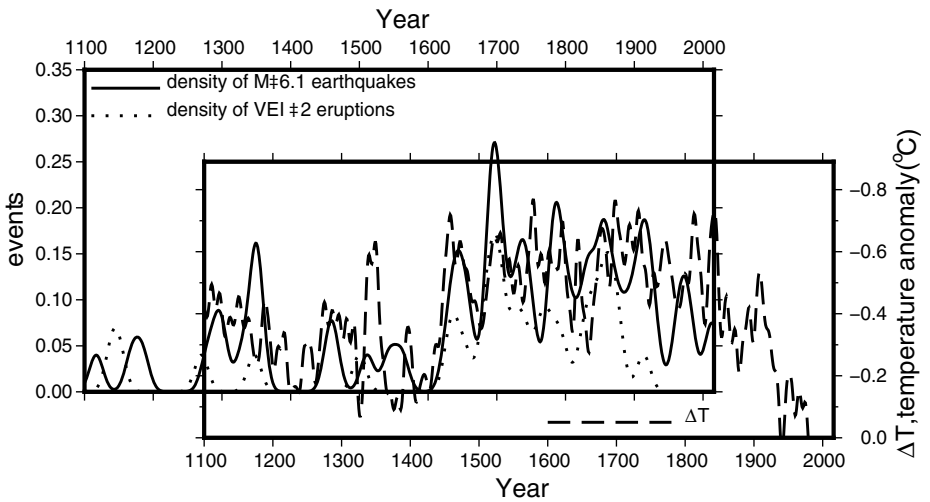

Figure 7. Comparison among the smoothed time density of Mw ≥ 6.1 earthquakes occurred in Italy since 1100, the smoothed time density of VEI ≥ 2 eruptions of Mt Vesuvius, and a reconstruction of the global surface temperature anomaly ΔT [30]. The plot of temperature is reversed (increasing values downward) and shifted by 174 years to evidence the estimated anticorrelation with the earthquakes.

of the global surface temperature [30]. In that case, a point process (the sequence of Mw ≥ 6.1 earthquakes in Italy occurred since 1100) was compared with a continuous time function (the time series of temperature) using binomial logistic regression [31]. The analysis found a significant negative correlation for a time lag of 174 years: the probability to have an earthquake during the year y has a negative dependence on the temperature recorded 174 years before (the higher the temperature, the lower the probability of an earthquake). The relationship is illustrated in **Figure 7** (modified from [12]), where the smoothed time density of earthquakes (continuous line) is plotted together to the time series of the global surface temperature anomaly ΔT (difference with the mean temperature in the reference period 1961–1990, dashed line), with the y-axis reversed (increasing values downward) and the x-axis translated by 174 years. In addition (in respect to the original figure), **Figure 7** reports the smoothed time density of the Vesuvius' eruptions (dotted line): even such curve matches the negative temperature anomaly, although the eruptive activity stops in the first half of the twentieth century.

The transformation from global surface temperature to water/ice surface load is not so immediate. Also, the physical justification of a delay of 174 years could be problematic. It is possible that other, even more local climate indexes are more appropriate. The paper [32] describes the common behavior of glaciers and lakes in west-central Europe over the last 3500 years. Representative of this, the authors report the advance/retreat time history of the Great Aletsch glacier (Alps of Valais, Switzerland), the largest glacier in the European Alps. In **Figure 8**, such data are compared with the time densities of Mw ≥ 6 earthquakes in Italy and VEI ≥ 2 Vesuvius' eruptions since the year 1100 (as the glacier data are given with low detail, the densities are smoothed for a large smoothing parameter, h = 40 years). The resemblance among the three curves is remarkable. In the post-1600 period, they share the bimodality with time lags extremely reduced in respect to the comparison with the temperature (about 50 years for the peaks near 1700). In the pre-1600 period, they have three common oscillations, although with

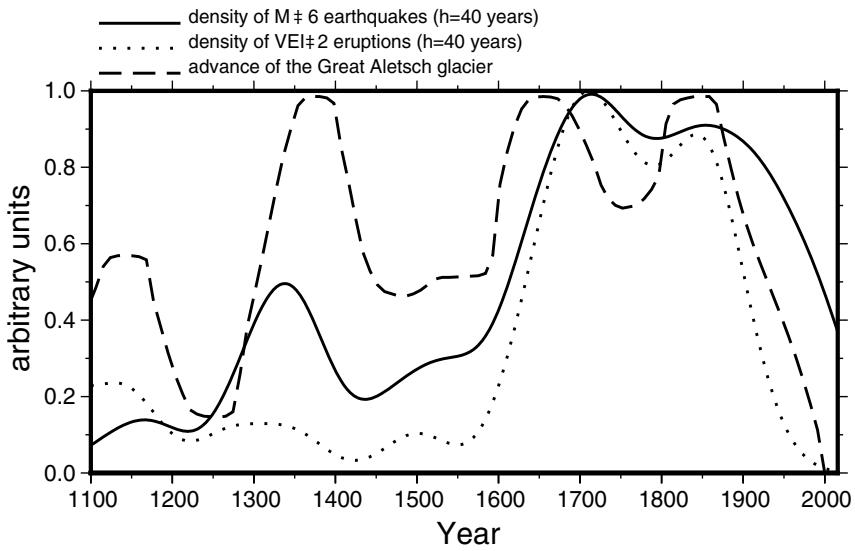

Figure 8. Comparison among the smoothed time density of Mw ≥ 6.0 earthquakes occurred in Italy since 1100, the smoothed time density of VEI ≥ 2 eruptions of Mt Vesuvius, and the fluctuation (increasing values indicate advance) of the Great Aletsch glacier according to [32].

different amplitude. The figure offers also an example of the lack of direct correspondence between temperature and ice extension. In fact, the Great Aletsch glacier was at a local minimum around 1450, a period characterized by low global temperature (**Figure 7**). Such finding indicates that other factors must be taken into consideration (e.g., the precipitation regime).

6. Conclusions

The analysis of updated and new data confirms the existence of a close relationship between the Italian seismicity and the volcanic activity in the Neapolitan area. Such a correlation involves not only the Mt Vesuvius but also the Campi Flegrei caldera, which was reactivated with a significant rate of uplift during the last 70 years. This type of seismic/volcanic correlation was previously explained as the effect of the elastic stress transfer from earthquakes sharing the same tectonic environment of the volcano (southern Apennines). This view implies a rather specific, event-to-event correspondence between earthquakes and eruptions. The evidences furnished in the present chapter indicate a looser, less specific correspondence, where the volcanic activity reflects the time density of a population of earthquakes, including also events located in northern Italy, an area dominated by a rather different stress regime (compressive instead of distensive). Continuous data from the geodetic monitoring of the Campi Flegrei also suggest that the time correlation is less episodic (i.e., related to events) and involves also a smooth evolution (e.g., the rather regular expansion of the caldera since 2004 illustrated in **Figure 6**). The picture here outlined suggests an alternative, common mechanism at the basis of both types of activity. The load/unload of the earth surface by climate processes is a possible candidate. The graphical comparison of **Figure 8** suggests that regional (e.g., European) instead of global effects should be

considered. The last point of interest emerging from the seismic/volcanic comparative analysis is the observed complementary behavior between the Vesuvius and the Campi Flegrei caldera. Although it could be a purely accidental effect, it encourages a holistic approach that looks at the Neapolitan volcanic district as a single integrated system rather than a set of distinct volcanoes.

Acknowledgements

This research was supported by Regione Autonoma Friuli Venezia Giulia and Regione Veneto. All the figures were produced using the Generic Mapping Tool, version 5.1.1 [33].

Author details

Pier Luigi Bragato

Address all correspondence to: pbragato@inogs.it

Istituto Nazionale di Oceanografia e di Geofisica Sperimentale—OGS, Centro di Ricerche Sismologiche, Udine, Italy

References

[1] Sparks RSJ, Biggs J, Neuberg JW. Monitoring volcanoes. Science. 2012;**335**:1310-1311. DOI: 10.1126/science.1219485

[2] Marzocchi W, Zaccarelli L, Boschi E. Phenomenological evidence in favor of a remote seismic coupling for large volcanic eruptions. Geophysical Research Letters. 2004;**31**:L04601. DOI: 10.1029/2003GL018709

[3] Nishimura T. Triggering of volcanic eruptions by large earthquakes. Geophysical Research Letters. 2017. DOI: 10.1002/2017GL074579

[4] Marzocchi W, Scandone R, Mulargia F. The tectonic setting of Mount Vesuvius and the correlation between its eruptions and the earthquakes of the Southern Apennines. Journal of Volcanology and Geothermal Research. 1993;**58**:27-41

[5] Nostro C, Stein R, Cocco M, Belardinelli ME, Marzocchi W. Two-way coupling between Vesuvius eruptions and southern Apennine earthquakes, Italy, by elastic stress transfer. Journal of Geophysical Research. 1998;**103**:24487-24504. DOI: 10.1029/98JB00902

[6] Bragato PL. Italian seismicity and Vesuvius' eruptions synchronize on a quasi 60-year oscillation. Earth and Space Science. 2015;**2**:134-143. DOI: 10.1002/2014EA000030

[7] Principe C, Tanguy JC, Arrighi S, Paiotti A, Le Goff M, Zoppi U. Chronology of Vesuvius activity from A.D. 79 to 1631 based on archeomagnetism of lavas and historical sources. Bulletin of Volcanology. 2004;**66**:703-724. DOI: 10.1007/s00445-004-0348-8

[8] Scandone R, Giacomelli L, Speranza FF. Persistent activity and violent strombolian eruptions at Vesuvius between 1631 and 1944. Journal of Volcanology and Geothermal Research. 2008;**170**:167-180. DOI: 10.1016/j.jvolgeores.2007.09.014

[9] Santacroce R, editor. Somma-Vesuvius, Quaderni de La Ricerca Scientifica 114. Vol. **8**. Roma: CNR; 1987. pp. 1-251

[10] Zollo A, D'Auria L, De Matteis R, Herrero A, Virieux J, Gasparini P. Bayesian estimation of 2D P-velocity models from active seismic arrival time data: Imaging of the shallow structure of Mt. Vesuvius (Southern Italy). Geophysical Journal International. 2002;**151**:566-582

[11] Pappalardo L, Mastrolorenzo G. Rapid differentiation in a sill-like magma reservoir: A case study from the Campi Flegrei caldera. Scientific Reports. 2012;**2**:712. DOI: 10.1038/srep00712

[12] Bragato PL. A statistical investigation on a seismic transient occurred in Italy between the 17th and the 20th centuries. Pure and Applied Geophysics. 2017a;**174**:907-923. DOI: 10.1007/s00024-016-1429-2

[13] Bragato PL. Periodicity of strong seismicity in Italy: Schuster spectrum analysis extended to the destructive earthquakes of 2016. Pure and Applied Geophysics. 2017b;**174**:3725-3735. DOI: 10.1007/s00024-017-1592-0

[14] Siebert L, Simkin T, Kimberly P. Volcanoes of the World. 3rd ed. Berkeley: University of California Press; 2010

[15] Newhall CG, Self S. The Volcanic Explosivity Index (VEI): An estimate of explosive magnitude for historical volcanism. Journal Geophysical Research. 1982;**87**:1231-1238. DOI: 10.1029/JC087iC02p01231

[16] Rovida A, Locati M, Camassi R, Lolli B, Gasperini P, editors. CPTI15, the 2015 Version of the Parametric Catalogue of Italian Earthquakes. Istituto Nazionale di Geofisica e Vulcanologia; 2016. DOI: 10.6092/INGV.IT-CPTI15

[17] Pondrelli S, Salimbeni S, Morelli A, Ekström G, Postpischl L, Vannucci G, Boschi E. European-Mediterranean regional centroid moment tensor catalog: Solutions for 2005-2008. Physics of the Earth and Planetary Interiors. 2011;**185**:74-81. DOI: 10.1016/j.pepi.2011.01.007

[18] Gardner JK, Knopoff L. Is the sequence of earthquakes in Southern California, with aftershocks removed, Poissonian? Bulletin of the Seismological Society of America. 1974; **64**:1363-1367

[19] Stucchi M, Meletti C, Montaldo V, Crowley H, Calvi GM, Boschi E. Seismic hazard assessment (2003-2009) for the Italian building code. Bulletin of the Seismological Society of America. 2011;**101**:1885-1911. DOI: 10.1785/0120100130

[20] Del Gaudio C, Aquino I, Ricciardi GP, Ricco C, Scandone R. Unrest episodes at Campi Flegrei: A reconstruction of vertical ground movements during 1905-2009. Journal of Volcanology and Geothermal Research. 2010;**185**:48-56. DOI: 10.1016/j.jvolgeores.2010.05.014

[21] De Martino P, Tammaro U, Obrizzo F. GPS time series at Campi Flegrei caldera (2000-2013). Annals of Geophysics. 2014;**57**:S0213. DOI: 10.4401/ag-6431

[22] Bowman AW, Azzalini A. Applied Smoothing Techniques for Data Analysis. Oxford: Oxford University Press; 1997

[23] Ripley BD. Modeling spatial patterns. Journal of the Royal Statistical Society. 1977;**B39**: 172-212

[24] Doss H. On estimating the dependence between two point processes. Annals of Statistics. 1989;**17**:749-763

[25] Gavin DG, Hu FS, Lertzman K, Corbett P. Weak climatic control of stand-scale fire history during the late holocene in southeastern British Columbia. Ecology. 2006;**87**:1722-1732

[26] Ader TJ, Avouac JP. Detecting periodicities and declustering in earthquake catalogs using the Schuster spectrum, application to Himalayan seismicity. Earth and Planetary Science Letters. 2013;**377-378**:97-105. DOI: 10.1016/j.epsl.2013.06.032

[27] Gutenberg B, Richter CF. Magnitude and energy of earthquakes. Annali di Geofisica. 1956;**9**:1-15

[28] McGuire B. Waking the Giant: How a Changing Climate Triggers Earthquakes, Tsunamis, and Volcanoes. Oxford: Oxford University Press; 2013

[29] Luttrell K, Sandwell D. Ocean loading effects on stress at near shore plate boundary fault systems. Journal of Geophysical Research. 2010;**115**:B08411. DOI: 10.1029/2009JB006541

[30] Mann ME, Zhang Z, Hughes MK, Bradley RS, Miller SK, Rutherford S, Ni F. Proxy-based reconstructions of hemispheric and global surface temperature variations over the past two millennia. Proceedings of the National Academy of Sciences of the United States of America. 2008;**105**:13252-13257. DOI: 10.1073/pnas.0805721105

[31] Venables WN, Ripley BD (2002) Modern Applied Statistics with S, fourth ed. New York: Springer, ISBN: 0-387-95457-0

[32] Holzhauser H, Magny M, Zumbühl HJ. Glacier and lake-level variations in west-central Europe over the last 3500 years. The Holocene. 2005;**15**:789-801. DOI: 10.1191/0959683605hl853ra

[33] Wessel P, Smith WHF, Scharroo R, Luis JF, Wobbe F. Generic mapping tools: Improved version released. EOS Transactions of the American Geophysical Union. 2013;**94**:409-410. DOI: 10.1002/2013EO45000

Chapter 3

Exploring the Base of the Volcano: A Case Study of an Active Stratovolcano, Mt. Zao, NE Japan

Shin Sato, Masao Ban, Teruki Oikawa,
Seiko Yamasaki and Yuki NIshi

Additional information is available at the end of the chapter

http://dx.doi.org/10.5772/intechopen.71677

Abstract

It is very important to explore the base of large volcanoes because older volcanoes with distinct petrological characteristics are sometimes hidden behind them. Such older volcanoes provide keys to investigate the change of magma genesis and tectonic setting during geological time. We newly found an older volcano in southern part of Zao volcano, located in Japan. We have investigated in detail the eruptive products outcropping in its southern part and found that some eruptive rocks with peculiar features form a new stratovolcano which is different from Zao volcano. We call this newly found volcano, the Hiyamizuyama volcano. We have performed K-Ar dating on the representative rocks, obtaining an old age of approximately 1.45 My. The rocks are calcalkaline andesites to dacites, having distinct chemical compositional features with respect to any other calcalkaline rock of the stages 2–6 of Zao volcano. Megacrystals and plutonic intrusions represent a distinct character of the eruptive rocks of the Hiyamizuyama volcano. The finding of this older volcano is also important in order to consider the long-term temporal variation of volcanism and magmatism in the northeastern sector of Japan.

Keywords: stratovolcano, eruptive history, K-Ar age dating, magmatic composition, crustal xenolith

1. Introduction

In the region where large volcanoes are present, sometimes older volcanoes are discovered even in well-investigated areas. It is because the newer large volcanoes sometimes cover the older volcanoes underneath. Such older volcanoes usually have distinct characters from the overlying younger volcano. Thus, the distinction and the characterization of such older volcanoes are very important not only in order to consider the characteristics of the volcanism and the magmatism in the area but also in order to examine the temporal change of the magma genesis in relationship

with the tectonic setting. For example, the Hawaii shield volcanoes are composed of surface alkaline lavas. However, it has been revealed that the surface alkaline lavas are underlined by a huge amount of tholeiitic lavas [1, 2]. The change of the rock composition is explained by the variations of the mantle-derived primary magma composition. The melting conditions change during the volcanic evolution when the basal oceanic plate moves through the hotspot. Another example is represented by the Fuji volcano, which is the largest stratovolcano in Japan. An older volcano, named the Pre-Komitake volcano, was recently discovered beneath the Fuji volcano [3]. The rocks from this volcano have distinct characteristics as compared to those of the Fuji volcano. The rocks from the Pre-Komitake volcano are adakitic in composition, whereas those of the Fuji volcano are normal basaltic to dacitic compositions of the island arc setting [4]. The adakitic magma is formed by melting of downgoing slab. Thus, in the Fuji volcano area, the slab melting occurred in the older age but did not continue. This change would reflect the variation of distribution of downgoing slabs beneath this area [5].

In the northeastern Japan, one of the representative subduction zones in the world, many stratovolcanoes are arranged along the volcanic front (**Figure 1**), for example, see [6, 7]. The Zao volcano is one of the most representative among these stratovolcanoes. This volcano has a long eruptive history of about 1 million years. We found an older volcano underlying the eruption products of the Zao volcano. We named this newly found volcano the Hiyamizuyama volcano. We show the geologic and petrologic features and the K-Ar age of this volcano. Also, we consider the magma genesis for the rocks of the Hiyamizuyama volcano examining the

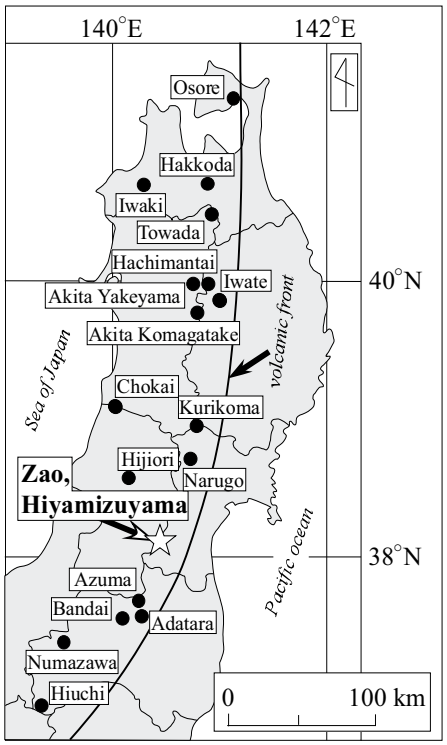

Figure 1. Locality map of Zao and Hiyamizuyama volcanoes. Eighteen active volcanoes, including Zao volcano, in NE Japan are plotted.

http://dx.doi.org/10.5772/intechopen.71677

time change in the rock compositions to a regional scale in relationship to the temporal change of the tectonic setting in the northeastern sector of Japan.

2. Geologic background

Zao volcano is an active stratovolcano in the volcanic front of the northeastern Japan (**Figure 1**). Its volcanic activity started approximately 1 Ma [8, 9] and comprised andesitic stratovolcano [10–14]. The volcanic activity is divided into six main stages based on the newest geologic study [14] (**Figure 2**). The first stage (ca. 1 Ma) is characterized by the subaqueous activity of

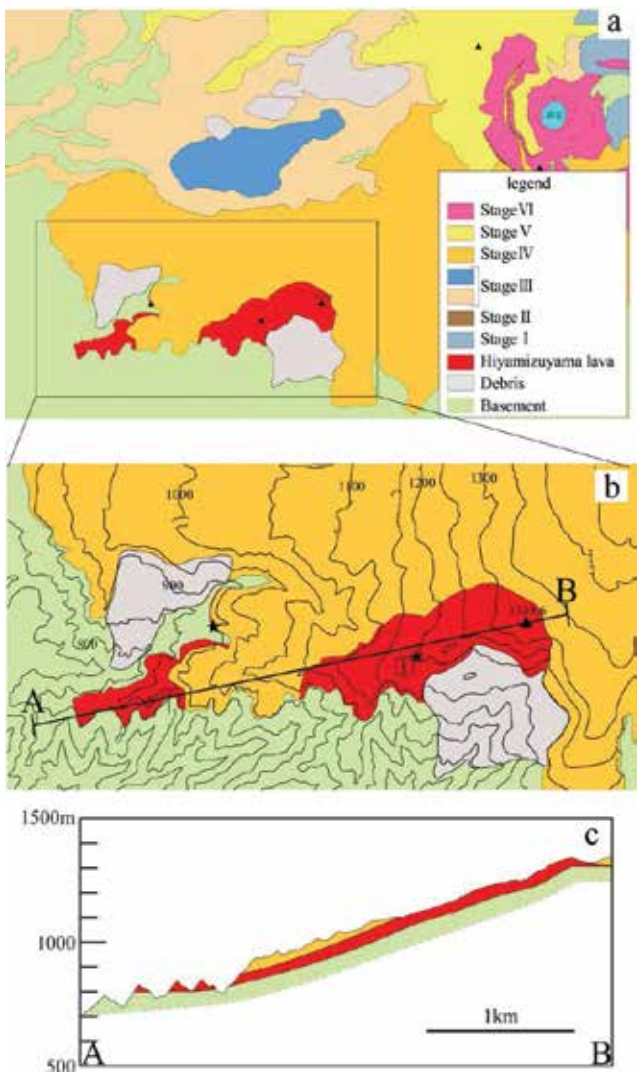

Figure 2. (a) and (b) Geological map of Zao volcano and the close-up view of Hiyamizuyama and the surrounding area (modified from Ref. [14]). (c) Geological cross-section of Hiyamizuyama volcano. Star mark represents well-exposed point.

low-K tholeiitic magma. Stages II–V (ca. 0.5–0.04 Ma) are characterized by the formation of middle-sized stratovolcanoes composed of medium-K calcalkaline basaltic andesite to dacite. Stage VI (ca. 35 ka to present) is characterized by explosive eruptions of medium-K calcalkaline series basaltic andesite to andesitic magmas [15–17].

3. Geologic feature of Hiyamizuyama volcano

The distribution of the eruptive rocks and the geologic section are presented in **Figure 2**. Hiyamizuyama eruptive rocks outcrop in the southern part of the Zao volcano. Previous studies [11, 12] pointed out that the eruptive rocks with peculiar petrologic features occur in the southern part of the Zao volcano, but the rocks were previously not well investigated and included in stage 3 of the Zao volcano.

The eruptive rocks consist of andesitic to dacitic massive lavas more than 10 m thick (**Figure 3**). The lavas are well exposed at the summit area of Hiyamizuyama volcano. In the outcrop of the summit area (star no.1 in **Figure 2**), the columnar joints can be well observed. The remarkable feature of these rocks is that the plagioclase megacrysts and plutonic inclusions as well as the mafic inclusions are characteristically identified by naked eyes. The mafic inclusions are ubiquitous in calcalkaline intermediate lavas, for example, see [18], but the plagioclase megacrysts and plutonic inclusions are not usually found in calcalkaline intermediate lavas. The details of the inclusions are described in the following section of petrologic features. Considering the distribution of this type rocks, the summit area to the western foot of Hiyamizuyama (**Figure 2a, b** would consist of this type of lavas. The lavas are covered by one of stage 3 lavas (Ichimaiishizawa lavas by [14]) of Zao volcano (**Figure 2c**). The estimated volume of the remaining lavas of Hiyamizuyama is about 0.075 km^3.

Figure 3. A photograph of the exposure (point of star no. 1 in **Figure 2**) of the lava at the summit area of Hiyamizuyama.

4. Analytical methods for petrologic analysis

More than 20 lava samples were collected from Hiyamizuyama volcano for petrologic analyses. Modal analysis is based on more than 2000 counts per thin section using optical microscope. The

proportions of groundmass and phenocrystic minerals were calculated on a vesicle-free basis. Whole rock major and trace element (Ba, Sr., Cr, Ni, V, Rb, Zr, Nb, and Y) compositions were analyzed using an X-ray fluorescence analyzer (RIX2000; Rigaku Corp.) at Yamagata University. Analyses were undertaken at an accelerating voltage of 50 kV and 50 mA currents. Preparation methods of glass disks and calibration for major and trace elements followed the method of [19] using GSJ geochemical reference samples "igneous rock series." Analytical errors of trace elements are 5% (Sr, Rb, Zr, Nb, Y, and Ni), 10% (Cr and V), and 5–15% (Ba) [20].

5. Petrographic features of rocks from Hiyamizuyama volcano

The rocks are quartz-bearing clinopyroxene-orthopyroxene andesite to dacite. These are gray in color and poorly vesiculated dense rocks. The photographs of the rocks as well as the inclusions and plagioclase megacrysts are shown in **Figure 4**.

Total volumes of phenocrysts are approximately 15%, which is a low value if compared to those of the rocks from the Zao volcano, for example, see [21]. The rocks from Zao volcano usually have more than 20% phenocrystic modal compositions. Volumes of phenocrystic plagioclase, clinopyroxene, and orthopyroxene are 9–11, ~1.5, and ~2.0%, respectively

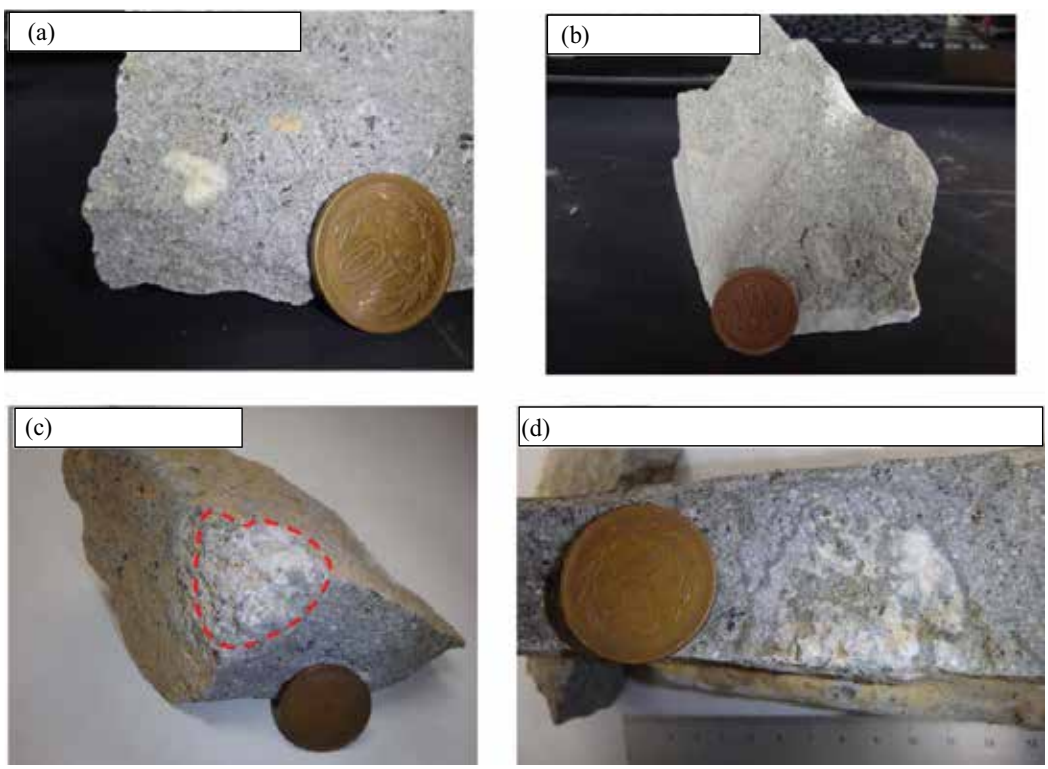

Figure 4. Photographs of the plagioclase megacrysts, the mafic inclusion, and the plutonic inclusion in the rocks from Hiyamizuyama volcano. (a) Plagioclase megacryst, (b) mafic inclusion, (c) plutonic inclusion (enclosed by the dotted red line), and (d) plutonic inclusion, which shows partial melting structure.

Sample no.	plg			Cpx	opx	ox	gm
vol.%	clear	dusty	patchy				
130,904–01-01	4.9	1.0	3.5	1.8	2.0	0.5	86.4
15,102,306–01	6.4	1.4	3.4	1.3	2.0	0.2	85.3

plg, plagioclase; clear, clear-type plagioclase; dusty, dusty zoned-type plagioclase; patchy, patchy zoned-type plagioclase; cpx, clinopyroxene; opx, orthopyroxene; and ox, oxide minerals.

Table 1. Modal compositions of representative rocks of Hiyamizuyama volcano.

(**Table 1**). Titanomagnetite phenocrysts are rarely observed in all samples and quartz phenocrysts occasionally present. Hyaloophitic-textured groundmass has microlites (up to 100 μm) of plagioclase, pyroxene, and rare titanomagnetite with interstitial glass. Photomicroscope images of representative phenocrystic minerals are displayed in **Figure 5**.

Plagioclase phenocrysts can be classified into three types. These are clear, dusty-zoned [22], and patchy-zoned [23] types. The clear type (**Figure 5a**) does not include glass inclusions and usually indicates euhedral in shape. Compositional zoning is sometimes observed. The dusty-zoned type (**Figure 5b**) has sieved-textured dusty zone in the rim part. The zone is composed of glasses, tiny grains of plagioclase, titanomagnetite, and mafic minerals. This zone is formed by resorption of the phenocrystic plagioclase, for example, see [22]. The patchy-zoned type (**Figure 5c**) is subhedral with oscillatory-zoned cores [18] having An-poor areas with rounded to irregularly shaped melt inclusions (ca. 300 μm), which constitute patches. The clear type is dominant among plagioclase phenocrysts. The second dominant

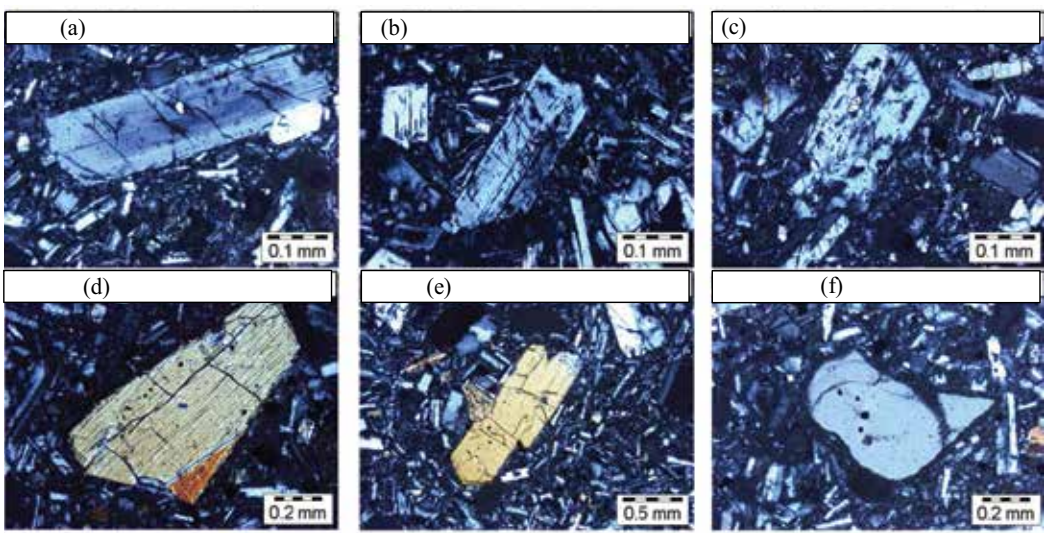

Figure 5. Photomicroscope images of the phenocrystic minerals. (a) Clear type plagioclase, (b) dusty-zoned type plagioclase, (c) patchy-zoned type plagioclase, (d) clinopyroxene, (e) orthopyroxene, and (f) quartz.

type is patchy-zoned type (**Table 1**). Most clinopyroxene (up to 0.4 cm) and orthopyroxene (ca. 0.9 cm) phenocrysts are euhedral to subhedral (**Figure 5d, e**). Quartz phenocrysts (up to 0.5 cm) show rounded form (**Figure 5f**). Crystal clots (up to 1 cm) composed of subhedral to anhedral plagioclase, orthopyroxene, clinopyroxene, and titanomagnetite are abundant.

The mafic inclusions are ubiquitously observed. These are light gray colored and usually less than 2.5 cm but sometimes up to several 10 cm in size. These are usually rounded form and sometimes show irregular shape. The texture is diktytaxitic, containing abundant interstitial glasses with bubbles between laths of the plagioclase and pyroxene (**Figure 6a**). The mafic inclusions are quenched products of mafic magmas which injected into intermediate to felsic magma chamber, for example, [18, 24]. The plagioclase megacrysts and the plutonic inclusions are less than the mafic inclusions in amount. The plagioclase megacrysts are up to 1.5 cm in size and belong to clear type. The corners are usually rounded. The plutonic inclusions are up to several cm in size. These consist of mostly plagioclase (up to 0.6 cm) and subordinately of quartz (up to 0.35 cm) with minor biotite (up to 0.5 cm). The fine grain veins invade into the inclusion along with the mineral boundaries **Figure 6b**. Sometimes, the veins can be observed by naked eyes (**Figure 4d**). These veins would be the mixture of host magma and the partial melt of the plutonic inclusion. The plagioclase grains are subhedral to anhedral and the quartz grains are anhedral. The biotites are mostly decomposed into finely grained plagioclases and titanomagnetites. The plutonic inclusions are classified into diorite according to the classification scheme of [25].

Among the petrographic features described earlier, the dissolution textures observed in the plagioclase phenocrysts (dusty zone and patchy zone) and the existence of mafic inclusion showing a quench texture indicate that the rocks of the Hiyamizuyama volcano were formed through magma mixing process as it happened in many calcalkaline rocks of the northeastern Japan [26–30]. On the other hand, the existence of partially melted plutonic inclusion, which is seldom reported from NE Japan active volcanoes, indicates the assimilation process. The texture suggesting partial melting and felsic nature of the plutonic inclusion indicate that the assimilation took place just before and during the eruption.

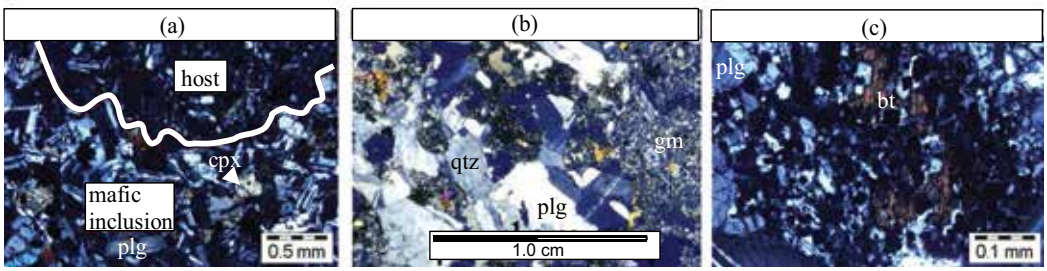

Figure 6. Photomicroscope images of the mafic inclusion (a), the plutonic inclusion (b), and the decomposed biotite (c) in the plutonic inclusion. gm, groundmass; plg, plagioclase; qtz, quartz; cpx, clinopyroxene; and bt, biotite.

6. Rock compositions of Hiyamizuyama volcano

The whole rock compositional data are shown in **Table 2**. For this study, major elements were normalized to a 100% volatile free basis with total iron (FeO*) calculated as FeO. The rocks are medium-K, calcalkaline andesite to dacite based on the classification scheme reported by Gill [31] (**Figure 7**). SiO_2 contents are 61.8–63.5 wt.%. The rocks define same chemical trends in SiO_2 variation diagrams (**Figure 8**). In K_2O-SiO_2 diagram, rocks from Hiyamizuyama volcano plotted on an area far away from those of stages 4–6. The area is near to the compositional ranges of stages 2 and 3 of Zao volcano, but still lower than the ranges. The compositions of the rocks of Hiyamizuyama volcano are compared to those from stages 2 and 3 of Zao volcano in other major elements and trace elements in SiO_2 variation diagrams (**Figure 8**). In the SiO_2 variation diagrams, rocks from Hiyamizuyama volcano are plotted far below in Ni and Sr and slightly below in MgO, Ba, Rb, and Nb from the areas of

Sample no.	**130904-01-01**	**1011-HM**	**HM01**	**130530-4**	**130530-5**
wt.%					
SiO_2	62.22	61.78	62.81	63.50	62.64
TiO_2	0.76	0.80	0.80	0.77	0.75
Al_2O_3	15.97	16.07	16.21	16.04	15.86
FeO*	7.09	7.24	7.27	7.03	7.21
MnO	0.16	0.16	0.16	0.15	0.15
MgO	2.76	2.81	2.84	2.56	2.81
CaO	5.83	6.18	6.19	5.79	6.30
Na_2O	3.32	3.38	3.41	3.40	3.38
K_2O	1.04	1.04	1.06	1.11	1.07
P_2O_5	0.10	0.09	0.11	0.11	0.10
	99.25	99.55	100.86	100.46	100.27
ppm					
Ba	357	335	337	347	332
Cr	11	12	12	11	10
Nb	4.4	4.4	4.6	4.3	4.1
Ni	N.D.	N.D.	N.D.	N.D.	N.D.
Rb	23	23	23	24	25
Sr	249	259	261	250	264
V	177	177	185	169	174
Y	31	30	30	42	44
Zn	83	84	85	80	82
Zr	118	113	113	115	111

Table 2. Whole rock major and trace element chemical compositions of rocks from Hiyamizuyama volcano.

http://dx.doi.org/10.5772/intechopen.71677

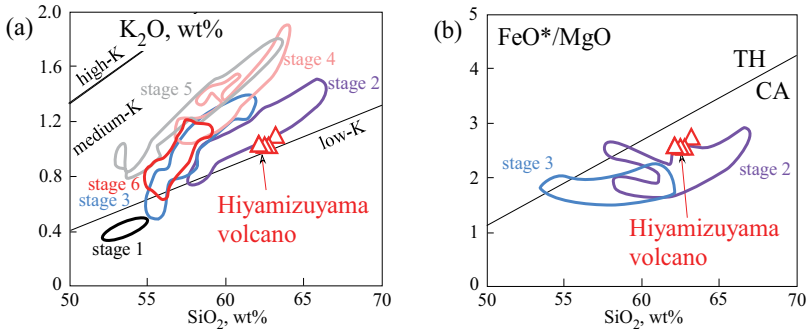

Figure 7. K_2O-SiO_2 (a) and FeO*/MgO-SiO_2 (b) diagrams for the rocks from Hiyamizuyama volcano. The areas of stages 1, 4, 5, and 6 of Zao volcano are from Ref. [14] and those of stages 2 and 3 are from Ref. [32]. Boundaries in the K_2O diagram are from Ref. [26]. Boundary of TH/CA is from Ref. [33]. The areas of stages 2 and 3 of Zao volcano are from Ref. [32].

rocks from stages 2 and 3 of Zao volcano. In the other elements, the rocks from Hiyamizuyama are in the area of stage 2, but plotted in higher part in TiO_2, Na_2O, and FeO*, whereas in lower part in CaO, Zr, and Cr. Thus, examining the whole rock compositions carefully, it is possible to distinguish the rocks from Hiyamizuyama volcano from those of Zao volcano.

7. Analytical methods for K-Ar dating

In a stainless bowl, approximately 80–100 g of the rock sample was crushed. The crushed grains were sieved to 180–250 μm in size. The sieved grains were cleaned with purified water and acetone in an ultrasonic bath. To minimize extraneous ^{40}Ar [34], the phenocrysts were removed by using an isodynamic separator (Frantz). The groundmass concentrated part was used for the analyses. Some portion of the groundmass concentrate was grinded to powder for the potassium analysis. Potassium concentration was measured by a flame emission photometer with an internal lithium standard and a peak integration method, similar to that described by Matsumoto [35]. About 100 mg of powdered sample was dissolved in a mixture of HF and $HClO_4$. After dried, it was dissolved in HCl and diluted. The lithium standard solution was added as internal standard to sample solution. Each sample was measured twice. Analytical error is 1%, estimated from standard deviation of multiple analyses of geological standards, provided by the National Institute of Advanced Industrial Science and Technology, Japan.

The argon isotopic measurement was performed using the peak height comparison (unspiked) method [36, 37]. We used the MM4500Ar mass spectrometer operated in static mode, which is connected to extraction and purification lines. The groundmass concentrated portion was wrapped in the copper foil and set in the line. To extract gases, the sample was melted in molybdenum crucible at 1500°C. The gases were purified with a Ti-Zr getter at ~700°C and two SAES getters at 200°C and room temperature, respectively. K–Ar age was calculated using the

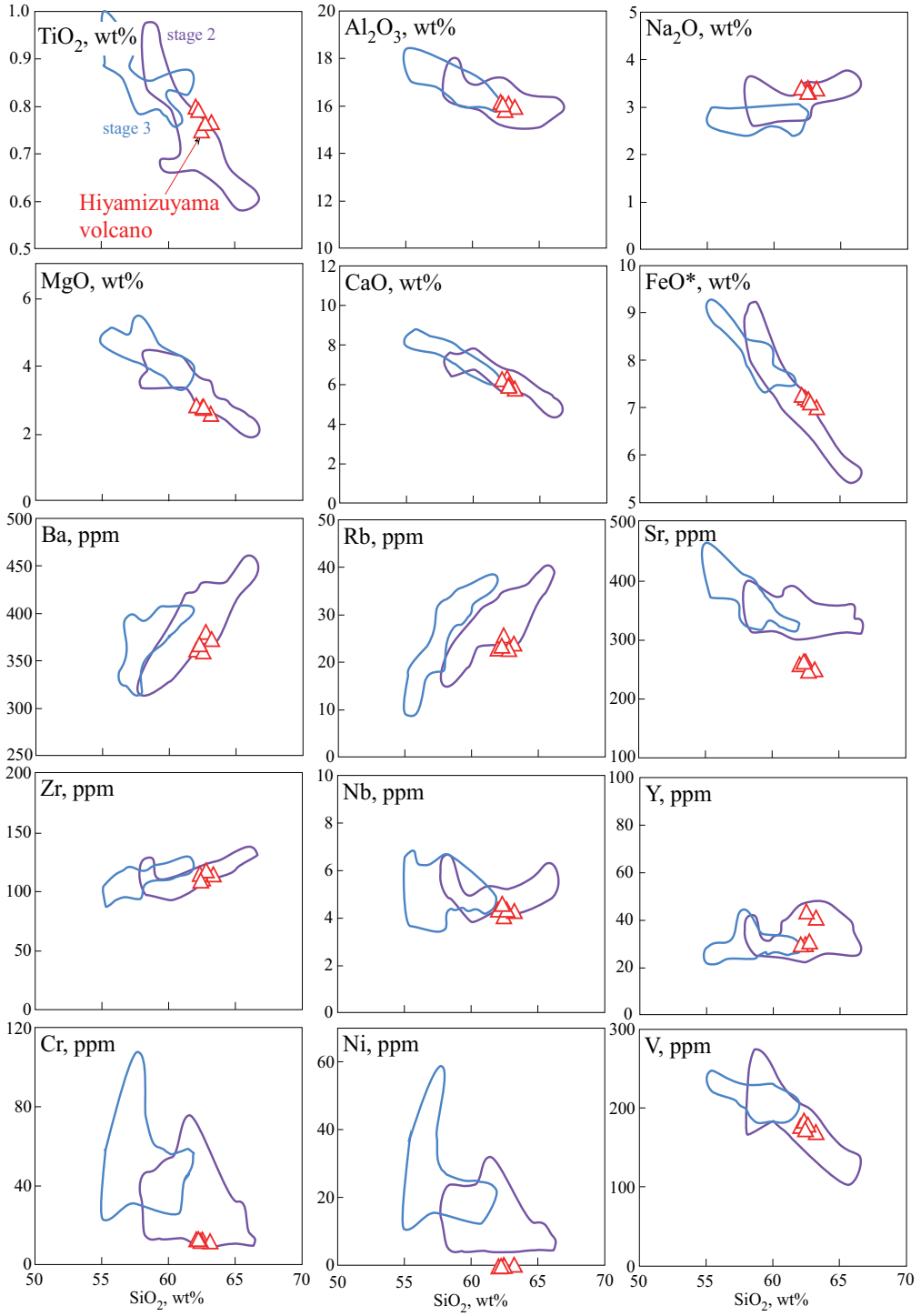

Figure 8. Major and trace elements SiO_2 variation diagrams of rocks from Hiyamizuyama volcano.

isotopic abundances and decay constants for ^{40}K recommended by the IUGS Subcommission on Geochronology ($^{40}K/K = 1.167 \times 10^{-4}$, $\lambda e = 0.581 \times 10^{-10}$ year^{-1}, $\lambda\beta = 4.962 \times 10^{-10}$ year^{-1}) [38]. We note that the initial $^{40}Ar/^{36}Ar$ ratio was obtained by applying the mass fractionation correction based on $^{38}Ar/^{36}Ar$ ratio, see [39, 40] in detail. All the analyses were conducted at the geochronology laboratory in the Geological Survey of Japan.

8. K-Ar age of Hiyamizuyama volcano

The K-Ar dating result on representative rock is presented in **Table 3**. Since the $^{38}Ar/^{36}Ar$ ratio of 0.1873 ± 0.0008 is very similar to the atmospheric value, the ages of the mass fractionation corrected and uncorrected are very similar. This means the mass fractionation effect is very limited for the age of this sample. Also, low nonradiogenic ^{40}Ar of 52.3% indicates the obtained age is very reliable.

The obtained age of 1.45 ± 0.03 Ma for the sample from Hiyamizuyama volcano is very old, which is much older than approximately 1 Ma, the age of the stage 1 Zao volcano. There are about 450,000 years gap between the activity of Hiyamizuyama volcano and the initiation of activity of Zao volcano.

9. Comparison of petrologic features with the other stratovolcanoes

(1) Temporal change of chemical compositions of frontal stratovolcanoes in NE Japan

Temporal change of petrologic features of frontal volcanoes in NE Japan during the past 4 million years was firstly examined by Ban et al. [41]. They revealed that (1) disruption of frontal volcanoes into petrologically distinct western and eastern groups, and those belonging to each group arrange near parallel to the elongated direction of the Japan trench, occurred at about 1.0–0.7 Ma, (2) the volcanoes with higher K_2O rocks appeared after the disruption, and (3) the western group includes the volcanoes with higher K_2O rocks and lower K_2O rocks, whereas the eastern group includes only volcanoes with lower K_2O rocks. These features are presented in K_2O (57.5) of the volcanoes in age-space variation diagram (**Figure 9**). We note that K_2O (57.5) is the K_2O contents of stratovolcanoes at 57.5% SiO_2. These features were recently reconfirmed by Takahashi [42].

(2) Comparison of K_2O (57.5) of Hiyamizuyama volcano with those of other frontal volcanoes in NE Japan in age-space diagram

Hiyamizuyama volcano is plotted in **Figure 9**. We can see three plots of low K_2O (57.5) volcanoes near the plot of Hiyamizuyama volcano. These three volcanoes are in northern part of NE Japan, whereas Hiyamizuyama volcano is in the central to southern part. Thus, Hiyamizuyama data indicate that the characteristics of temporal change in petrologic features revealed by Ban et al. [41] are those of whole NE Japan frontal volcanoes. Such change, occurred in whole arc, must reflect the changes of regional tectonics.

Sample no.	K_2O (wt.%)	Sample wt (g)	int.^{40}Ar (V)	^{36}Ar (10^{-9}mlSTP/g)	^{38}Ar/^{36}Ar	^{40}Ar/^{36}Ar	int.^{40}Ar/^{36}Ar	rad.^{40}Ar (10^{-9}mlSTP/g)	non rad.^{40}Ar	K-Ar age (Ma)	uncorrected age (Ma)
Z12101105	0.98	0.644	0.99	0.17	0.1873 ± 0.0008	576 ± 6	296 ± 2	46.5 ± 0.8	52.3	**1.45 ± 0.03**	1.45 ± 0.02

*uncorrected age = mass fractionation of initial $^{40}Ar/^{36}Ar$ ratios are uncorrected.

The age calculation is the same as the conventional K-Ar dating procedure.

The decay constants used in the present study are 4.96X10–10/y, $\lambda e = 0.58X10^{-10}$/y, $\lambda\beta = 4.962 \times 10^{-10}$/y,

and 40 K/K = 0.01167 atom% (Steiger and Jäger [38]).

Errors are given at the one σ uncertainty level.

Table 3. K-Ar age data by the peak comparison method for the sample from Hiyamizuyama volcano.

http://dx.doi.org/10.5772/intechopen.71677

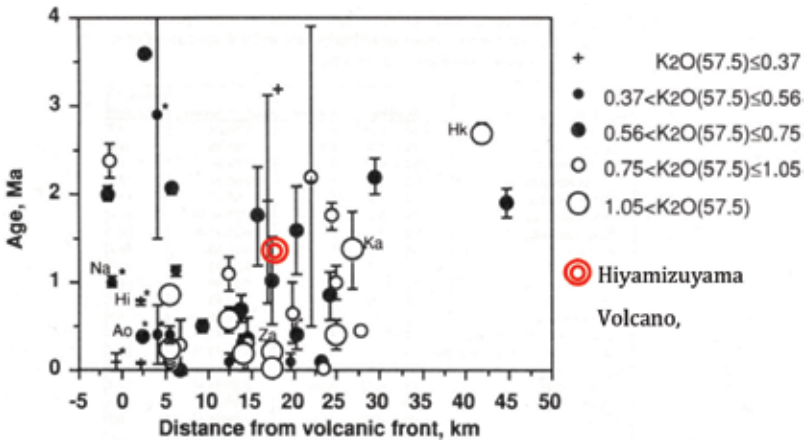

Figure 9. Temporal variation of the K_2O content for the volcanoes distributing around volcanic front of NE Japan arc during the past 4 million years [36]. Double circle, Hiyamizuyama volcano (K_2O (57.5) = 0.82).

It is suggested that regional uplift of basements of volcanic front region in NE Japan started at about 1.0–0.6 Ma, for example, see [43]. This uplift would be caused by the enlargement of the crust. The increased stress of E-W direction, caused by the speed up of westward movement of the Pacific plate, would accelerate the rate of the formation of magma in the wedge mantle. The ascended magma would underplate beneath the crust under volcanic front and resulted in the enlargement of the crust [44]. If the lower part of the crust gained the thickness, depths of magma formation areas, upper most mantle for the basaltic magma and lower crust for the intermediate to felsic magma, become deeper. The magmas formed in the deeper areas would have higher K_2O contents, because lower degrees of melting are expected when the melting depth gets deeper. The appearance of volcanoes with higher K_2O rocks would suggest that the lower crust gained thickness effectively beneath the western group after approximately 1.0 Ma. We note the coexistence of the volcanoes with lower K_2O rocks as well as with higher K_2O rocks in the western group would indicate that the thickening would be heterogeneously occurred.

10. Summary

We newly found Hiyamizuyama volcano in southern part of Zao volcano. We performed K-Ar dating and obtained the age of 1.45 Ma. Hiyamizuyama volcano was formed about 450,000 years before the initiation of Zao volcano.

The petrologic features of this volcano differ from those of Zao volcano. These include (1) lower phenocrystic modal composition, (2) including plagioclase megacrysts, (3) possessing plutonic inclusions, and (4) distinct whole rock composition, especially low-K_2O content.

Discovery of this older volcano is important to consider long-term temporal variation of volcanism and magmatism in this region as well as whole NE Japan.

Acknowledgements

We acknowledge Drs. A. Matsumoto, Y. Ishizuka, and T. Nakano for their continual support of K-Ar dating in this research. We are grateful to Mr. G. Kawano and T. Takano for their field assistance and useful comments on this study. We also acknowledge Yamagata and Miyagi Prefectural Governments for the permission of field observation. This work was financially supported in part by grant-in-aid for Scientific Research from the Japan Society for the Promotion of Science to M. Ban (no. 22540487; 17K05701). This study was supported by the Earthquake Research Institute The University of Tokyo Joint Usage/Research Program and the Integrated Program for Volcano Research and Human Resource Development by MEXT Japan.

Author details

Shin Sato[1], Masao Ban[2]*, Teruki Oikawa[3], Seiko Yamasaki[3] and Yuki NIshi[1]

*Address all correspondence to: ban@sci.kj.yamagata-u.ac.jp

1 Graduate School of Science and Technology, Yamagata University, Yamagata, Japan

2 Faculty of Science, Yamagata University, Yamagata, Japan

3 Geological Survey of Japan, Tsukuba, Japan

References

[1] MacDonald GA, Katsura T. Chemical compositions of Hawaiian lavas. Journal of Petrology. 1964;**5**:82-133. DOI: 10.1093/petrology/5.1.82

[2] MacDonald GA. Composition and origin of Hawaiian lavas. Geological Society of America Memoirs. 1969;**116**:477-522. DOI: 10.1130/MEM116-p477

[3] Yoshimoto M, Fujii T, Kaneko T, Yasuda A, Nakada S, Matsumoto A. Founding of this older volcano is important to consider long-term temporal variation of volcanism and magmatism in this region as well as NE Japan. Evolution of Mount Fuji, Japan: Inference from drilling into the subaerial oldest volcano, pre-Komitake. Island Arc. 2010;**9**:470-488. DOI: 10.1111/j.1440-1738.2010.00722.x

[4] Shibata T, Suzuki J, Yoshikawa M, Kobayashi T, Miki D, Takemura K. Geochemical and Sr-Nd-Pb isotopic constraints on the origin and magmatic evolution of Quaternary lavas of Sakurajima volcano, southern Kyushu Island, Japan. Bulletin of the Volcanological Society of Japan. 2013;**58**:43-58. DOI: 10.18940/kazan.58.1_43

[5] Ichihara M, Adam C, Vidal V, Grosse P, Mibe K, Orihashi Y. Dots-and-lines approach to subduction volcanism and tectonics. Journal of Geography. 2017;**126**:181-193. DOI: 10.5026/jgeography.126.181

[6] Yagi K, Kawano Y, Aoki K. Types of quaternary volcanic activity in northeastern Japan. Bulletin of Volcanology. 1963;**26**:223-235. DOI: 10.1007/BF02597288

[7] Tamura Y, Tatsumi Y, Zhao D, Kido Y, Shukuno H. Distribution of quaternary volcanoes in the Northeast Japan arc: geologic and geophysical evidence of hot fingers in the mantle wedge. Proceedings of Japan Academy, Series B. 2001;**77**:135-139. DOI: 10.2183/pjab.77.135

[8] Takaoka N, Konno K, Oba Y, Konta T. K-Ar datings of lavas from Zao Volcano, northeastern Japan. Journal of Geological Society of Japan. 1989;**95**:157-170. DOI: 10.5575/geosoc.95.157

[9] Yamasaki S, Ban M, Oikawa T. Reconstruction of the volcanic history of Zao volcano based on the new dating. Abstracts. Volcanological Society of Japan. 2014;135

[10] Oba Y, Konta T. Geology and petrology of Central Zao volcano, Yamagata Prefecture. Bulletin of the Yamagata University Natural Science. 1989;**12**:199-210

[11] Sakayori A. Magmatic evolution of Zao volcano, Northeast Japan. Bulletin of Volcanological Society of Japan. 1991;**36**:79-92. DOI: 10.18940/kazan.36.1_79

[12] Sakayori A. Geology and petrology of Zao volcano. Journal of Mineralogy Petrology and Economic Geology. 1992;**87**:433-444. DOI: 10.2465/ganko.87.433

[13] Ban M. Zao Volcano. Journal of Geological Society of Japan. 2013;**119**:120-133. DOI: 10.5575/geosoc.2013.0017

[14] Ban M, Oikawa T, Yamasaki S: Geological map of Zao volcano. Geological map of volcanoes: Geological Society of Japan. 2015;**18**:1-8

[15] Kawano G, Ban M, Oikawa T. Stratigraphy and temporal change in chemical compositions of eruption products in Umanose agglutinate activity, Zao volcano. Japan Geoscience Union Meeting 2014 Proceedings. SVC54-p10

[16] Miura K, Ban M, Yagi K. The tephra layers distributed around the eastern foot of the Zao volcano–Ages and volumes of the Za–To 1 to 4 tephras. Bulletin of the Volcanological Society of Japan. 2008;**53**:151-157. DOI: 10.18940/kazan.53.5_151

[17] Miura K, Ban M, Ohba T, Fujinawa A. Sequence of the 1895 eruption of the Zao volcano, Tohoku Japan. Journal of Volcanology and Geothermal Research. 2012;**247–248**:139-157. DOI: 10.1016/j.jvolgeores.2012.08.005

[18] Bacon CR. Magmatic inclusions in silicic and intermediate volcanic rocks. Journal of Geophysical Research. 1986;**91**(B1):6091-6112. DOI: 10.1029/JB091iB06p06091

[19] Yamada Y, Kohno H, Murata M. A low dilution fusion method for major and trace element analysis of geological samples. Advances in X-Ray Analysis. 1995;**26**:33-44

[20] Ban M, Takahashi K, Horie T, Toya N: Petrogenesis of mafic inclusions in rhyolitic lavas from Narugo volcano, northeastern Japan. Journal of Petrology. 2005;**46**:1543–1563. DOI:10.1093/petrology/egi025

[21] Ban M, Sagawa H, Miura K, Hirotani S. Evidence for a short lived stratified magma chamber: petrology of the Z-To 5 tephra layer (c. 5.8 ka) at Zao Volcano, NE Japan. In: Annen C, Zellmer GF, editors. Dynamics of crustal magma transfer, storage and differentiation. Vol. **304**. London. Special Publications: Geological Society; 2008. pp. 149-168. DOI: 10.1144/SP304.8

[22] Tsuchiyama A. Dissolution kinetics of plagioclase in the melt of the system diopside–albite–anorthite, and origin of dusty plagioclase in andesites. Contributions to Mineralogy and Petrology. 1985;**89**:1-16. DOI: 10.1007/BF01177585

[23] Vance JA. Zoning in Igneous plagioclase: patchy zoning. Journal of Geology. 1965;**73**:636-651. DOI: 10.1086/627099

[24] Eichelberger JC. Vesiculation of mafic magma during replenishment of silicic magma reservoirs. Nature. 1980;**288**:446-450. DOI: 10.1038/288446a0

[25] Streckeisen A. To each plutonic rock its proper name. Earth-Science Reviews. 1976;**12**: 1-33. DOI: 10.1016/0012-8252(76)90052-0

[26] Ban M, Yamamoto T. Petrological study of Nasu-Chausudake Volcano (ca. 16 ka to Present), northeastern Japan. Bulletin of Volcanology. 2002;**64**:100-116. DOI: 10.1007/s00445-001-0187-9

[27] Toya N, Ban M, Shinjo R. Petrology of Aoso volcano, northeast Japan arc: Temporal variation of the magma feeding system and nature of low-K amphibole andesite in the Aoso–Osore volcanic zone. Contributions to Mineralogy and Petrology. 2005;**148**:566-581. DOI: 10.1007/s00410-004-0621-z

[28] Hirotani S, Ban M. Origin of silicic magma and magma feeding system of Shirataka volcano, NE Japan. Journal of Volcanology and Geothermal Research. 2006;**156**:229-251. DOI: 10.1016/j.jvolgeores.2006.03.020

[29] Hirotani S, Ban M, Nakagawa M. Petrogenesis of mafic and associated silicic end-member magmas for calc-alkaline mixed rocks in the Shirataka volcano, NE Japan. Contributions to Mineralogy and Petrology. 2009;**157**:709-734. DOI: 10.1007/s00410-008-0360-7

[30] Takebe Y, Ban M. Evolution of magma feeding system in Kumanodake agglutinate activity, Zao Volcano, northeastern Japan. Journal of Volcanology and Geothermal Research. 2015;**304**:62-74. DOI: 10.1016/j.jvolgeores.2015.07.030

[31] Gill JB. Orogenic Andesites and Plate Tectonics. Berlin-Heidelberg-New York: Springer-Verlag; 1981. p. 358

[32] Sato S, Ban M, Oikawa T, Yamasaki S. Geological and petrological study of Torikabutoyama-Yokokurayama, Old-Kumanodake, Nakamaruyama edifices in Zao volcano. In: Japan Geoscience Union Meeting 2016 Proceedings. SVC48–06

[33] Miyashiro A. Volcanic rock series in island arcs and active continental margins. American Journal of Science. 1974;**274**:321-355

[34] Ozawa A, Tagami T, Kamata H. Argon isotopic composition of some Hawaiian historical lavas. Chemical Geology. 2006;**226**:66-72. DOI: 10.1016/j.chemgeo.2005.10.001

[35] Matsumoto A. Improvement for determination of potassium in K–Ar dating. Bulletin Geological Survey of Japan. 1989;**40**:65-70

[36] Matsumoto A, Uto K, Shibata K. K–Ar dating by peak comparison method - new technique applicable to rocks younger than 0.5 Ma. Bulletin Geological Survey of Japan. 1989;**40**:565-597

[37] Sudo M, Tagami T, Sato K, Hasebe N, Nishimura S. Calibration of a new Ar analytical system for the K–Ar dating method and analytical results of K-Ar age known samples. Memoirs of the Faculty of Science, Kyoto University Series of Geology Mineral. 1996;**58**:21-40

[38] Steiger RH, Jäger E. Convention on the use of decay constants in geo-and cosmochronology. Earth and Planetary Science Letters. 1977;**36**:359-362. DOI: 10.1016/0012-821X(77)90060-7

[39] Matsumoto A, Kobayashi T. K–Ar age determination of late Quaternary volcanic rocks using the "mass fractionation correction procedure": application to the younger Ontake volcano, central Japan. Chemical Geology. 1995;**125**:123-135. DOI: 10.1016/0009-2541(95)00062-Q

[40] Yamasaki S, Sawada R, Ozawa A, Tagami T, Watanabe Y, Takahashi E. Unspiked K–Ar dating of Koolau lavas, Hawaii: Evaluation of the influence of weathering/alteration on age determinations. Chemical Geology. 2011;**287**:41-53. DOI: 10.1016/j.chemgeo.2011.05.003

[41] Ban M, Oba Y, Ishikawa K, Takaoka N. K-Ar dating of Mutsu-Hiuchidake, Osoreyama, Nanashigure, and Aoso volcanoes of the Aoso-Osore volcanic zone -The formation of the present volcanic zonation of the Northeast Japan arc. Journal of Mineralogy Petrology and Economic Geology. 1992;**87**:39-49. DOI: 10.2465/ganko.87.39

[42] Takahashi T, Hirahara Y, Miyazaki T, Senda R, Chang Q, Kimura J-I, Tatsumi Y. Primary magmas at the volcanic front of the NE Japan arc: Coeval eruption of crustal low-K tholeiitic and mantle-derived medium-K calc-alkaline basalts at Azuma volcano. Journal of Petrology. 2013;**54**:103-148. DOI: 10.1093/petrology/egs065

[43] Yoshida T, Kimura J-I, Yamada R, Acocella V, Sato H, Zhao D, J. Nakajima J, Hasegawa A, Okada T, Honda S, Ishikawa M, Ardiansyah Prima OD, Kubo T, Shibazaki B, Tanaka A, Imaizumi T. Evolution of late Cenozoic magmatism and the crust–mantle structure in the NE Japan Arc. Go'mez-Tuena A, Straub SM, Zellmer GF, editors. Orogenic andesites and crustal growth. Geological Society of London. Special Publications. 2013;**385**:335-387. DOI: 10.1144/SP385.15

[44] Yoshida T, Nakajima J, Hasegawa A, Sato H, Nagahashi Y, Kimura J-I, Tanaka A, Ardiansyah Prima OD, Oguchi T. Evolution of late Cenozoic magmatism in the NE Honshu Arc and its relation to the crust–mantle structures. Quaternary Research. 2005;**44**:195-216. DOI: 10.4116/jaqua.44.195

Chapter 4

The Emissions of the Tagoro Submarine Volcano (Canary Islands, Atlantic Ocean): Effects on the Physical and Chemical Properties of the Seawater

Juana Magdalena Santana-Casiano,
Melchor González-Dávila and Eugenio Fraile-Nuez

Additional information is available at the end of the chapter

http://dx.doi.org/10.5772/intechopen.70422

Abstract

This chapter presents the changes and evolution of the physical and chemical properties of the seawater south of the El Hierro Island (Canary archipelago, Atlantic Ocean) as a consequence of the emissions of the Tagoro submarine volcano, over a 6 year study from 2011 to 2016. Since the eruption, a series of oceanographic studies have been carried out in the area focusing on the evolution of the redox potential and the pH, two master variables that control the chemical equilibrium in sea water. The changes experienced by the carbon dioxide system, the variations in the concentration of Fe(II) and their correlation with the decrease in the pH during the evolution of the volcano, from the beginning of the eruptive stage to the post-eruptive phase, are discussed. The increased TDFe(II) concentrations and the low associated pH_T values have controlled the occurrence of an important fertilization event in the sea water around the volcano at the Island of El Hierro, providing optimal conditions for the regeneration of the area. The sites like the Tagoro submarine volcano, in its degasification stage, provide an excellent opportunity to study the carbonate system in a high CO_2 world, the volcanic contribution to the global volcanic carbon flux and the potential environmental impact of these emissions on the surrounding ocean and the ecosystem.

Keywords: submarine volcano, CO_2, acidification, fertilization, pH, ferrous iron, redox potential

1. Introduction

The eruption of a volcano in the ocean generates important changes in the physical and chemical properties of the sea water that also affects the marine organisms in the area. When this eruption occurs in distant and deep places, they may go unnoticed if they are not specifically monitored.

However, when these eruptions occur near shore, in shallow areas, the effects are more evident. Moreover, they directly emit fluids into the photic zone where they influence the primary production. The emitted metals, such as iron are biologically essential micronutrients whereas others, such as the copper, can be toxic at nanomolar concentrations [1].

This chapter focuses on the geochemical changes observed in the seawater around the shallow submarine volcano Tagoro, Canary Islands, Atlantic Ocean, from its eruption period in 2011 until its degasification stage between 2012 and 2016. Since its eruption, a series of oceanographic studies has been carried out in the area and the evolution of some physical and chemical properties has been monitored. The study has been divided into two parts. The first one covers the eruptive phase, which lasted 5 months, from October 2011 until March 2012. At this time, drastic changes in the carbon dioxide system and in the emissions of reduced species were observed south of the El Hierro Island as well as an enrichment of Fe(II) and nutrients, which generated an episode of natural ocean acidification and a fertilization event [2, 3]. The second part focuses on the post-eruptive phase, during which noticeable anomalies in the carbon dioxide parameters and Fe(II) were only found close to the main crater of the volcano. Physicochemical anomalies were still observed in 2016 close to the volcanic area. During the second period, the studies were concentrated in the volcanic edifice, and different sampling strategies, including high-resolution sampling along the volcanic edifice and tow-yo and yo-yo studies, were undertaken in order to detect the anomalies [4].

2. The underwater eruption and changes observed in the surface water

2.1. Geological setting

The island of El Hierro is the westernmost island of the Canary Archipelago located in the north-eastern Atlantic Ocean. The Canary Islands were originated in the Early Miocene as the African plate moved over a mantle hotspot [5, 6]. The islands show a general age progression from the eastern islands (>20 Ma) toward western islands (<2 Ma) [7]. The El Hierro Island is the youngest, with 1.12 million years of age [8]. The oldest subaerial rocks in El Hierro have been dated back at 1.12 ± 0.02 Ma and the only known subaerial prehistoric eruptions have been dated back to 4000 and 2500 year ago [8]. The island is the emergent top of a volcanic shield, which rises from 3800 to 4000 m depths and grows up to 1500 m above sea level. Its subaerial part (280 km^2) shows the characteristic shape of three convergent rifts, separated by at least three important landslides [9–11].

The submarine eruption of the Tagoro volcano, in 2011, was the first submarine eruption reported in about 600 years of historical records in the Canary Islands and the first one to be monitored from the initial caldera unrest [12].

2.2. A new submarine volcano

In October 2011, after 3 months of volcanic unrest with more than 12,000 earthquakes ($M < 4.3$) and 5 cm of ground deformation [12], a submarine eruption took place in the island of El Hierro, in the north-eastern Atlantic Ocean, in a shallow coastal area, at a depth of 300 m

http://dx.doi.org/10.5772/intechopen.70422

(**Figure 1**). The volcano was located 1.8 km south of the island of El Hierro at 27°37′07″N–017°59′28″W. Over 5 months, the volcanic edifice grew up to 88 m below sea level. During that period, six geophysical surveys were carried on board the *R/V Ramón Margalef* in order to monitor the changes in the bathymetry of the area [13, 14]. Moreover, several hydrographic cruises were carried out to study the changes in the physical, chemical and biological properties in the water column from the beginning of the eruptive stage to the post-eruptive phase [2–4].

The evolution of the volcanic edifice between 2011 and 2012 [13, 14] can be briefly described as follows:

- The first survey in the area was carried out on October 23. The base of the active volcano was found at a depth of 300 m. The volcano was located on a rift with lava flowing south-westwards. It was 650 m wide and its peak was situated at a depth of 220 m below the sea level.
- In January 2012, the cone had risen to a depth of 130 m.
- In February 2012, it reached its maximum elevation of 88 m below sea level.

While both the structure and the height of the volcano were changing, the emission of fluids gave rise to a plume in the water column that, due to the currents, also extended to its surroundings. The emission plume was also modified during that time by the dynamics of both the volcano growth and the oceanographic conditions [3]. Additionally, in the surface, the plume was

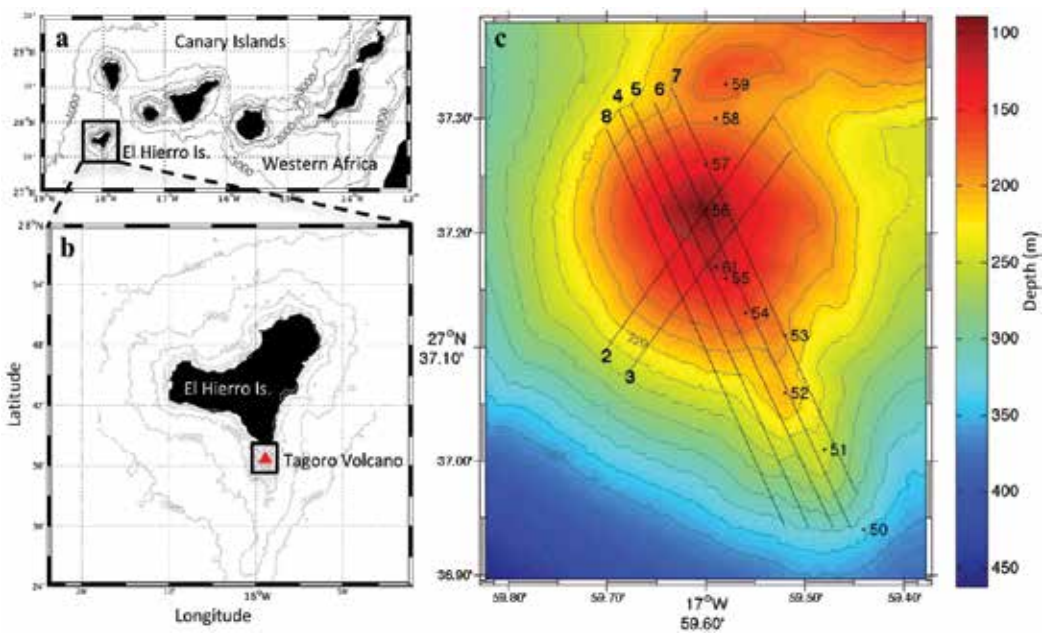

Figure 1. (a) Location of the volcanic edifice within the Canary Archipelago. (b) Island of El Hierro with the location of the submarine volcano Tagoro. (c) Location of the tow-yo lines and CTD stations. The maps were generated using Matlab 7.12 R2011a.

affected by changes in the meteorological and hydrodynamic conditions. In the first months, the plume (**Figure 2**) was observed from the coast and also through satellite images [15, 16].

2.3. Signal of the eruption in the sea surface

In the surface waters, evident signals were observed as a consequence of the volcanic emissions in the first 5 months of the eruption. The most important were observed around the volcanic edifice (**Figure 3**), but the effect of the volcano emissions reached the whole southern part of the Island of El Hierro. Some influences were also observed in the northern part, as a consequence of the currents in the area [16]. The most important observations in the surface waters were:

- The discolouration of the water ranging from light-green to milky-blue to a dark brown colour.
- Bubbling and degassing.
- Abundant rock fragments floating on the ocean.

The strongest eruptive episode took place between November 5 and 8 with large bubbles rising to 10–15 m above sea level [3].

The eruption produced lava balloons that were collected while floating and degassing at the sea surface above the vent [17]. Studies from petrological and geophysical data indicated that

Figure 2. (a) A true colour, high-resolution RapidEye satellite image featuring a gigantic stain visible on the surface of 'El Mar de las Calmas' (November 26, 2001). (b) Image acquired by the Advanced Land Imager (ALI) aboard the Earth Observing-1 satellite (NASA award-winning image 2013).

http://dx.doi.org/10.5772/intechopen.70422

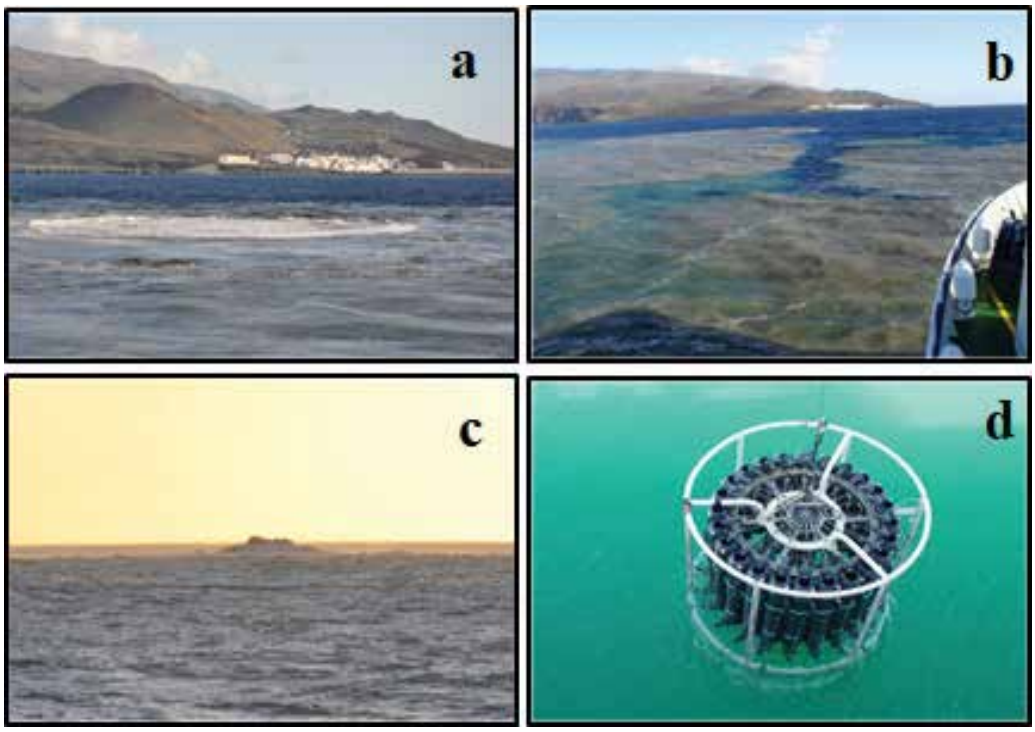

Figure 3. Signals observed in the surface waters as a consequence of the volcanic emissions. (a) Surface seawater bubbling (November 5, 2011). (b) Colour patches in the surface waters. (c) A 10-m emerged high bubble (November 5, 2011). (d) Light green seawater surface.

mantle-derived basanite magma intruded the lower crust, where it migrated sub-horizontally for ~15 km, and then rapidly transited to the surface, all within a few months [18–20].

3. Eruptive phase and changes in the chemistry of sea water

During the eruptive phase that lasted 5 months (October–March), important changes in the carbon dioxide system and in the emissions of reduced species were observed south of the El Hierro Island. Over this period, intensive water column sampling was carried out. The samples were taken with a conductivity-temperature-depth sensor (CTD)-rosette with 24 Niskin bottles. The pH in total scale (pH_T), the total dissolved inorganic carbon (C_T), the total alkalinity (A_T), Fe(II) and the total sulfur reduced species were measured, together with the temperature, the salinity and the dissolved oxygen. The nutrients and the fugacity of CO_2 (fCO_2) were also analyzed in the most of cruises.

3.1. Changes in the pH and carbonate system

Due to the volcanic emissions of CO_2, SO_2 and H_2S/HS^-, important changes were observed in the pH, with values lower than 6. The largest anomalies, $\Delta pH = 2.9$, were observed in November 5, 2011, during the explosive event, where a 10 m high bubble emerged from the sea surface. The C_T and the A_T also changed, in the surface waters around the volcano, where anomalous values

of C_T and A_T of 7682 and 1338 μmol kg^{-1} were measured, respectively (**Figure 4**). Normal surface values for the area are 2100 μmol kg^{-1} for C_T and 2430.1 μmol kg^{-1} for A_T.

The CO_2 exchanged between the ocean and the atmosphere after being emitted by the volcano was calculated using pH_T and C_T data. $fCO_{2(pH,CT)}$ increased to values as high as 155,000 μatm, reaching 230,316 μatm just after the bubble emerged. The surface seawater in the south-west of the island had $fCO_{2(pH,CT)}$ values in the range of 11,000–19,000 μatm. fCO_2 in the areas unaffected by the volcanic emissions was of 414 ± 2 μatm.

The flux of CO_2, FCO_2, exchanged during the week of the explosive event (November 4–9) was 5×10^{10} gd^{-1}. fCO_2 was computed considering an affected area of 385 km^2 and using a weekly mean wind speed of 7.5 ms^{-1} [3]. The studies carried out by Longpré et al. [17] with samples of

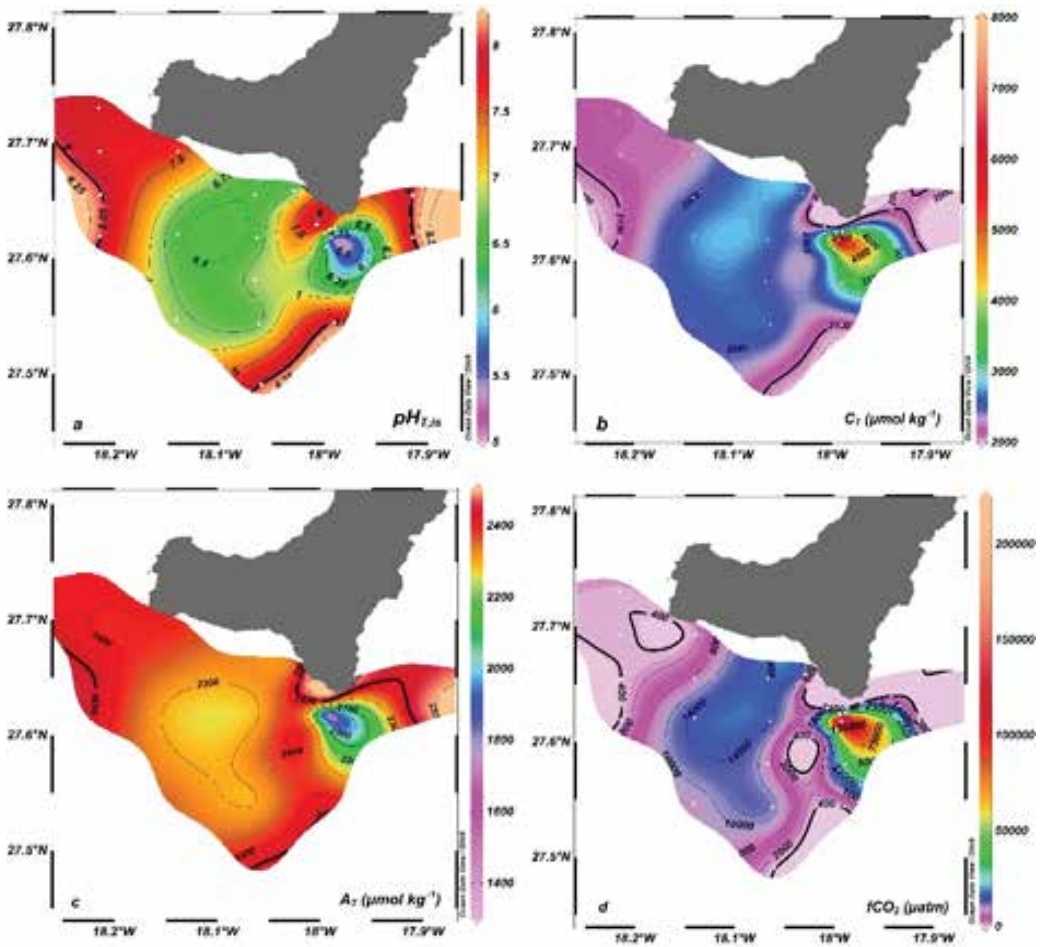

Figure 4. Distributions of the carbonate system variables at 5 m depth around the volcanic area. (a) $pH_{T,is}$ in total scale at in situ conditions. (b) Total dissolved inorganic carbon (C_T, μmol kg^{-1}). (c) Total alkalinity (A_T, μmol kg^{-1}) (d) fCO_2 (μatm).

basanite lava balloon indicated that the initially high volatile contents of this material and the intense shallow level of degassing led to submarine Strombolian-type explosivity at El Hierro [17]. The authors stated that their conclusions were consistent with the construction of a 200–300 m tall submarine cone [14], and the strong bubbling at the ocean surface. They estimated that the Tagoro eruption released at least 1.3–2.1 Tg CO_2 and 1.8–2.9 Tg S to the environment. However, they emphasize that these amounts must be considered as minima, particularly for CO_2. Taking into account the fluxes of the CO_2 calculated in the water column during the week from November 4th to 9th, 2011 by Santana-Casiano et al. [4], coincident with the most intense bubbling and degassing at the surface water, and extrapolating over the entire course of the eruption (147 days), they estimated an upper limit of 7.4 Tg CO_2 for the CO_2 emissions [17].

3.2. Emission of reduced species and changes in E_x and O_2

During the period of volcanic activity, the emission of reduced species such as iron and sulfur, contributed to decrease both the redox potential (E_R) and the concentration of dissolved oxygen (O_2) in the system (**Figure 5**). The oxygen decreased due to the oxidation of the reduced species emitted by the volcano. The presence of these reduced species produced low redox potential which reached values of −0.03 V. Background redox potential was 0.2 V.

Fe(II) species were present as Fe^{2+}, $Fe(OH)^+$, $Fe(OH)_2$, $FeCl^+$, $Fe(HCO_3)^+$ and FeHS [21]. The concentration of Fe(II) reached values higher than 50 μmol kg^{-1}. Normal dissolved Fe(II) values in the ocean surface are <0.2 nM. The reduced sulfur species were present as H_2S, HS^-, S^{2-}, S^0, SO_3^{2-}, S_x^{2-}, $S_2O_3^{2-}$ and $S_4O_6^{2-}$ [22] with a total concentration of 476 μmol kg^{-1} in the stations close to the volcano.

The flux and oxidation of Fe(II) and reduced sulfur species were so high that oxygen values were often below detection limit. Patches of anoxia at 100 m depth in the affected area were observed. The low oxygen concentrations in these waters together with the low pH_T values contributed to the high mortality of marine biota that was observed in the area after the first two months of the eruption [2].

3.3. Nutrient enrichment in the area

An important input of nutrients was produced in the area. Concentration of nitrate and silicate higher than 3 and 17 μmol kg^{-1}, respectively, were found in the surface waters, while at 100 m depth, values increased to 8 μmol kg^{-1} for the nitrate and 23 μmol kg^{-1} for silicate. In the oligothrophic areas not affected by the volcano, the concentration of these nutrients in the first 100 m is close to the detection limit. Phosphate values increased by one order of magnitude between 100 and 125 m depths, reaching maximum values of 0.6 μmol kg^{-1}. In surface water, the total value of Fe(II) was 12.7 μmol kg^{-1}, where 3.3 μmol kg^{-1} was dissolved and thus bio-available for the marine organisms. These compounds were directly introduced into the photic zone where they affected the primary production. The presence of nutrients together with the input of Fe(II) produced an enrichment in this oligotrophic area, resulting in a fertilization event caused by the shallow volcano emissions [3].

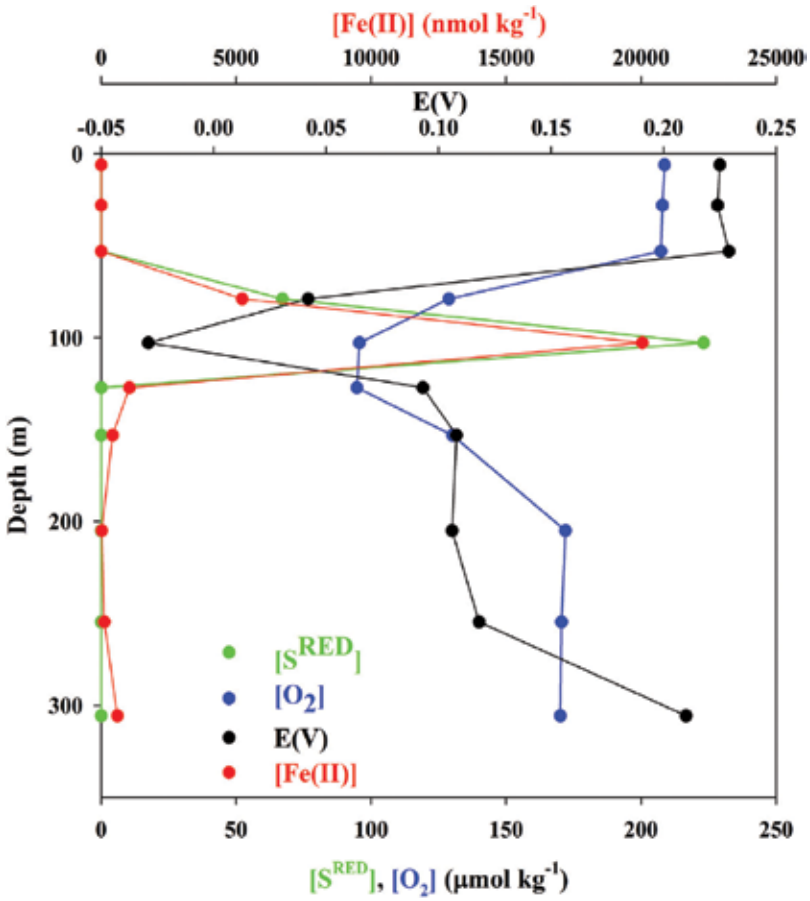

Figure 5. Vertical profiles of reduced sulfur species (green), total Fe(II) (red), dissolved oxygen concentration (blue) and redox potential (black) during November 2011.

3.4. pH and E_x, two variables that control the chemical equilibria

In the context of climatic change, it is known that due to anthropogenic CO_2 emissions the pH in the ocean surface waters is decreasing by about 0.02 pH units/decade and it will decrease by about 0.3–0.4 units at the end of this century [23, 24]. In the El Hierro waters, the pH decreased by 3 units in less than 1 week. As a result of the ongoing magmatic activity, the submarine eruption produced an unprecedented episode of severe acidification that affected the chemical equilibria in the sea water (**Figure 6**). As a consequence of the emission of reduced species, the E_x drastically changed from values higher than 0.2 V, characteristic of oxygenated waters, to values lower than −0.1 V, due to the corrosive environment. In **Figure 6**, the chemical speciation for normal ocean conditions is represented in blue (by dots) and the changes due to the volcanic emissions in orange (by stripes). Changes in the CO_2 (**Figure 6a**) and Fe(II) speciation were produced (**Figure 6b**).

In the oceanic regions where submarine volcanoes experience magmatic or hydrothermal activity, the physicochemical properties of sea water change, modifying the system. The changes

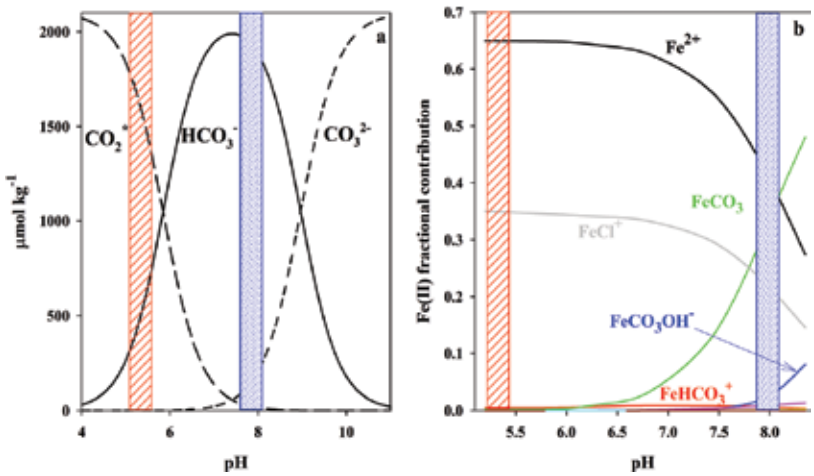

Figure 6. Chemical speciation of the (a) carbonate system and (b) Fe(II) in seawater as a function of the pH.

observed in pH_T were a consequence of the emissions of CO_2, SO_2 and H_2S/HS^- the submarine volcano (Eqs. (1)–(5)). As soon as the volcanic fluid mixes with seawater, the dissolved reduced species, Fe(II), Mn(II) and H_2S/HS^-, produce changes in the E_x. These species in contact with the oxygenated seawater are oxidized, consuming oxygen and acidifying the system (Eqs. (6)–(9)). The emission of Fe(II) also contributed to acidifying the system due to the reaction of Fe(II) with H_2S (Eq. (10)). Part of the pH decrease is compensated by reactions that also contribute to increase the alkalinity (Eqs. (11)–(13)).

After its emission, Fe(II) is oxidized (Eq. (8)) and precipitates into various mineral forms, mainly oxy-hydroxide [25, 26] forming massive deposits of iron. A fraction of the total emitted iron (4%) is stabilized against loss from solution due to complexation by dissolved organic ligands (Eq. (14)), or by incorporation into inorganic or organic colloids which reside within the dissolved size fraction [27, 28]. Moreover, reduced species of Fe and S form FeS colloidal complexes (Eq. (12)), which remain suspended in the water and are modified as the pH changes [29]. These nanoparticles can remain suspended in the deep sea for years with slower settling rates [30], solubilizing and releasing the Fe(II).

$$CO_2 + H_2O = H_2CO_3 \quad (1)$$

$$H_2CO_3 = H^+ + HCO_3^- \quad (2)$$

$$3SO_2 + 2H_2O = S(0) + 2H_2SO_4 \quad (3)$$

$$4SO_2 + 4H_2O = H_2S + 3H_2SO_4 \quad (4)$$

$$HS^- + 4H_2O = SO_4^{2-} + 10\,H^+ + 8e^- \quad (5)$$

$$H_2S + O_2 = 2H^+ + SO_4^{2-} \quad (6)$$

$$Mn(II) + ½\,O_2 + H_2O = MnO_2 + 2\,H^+ \quad (7)$$

$$Fe(II) + ¼\ O_2 + H_2O = ½\ Fe_2O_3 + 2\ H^+ \quad (8)$$

$$FeS + 9/8\ O_2 + H_2O = ½\ Fe_2O_3 + H_2SO_4 \quad (9)$$

$$Fe(II) + H_2S = FeS + 2\ H^+ \quad (10)$$

$$FeS + 4\ MnO_2 + 8\ H^+ = 4\ Mn(II) + SO_4^{2-} + Fe(II) + 4\ H_2O \quad (11)$$

$$FeS + 2\ Fe(OH)_3 + 6\ H^+ = 3\ Fe(II) + S(0) \quad (12)$$

$$2NaAlSi_3O_8 + 2\ CO_2 + 3\ H_2O = Al_2Si_2O_5(OH)_4 + 2\ Na^+ + 2\ HCO_3^- + 4\ SiO_2 \quad (13)$$

$$Fe(II) + L = Fe(II) - L \quad (14)$$

The conclusions obtained by Longpré et al. [17] through study of volatiles and trace element concentrations from the Tagoro lava balloons agreed with the changes in the carbonate variables and redox species observed in the water column. They also indicated a strong degassing and associated redox change of the initially volatile-rich and oxidized magma as it ascended from the mantle to produce the submarine eruption.

3.5. Effect of the chemical emissions on the biota

The volcanic emissions had important consequences on the biota. Organisms were observed to modify their distribution and survival and there was an alteration of the diurnal vertical migration of the pelagic communities [2]. Small picophytoplankton, such as *Prochlorococcus* and *Synechococcus*, showed a significant decline in abundance in the volcanic area at depths greater than 75 m if compared to that one in unaffected stations. However, heterotrophic prokaryotes increased with depth [2]. With respect to the bacterioplankton, there was an important change and groups often associated with deep-sea hydrothermal vents or sulfur-rich springs were observed [31]. The increase in temperature and acidification, the decrease in oxygen and the precipitation of chemical compounds resulted in a reduction of the epipelagic stocks and a disruption of the nocturnal ascent of mesopelagic organisms [32]. Once the eruption ceased, the distribution and abundances of the pelagic biota returned to baseline levels.

The increased amount of nutrients in the euphotic zone, together with the high dissolved iron concentrations, may contribute to the regeneration of the productivity in the area. The findings highlight that the same volcano that was responsible for the creation of a highly corrosive environment, affecting marine biota, has also provided the nutrients required for the rapid recuperation of the marine ecosystem.

4. The post eruptive phase and effects on the water chemistry

In March 2012, the magmatic activity stopped and the system evolved into a degasification phase. In April, the composition of the gases close to the summit was primarily CO_2 with dissolved reduced S species below 1 μmol kg^{-1} in the water column. The affected area was

reduced to 0.5 km around the main crater of the volcano. In this area, a decrease of pH_T values to 6.1 (1.9 units below the normal values) was observed and the C_T was 4191 μmol kg^{-1} [3]. The evolution of the chemical properties during the post-eruptive phase was studied from 2013 to 2016. The physical and chemical anomalies were still being observed close to the volcanic area. During this period, the study was concentrated in the volcanic edifice and a transect following the main cone was repeated twice a year. In order to detect anomalies, different strategies over the volcanic edifice, high-resolution study, yo-yo (**Figure 7a**) and tow-yo (**Figure 7b**) studies, were also followed.

4.1. High-resolution study over the volcanic edifice

During the degasification phase, the oceanographic study of the area was mainly concentrated in the volcanic edifice. High-resolution sampling along the volcano was repeated twice every year from 2013 to 2016. In these studies, 10 stations following the alignment of the main and secondary cones of the submarine volcano were repeated (**Figure 1c**). In these stations, water samples were taken at different depths and the signal of CTD, pH and oxidation-reduction potential (ORP) sensors were also recorded.

The vertical distributions of pH and C_T, A_T and Fe(II) along the high-resolution section across the volcano were measured. Negative anomalies in pH values and positive anomalies in C_T, A_T and TDFe(II) were observed close to the main crater [4, 33]. In **Figure 8**, the anomalies in pH and C_T are shown between stations 53 and 56 for the cruises on March and November 2013 (**Figure 8**). The results from these cruises also confirmed important positive anomalies in TDFe (II), coincident with negative anomalies in pH located in the proximity of the main cone [33].

4.2. Yo-yo studies

The yo-yo studies consist of raising and lowering the rosette with the CTD sensors at one location and taking samples at different depths. In the Tagoro volcano, the stations were selected from the results obtained in the high-resolution study (**Figure 8**).

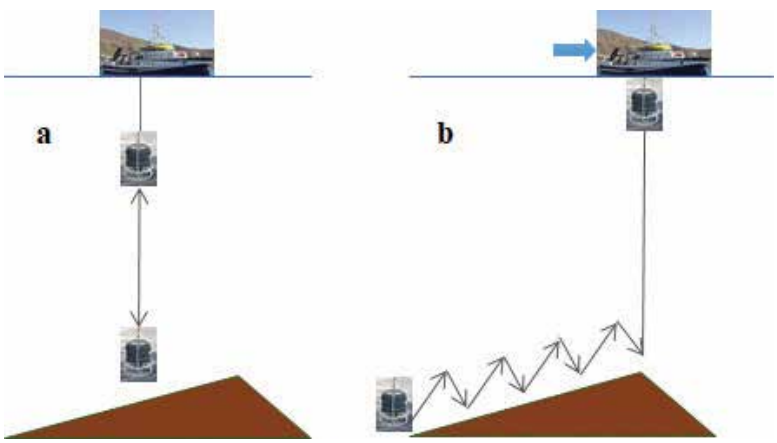

Figure 7. Diagram showing (a) a yo-yo and (b) a tow-yo procedure with CTD-pH-ORP sensors coupled to a rosette.

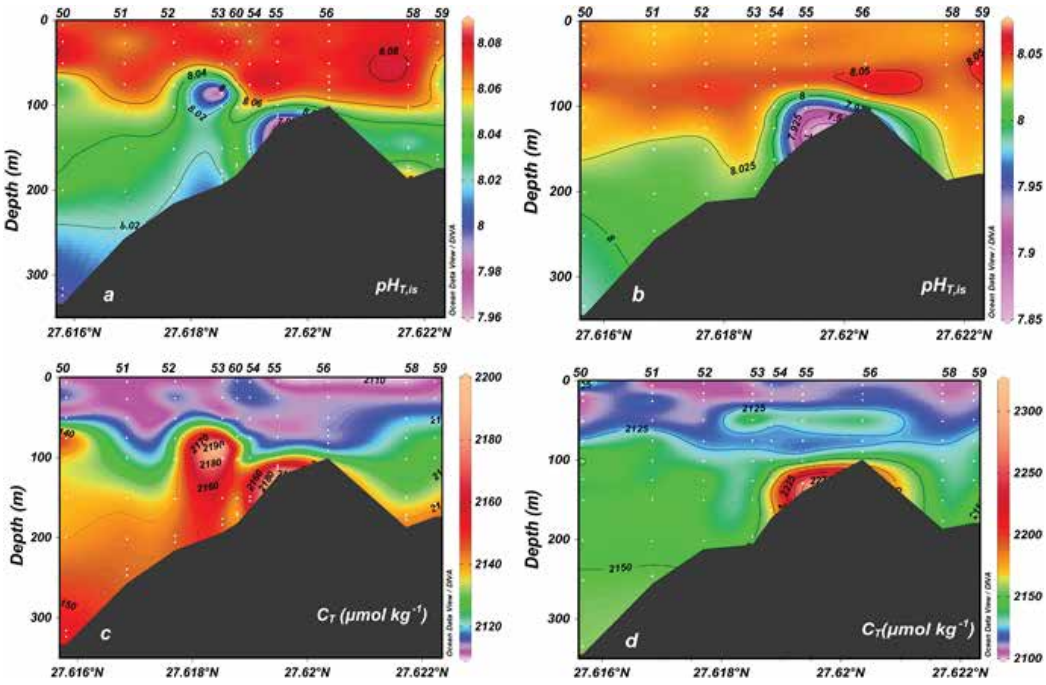

Figure 8. High-resolution studies. $pH_{T,is}$ distribution during VULCANO cruises (a) March 2013 and (b) October 2013. C_T distribution during (c) March 2013 and (d) October 2013.

In order to obtain continuous records of pH and ORP during the yo-yo, together with temperature and salinity measurements, a pH sensor was added to the normal rosette-CTD package in November 2013, and an ORP sensor in March 2014. In this way, CTD-pH-ORP yo-yo studies were carried out at the selected stations, from the surface to 2–3 m above the seabed. Water column sampling for discrete pH, A_T, C_T and TDFe(II) was carried out in the cast where maximum anomalies were detected with the sensors. The time between each cast was 10 min and the total duration of the yo-yo study was between 6 and 10 h. Anomalous values of pH, C_T, A_T and TDFe(II) were observed close to the bottom around the main crater area during the yo-yo study. The pH values were lower than those expected at that depth, and C_T and A_T values higher than usual. There was a high correlation between the anomalies observed for the different variables measured in all the cruises from 2013 to 2016 (**Figure 9**). The yo-yos carried out at station 56 (with 38 casts) and station 61 (with 61 casts) in March 2014 also showed an important fluctuation in pH and δ(ORP)/δt signals related mostly with direction and velocity changes in the local currents, associated with an M2 tidal mode with a period of 12 h. The anomalous values found again in the variables sampled (pH, C_T and A_T) were internally consistent. Therefore, those anomalies were related to CO_2 additions from the hydrothermal vents without other acid gasses acting in a significant way [4]. The fluid emissions producing these changes were ~57% CO_2 and 43% carbonate alkalinity (HCO_3^-, CO_3^{2-}). Positive anomalies for TDFe(II) were also observed and were well correlated with the decrease in pH [33]. A decrease in pH contributed to decrease the oxidation rate of Fe(II) [34] and favoured the persistence of this metal in the medium.

http://dx.doi.org/10.5772/intechopen.70422

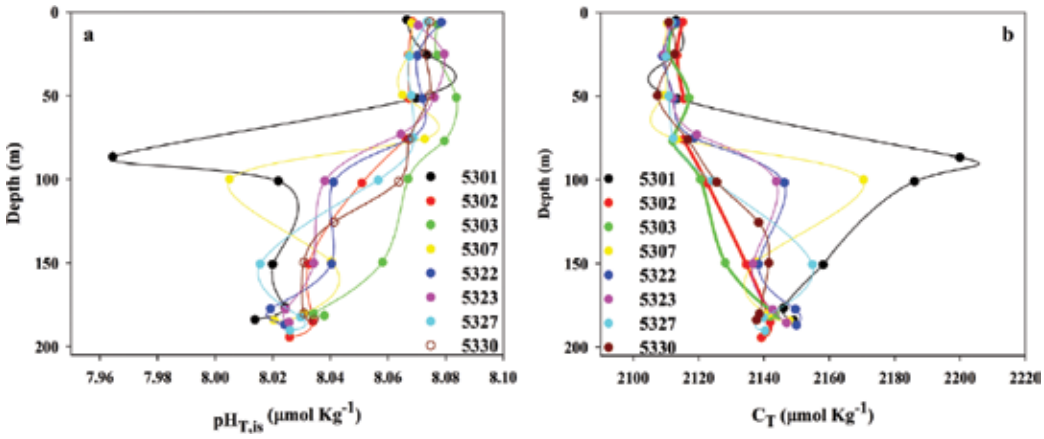

Figure 9. Yo-yo study for the carbonate variables (a) $pH_{T,is}$ and (b) C_T (µmol kg^{-1}) at the station 53, during VULCANO cruise March 2013.

4.3. Tow-yo studies

In the tow-yo studies, the SeaBird 911+ CTD-pH-ORP sensors were towed by the ship, moving at a velocity of 0.4 knots, following a saw tooth pattern by a continuous lowering and raising of the instruments between 2–3 and 40 m above the seafloor, from the base to the top of the submarine volcano. At least seven tow-yos were carried out in the area (**Figure 1c**). Four parallel tow-yos followed the topography of the principal and secondary cones and another two tow-yos were perpendicular to these.

The characteristic reduced and acid emissions of the fluids from the submarine volcano Tagoro allowed us to detect anomalies related with changes in the chemical potential and the proton concentration using ORP and pH sensors, respectively [4]. The combination of ORP and pH sensors with the CTD was used since 2014. The ORP sensor responded very quickly to the presence of reduced chemicals in the water column and the magnitude of this change was examined by the time derivative of ORP, δ(ORP)/δt. For pH changes, ΔpH was defined as the mean pH for each depth at a reference station, in an area not affected by the vent emission, subtracted from each point measured near the volcanic edifice. When δ(ORP)/δt and ΔpH versus latitude were plotted, the anomalies in pH and ORP were observed to follow the same pattern in latitude and longitude (**Figure 10**). This indicated that the emissions of both acid and reduced components must be produced in the same area.

ΔpH values of −0.25 at 100 m depths, as obtained in 2014, cannot be explained by the arrival of water from the surrounding depths [4]. This ΔpH corresponds with a pH value of 7.89, and is only found at a depth of 900 m in the unaffected surrounding water. The same behaviour was observed in November 2015 and 2016 cruises for pH, with ΔpH lower than −0.25 (**Figure 10**), clearly indicating that the degasification process was still taking place. Anomalous ORP values were also observed (**Figure 10**) at the same latitude as the pH anomalies.

Contour maps of the affected surface over the volcano can be obtained from the anomalies of ORP and pH observed in the tow-yo studies. The area of emission during VULCANO0314 was

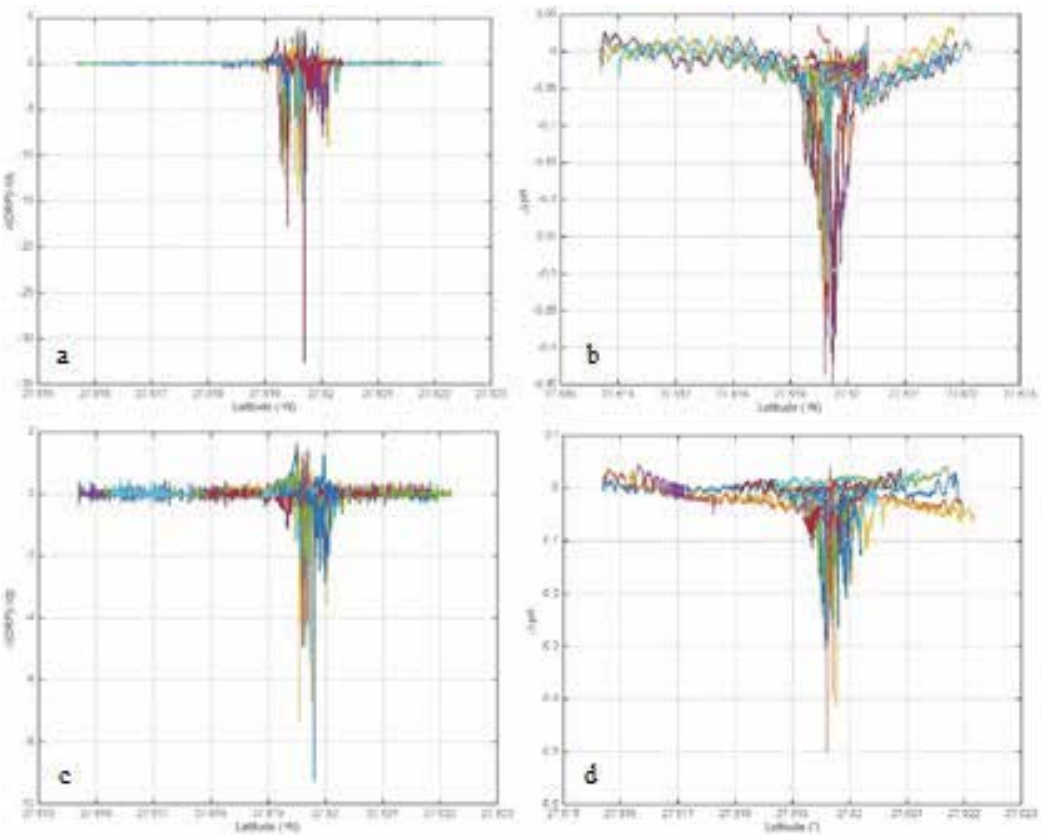

Figure 10. Plots of (a) δ(ORP)/δt and (b) ΔpH versus latitude obtained from tow-yos during VULCANO cruise October 2015 and 2016 (c) δ(ORP)/δt and (d) ΔpH versus latitude during VULCANO 2016.

13,000 ± 800 m^2 and the volume affected 206,000 ± 50,000 m^3. **Figure 11** shows the locations of the anomalous ORP values and the position of the emitting vents for the 2014 and 2016 cruises.

CO_2 fluxes from the volcanic edifice can also be estimated from the calculated anomaly area for every contour, the current speed and the average anomalies of C_T. In the Tagoro volcano, the

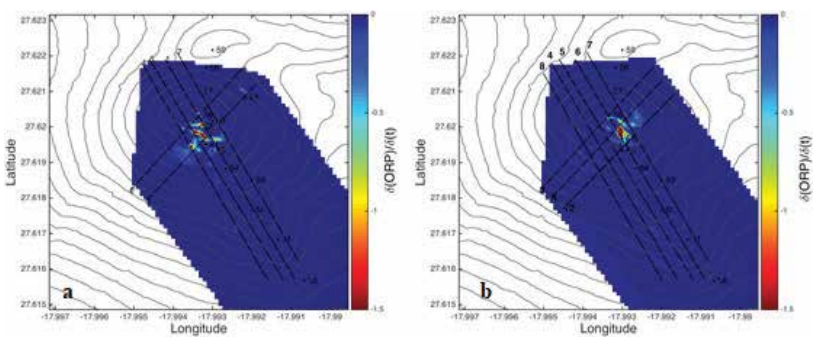

Figure 11. (a) Distribution map of δ(ORP)/δt showing areas affected by diffuse venting during March 2014 (b) March 2016.

http://dx.doi.org/10.5772/intechopen.70422

input of CO_2 along multiple sections combined with measurements of oceanic currents produced an estimated volcanic CO_2 flux of $6.0\ 10^5 \pm 1.1\ 10^5$ kg d^{-1} principally transported to the south-west. This emission of CO_2 reduced pH by ~ 0.25–0.30, altering the balance of protons in the surrounding ocean and increasing the seawater acidity by ~20 %.

5. Diving by the volcano

In February 2016, the Tagoro volcano was visited during the POS494-2 with the submersible JAGO (GEOMAR) for direct observation of the eruption site. The JAGO can take two people, a pilot and a scientific observer, to water depths of maximum 400 m. The objectives of POS494-2 were to take a high-resolution video documentation, mapping the eruption site, to sample the fluids and other volcanic and hydrothermal products that formed at the seafloor and to collect chemical and physical sensor data around the active sites (CTD, ORP and pH) 4 years after the eruption [35]. Two dives were done around the volcano, starting not far from the area where strong chemical anomalies had been measured 4 months before. The first visual inspection carried out in the JAGO showed that the anomalous area was an oval-shaped depression of at least several meters in depth and about 10–15 m in diameter. It was situated at the south-eastern flank of the volcano at a depth of 126 m, about 38 m lower than the summit of the volcano. The volcanic rocks at the edges and inside the depression were coated in orange-coloured Fe-oxides. Several pieces of volcanic rock and crusts were collected. Warm water was also seeping diffusely through sediment pores at the bottom of the crater, and occasionally more focused through small vent holes and chimneys that were up to 5 cm high. These chimneys and the orange-coloured Fe-oxides (**Figure 12**) were also observed in the HD images from the ROV Liropus 2000 during VULCANA-0417-ROV cruise. Temperature measurements 20 cm inside the sediment close to a vent site revealed 38°C while the temperature of the ambient seawater was 20°C [35]. Fluid samples were taken with a Teflon bottle directly from the emission vents and compared with the samples obtained at 1 m depth with a Niskin bottle for pH and Fe(II). pH values as low as 7.05 were found, and Fe(II) concentrations higher than

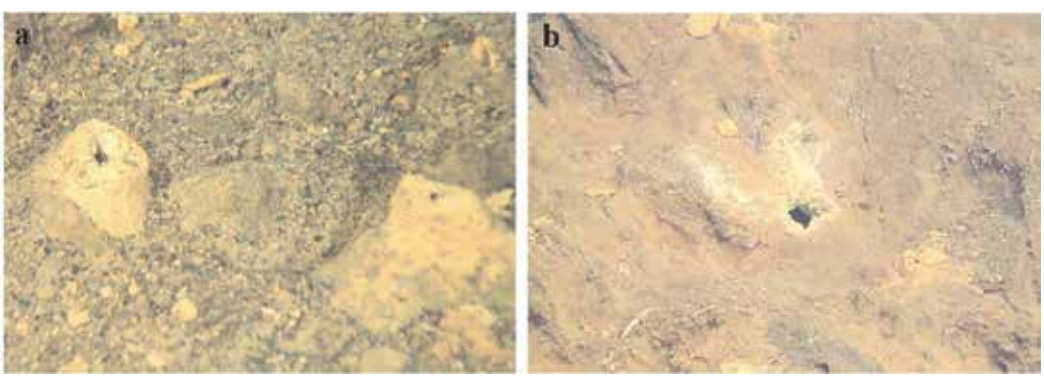

Figure 12. HD images obtained with a Liropus 2000 ROV on board R/V Ángeles Alvariño (Spanish Institute of Oceanography) during April 2017 VULCANA cruise, showing (a) two chimneys and (b) one vent, located in the north flank of the main crater of the submarine volcano Tagoro.

5□M measured compared with the reference values of pH = 7.99 and Fe(II) concentration below 0.5 nM. It was observed that the emission was diffuse and it was close to the floor.

With regard to the ecology in the area, it was observed that the volcanic black rocks were already partly colonized by bivalves (small oysters), brachiopods, sponges and whip corals and a thin coat of whitish bacteria covers most of the surfaces around the vents [35]. A detailed microscopic and molecular study carried out near the summit of the volcanic cone, at about 130 m depth, revealed that the bacteria covers were composed of filaments made of bacterial trichomes enveloped within a sheath and colonized by epibiotic bacteria [36]. This system showed an unprecedented array of metabolic pathways, spanning from the exploitation of organic and inorganic carbon released by volcanic degassing to the uptake of sulfur and nitrogen compounds, providing key competitive advantages for the colonization of the new habitat created by the submarine eruption [36].

6. Conclusions

Sites like the submarine volcano Tagoro, in its degasification stage, provide an excellent opportunity to study the carbonate system, the volcanic contribution to the global volcanic carbon flux, the emissions of trace metals such as TDFe(II) and the potential environmental impact of these emissions on the marine ecosystem.

The inputs of CO_2 along multiple tow-yo sections, combined with measurements of oceanic currents, produced an estimated volcanic CO_2 flux of 6.0 10^5 ± 1.1 10^5 kg d^{-1}, mainly transported to the south-west. These emissions also alter the balance of protons in the surrounding ocean, increasing the seawater acidity by ~20 %. The flux of CO_2 from the Tagoro volcano is comparable to that at other submarine volcanoes like NW Rota-1 (~1 ± 0.25 10^6 kg d^{-1}, an erupting submarine volcano in the Mariana arc) but relatively small compared to both the global volcanic flux of CO_2 (~0.1%) and the anthropogenic flux (~0.002%). The global volcanic flux of CO_2 is estimated to be ~ 7.2 10^8 kg d^{-1} considering mid-ocean ridges, arcs and plumes.

The emission of CO_2 from submarine volcanoes generates local ocean acidification that affects the chemical equilibrium and speciation and could impact biological communities, with especially important consequences for organisms that use calcium carbonate in their structures. These emissions also alter the balance of protons in the surrounding ocean, increasing the sea water acidity by ~20 %.

From the yo-yo studies, important anomalies in both pH_T and TDFe(II) were observed. The increased TDFe(II) concentrations and the low associated pH_T values may be causing an important fertilization event in the seawater around the volcano near the Island of El Hierro, providing optimal conditions for the regeneration of the area.

Acknowledgements

This work was supported by the Ministerio de Economía y Competitividad from the Spanish Government, through the ECOFEMA (CTM2010-19517), EACFe (CTM2014-52342-P), VULCANO

(CTM2012-36317) and VULCANOII (CTM2014-51837-R) projects, by the Spanish Institute of Oceanography through the Bimbache (2011–2012) and VULCANA (2015–2017) projects and by the European project CARBOCHANGE (contract 264879). The CETOBAPH-CGL2009-1311218 project provided us the opportunity to visit the volcano in April 2012. We thank the Captains of the R/V Ramón Margalef, Ángeles Alvariño and R/V Cornide Saavedra, and their crews for their help during this research. E. Baker, J.A. Resing, and S. Walker from the NOAA/PMEL are thanked for their advices and collaboration during VULCANO0314. P. Herzig from GEOMAR is thanked for his invitation to participate in POS494 and give us the opportunity to use the JAGO submergible in the volcano. M. Hannington, GEOMAR group and JAGO team are thanked for its collaboration during POS494 and J. González-Santana for her kind revision of the English and her comments.

Author details

Juana Magdalena Santana-Casiano[1]*, Melchor González-Dávila[1] and Eugenio Fraile-Nuez[2]

*Address all correspondence to: magdalena.santana@ulpgc.es

1 Instituto de Oceanografía y Cambio Global (IOCAG), Universidad de Las Palmas de Gran Canaria, Las Palmas de Gran Canaria, Spain

2 Instituto Español de Oceanografía, Centro Oceanográfico de Canarias, Santa Cruz de Tenerife, Spain

References

[1] Klein C, Pichler T, Koschinsky A. Geochemical characteristics, speciation and size-fraction of iron (fe) in two marine shallow-water hydrothermal systems, Doinica, Lesser Antilles. Geochemical Geology. 2017;**454**:44-53. DOI: 10.1016/j.chemgeo.2017.02.021

[2] Fraile-Nuez E, González-Dávila M, Santana-Casiano JM, Arístegui J, et al. The submarine volcano eruption at the island of El Hierro: physical-chemical perturbation and biological response. Scientific Reports 2012;**2**:1-6

[3] Santana-Casiano JM, González-Dávila M, Fraile-Nuez E, de Armas D, González AG, Domínguez-Yanes JF, Escánez J. The natural ocean acidification and fertilization event caused by the submarine eruption of El Hierro. Scientific Reports 2013;**3**:1-8

[4] Santana-Casiano JM, Fraile-Nuez E, González-Dávila M, Baker ET, Resing JA, Walker SL. Significant discharge of CO_2 from hydrothermalism associated with the submarine volcano of El Hierro Island. Scientific Reports 2016;**6**:25686. DOI: 10.1038/srep25686

[5] Carracedo JC, Day S, Guillou H, Rodríguez Badiola E, Cañas JA, Pérez-Torrado FJ. Hotspot volcanism close to a passive continental margin: The Canary Islands. Geological Magazine 1998;**135**:591-604. DOI: 10.1017/S0016756898001447

[6] Schmincke HU, Sumita M. Geologial Evolution of the Canary Islands. Koblenz, Germany: Görres-Verlag; 2010. 200 p

[7] Carracedo JC, Pérez FJ, Ancochea E, Meco J, Hernán F, Cubas CR, Casillas R, Rodríguez E, Ahijado A. Cenozoic volcanism II: The Canary Islands. In: Gibbons W, Moreno T, editors. The Geology of Spain. London: Geological Society of London; 2002. pp. 439-472

[8] Guillou H, et al. K-Ar ages and magnetic stratigraphy of a hotspot-induced, fast grown oceanic island: El Hierro, Canary Islands. Journal of Volcanology and Geothermal Research. 1996;**73**:141-155

[9] Gee MJR, Watts AB, Masson DG, Mitchell NC. Land-slides and the evolution of El Hierro in the Canary Islands. Marine Geology. 2001;**177**:271-293

[10] Masson DG. Catastrophic collapse of the volcanic island of Hierro 15 ka ago and the history of landslides in the Canary Islands. Geology. 1996;**24**(3):231-234

[11] Masson DG, Watts AB, Gee MJR, Urgeles R, Mitchell NC, Le Bas TP, Canals M. Slope failures on the flanks of the western Canary Islands, Earth Science Reviews. 2002;**57**:1-35. DOI: 10.1016/S0012-8252(01) 00069-1

[12] López, C, et al. Monitoring the volcanic unrest of El Hierro (Canary Islands) before the onset of the 2011-2012 submarine eruption. Geophysical Research Letter. 2012;**39**:L13303

[13] Rivera J, Lastras G, Canals M, Acosta J, Arrese Hermida N, Micallef A, Tello O, Amblas D. Construction of an oceanic island: Insights from the El Hierro (Canary Islands) 2011–2012 submarine volcanic eruption. Geology. 2013;**41**:355-358. DOI: 10.1130/G33863.1

[14] Rivera Hermida N, Arrese B, González-Aller D, Sánchez de Lamadrid JL, Gutiérrez de la Flor D, Acosta J. Bathymetry of a new-born submarine volcano: El Hierro Canary Islands. Journal of Maps. 2014;**10**:82-89. DOI: 10.1080/17445647.2013.849620

[15] Eugenio F, Martin J, Marcello J, Fraile-Nuez E. Environmental monitoring of El Hierro Island submarine volcano, by combining low and high resolution satellite imagery. International Journal of Applied Earth Observation and Geoinformation. 2014;**29**:53-66

[16] Coca J, Ohde T, Redondo A, García-Weil L, Santana-Casiano JM, González-Dávila M, et al. Remote sensing of the El Hierro submarine volcanic eruption plume. Journal of Remote Sensing. 2014;**35**(17):6573-6598. DOI: 10.1080/01431161.2014.960613

[17] Longpré MA, Stix J, Klügel A, Shimizu N. Mantle to surface degassing of carbon- and sulfur-rich alkaline magma at El Hierro, Canary Islands. Earth and Planetary Science Letters. 2017;**460**:268-280

[18] Longpré MA, Klügel A, Diehl A, Stix J. Mixing in mantle magma reservoirs prior to and during the 2011–2012 eruption at El Hierro, Canary Islands. Geology. 2014;**42**:315-318. DOI: 10.1130/g35165.1

[19] Martí J, Castro A, Rodríguez C, Costa F, Carrasquilla S, Pedreira R, Bolos X. Correlation of magma evolution and geophysical monitoring during the 2011–2012 El Hierro (Canary

Islands) submarine eruption. Journal of Petrology. 2014;**54**:1349-1373. DOI: 10.1093/petrology/egt014

[20] Meletlidis S, Di Roberto A, Cerdeña ID, Pompilio M, Bertagnini A, Benito-Saz MA, Del Carlo P, Aparicio SSM. New insight into the 2011–2012 unrest and eruption of El Hierro Island (Canary Islands) based on integrated geophysical, geodetical and petrological data. Annals of Geophysics. 2015;**58**:S0546. DOI: 10.4401/ag-6754

[21] Stumm W, Morgan JJ. Aquatic Chemistry. Chemical Equilibria and Rates in Natural Waters. 3rd ed. Wiley; New York 1996. 1040 p

[22] Rickard D, Luther III GW. Chemistry of iron sulphides. Chemistry Review. 2007;**107**:514-562

[23] Caldeira K, Wickett ME. Anthropogenic carbon and ocean pH. Nature. 2003;**425**:365

[24] Orr JC, et al. Anthropogenic ocean acidification over the twenty-first century and its impact on calcifying organisms. Nature. 2005;**437**:681-686

[25] Resing JA, Sansone FJ. The chemistry of lava-seawater interactions: The generation of acidity. Geochimica Cosmochimica Acta. 1999;**63**(15):2183-2198

[26] de Baar HJW, de Jong JTM. Distributions, sources and sinks of iron in seawater. In: Turner DR, Hunter KA, editors. The Biogeochemistry of Iron in Sea Water. New York: John Wiley & Sons Ltd; 2001. 123 p

[27] Bennett SA, et al. The distribution and stabilisation of dissolved Fe in deep-sea hydrothermal plumes. Earth and Planetary Science Letters. 2008;**270**(3):157-167

[28] Resing JA, et al. Basin-scale transports of hydrothermal dissolved metals across the South Pacific Ocean. Nature. 2015;**523**:200-203

[29] Luther GW, et al. Chemical speciation drives hydrothermal vent ecology. Nature. 2001;**410**(6830):813-816

[30] Yücel M, Gartman A, Chan CS, Luther GW. Hydrothermal vents as a kinetically stable source of iron-sulphide-bearing nanoparticles to the ocean. Nature Geoscience. 2001;**4**(6): 367-371

[31] Ferrera I, Arístegui J, González JM, María F, Montero MF, Fraile-Nuez E, Gasol JM. Transient changes in bacterioplankton communities induced by the submarine volcanic eruption of El Hierro (Canary Islands). PLoS One. 2015;**10**(2):e0118136. DOI: 10.1371/journal.pone.0118136

[32] Ariza A, Kaartvedt S, Røstad A, Garijo JC, Arístegui J, Fraile-Nuez E, Hernández-León S. The submarine volcano eruption off El Hierro Island: Effects on the scattering migrant biota and the evolution of the pelagic communities. PLoS One. 2014;**9**(7):e102354

[33] Santana-González C, Santana-Casiano JM, González-Dávila M, Fraile-Nuez E. Emissions of Fe(II) and its kinetic of oxidation at Tagoro submarine volcano, El Hierro. Marine Chemistry. 2017. DOI: 10.1016/j.marchem.2017.02.001

[34] González-Dávila M, Santana-Casiano JM, Millero FJ. Competition between O_2 and H_2O_2 in the oxidation of Fe (II) in natural waters. Journal of Solution Chemistry. 2006;**35**(1):95-111

[35] Hannington MD, et al. Assessment of the Ongoing Magmatic-Hydrothermal Discharge of the El Hierro Submarine Volcano, Canary Islands by the Submersible JAGO. RV POSEIDON. GEOMAR Helmholtz Centre for Ocean Research Kiel, Instituto de Oceanografia y Cambio Global, Instituto Espanol de Oceanograia. Cruise Report POS494-2. July 2016; p 88. DOI: 10.13140/RG.2.1.1009.8162

[36] Danovaro R, Canals M, Tangherlini M, Dell'Anno A, Gambi C, et al. A submarine volcanic eruption leads to a novel microbial habitat. Nature and Ecology Evolution. 2017;**1**:0144. DOI: 10.1038/s41559-017-0144

Chapter 5

The Characteristics of Volcanic Eruption in Indonesia

Eko Hariyono and Liliasari S

Additional information is available at the end of the chapter

http://dx.doi.org/10.5772/intechopen.71449

Abstract

This chapter discusses the unique characteristics of the volcanic eruptions in Indonesia. We know that Indonesia has 147 volcanoes and 76 of them are active volcanoes and spread along the islands of Java, Lesser Sunda, Sumatra, and Celebes. The characteristics of Indonesian volcanoes are quite unique in terms of the formation process, eruption phenomenon, and the resulting natural disasters. Most volcanoes in Indonesia consist of stratovolcanoes, but this does not mean that the resulting eruptions are always explosive and they have a long period. This can be seen from the activity of Semeru that always erupts effusively every day, Sinabung that has a very short eruption period, Tangkuban Perahu eruption that occurs suddenly with the lack of early signs, and Merapi and Kelud that have eruption period that is getting shorter. Based on the results of our study it can be known that the types of volcanic eruption are influenced by the structure of the constituent rocks of the volcanoes. However, the presence of external control factors in the form of large-scale earthquakes will affect their periodicity. The large earthquakes can affect the stability of the magma chamber that can trigger a premature eruption.

Keywords: volcanic eruption, natural disaster, Indonesia volcano

1. Introduction

Indonesia is one of the equatorial countries located in the Pacific Ring of Fire. These areas have formed a horseshoe of approximately 40,000 km (25,000 miles) from South America to North America through the Bearing Strait, Japan up to New Zealand. Along the Ring of Fire, there are 452 volcanoes, of which 75% are in active status. It can be said that Indonesia is a country having the most active volcanoes in the world.

Indonesia has a great number of volcanoes in the world. There are 147 volcanoes, and 76 of them are the active volcanoes and spread along the islands of Sumatra, Java, Celebes, and Lesser Sunda (**Figure 1**). This means Indonesia has a tremendous opportunity to face eruption disaster in next future. It can be said that Indonesia is the windows of volcanic world.

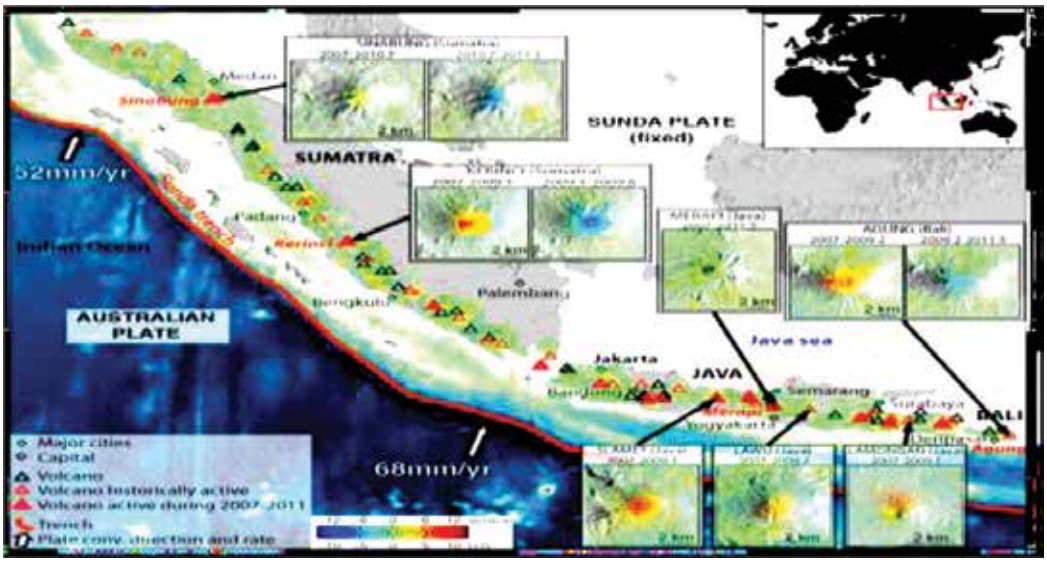

Figure 1. The map of volcanoes distribution in Java and Sumatera Island (www.rsmas.miami.edu).

The volcanic eruption is one of the terrible types of natural disasters in Indonesia. In addition to the high casualties, the eruption disaster is also followed by large-scale infrastructure damage and by changes in social institutions and in the long-term economic impact. One example is the eruption of Mount Sinabung. Based on the record from the Center for Volcanology and Geological Hazard Mitigation or Pusat Vulkanologi dan Mitigasi Bencana Geologi (PVMBG), Sinabung has shown the eruptive activity since 2010 until now. Hot clouds (Indonesian = wedus gembel) and volcanic ash are constantly out of volcano ventilation. They damage most of the surrounding agricultural areas around the mountain. In addition to the economic impact, this condition is also very unfavorable for the psychological community. They live in the shadow of fear of eruption disaster.

Besides the Sinabung eruption, Indonesia has 20 most active volcanoes of Merapi, Kaba, Kerinci, Anak Krakatau, Papandayan, Slamet, Bromo, Semeru, Batur, Rinjani, Sangeang Api, Rokatenda, Egon, Soputan, Lokon, Gamalama, Dukono, Karangetang, Ibu, and Talang. Although the level of awesomeness is not as big as the previous disaster, the impact of the eruption on the environment and society is quite alarming. This is very disturbing to life and economic stability of the community around the volcanoes. Based on the record from the global database on natural and technological disaster or emergency events database (EMDAT**)**, volcanic eruption is the third greatest disaster in Indonesia after flooding and earthquakes and also has the second highest number of casualties after the earthquakes (**Figure 2**).

The characteristics of Indonesian volcanoes are enticing in terms of the formation processes, eruption phenomena, and generated impacts. Usually, the types of volcanoes are represented by stratovolcanoes. They were shaped as results of subduction of the earth crust in subduction zones, but this does not mean that the resulting eruption is always explosive and in long periods. This can be seen from the activity of Semeru as a stratovolcano that erupts every day

http://dx.doi.org/10.5772/intechopen.71449

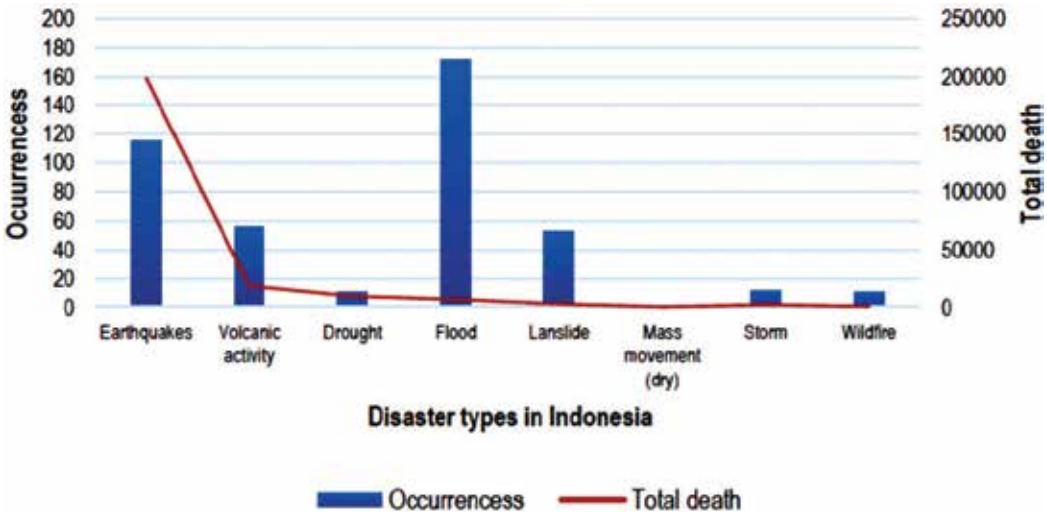

Figure 2. Disaster impact in Indonesia from 1900 to 2016 (modified from EMDAT, 2016) [1].

effusively with low explosive. Others from Sinabung relatively have short eruption duration and are unpredictable when it stops. Tangkuban Perahu eruption features occurred suddenly, showing weak initial signs. Merapi and Kelud have an increasingly short eruption period.

These phenomena are very interesting to be discussed in depth. Starting from eruption parameters until surrounding impact, there are many unanswered questions about the idiosyncrasy of volcanoes in Indonesia. This chapter will describe in detail the characteristics of several volcanoes and their impact on the environment and society. Through the study, it is expected to provide an overview of the volcanic eruption phenomena in Indonesia.

2. The profile of characteristic volcanic eruption in Indonesia

Some examples of Indonesian volcanoes are considered to have differences compared with the volcanoes in general, among others, Merapi, Semeru, Kelud, Tangkuban Perahu, and Sinabung. The five volcanoes represent the discrepancy of the characteristics of hundreds of volcanoes in Indonesia. The first four volcanoes occur on the Java Island, while Mount Sinabung is located on the Sumatra island.

Mount Merapi is a large Quaternary stratovolcano that is located in Sunda arc [2]. It is known as the most active volcano in the world and is considered the most dangerous volcano with pyroclastic flows generated by the collapse of the lava domes [3]. The mountain is an andesitic volcano and located in central sector of Java [4], between the Java Sea and the Indian Ocean, having a height of 2986 m above the sea level (**Figure 3**). The Merapi is located on 7° 32′30″ South latitude and 110° 26′ 30″ East longitude and lies in a subduction zone between the Indo-Australian and Eurasian plates. This location has controlled the volcanic activity in Sumatra, Java, Bali, and Lesser Sunda [5].

Figure 3. Merapi location map in central of Java (rinjanionline.com).

Mount Merapi is a volcanic cone having a magma composition from basaltic to basaltic-andesitic [6], with silica content (SiO_2) ranging between 52 and 56%. Based on the silica content, it can be resumed that the eruption of Mount Merapi is mildly explosive. The nature of the basaltic andesitic magma is capable to flow from short to not too long distances and to destroy the surrounding settlements.

The unique characteristics of the eruption of Merapi can be seen from the changes in the eruptive cycle. As shown in **Figure 4**, since the sixteenth century, Mount Merapi erupted 80 times with a period of 4 years and a remaining time of about 1–18 years. From the starting eruption until the mid-eighteenth century, Merapi eruption index tended to increase but decreased in the mid-nineteenth century and increased in turn in the early twentieth century, with the volcanic explosivity index (VEI) ranging between 1 and 2.

The longest period of quiescence of the Merapi volcano was recorded in the eighteenth century, when the eruptions had a low index. In the middle of the twentieth century, the Merapi eruptions were consistent with the emplacement of effusive lava domes and generated pyroclastic materials having a small volume [7]. The pyroclastic flows dominated the eruptions in the twentieth century, but much larger eruptions occurred in the nineteenth century. Although the periodic interval is shorter, the Merapi explosivity index was constant at each eruption period and suddenly increased reaching the highest index (VEI 4) in the 2010 eruption (**Figure 4**).

The most dangerous eruption from Merapi is the hot cloud (Indonesian = wedus gembel). It is said "wedus gembel" because the resulting hot clouds are clumps like wool. This hot cloud is a pyroclastic flow generated from the lava dome fall due to mixtures between hot gases and volcanic particles and moving down the slopes of volcanoes with high speed [9]. The temperatures of the hot clouds range between 500 and 600°C and they are capable to move at speeds of up to 100 km/h. The high temperature of hot clouds can burn all the surrounding objects.

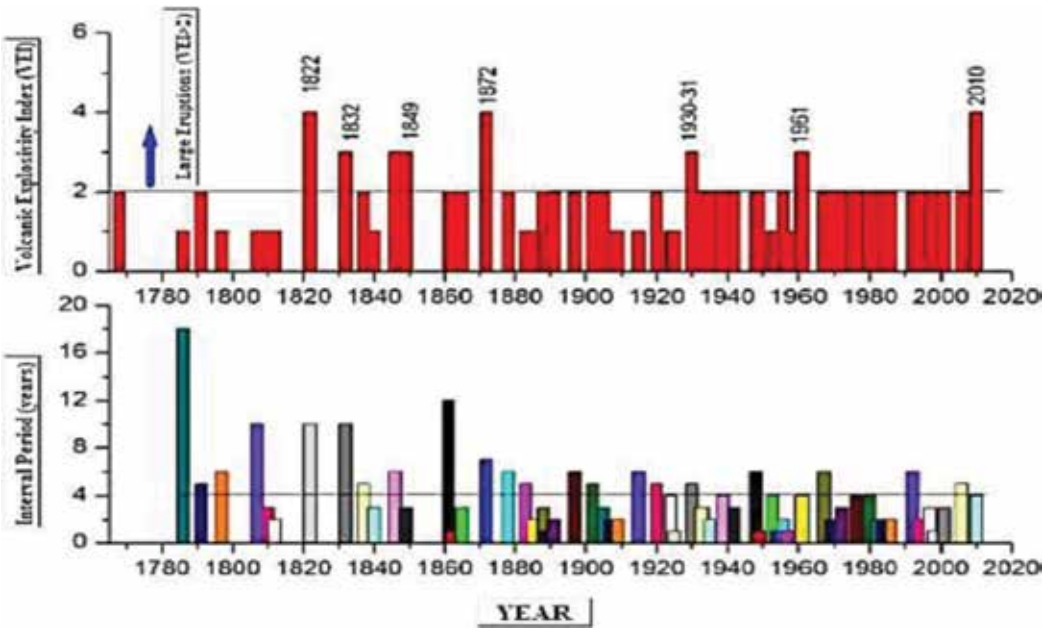

Figure 4. Merapi eruption statistics since the eighteenth century [8].

The eruption is also owned by Semeru. Semeru is one of the most active volcanoes in East Java. This mountain is better known as the peak of Mahameru because it has highest mountains on the Java island [10]. Semeru is located on 08′06.5′ South latitude and 112°55′ East longitude. It has a height of 3676 m above sea level. It is a stratovolcano composed of andesitic rocks, with a silica content ranging between 46.5 and 60%.

Mount Semeru eruption was recorded since 1818 with an average eruption period ranging between 1 and 3 years. The characteristics of the Semeru eruption are different from that of Merapi. The type of eruption of the Semeru is Strombolian, because it involves the fragmentation of low viscosity basaltic magma by volatile degassing [9]. Other volcanological studies have suggested that the Semeru eruption type is vulcanian with VEI ranging between 2 and 3, because it has generated eruption columns, lava dome growth, and small pyroclastic flow [11], has produced basaltic incandescent lavas; and was accompanied by hot clouds. The greatest eruption occurred in 1944. The eruption resulted in a hot cloud with a volume of 6.8 million m^3 and the number of victims of the hot cloud reached seven people [5].

Semeru is known as liquid lava that always comes out every day. **Figure 5** shows the location map of Semeru and drainage channel that was constructed in 2010. This lava path leads to S and SE volcano, which is a densely populated settlement.

Since 1967, on average, every 15 min there is an eruption with a low explosivity index [12]. However, the eruption of Mount Semeru is considered not dangerous. The local government still allows tourists to perform climbing activities that usually start from the village of Ranu Pane, located to the north of the volcano. People around Mount Semeru believe if eruptions

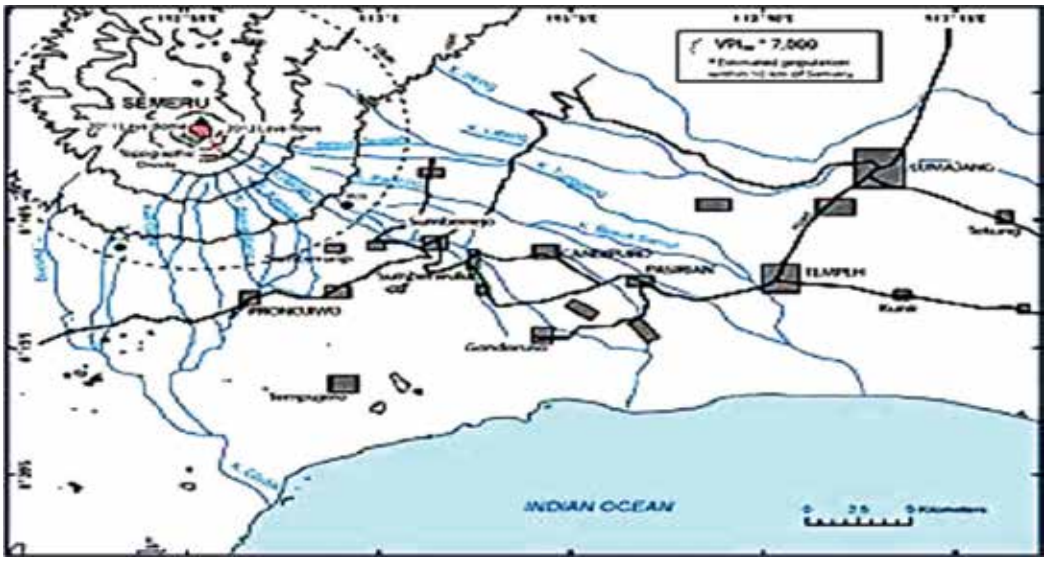

Figure 5. Semeru map and drainage channel (https://volcano.si.edu).

happen every day, Semeru remains safe because it will not be possible to erupt on a large scale. The increasing frequency of the Semeru eruption is becoming a unique geological phenomenon in Indonesia that is being investigated by volcanologists related to its causal factors.

The eruption characteristic is also experienced by Sinabung. It has happened in the last years and has been very difficult to predict. Mount Sinabung is part of an ancient volcano (Toba) and has an altitude of 2460 m asl, and the peak geography is in 3°10′ North and 98°23.5′ East latitude. The mountain was formed due to a fracture on the northwestern edge of the basin of Mount Toba [5]. It is located on the Sumatra Island belt produced from the Indo-Australian plate subduction process under the Eurasiatic plate [13].

Sinabung includes a stratovolcano showing its activity after a period of quiescence of 400 years [3]. This type of volcanic edifice is characterized by a tall conical building structure and is built by many layers of hardened lavas, tephra, pumices, and volcanic ashes [14]. The characteristics of the Sinabung eruption are different from that of the other volcanoes in Indonesia. In addition, they are difficult to predict, although a relatively short duration of the eruption has been observed. One of the volcanic products of Sinabung is a hot cloud capable of damaging the surrounding environment (**Figure 6**).

The relationships between the Sinabung and the Toba volcanoes are very close. This context can be known from the structure of their constituent rocks. Based on the results of the morphologic study of the Sinabung rocks, it can be known that the basement of the Sinabung volcanites consists of limestones and of the pyroclastic deposits of Toba [5]. These lithologies should have controlled the Sinabung eruptions that were always accompanied by thick eruptive products with a relatively high frequency of eruption.

http://dx.doi.org/10.5772/intechopen.71449

Figure 6. Sinabung eruption with hot clouds [15].

On the other hand, Mount Kelud is one of the active volcanoes in eastern Java. Now it has entered into a period of quiescence after a major eruption occurred in 2014. Although the altitude of the volcano is lower than Merapi, Semeru, and Sinabung (1731 masl), Mount Kelud is also classified as a stratovolcano. This mountain was formed after the subduction of the Indo-Australian and Eurasian plates. Mount Kelud eruption was known due to the volume of ashes that were distributed widely until the radius, reaching hundreds of kilometers and covering almost all of the Java Island (**Figure 7**). Besides flowing lavas and resulting ashes, the eruption disaster also comes from the mud flows and from the floods that damage the surrounding environment.

Figure 7. Distribution of Kelud ash in Java [15].

The eruption phase of Kelud is well ordered relatively and got into a rest period after a major eruption in 2014. The Kelud activity is still present. This can be seen from the various signs of volcanic activity that were recorded by the monitoring officer. One of the interesting natural phenomena is the birth of the Kelud Son (Anak Kelud), which occurred during the 2007 eruption. It indicates that the volcano is still active.

The characteristics of the Kelud eruption were influenced by the silica content, relatively high. The eruption type is Pelean, attributed by thick lava bursts containing more than 66% SiO_2 [16] that inhibit the flow of gas and steam. This causes great shocks during eruptions and produces a very high explosive sound, which can disturb the upper atmosphere layers (ionosphere) [17]. The body structure of Kelud is stronger than the other volcanoes. The volcanic products are represented by pyroclastic rocks due to flows, fall-out, or lavas with the composition of K-basalts and K-andesites. This composition controls the factor that the probability of lava dome collapses is small, so that the hot clouds are not generated from the Kelud eruption.

Figure 8 shows the Kelud eruption activity during the twentieth century, when the times of eruption were getting shorter and shorter. Based on this figure, it can be predicted that the Kelud volcano will erupt again at intervals of around 21.3 years. Then the next eruption is predicted to occur after 2030.

The next interesting discussion deals with the eruption of Tangkuban Perahu. This is one of the active volcanoes in Indonesia. It is a stratovolcano located on the highland area of Bandung West Java, with the height of 2087 masl (**Figure 9**). Tangkuban Perahu was formed from the calderic collapse of the Sunda Mountain [18]. Rows of mountains when viewed from a distance looks like a boat upside down and then were called Tangkuban Perahu, which means an upside down boat.

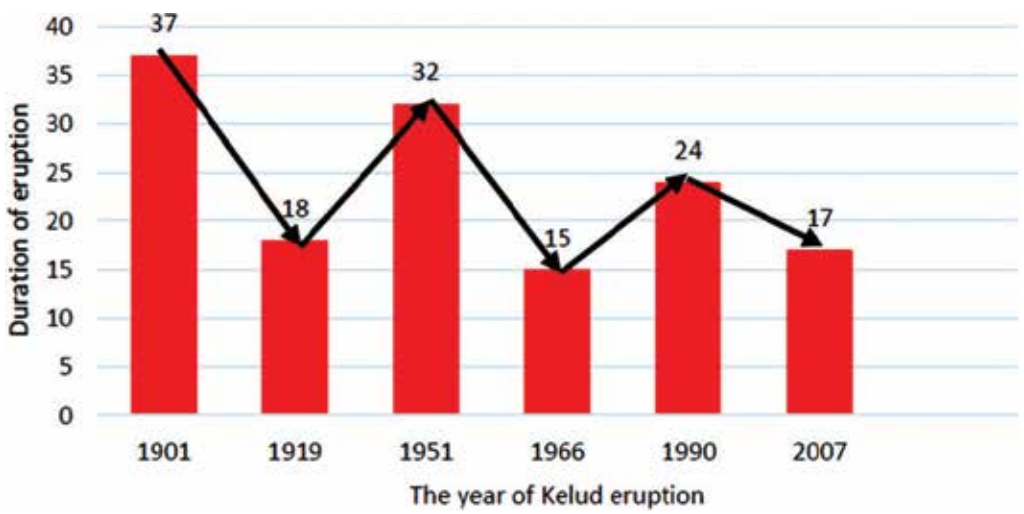

Figure 8. An interval of eruption of Kelud after twentieth century [5].

http://dx.doi.org/10.5772/intechopen.71449

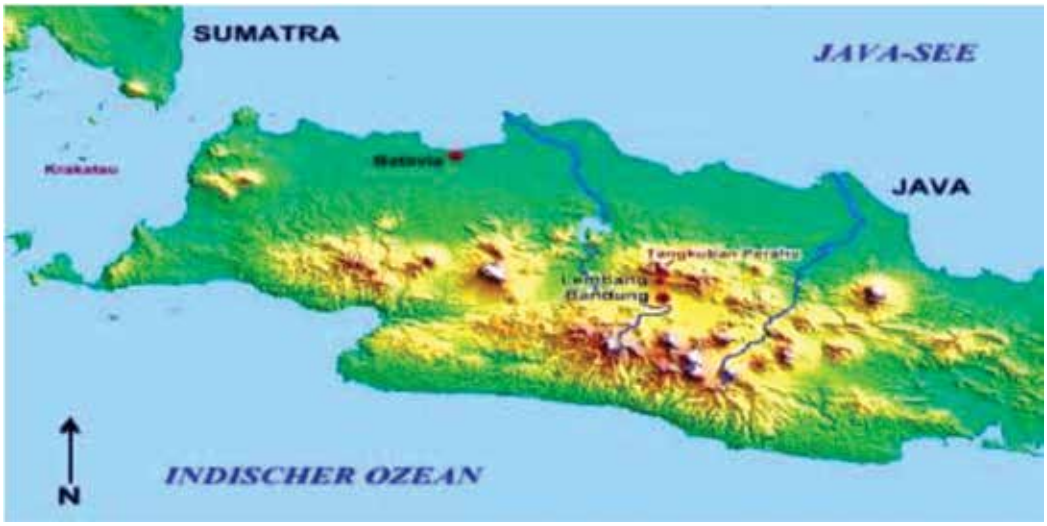

Figure 9. Tangkuban Perahu location in West Java (en.wikipedia.org).

The effusive pattern of the eruption with minimal signs makes the eruption of Tangkuban Perahu quite unique. Besides, it has a great geothermal potential, and the eruption characteristics of this volcano are different from that of the other volcanoes in Indonesia. Since the nineteenth century, the eruption of Tangkuban Perahu volcano is phreatic by producing ash without lava flow, hot clouds, or incandescent rocks. However, it does not mean that the eruption of Mount Tangkuban Perahu is not dangerous for the people around it. One of the eruption products to watch out for are the poisonous gases CO, CO_2, and SO_2 that harm human health or even cause death if inhaled in large quantities.

The large eruption of Tangkuban Perahu occurred in the eighteenth century by spewing material eruption enough and until the formation of eight crater lakes. After that eruption, its activity became weak. One of the uniqueness of the eruption of Tangkuban Perahu was the lack of eruption signs that were not very clear. Sometimes only detected the appearance of earthquakes tremor by monitoring stations sign the volcano have been erupted. This makes it very difficult for volunteer observers to determine the eruption status. However, the weak eruption still makes an eruption activity not too dangerous to the surrounding community.

3. The changes of volcanoes' behavior in Indonesia

Volcanoes and earthquakes are interconnected phenomena. But, in general, earthquake is one of the physical parameters to recognize volcanic activity. If the quantity and frequency of the earthquake are higher, it can be said that the activity of the volcano is higher too. This earthquake is called a volcanic earthquake. Based on the results of the latest geological research, an earthquake can affect the activity of the volcano, especially the earthquake that has a high Richter scale (RS) rating [19]. Earthquakes with great power affect the viscosity of magma and eruption style [7].

The effects of the earthquakes on the eruptive behavior are experienced by several volcanoes in the world. Based on the results of previous studies, it was shown that the large earthquakes followed by the eruptive activity include the earthquakes in the Hawaiian Islands, followed by Kilauea and Mauna Loa volcanic eruptions, the Landers earthquake, which triggered the eruption of Caldera Long Valley in 1992 and Denali Earthquake in 2002, triggering a local volcanic activity in North America [20].

Figure 10 shows the differences of volcanic eruption patterns before and after big earthquakes. Before the earthquakes, the volcanic eruption around the earthquake fields had a large time interval and the eruption frequency small. On the contrary, after the earthquakes, the eruption time interval tends to be small and the frequency large.

The impact of large earthquakes on changes in volcanic behavior is also experienced in Indonesia. In 2001 and 2006, the central Java region experienced an earthquake with a strength of 6.3 RS. The earthquake in 2001 caused the rise of Merapi fumarole temperature, while the earthquake in the year of 2006 caused the increase of magma extrusion and pyroclastic flow [21].

One example of changes in volcanic eruption behavior is Mount Merapi. It is one of the most active stratovolcanoes in Indonesia characterized by the growth of lava domes and dome falls accompanied by dangerous pyroclastic flows [22]. Over the past decade, Merapi had a small eruption every 2–6 years with an average VEI <3 and a low eruption volume (1×10^6–4×10^6 m^3) [23].

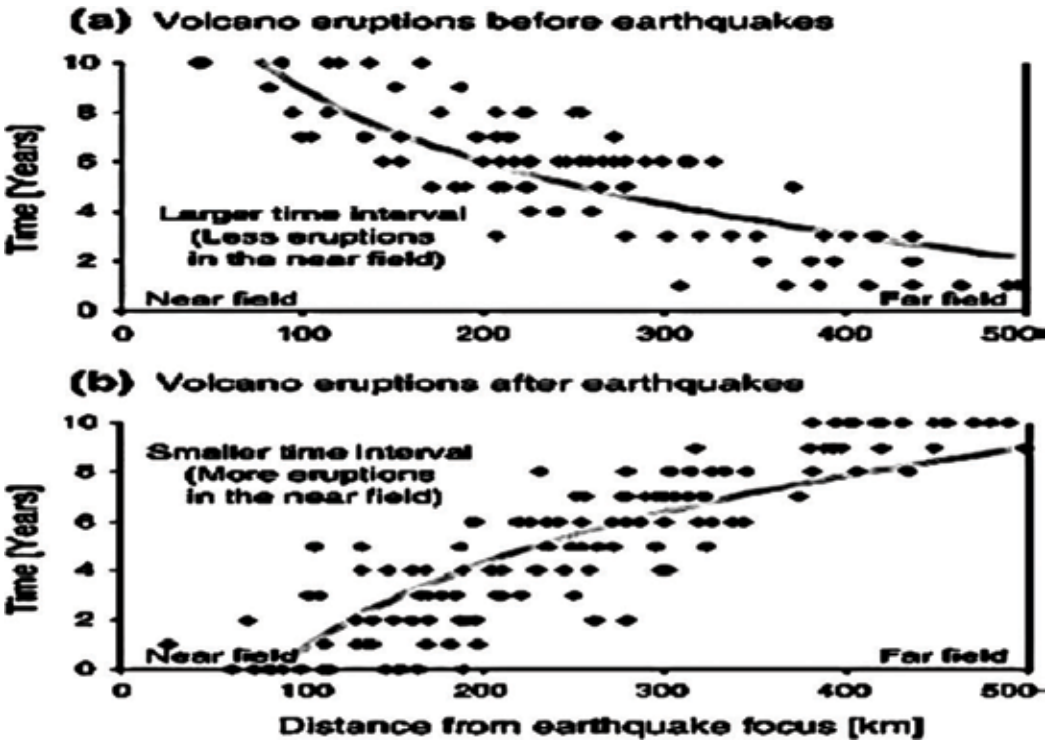

Figure 10. Scatter diagram of the relationship between the distance and time of eruption (a) before and (b) after the earthquake in Kuril and Kamchatka Islands [20].

http://dx.doi.org/10.5772/intechopen.71449

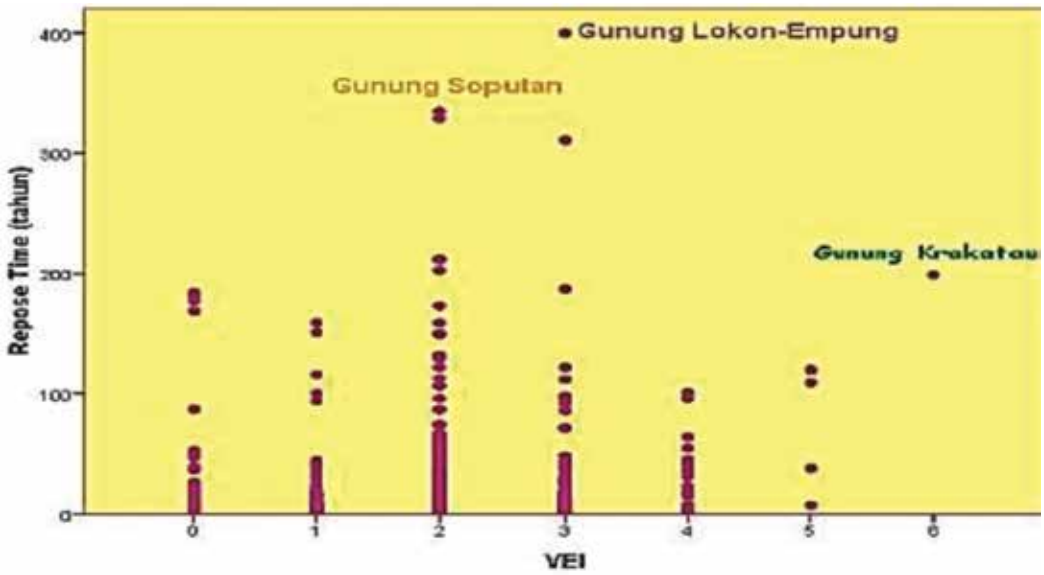

Figure 11. Correlation between repose time and VEI for multiple volcanoes in Indonesia [24].

The changes in volcanic eruptive behavior in Indonesia can be seen both from the VEI and the repose time (**Figure 11**). As a general rule, the longer the repose time of the volcano, the bigger the eruptive activity, but it's not so now. This statement is supported by a study that pointed out that the repose time does not affect the volcanic eruption index in Indonesia [24].

4. The eruption crisis of Indonesian volcanoes in the last decade

Indonesia cannot be separated from the volcano phenomenon [25]. This is a consequence as an equatorial state located at the meeting of three giant plates (Eurasian, Indo-Australian, and Pacific) (**Figure 12**). The three plates collide with each other (the Indo-Australian plate slips under Eurasia); therefore, Indonesia becomes the epicenter of earthquakes, volcanic tracks, and faults or ruptures [26]. Plate meeting areas allow for earthquakes and other disaster.

Being a country prone to eruption disaster, 10% of the Indonesian population lives in a volcanic region [27]. This condition is potential for large casualties when the eruptions occur. The Merapi eruption, which occurred in 2010, included a large eruption with the death of 386 residents and about 17,000 people facing respiratory problems [28].

The volcanic eruption activity in Indonesia has a diverse impact on the environment. The last 5 years of eruption of Merapi, Kelud, and Sinabung produced abundant materials that are beneficial for soil fertility. But many problems arise from excessive material eruptions, such as lava floods that can endanger the surrounding community. The volcanic products can pose a significant disaster if it affects people, agricultural areas, transportation and facility networks, and other social infrastructure [29]. Explosive eruption of volcanic with VEI > 3

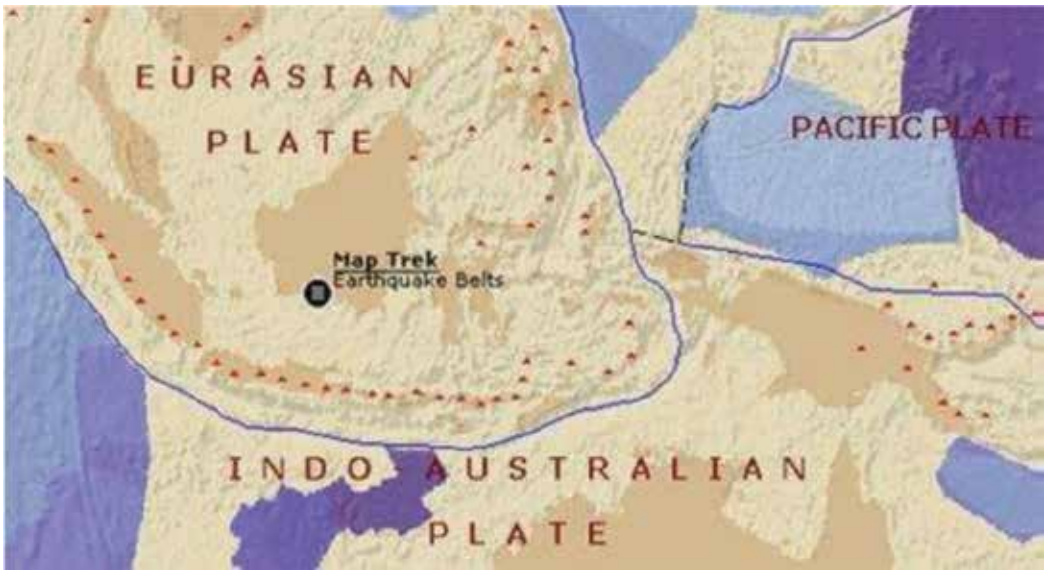

Figure 12. Indonesia is located between three wide plates, such as the Eurasian plate, the Pacific plate, and the Indo-Australian plate (Indonesia geology map library, 2017).

as experienced by Kelud in the eruption of 2014. Volcanic material and gas of the mount can directly reach the height of the stratosphere [30], where aerosols stay for a long time, affecting the weather and climate [31–33].

Aerosol stratosphere plays an important role in climate regulation and atmospheric chemistry [34]. The gas emissions significantly affect the environment at different scales, depending on the extent of the gas emissions removed from the source prior to the deposition [35]. The explosive eruption injects sulfur into the stratosphere in the form of SO_2 and H_2S that bind to form aerosol (H_2SO_4) [36].

In small eruptions, sulfate aerosols formed after SO_2 oxidizes to form H_2SO_4 and can increase Earth's albedo by scattering short-wave radiation [37]. This greatly helps the global temperature drop.

Some volcanoes to watch out for in the last decade are Sinabung. Based on PVMBG data on the evaluation report of volcanic activity level recorded in June 2017, there was one volcano at level IV, 5 volcanoes at level III, 17 volcanoes at level II, and 49 volcanoes at normal (level I). The eruption type of Mount Sinabung is a vulcanian that is characterized by a smoke cloud as high as 5–6 km and effusive lava and causes the evacuation of 12,000 inhabitants [38]. Based on data of BNPB, temporary losses due to eruption of Mount Sinabung since 2013 until 2014 reached 1.49 trillion [15]. A large number as a result of sustained eruption and due to a continuous and unpredictable eruption have a negative impact on the community psychology around Sinabung. Significantly reducing hazards is necessary in order to minimize the damage [39].

In general, the number of people affected because of an eruption is relatively larger compared to other natural disasters in Indonesia. Based on **Figure 13**, the biggest eruption-affected population is on the island of Java. Once of the dangers of the volcanic eruption in Indonesia with all its characteristics and changes, there needs to be an improvement of the pattern of improving public preparedness in facing it. One way of doing that is by developing a pattern

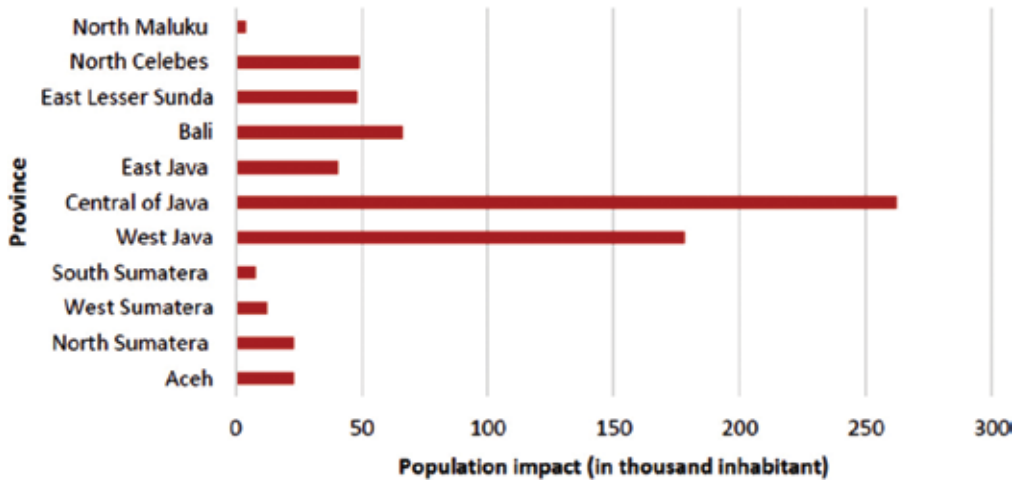

Figure 13. Matrix of population affected by the eruption of a volcano [26].

of mitigation into adaptation. Adaptation to the environment is indispensable when danger is inevitable [40]. The people must be aware that besides the blessings given by the volcano, there are hidden disasters that will come any time. If the people are more aware of the environment around the volcano, they more certainly will be safer in the face of danger.

5. Mitigation experience and public preparedness

Almost all the countries that have volcanoes will face the problems of eruption disaster and Indonesia is currently experiencing it. The problem of dealing with eruption disaster in Indonesia lies in the high number of people living around the volcanoes [41]. Due to the increase of population around the volcano, the impact of eruptions on communities increased. This condition is getting worse due to lack of public awareness of the eruption disaster.

Merapi eruption experience in 2010 left a bitter memory for the history of volcano eruption in Indonesia. As a result of eruptions and hot clouds, up to 277 people were killed [42]. But this number is relatively smaller than the previous eruption victims. It all depends on the level of eruption that occurred. The higher level of volcanic eruption have an impact on the more damage. However, the number of victims will be minimized if disaster mitigation is well implemented.

The characteristics of eruptive disasters differ from one disaster to the other natural disasters. They may occur at any time and they are difficult to predict [43]. The lack of historical data of Indonesia volcano eruption causes the preparation in the face of eruption disaster must be improved. This should be done to anticipate volcanic behavior changes that occur often lately.

The difficult case is predicting volcanic activity of the Sinabung eruption. The Sinabung activity is difficult to predict. After it entered a 400-year rest period, Sinabung has erupted continuously until now. The government continues maximizing the techniques and monitoring equipment of the volcano by providing more accurate information in accordance with the latest volcanic activity in Indonesia. This is closely related to mitigation efforts of the community.

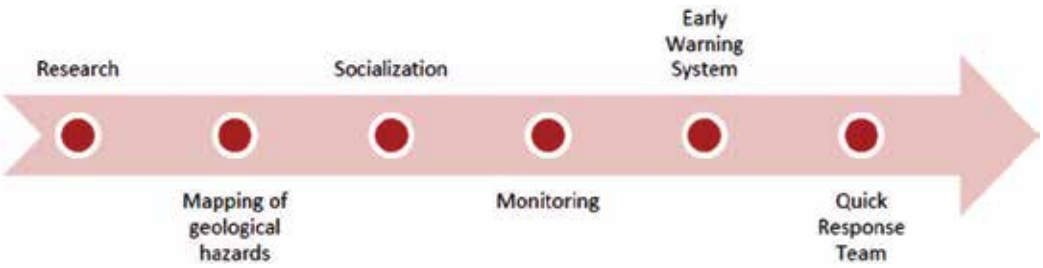

Figure 14. Step of geological hazard mitigation effort in Indonesia.

The Indonesia government has implemented six stages in efforts to minimize the victims of eruption disasters (**Figure 14**). This was done to support the accuracy and speed in providing services to the society in the face of eruption disaster. Research is conducted to analyze eruption model to support early warning system. Mapping of geophysical hazards to produce disaster maps that are indispensable for identifying disaster areas. Socialization to build public awareness and knowledge in eruption disaster areas. Monitoring has been done to observe, record, and analyze volcanic activity. Early warning system (EWS) to describe the status of volcanic activity and quick response team (QRT) to evaluate the condition of volcano during the crisis and the results were presented to the government and the community.

The concept of eruptive disaster mitigation in Indonesia is well developed. One of the handlings that was considered successfully by the international community is the evacuation of the population due to eruption of Merapi that occurred in 2010, the eruption of Kelud in 2014 without a victim, and the Sinabung eruption in 2017. There is a significant decrease of loss of lives from the successful mitigation of the government.

The success of mitigation in Indonesia can be seen in **Table 1**. Based on the table, there is a significant relationship between the number of casualties and the evacuated people. If the number of people evacuated is larger, then the victims of eruption become smaller.

The greatest challenge in implementing the disaster mitigation program in Indonesia is the awareness of the local government and the community. The problems of eruption are not

Countermeasures	Time period	Number of refugees	Fatalities
No mitigation action yet	1700–1920	0	More than 150,000
There has been a countermeasure system but not yet perfect	1950–1979	More than 5000	1613
The countermeasure system is good, using modern equipment to monitor volcano, communication network is good, public understanding about the danger of eruption has increased	1980–2004	232,197	105

Source: PVMBG 2014 Presentation.

Table 1. Mitigation effects to eruption fatalities in Indonesia.

only the responsibility of community or government separately, but it also becomes part of all components of the nation together. All of them must be involved in finding solutions. If all the components of the nation act in accordance with their role, Indonesia will be better prepared to face the challenges of eruption in the future.

6. Disaster risk reduction based on ethno mitigation

Indonesian society has a different perspective on volcano. Volcano is considered as a representation of greatness and beauty. Its existence is very important for the life of the people who live around. The communities on the slopes of the mountains have the belief that the eruptions cannot be separated from the contribution of supernatural forces. This can be seen from the belief of the people on the slopes of Merapi. They thought that Mount Merapi is not just a mountain, but a settlement of spiritual beings or invisible spirits [44].

Volcano disaster provides a meaningful example of how communities apply cultures, religions, and ceremonies to communicate and remember disaster risks and mitigation strategies [45]. But the understanding of the society is based on myth only and it is not based on scientific knowledge and the existence of the culture is not widely understood by the community. The culture role is very important to reduce disaster risk and people's vulnerability [46].

The ritual offerings tradition was packaged in local culture by involving almost all elements of society that are able to build strong emotional bonds between communities around the mountain. The attitude of togetherness and mutual cooperation are very important in building community resilience in the face of eruption. The culture of mutual cooperation promotes positive values such as social harmony and mutually beneficial relationships within disaster-affected areas.

Local people's knowledge of the volcano environment around also greatly contributes to the success of the eruption disaster. Based on information from the people who live on the slopes of Kelud, it is known that the animals that descended the slope because of the eruption of Kelud include wasps, birds, monkeys, deer, and pythons. The changes in animal behavior were caused by the changes of environmental conditions, including higher local temperatures, increased gases concentrations (it can cause disruption of animal respiratory systems), and increasingly polluted environment due to the aerosols released. These signs are very important for local people in predicting eruptions.

Each or group of animals has a specific frequency range [47]. Birds are unable to hear the ultrasonic sound (>20,000 Hz) but they are capable of hearing an infrasonic sound (<20 Hz) [48]. These specific frequencies are used by animals to identify unknown threats from nearby environments. Based on the review of some literatures, the threshold frequencies of various animals are presented in **Table 2**.

Bangbara has the ability to hear high-frequency (ultrasonic) sounds, deer and mountain monkeys are able to respond to sounds at a medium level or equal to the hearing (audiosonic), and birds and pythons are able to hear infrasound frequencies. When volcanoes started to activate by emitting gas with high-frequency sound waves, only Bangbara wasps responded to these and this frequency level cannot be heard by others.

No.	Animal name	Family	Threshold frequency (Hz)
1.	Bangbara	Insect	25,000–50,000
2.	Deer	Mammals	500–32,000
3.	Monkey	Mammals	63–16,000
4.	Birds of Knee	Aves	200–4000
5.	Python	Reptile	80–160

Table 2. Threshold frequency of some animals on the slopes of Kelud.

The python has the lowest threshold frequency compared to other animals. This causes the snake to be able to respond to low-frequency vibrations. In addition, python snakes crawl on the ground and are less sensitive to changes in temperature and air conditions. The python is more sensitive to the vibrations it senses through its body than the smell through the nose [49]. At the time of vibration caused by the volcanic activity with increasing amplitude, the snake will soon evade. This condition can be a final marker when the Kelud will erupt.

The ability of animals around the slopes of Kelud in response to environmental changes can be arranged in sequence based on the level and speed of response. Changes in animal behavior are very interesting to be studied more deeply. It is very likely to be a traditional volcanic eruption warning system or traditional volcanic alert level (TVAL). This system will be more easily communicated to the people on the slope of Kelud as it is in accordance with the local knowledge and indispensable as a consideration in making decisions [50].

Local wisdom of mountain community is very potential as a basic in developing disaster risk reduction model that suits with the characteristics of the local community. In addition to preserving local wisdom as a local culture, it can help communities to face the eruption disaster.

Author details

Eko Hariyono and Liliasari S*

*Address all correspondence to: liliasari@upi.edu

School of Postgraduate Studies, Universitas Pendidikan Indonesia, Bandung, Indonesia

References

[1] Djalante R. Research trends on natural hazards, disasters, risk reduction and climate change in Indonesia: A systematic literature review. Natural Hazards Earth System Sciences Discussion. 2016;**342**. DOI: 10.5194/nhess-2016-342

[2] Chadwick JP, Troll VR, Ginibre C, Morgan D, Gertisser R, Waight TD, Davidson JP. Carbonate assimilation at Merapi Volcano, Java, Indonesia: Insights from crystal isotope stratigraphy. Journal of Petrology. 2007;**48**:1793-1812

[3] Iguchi M, Ishihara K, Surono, Hendrasto M. Learn from 2010 Eruption at Merapi and Sinabung Voelcanoes in Indonesia. Annuals of Disaster Prevention Research Institute, Kyoto University No. 54 B; 2011

[4] Thouret JC, Lavigne F, Kelfoun K, Bronto S. Toward a revised hazard assessment at Merapi volcano, Central Java. Journal of Volcanology and Geothermal Research. 2000;**100**:479-502

[5] PVMBG. Data Dasar Gunungapi Indonesia [Basic Data of Indonesia Volcanoes]. Ministry of Energy and Mineral Resource, Geology Department; 2010

[6] Gertisser R, Charbonnier SJ, Keller J, Quidelluer X. The geological evolution of Merapi volcano, central Java, Indonesia. Bulletin of Volcanology. 2012;**74**:1213-1233

[7] Preece K, Gertisser R, Barclay J, Charbonnier SJ. Transitions between explosive and effusive phasesduring the cataclysmic 2010 eruption of Merapi volcano, Java, Indonesia. Bulletin of Volcanology. 2016;**78**:54. DOI: 10.1007/s00445-016-1046-z

[8] Subandriyo. Sejarah Erupsi Gunung Merapidan Dampaknya Terhadap Kawasan Borobudur [the history of the Merapi eruption and its impact on the Borobudur area]. In: Sutopo M, editor. Menyelamatkan Candi Borobudur dari Erupsi Merapi [Save Borobudur Temple from Merapi Eruption]. Magelang: BalaiKonservasi Peninggalan Borobudur; 2011. p. 86-96

[9] Carey SN. Understanding the physical behavior of volcano. In: Marti J, Ernst GGJ, editors. Volcanoes and the Environment. New York: Cambridge University Press; 2005. p. 1-54

[10] Favalli M, Karatson D, Yepes J, Nannipieri L. Surface fitting in geomorphology—Examples for regular-shaped volcanic landforms. Geomorphology. 2014;**221**:139-149

[11] Konstantinou KI, Perwita CA, Maryanto S, Surono, Budianto A, Hendrasto M. Maximal Lyapunov exponent variations of volcanic tremor recorded during explosive and effusive activity at Mt Semeru volcano, Indonesia. Nonlinear Processes Geophysics. 2013;**20**:1137-1145

[12] Gomez C, Lavigne F. Transverse architecture of lahar terraces, inferred from radar grams: Preliminary results from Semeru Volcano, Indonesia. C. Version of Record Online. 2010. pp. 1116-1121. DOI: 10.1002/esp.2016

[13] Sutawidjaja IS, Prambada O, Siregar DA. The August 2010 phreatic eruption of Mount Sinabung, North Sumatra. Indonesian Journal of Geology. 2013;**8**:55-61

[14] Julian R, Suharno. Studigelombangseismikgempavulkanikgunungsinabunguntukmenentukankarakteristikmekanismevulkanik (Study of Seismic Wave of Volcanic Earthquake of Mount Sinabung to Determine the Characteristics of Volcanic Mechanism) [Internet]. 2013. Available from: http://download.portalgaruda.org/article.php?article=329842&val=7701 [Accessed: August 08 2017]

[15] BNPB. 2015. Info Bencana (Disaster Information). June Edition 2015

[16] Zobin VM. Introduction to Volcanic Seismology. Amsterdam: Elsevier Science B.V; 2003. 5 p

[17] Nakashima Y, Heki K, Takeo A, Cahyadi MN, Aditya A, Yoshizawa K. Atmospheric resonant oscillations by the 2014 eruption of the Kelud volcano, Indonesia, observed with the ionospheric total electron contents and seismic signals. Earth and Planetary Science Letters. 2016;**434**:112-116

[18] Thouret JC. Volcanic geomorphology—An overview. Earth-Science Reviews. 1999;**47**: 95-131

[19] Luppi M, Miller SA. Short-lived tectonic switch mechanism for long-term pulses of volcanic activity after mega-thrust earthquakes. Solid Earth. 2014;**5**:13-24

[20] Eggert S, Walter TR. Volcanic activity before and after large tectonic earthquakes: Observations and statistical significance. Tectonophysics. 2009. DOI: 10.1016/j.tecto.2008.10.003

[21] Walter TR, Wang R, Zimmer M, Grosser H, Lühr B, Ratdomopurbo A. Volcanic activity influenced by tectonic earthquakes: Static and dynamic stress triggering at Mt. Merapi. Geophysical Research Letters. 2007;**34**:L05304, 10.1029/2006GL028710

[22] Wegler U, Lühr BG, Snieder R, Ratdomopurbo A. Increase of shear wave velocity before the 1998 eruption of Merapi volcano (Indonesia). Geophysical Research Letters. 2006;**33**:L09303. DOI: 10.1029/2006GL025928

[23] Bignami C, Ruch J, Chini M, Neri M, Buongiorno MF, Hidayati S, Sayudi DS, Surono. Pyroclastic density current volume estimation after the 2010 Merapi volcano eruption using X-band SAR. Journal of Volcanology and Geothermal Research. 2013;**26**:236-243

[24] Kiswiranti D. Temporal statistical analysis of the volcanic eruptions in Indonesia. Berkala MIPA. 2013;**23**(**3**):211-217

[25] Hariyono E, Liliasari, Tjasyono B, Madlazim. Volcanic eruption crisis and the challenges of geoscience education in Indonesia. AIP Conference Proceedings. 2016;**1708**:080004. DOI: 10.1063//1.4941190

[26] BNPB. Indeks Rawan Bencana Indonesia (Indonesian Disaster Prone Index). 2011. Direktorat Pengurangan Resiko Bencana. Deputi Bidang Pencegahandan Kesiapsiagaan

[27] Wirakusumah AD, Bacharudin R. Volcanic hazard mapping in Indonesia. CEOSEA '98 Proceedings. qJ, CeoL. Soc. IIla La Yia BuLL. 1999; **205**; 21

[28] Daniell JE. The CATDAT Damaging Earthquakes Database—2010—The Year in Review. Published in various locations. 2011. 41pp

[29] Tilling RI. Volcanism and associated hazards: The Andean perspective. Advances in Geosciences. 2009;**22**:125-137

[30] Kylling A. Ash and ice clouds during the Mt Kelud February 2014 eruption asinterpreted from IASI and AVHRR/3 observations. Atmospheric Measurement Techniques. 2016;**9**:2103-2117

[31] Bala G. Are volcanic eruptions causing the current global warming? Current Science. 2016;**110**:283-284

[32] Sigl M, Winstrup M, McConnell JR, Welten KC, Plunkett G, Ludlow F, et al. Timing and climate forcing of volcanic eruptions for the past 2,500 years. Nature. 2015;**523**:543-549. DOI: 10.1038/nature14565

[33] Guevara-Murua A, Hendy EJ, Rust AC, Cashman KV. Consistent decrease in North Atlantic tropical cyclone frequency following major volcanic eruptions in the last three centuries. Geophysical Research Letters. 2015;**42**:9425-9432. DOI: 10.1002/2015GL066154

[34] Abo M, Shibata Y, Nagasawa C. Lidar observation of the Kelut volcanic stratosphere aerosols at Kototabang, Indonesia. EPJ Web of Conferences. 2016;**119**:07005. DOI: 10.1051/epjconf/201611907005

[35] Pfeffer MA, Langmann B, Graf HF. Atmospheric transport and deposition of Indonesian volcanic emissions. Atmospheric Chemistry and Physics. 2006;**6**:2525-2537

[36] Maher N, McGregor S, England MH, Sen Gupta A. Effects of volcanism on tropical variability. Geophysical Research Letters. 2015;**42**:6024-6033. DOI: 10.1002/2015GL064751

[37] Gray TM, Bennartz R. Automatic volcanic ash detection from MODIS observations using a back-propagation neural network. Atmospheric Measurement Techniques. 2015;**8**: 5089-5097

[38] Chaussard E, Amelung F, Aoki Y. Characterization of open and closed volcanic systems in Indonesia and Mexico using InSAR time series. Journal of Geophysical Research: Solid Earth. 2013;**118**:3957-3969. DOI: 10.1002/jgrb.50288

[39] Bakkour D, Enjolras G, Kast R, Thouret JC. The Adaptive Governance of Natural Disasters: Insights from the 2010 Mount Merapi Eruption in Indonesia. Avenue Raymond Dugrand C.S. 79606. Montpellier Cedex 2: Document de Recherce. Unite de Formation et de Recherched'Economie; 2013

[40] Cho SE, Won S, Kim S. Living in harmony with disaster: Exploring volcanic hazard vulnerability in Indonesia. Sustainability. 2016;**8**:848. DOI: 10.3390/su8090848

[41] Surono M, Jousset P, Pallister J, Boichu M, Buongiorno MF, et al. The 2010 explosive eruption of Java's Merapi volcano—A '100-year' event. Journal of Volcanology and Geothermal Research, Elsevier. 2012;**241-242**:121-135

[42] Subandi MA, Achmad T, Kurniati H, Febri R. Spiritualy, gratitude, hope and post-traumatic growth among the survivors of the 2010 eruption of Mount Merapi in Java, Indonesia. Australasian Journal of Disaster and Trauma Studies. 2014;**18**:1

[43] Donovan A, Eiser JR, Sparks RSJ. Scientists' views about lay perception of volcanic hazard and risk. Journal of Applied Volcanology. 2014;**3**:15

[44] Donovan. Doing social volcanology: Exploring volcanic culture in Indonesia. Area. 2010;**42**(1):117-126. DOI: 10.1111/j.1475-4762.2009.00899.x

[45] Troll VR, Deegan FM, Jolis EM, Budd DA, Dahren B, Schwarzkoff LM. Ancient oral tradition describes volcano earthquake interaction at Merapi volcano Indonesia. Swedish Society for Antropology and Geography. 2015;**97**:137-166

[46] Thompson PDP. Leveraging learning to improve disaster management outcomes. International Journal of Disaster Risk Science. 2012;**3**:195-206

[47] Sonone JD, Patil DA, Rane KP. Irritating and hearing frequency identification and generation to avoid animal accident. International Journal of Innovative Research in Science, Engineering, and Technology. 2014;**3**:14454-14464

[48] Beason RC. What can birds hear? In: Timm RM, Gorenzel WP, editors. Proc. 21st. Vertebr. Pest Conf. Davis: Published at University of California; 2004. p. 92-96

[49] Parkhurst J. Managing Wildlife Damage: Snakes. Virginia Cooperative Extentions Pubication 420-021 [Internet]. 2010. Available from: www.ext.vt.edu

[50] Potter SH, Jolly GE, Neal VE, Johnston DM, Scott BJ. Communicating the status of volcanic activity: Revising New Zealand's volcanic alert level system. Journal of Applied Volcanology. 2014;**3**:13

Chapter 6

Layered Gabbroids of the Pekulney Ridge, Chukotka, Northeastern Russia: Geology, Petrography, Age, and Geodynamics

Irina L'vovna Zhulanova

Additional information is available at the end of the chapter

http://dx.doi.org/10.5772/intechopen.74994

Abstract

The author has actualized the data obtained by her own research and from publications to conclude that gabbroids in the northern part of the Pekulney Ridge build a large intrusion, named Svetlorechensky. It belongs to the type special for the region: it possesses features of layered plutons and multiphase intrusions. It is classified as a petrotype of a gabbro complex of the same name, whose bodies are present in the southern part of the ridge, as well. The establishing of the Svetlorechensky complex took place in the Early Cretaceous (most probably in the Hauterivian). The original composition of the parent magma was characterized as typical island arc tholeitic basalt. Amphibole-two-pyroxene rocks of the Pekulneyveem River basin, supposedly dated back to the Archean by previous researchers, build the marginal series in the first intrusive phase of the Svetlorechensky pluton. Among the host complexes, the author has established stratified high-temperature metamorphic formations, supposedly Paleozoic, and "pre-Svetlorechensky" gabbroids. The deep structure reconstruction for the pluton permitted to interpret it as a heavily asymmetric harpolith, localized in the hanging side of a long-developed ancient island arc uplift.

Keywords: petrographic convergence, Cretaceous magmatism, layered gabbroids, high-alumina basalt, island arc, Chukotka region

1. Introduction

Large linear structures, housing great volume of basites and ultrabasites, in its current understanding, are interpreted as fossil boundaries of lithospheric plates, where geodynamically heterogeneous complexes are mechanically joined. Simultaneously, they have

to be autonomous structures of sufficiently long development, as, parallel to collision and (or) accretion deep processes of the earth crust neoformation occur. Distinguishing the in situ-formed complexes remains one of the least developed aspects of the geodynamics. The Pekulney Ridge is extremely favorable for this purpose.

The Pekulney Ridge is located in the farthest part of northeastern Asia, in the Chukotka Autonomous District of the Russian Federation. As a weakly bent arc, it stretches for 250 km from the Anadyr River Valley north northeastward, between its largest left tributaries, the Tanyurer and Belaya rivers (**Figure 1**, Inset map). It is a young, highly dissected mountain system, which joins Cenozoic depressions and the Chukotka Upland. The clearly expressed axis of the system (the ridge s. stricto) is 15–25 km wide. Its section, comprehensively characterized below, is about 50 km long (**Figure 1**) and located in the highest elevated part of the ridge. The relief here is of an alpine-type. Relative height differences between watersheds and valleys reach 1000 m, absolute elevations of the highest peaks approach 1400 m. Exposure is good everywhere with numerous bedrock yields. At the trough valley bottoms, abundant are enormous glacier blocks composed of the strongest types of gabbroids. On their ideally prepared surfaces, one can observe fine peculiarities of intrusive body structures. In particular, in this way, rare spheroidal gabbros, or orbicular allivalites, were found and comprehensively studied [1].

In the course of time, the number of disputable issues increases and the debate sharpens. It is determined, firstly, by the ridge location at the joint of two largest tectonic units, traditionally distinguished in the Far North-East of Asia: the Chukotka Folding System, a part of the single Verkhoyansk-Chukotka Mesozoic Area and the Anadyr-Koryak Folding System, which refers to the Cenozoic Koryak-Kamchatka Area; and, second (and important), by the fact that the boundary between Mesozoides and Cenozoides is concealed under Cretaceous accumulations of the Okhotsk-Chukotka Volcanogenic Belt (**Figure 1**, Inset map). Scholars, based on the plate tectonics, also suggest contradictory models of relations between Mesozoides and Cenozoides. Recently, the Chukotka Mesozoides began to be regarded as a part of the Arctic Craton. In this situation, the Pekulney Ridge structures attract more and more attention, especially since they are exposed far better than the two other pre-Cenozoic elevations of the Anadyr-Koryak System, located on the left bank of the Anadyr River (from the west to the east): Kanchalan and Zolotogorsky (the entry part of the Anadyr River).

The present work introduces the results of studying the Pekulney Ridge holocrystalline basites, exposed on the area about 200 km^2 north from the latitude 66°00′ N (it serves as a conventional border between the northern and the southern parts of the ridge, differing in their geological structures). On top of everything, these rocks are interesting because in the late 1970s, when the USSR activated the research of the transitional zone from the Asian continent to the Pacific Ocean, a new interpretation of their origin was offered. If the first geologists had considered them intrusive gabbroids of the Early Cretaceous [2–4], later these rocks were interpreted as an uplift of the Archaean continental crust, which radically changed the view of the area tectonics [5, 6].

In order to possibly solve disputable issues, in 1981–1984, the author performed specialized geologic and petrologic research of basites in the northern part of the Pekulney Ridge. They included the geological mapping of the area of presumably Precambrian complexes on the topographic base, the comprehensive study of their petrographic and geochemical peculiarities

http://dx.doi.org/10.5772/intechopen.74994

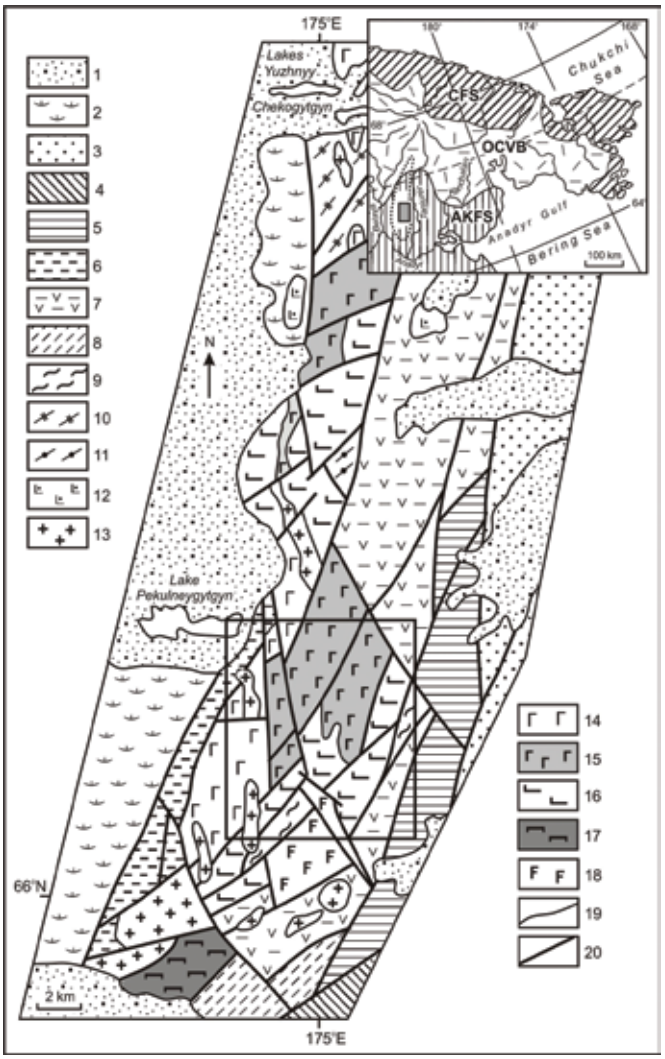

Figure 1. Schematic geological map of the northern part of the Pekulney Ridge (compiled by Zhulanova using [4, 14]): 1—quaternary sediments; 2—Upper Cretaceous and Paleogene terrigenous and volcanic deposits; 3—Upper Cretaceous terrigenous and volcanic deposits; 4—Aptian-Albian terrigenous and volcanic deposits; 5—Hauterivian-Barremian terrigenous deposits (sandstones, aleurolites, gravelites, conglomerates); 6—Tythonian-Valanginian volcanogenic and terrigenous deposits (Gruntovskaya Strata); 7—Middle Jurassic-Lower Cretaceous siliceous-volcanogenic deposits (Pekulneyveemskaya Suit); 8—Greenschists (Pekulneyveemskaya Suite dynamometamorphism products); 9—presumably Middle-Upper Paleozoic metasandstones, metalelevolites, graphite-biotite, sericite-siliceous schists, metariolites, metabasalts (Pekulneigytgynskaya Strata); 10–11—presumably Paleozoic metamorphic formations (Sbornenskaya Strata): 10—amphibolites, biotite-amphibole schists granitized, 11—garnet-biotite-hypersthene paragneisses, garnet-sericite-graphite microschists; 12–17—intrusive complexes: 12—Paleocene-Eocene Televeemsky (gabbronorites), 13–17—Early Cretaceous: 13—Yanranaysky (granodiorites, granites), 14–16—Svetlorechensky two-phase: 14—additional phase (amphibole, biotite-amphibole gabbro), 15–16—main phase: 15—edge series (amphibole microgabbronorites, pyroxene-amphibole gabbro), 16—layered series (plagioclase peridotites, troctolites, olivine gabbro, gabbroanorthosites, anorthosites); 17—Ostantsovogorsky (picrites, metadolerites, peridotites); 18—pre-Cretaceous uralitized gabbro; 19—geological boundaries; 20—tectonic disturbances. Black frame indicates area of **Figure 2**. *Inset map*: Tectonic Scheme of the Chukotka Peninsula: AKFA—Anadyr-Koryak Fold Area, CFS—Chukotka Fold System, OCVB—Okhotsk-Chukotka volcanogenic belt. The points outline shows the Pekulney Ridge. A gray rectangle indicates area of **Figure 1**.

and the chemical composition of minerals. Pertsev, the then alumnus of the Lomonosov State University in Moscow, participated in field works and material processing. Analytical research was performed at NEISRI and VSEGEI (St. Petersburg, Russia).

Our general task within the framework of the research program was the problem of the basement of the Anadyr-Koryak System with its numerous ophiolite complexes [7, 8]. Respectively, beside basites of the northern part of the Pekulney Ridge, we studied metamorphic formations, basites, and ultrabasites, spread in the south, in the upper flows of the Levaya Bychya and Severny Pekulneyveem rivers. According to the common viewpoint, they belong to the ophiolite association forming a sovereign tectonic structure. Our observations yielded some principally new data that permit to interpret the history of its geological development within a holistic geodynamic model [9, 10]. Later on, Pertsev paid most attention to petrologic peculiarities of depth ultramafites [11].

Field works were conducted in a close contact with geologists from the Anadyr Expedition of the North-East Geological Association of the USSR Ministry of Geology, who performed geological 1:50,000 mapping and prospecting (the party manager Semyonov). In the summer of 1981, there worked a field party from the Far East Geological Institute (Vladivostok, Russia), headed by Shul'diner [12], a prominent expert in the Siberian and Far Eastern Archaean. Thus, during the field season of 1981, we had an opportunity to perform a series of fundamental observation together with experienced practitioners and scholars. Finally, our research permitted to conclude that the pioneers were right about the intrusive nature and the Early Cretaceous age of basites of the northern part of the Pekulney Ridge. According to our data, these rocks make a large layered pluton with an additional phase of amphibolic gabbro, followed by veins of amphibolic plagiogranites. We named the massif Svetlorechensky (after the Svetlaya River), and consider it a petrotype of the cognominal two-phase intrusive complex of Early Cretaceous gabbro [13]. Among complexes housing the Svetlorechensky layered pluton, stratified metamorphic formation of the supposedly Paleozoic age and "pre-Svetlorechensky" gabbroids were established for the first time.

The acute discussion of the 1980s interested a wide range of experts in the Pekulney Ridge, which resulted in additional data on geochemistry and isotopic age of the basites. They are discussed further within the context of our main task. In 2009, the Federal Unitary Enterprise "Georegion" (City of Anadyr) had completed the second-generation sheets of the Federal Geological Map with the scale 1:200,000 for the Pekulney Ridge to the south of the latitude 66°40′ N (map author Gul'pa), which have adequately reflected most of our data [14].

2. Area geology and tectonics: factual data and theoretical discussions in brief retrospective

2.1. Historical background

The geological study of the Anadyr area was pioneered by a prominent Russian geologist of a tragic fate, Polevoy (1873–1938). Today, however, various activities of his expedition, which

http://dx.doi.org/10.5772/intechopen.74994

worked in 1911–1913, are rather of historic than of geological interest [15–17]. The systematic study of the Belaya and Tanyurer interfluve has lasted a little longer than 50 years. Since the mid-1950s, organizations responsible to the USSR Ministry of Geology conducted geological survey and prospecting of various scales and directions here; the data obtained were generalized on sheets of Federal Geological Maps of 1:1,000,000 and 1:200,000 scale (further referred, respectively, as FGM-1000/1 and FGM-200/1). The first important advance was the production of a small-scale map including the whole Pekulney Ridge (FGM-1000/1 Q-60 Sheet) [2]. The map author Kaygorodtcev diagnosed an Early Cretaceous ophiolite association in the Pekulney Ridge. As ophiolites, he classified (1) siliceous-volcanogenic deposits with dominant basaltoids (mostly spilites), (2) ultramafites, (3) gabbroids, (4) products of metamorphism and metasomatism of formations, including eclogite-like rocks, which he had originally established [18, 19]. Siliceous-volcanogenic deposits were described under the name of the Pekulneyveemskaya Suite of the supposedly Late Jurassic-Valanginian age, the oldest in the stratigraphic section of the area. The opinion of eclogite-like rocks as products of selective alteration of magmatic rocks was supported by the researchers who later studied the ultramafite-mafite magmatism of the Anadyr-Koryak System as a whole; they also reported the first epidote blueschists found in the Pekulney Ridge [20]. It was found that the ophiolite association in its complete manifestation is spread only in the axis part of the southern half of the ridge, and essential differences in the structures of its eastern and western slopes were exposed. On the western slope, Lower Cretaceous terrigenous-volcanogenic masses were mapped, in which andesite and dacite tuffs and lavas predominate, while basic volcanites are rare. On the eastern slope, stratigraphically above the Pekulneyveemskaya Suite, the Valanginian mass (conglomerates, sandstones, aleurolites, basalts, andesites, rhyolites, their tuffs) was distinguished, which is covered by Aptian-Albian terrigenous rocks laid with angular displacement and basal conglomerates. Late Cretaceous deposits spread in the eastern and western slope foothills visibly differ from each other. Besides, developed only on the western slope are intrusive granitoid massifs; the pebbles of those were found in the Aptian-Albian conglomerates. Summarizing the exposed peculiarities, Kaygorodtcev interpreted the Pekulney Ridge as an inherited anticline elevation, whose history, starting at least from the Valanginian, had been controlled by an axis deep fault, which he named Pekulney [18, 19].

In the northern part of the ridge, among intrusive formations, gabbroids play the main part; the western slope of the ridge is almost completely composed from them (**Figure 1**). Valanginian deposits, shown as the Pekulneyveem Suite, are exposed mostly on the eastern slope here; however, their composition (terrigenous variations of sedimentary rocks, andesites, dacites) is similar to that of the pre-Upper Cretaceous section of the western slope. In the sand-gravelite-conglomerate mass with intermittent components, presumably referred to the Hauterivian, pebbles of greenschists, spilites, jaspers, gabbro, and granitoids were found. The issue of tectonics in this part of the ridge attracted no special attention at that time.

The data on Early Cretaceous ophiolites present in the southern part of the Pekulney Ridge were sufficient for making a conclusion on the tectonic kinship of the left bank of the Anadyr River with the Koryak Upland and considering both area elements of the Anadyr-Koryak Cenozoic Folding System. Within the system, the Pekulney Ridge structures are most often

included in the Talovsk-Pekulney ophiolite zone as its northeasternmost section. As a whole, the zone is a narrow arc, weakly bent southeastward, over 750 km long. Its southern flank reaches the eastern coast of the Penzhinskaya Bay, Sea of Okhotsk; some of it is traced on its western coast (Taygonos Peninsula) and farther goes into the sea [21].

The situation dramatically changed in the mid-1970s. Ideologically, the research was based on the concept formulated by the Director of GIN, Member of RAS Peive in the late 1960s; in the USSR, it was coined as the new geosyncline theory, or the concept of constructive tectogenesis. According to the concept, ophiolites were interpreted as products of the early (oceanic) stage of geosyncline development, regularly followed by the middle (island arc) and the final (orogenic) stages, which determines the formation of the continental-type earth crust. The originality, therefore, was in matching primary geosynclines with oceans and interpreting their evolution as the process of turning the oceanic crust into the continental one [22, 23].

Nekrasov was the first to analyze the structure of the Pekulney Ridge from this viewpoint [5]. He defined geological complexes of the southwestern and northern parts of the ridge as autochthon, on which ophiolites are thrusted from the southeast. In the contact zone between the autochthon and allochthon, serpentinite mélange was distinguished. In Nekrasov's scheme, basites of the northern part of the ridge, revealed on the right bank of the Pekulneyveem River between Lake Pekulneygytgyn and Lake Romb (**Figure 2**), played the main part. Their amphibole-two-pyroxene composition, fine-grain structures with orientation elements, and the presence of the clearly separate leucocratic ("enderbitic", according to Nekrasov) phase, sometimes likening the rocks to migmatites, made the set of attributes that permitted to define those formations as crystalline schists of the granulite facies of metamorphism. According to the original interpretation by Nekrasov, they compose the core of the dome-like swell of the autochthon basement and are sequentially followed, at its eastern wing (upward), by gabbronorites, gabbroic anorthosites, olivine-pyroxene gabbro, gabbro-pegmatites, amphibolic gabbro, diorites, and plagiogranites. He compared the whole rock association with the Archaean granulite complex of the Anabar Shield of the Siberian Platform, and interpreted it as a swell of the granulite-basite ("basalt") layer of the continental-type earth crust. Ultramafic rocks of the Pekulney Ridge southern part, shown on FGM-1000/1 and FGM-200/1 as Earle Cretaceous intrusions (lherzolites, wehrlites, dunites, etc.), as well as eclogite-like rocks, were interpreted as tectonic fragments (rafts) from the mantle basement, underlaying the Archaean continental crust revealed in the north of the ridge [5]. Those data, together with their tectonic interpretation, made a veritable sensation for geologists studying the North-East of Asia, because by the mid-1970s, the view of the epioceanic nature of the Koryak-Kamchatka Folding Region, including its western half, the Anadyr-Koryak System, was widely acknowledged.

By the time we started our research (1981), some new data on the ridge geology had appeared. Thus, in the upstream of the Pekulneyveem River, the carbonate-terrigenous-coaly mass (supposedly Late Paleozoic-Early Mesozoic and believed to be laid above granulite-basites) was distinguished. The idea of Late Jurassic-Early Cretaceous ophiolites in the southern part of the Pekulney Ridge having been formed in the zone of stretching of the old continental crust, analogous to the Chukotka Mesozoic basement, was formulated. It was suggested that two petrographically close gabbroid complexes presented in the northern part of the Pekulney Ridge: (1) Early Precambrian; (2) Mesozoic, simultaneous to the process of the earth crust

http://dx.doi.org/10.5772/intechopen.74994

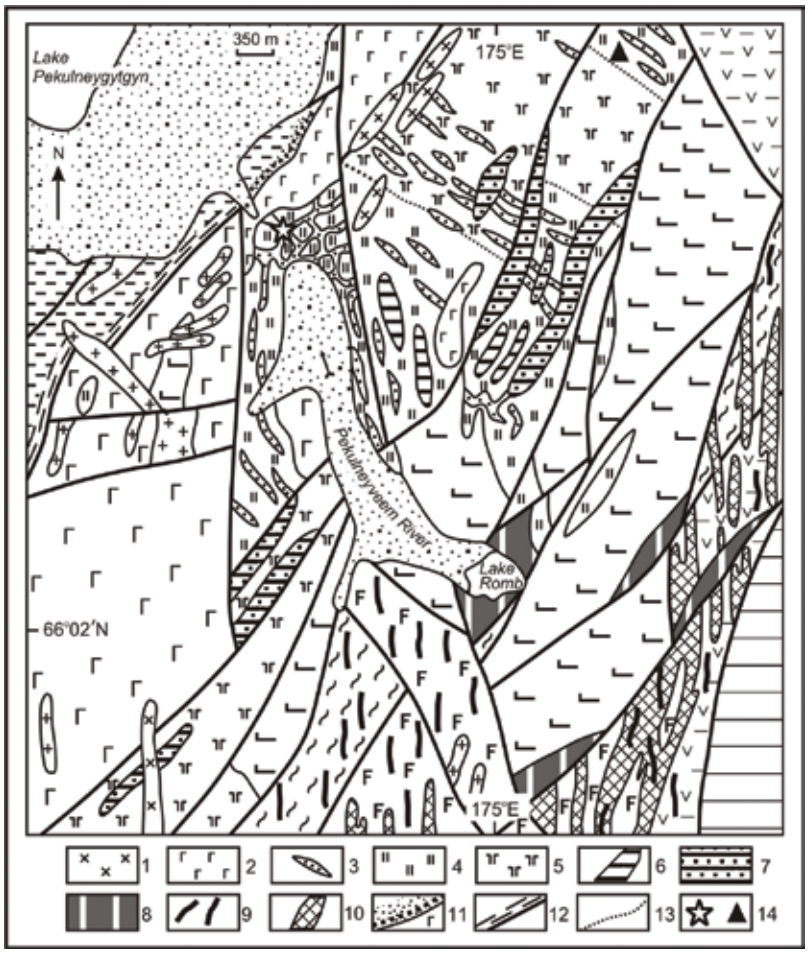

Figure 2. Geological map of the Pekulneyveem River upper basin area (compiled by I. Zhulanova): 1–8—Svetlorechensky pluton: 1–2—additional intrusive phase: 1—amphibole plagiogranites, 2—amphibole gabbro; 3–8—main intrusive phase: 3–5—edge series: 3—hypersthene tonalites veins, 4—amphibole microgabbronorites, 5—pyroxene-amphibole gabbro; 6–8—layered series: 6—ophitic leucogabbro, 7—olivine-amphibole gabbronorites, 8—melanocratic troctolites, plagioclase peridotites; 9—Early Cretaceous Poperechninsky Complex (the parallel gabbro-metadolerites—plagiogranite-porphyry dikes); 10—Middle Jurassic-Early Cretaceous Ostrozubsky Complex (metadolerites—plagiogranites), 11—hornfelses in the exocontact of the gabbro intrusion; 12—dynamometamorphism zones; 13—facies boundaries within the intrusions; 14—the asterisk indicates the mouth of the Raysky Creek, the triangle is the sample 565б location. See **Figure 1** for the remaining symbols.

stretching. Soon this model was theoretically shaped in the hypothesis on the two types of ophiolites present in the Anadyr-Koryak System: the first are fragments of the primary oceanic crust, on which Early Paleozoic geosynclines were laid; the second appeared in mid-Paleozoic and Late Jurassic-Cretaceous marginal seas on the island-arc stage of geosyncline development as result of gapping the continental crust [24].

The next discovery was the information about the fact that the mélange zone (cement and outliers) in the southern part of the Pekulney Ridge is not laid by serpentinites but by ultrabasic volcanites: meimechites and picrites [25]. Most geologists concluded that they referred to the

Hauterivian, and that their composition corresponded the picrite-basalt volcanic-plutonic complex [26]. The data on the Pekulney Ridge structure combining the complex of the old continental crust with Mesozoic ophiolites and ultrabasic volcanites made the area one of the most interesting ones in the Anadyr-Koryak System. In the early 1980s, the USSR Ministry of Geology chose the Pekulney Ridge as the primary test site for arranging methodological works on implementing new geodynamic concepts into the geological mapping practice. The new concepts included the lithospheric plate tectonics; its most acknowledged supporter in the USSR was the world-famous geologist Zonenshain (1929–1993) [27–29]. The first works on this topic at the Pekulney Ridge and in some other areas within the Anadyr-Koryak System were performed by employees of the Federal Association "Aerogeologiya" (Moscow) in 1983–1990. The main scientific result was presented in a publication [30]. It considered the Pekulney Ridge structures together with other uplifts of the left bank of the Anadyr River: Kanchalansky, Zolotogorsky, though their geological structures differ. The two orthogonal island arcs, Pekulney and Kanchalan-Zolotogorsky, were reconstructed for Late Jurassic-Early Cretaceous stage of the area developmenthis. This explanation is principally close to the one offered earlier [21].

The view of the current tectonic structure of the Pekulney Ridge, elaborated on the base of plate tectonics postulates, is at first sight close to that suggested in publications [5, 6]: both distinguish the autochthon, the allochthon, and the neoautochthon. However, if in the first model, the Mesozoic ophiolite zone interpreted as result of old continental crust riftogenesis, in the plate tectonics model, the main place is taken by the data permitting to conclude that the formation of the Late Jurassic-Early Cretaceous island arc and Mid-Jurassic-Early Cretaceous masses, currently building the allochthon (ophiolites) was divided by the vast space of the Paleopacific. The issue of the nature of the Early Mesozoic island arc basement drew no special attention in this context. Here, the author of monograph [30] followed the compromising interpretation of the nature of basites in the northern part of the Pekulney Ridge, proposed by Nekrasov in the late 1980s [31, 32]. Works by the "Aerogeologiya" team, ideologically following Zonenshain, practically completed the history of the Pekulney Ridge geological studies in the twentieth century.

2.2. Modern problems and opportunities

The first decade of the twenty-first century is marked with compiling the second-generation sheets of the Federal Geological Map of the Russian Federation 1:200,000 scale (further referred to as FGM-200/2), published in 2009 [14]. The methodology for this kind of work allows to compile new medium-scale maps significantly advanced deciphering the geological structure of the unique, from many viewpoints, area of the Pekulney Ridge. According to the requirements of the Stratigraphic and the Petrographic Codes of the Russian Federation, all mapped units (series, suites, and strata of stratified deposits, magmatic and metamorphic complexes) obtain proper names [33, 34]. Some of them correspond to earlier distinguished subdivisions, but many units received such names for the first time. It is most essential for us that the Legend of the Koryak Sheet Series (LKS-200) includes basites of the northern part of the Pekulney Ridge as a two-phase Svetlorechensky gabbro complex of the Early Cretaceous age (breaks through the Tithonian-Valanginian Gruntovskaya Strata, is overlaid by the Hauterivian Ostantsovogorsky Strata). Stratigraphic units have been distinguished: presumably Middle-Upper Paleozoic, essentially Pekulneygytgynskaya Strata and Sbornenskaya

http://dx.doi.org/10.5772/intechopen.74994

Strata of high-temperature metamorphic rocks conventionally dated by the Paleozoic [14]. The LKS-200 team also supported our conclusion that in the southern part of the Pekulney Ridge, among deep rafts spatially joining ultramafites, there also is a wide enough set of metamorphic rocks, petrographically identical to cognominal Lower Archaean rocks from the basement of the Omolon Massif and the Avekovsky crystalline block of the Taygonos Peninsula [10]. They are included in LKS-200 as an supposedly Archaean Plagiogneiss Strata. The author of this chapter has offered the name for it—Kruglogorskaya (after Mt. Kruglaya) [35].

At the turn of the twentieth century, the range of scientific research in Russia, including geological studies, was significantly reduced for the reasons beyond academia. Nevertheless, many holders of the Pekulney Ridge rocks collections continued laboratory research; some managed to conduct field works, and some new data were obtained [36–43]. The overwhelming majority have been concentrated in the southern half of the Pekulney Ridge. The exception is the generalizing publication [44] devoted to the geodynamical interpretation of $^{40}Ar/^{39}Ar$ dates for mafites of the Anadyr-Koryak Region, as well as the latest elaborations by Nekrasov, where the Pekulney Ridge structures are discussed in the wide tectonic context as one of the elements of a complex zone of the Arctic Craton joining structures of the Koryak-Kamchatka and Verkhoyansk-Chukotka folding areas [45, 46]. So far, to our utter regret, the perspectives for further studying the Pekulney geology remain obscure.

3. Svetlorechensky gabbro complex: general issues

3.1. Why distinguish

It has been noticed above that, for a long while, the northern part of the Pekulney Ridge had been significantly less studied than its southern part. Therefore, an opportunity to revise the views of one of geological complexes in a less studied area could not be excluded a priori. Discussions on Precambrian or Phanerozoic age of some formations in Northeast Asia have been occasionally raised these days, as well. But they are all characteristically associated with metamorphic rocks. The "Precambrian foundation or Mesozoic intrusive massif" alternative has emerged in the area for the first time. Its solution certainly required stronger reasoning than that Nekrasov had restricted himself to [5, 31, 32]. He observed proper crystalline schists at the site of approximately 20 km^2, while the total area, occupied with fully crystalline basites in the northern part of the Pekulney Ridge, is no less than 200 km^2 [2–4]. We have mapped the basic rock massif from its southern end in the outflows of the Levaya Svetlaya River (some farther to the south of 66°00′ N) to the South Chekogytgyn Lake, which makes two-thirds of its total length and about three-fourths of its area (**Figure 1**). The host rocks have also been studied; most comprehensively, three sites, where FGM-200/1 [3, 4] shows crosscutting relations of basites with Lower Cretaceous deposits. The obtained data permitted to reconstruct a large intrusive massif named Svetlorechensky layered pluton, and to grant it the status of a petrotype of the Early Cretaceous Svetlorechensky gabbro complex. This meant that the homologs to Svetlorechensky pluton might be found in other areas within the Pekulney Ridge, as well.

This conclusion was quite explicitly grounded. Parallel to our works (1980–1982), Sterligova (Central Complex Topical Expedition, City of Magadan) studied magmatic complexes in the

southern part of the Pekulney Ridge. On the right bank of the Severny Pekulveyem River, for the first time, she mapped and comprehensively described the gabbro massif (named Pravoberezhny, in whose identity with Svetlorechensky complex we did not doubt). Further on, our opinion was convincingly confirmed [14]. Additional study of the area exposed that Svetlorechensky-type gabbroids were quite widely spread in the southern part of the Pekulney Ridge (**Figure 3**). Data on their relations with hosting Tithon-Valanginian deposits (Gruntovskaya Strata) and other intrusive complexes in the area as well as new definitions of isotopic age are of particular importance.

3.2. Svetlorechensky layered pluton: geology, petrography, genesis issues, age

3.2.1. Preliminary notes

Starting our works in the northern part of the Pekulney Ridge, we formulated two main questions: (1) what is the nature of finely grained amphibole-two-pyroxene rocks described as

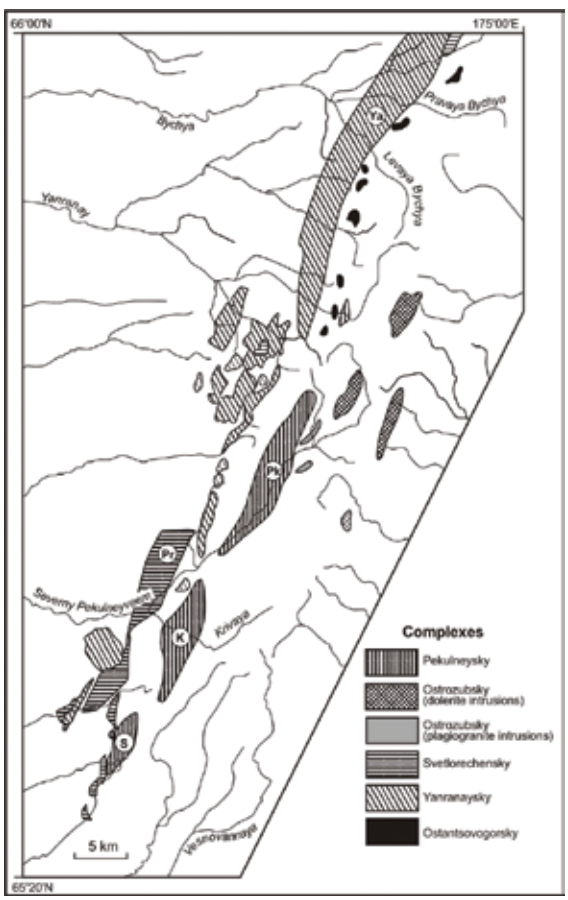

Figure 3. Scheme for placing intrusions within the boundaries of the Q-60-XIX Sheet of the State Geological Map (according to [14], with simplification): the letters in the circles indicate intrusions: K—Krivorechensky, Pk—Pekulneysky, Pr—Pravoberezhny, S—Stoybishchny, Ya—Yanranaysky. Explanations are in the text.

http://dx.doi.org/10.5772/intechopen.74994

crystalline schists of the granulite facies of metamorphism [5]? and (2) what are interrelations of "crystalline schists" with certainly magmatic rocks (gabbro-anorthosites, anorthosites, olivine-pyroxene gabbro, amphibole gabbro, amphibole-biotite diorites, tonalites, and plagiogranites), the second component of the Archean "granulite-basite" association, according to [5]? We should notice immediately that the "finely striped garnet gabbronorites," which originally were considered a linchpin between "crystalline schists" and "coarsely striped magmatic gabbroids" [5, 6], were not further on proved to be present in the Pekulney Ridge [1, 7, 10, 14, 30–32]. From the very beginning, it was clear that in such a complicated area, in the absence of paleontologically dated Late Precambrian and Paleozoic deposits, the problem of the Early Precambrian cannot be solved by direct geological observations. The most efficient appeared the multilateral study of finely grained "amphibole-two-pyroxene crystalline schists" and their comparison with eponymous Archean rocks by a maximally possible number of characteristics. The task was easier to solve due to the extensive factual materials on authentic Archean granulites of the Omolon-Taygonos District of Northeast Asia (summarized somewhat later [47]). The question on "crystalline schists" interrelations with layered gabbroids required systematic geological mapping of the "granulite-basite" spread area. We used it as a base for the Federal Topographic Map of 1:25,000 scale.

The studied area is peculiar not only for its highly dissected alpine-type relief but also for its tense inner, primarily fault, tectonics. On any geological map [2, 4, 14], it is conspicuous that almost all contacts between geological bodies of more or less significant volume go along faults (**Figure 1**). In the contemporary structure, the basite massif, from which "Precambrian" was distinguished, looks like a large fissure body with its length (about 60 km) 10-fold exceeding its width (2–8 km). In the summer of 1981, field observations were started together with colleagues from Anadyr and Vladivostok (see Introduction), in the area of the Raysky Creek (right tributary of the Pekulneyveem River near its outlet from the mountains), which had been known as a key for the "Archean crystalline schists and enderbites" [5, 6] (**Figure 2**). Our thorough and purposeful observation allows to suggest that the metamorphic rocks are absent in the area. Moreover, the very first routes showed that even in their Pekulney, "crystalline schists" are limitedly spread, and that they promptly change to evenly grained gabbro, rich in hornblende and possessing all characteristics of magmatic rocks, very fresh, at that. In other words, similarity of Pekulney amphibole-two-pyroxene basites and minerally identical crystalline schists of the granulite facies is exterior. In the case discussed here, it is associated with the influence of the Earth gravity field, which determines both supracrustal mass layering and most of oriented textures observed in endogenous formations. The same conclusion applies to "enderbites" supposedly associated with "amphibole-two-pyroxene crystalline schists" [5]. In fact, observed in rock exposures along the Raysky Creek are crosscutting veins of hypersthene tonalities, whole mutually parallel orientation, vaguely resembling the layered migmatite texture, is determined by host basites banding (see below). We define Nekrasov's amphibole-two-pyroxene "crystallineschists" as amphibole microgabbronorites. This name does not imply all distinctive structural characteristics of these rocks, but is convenient because it promptly distinguishes a disputable group of rocks from other variants of gabbro rich in hornblende, mostly medium-grained, in the studied area. Medium-grained hornblende-rich gabbro falls into three petrographic groups: (1) pyroxene-amphibole, (2) amphibole, and (3) biotite-amphibole.

3.2.2. Hornblende-rich gabbro

Spatially, all the four groups of hornblende-rich gabbro are closely interconnected and inclined to the western part of the ridge (**Figures 1**, **2**). All of them form a petrographically unified series, where each consequent phase exposes similarity to the preceding one, while the end members significantly differ from each other. Simultaneously, geological relations among rocks of the distinguished groups are more sophisticated. Let us characterize the rocks that served as the subject of discussion in more detail.

Amphibole microgabbronorites: structure, composition, correlation with basic crystalline schists of the granulite facies: Amphibole microgabbronorites of the discussed area are notable for their quite original banded structure, really making them look somewhat similar to crystalline schists. On the background of finely grained (0.1–0.8 mm) bluish-dark-gray basic mass, they contain boldly distinguished lenticular polycrystalline aggregates of black "cribrose" hornblende, reaching a few centimeters in length (most frequently 0.5–1.5 cm). They are always mutually parallel-oriented and concentrate into bands to a few centimeters wide, separated by much wider bands, where amphiboles cannot be distinguished through a naked eye. Similarity of the basites described here with metamorphous formation is strengthened by the presence of weak leucogabbro veinlets similar to the migmatite leucosome. Characteristically, in the vicinity of leucogabbro veinlets, lenticular segregations of hornblende are absent, but on their boundaries, its subautomorphic crystals and nests are often differentiated (**Figure 4**).

Through the microscope, signs of the magmatic origin of the rocks under discussion are established unequivocally. The fine-grained mass (plagioclase 50–60%, clinopyroxene 20–25%, hornblende 10–15%, hypersthene 5–8%, magnetite 5–10%, singular grains of apatite, ilmenite, zircon) exposes the clear trachytoid structure determined by the oriented location of strongly elongated plagioclase laths. They are almost always weakly zonal. The anorthite molecule content is most frequently about 80% but subject to noticeable fluctuations (95–55%). Chemical composition of rock-forming minerals is presented in **Table 1**.

Characteristic is microbanding of spots that externally seem homogeneous. It is associated with varied granulity and layer composition. Millimeter "leucosomes" are utmost in grain size and plagioclase content in the range of such differentiation. Characteristics for clinopyroxene-pale diopside are its reactional ratios with hornblende, inside which it is often kept as separate inclusions, fading simultaneously. General mafic index is about 25%; alumina content, 0.69–1.68%; sodium is completely absent. Large subsolidus calcium hornblende aggregation, with its typical brownish-gray or brownish-green color, has poikilocytic structure due to chaotically oriented inclusions represented by finest plagioclase laths and hypersthene grains. General mafic index of hornblende is 33–35%. The equation calculation showed that practically all the alumina in it is within the quarter coordination. Hypersthene most frequently forms small, partly automorphic crystals with clear pleochroism. Its general mafic index is slightly higher than that of hornblende (36–38%). The typomorphic peculiarity of microgabbronorites is a high content of magnetite, which forms large independent aggregation, as well as numerous smaller inclusions in plagioclase and clinopyroxene. According to the data from the microprobe analysis, it is practically pure magnetite with small admixtures of Ti, Al, Mg, Mn, and Ca. The comparative petrographic and mineralogical characteristics of amphibole microgabbronorites

http://dx.doi.org/10.5772/intechopen.74994

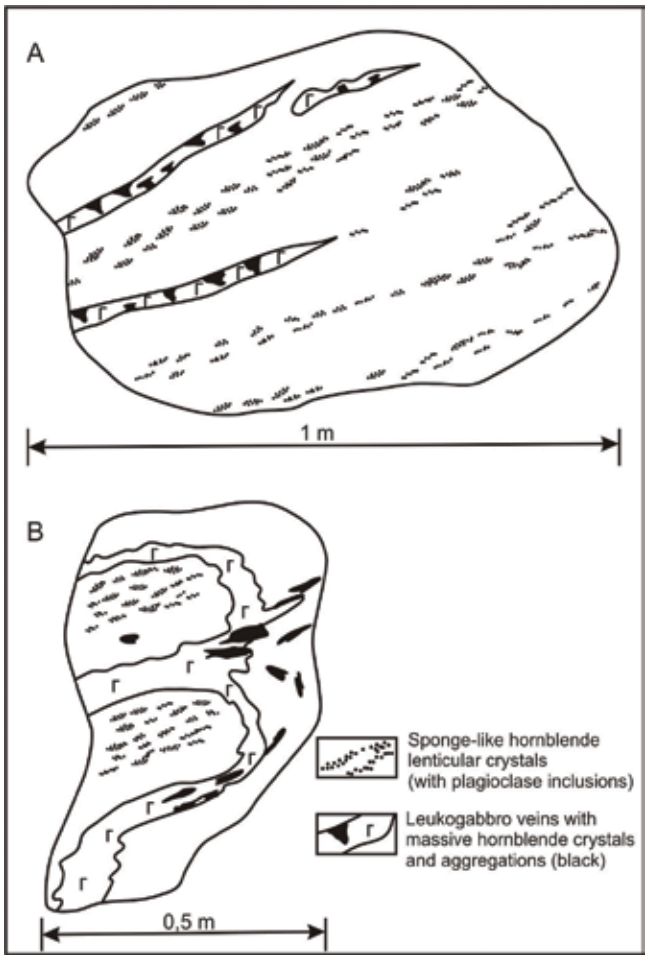

Figure 4. Banded texture of amphibole microgabbronorites in a natural outcrop (sketch by I. Zhulanova): the sections orient respectively: A—perpendicular, B—parallel to banded texture.

and mineralogically identical (amphibole-two-pyroxene) Archean crystalline schists obviously confirm the genetic difference between the two groups of rocks (**Tables 2** and **3**).

But the deep genetic difference between amphibole microgabbronorites and basic granulites is most completely revealed by the analysis of peculiarities of the bulk chemical composition of the rocks (**Table 4**, column 1). The available selection of nine analyses is sufficiently homogeneous. Among general peculiarities, the most conspicuous is the low grade of silicic acid in some samples. Only one of nine analyses has an average of this parameter (48%). All the rest are at the lower limit of SiO_2 content accepted for normal basic rocks (45%), and even go lower (to 41%). Extremely low is also the content of metalloids, especially potassium. On the other hand, the alumina content in amphibole microgabbronorites is sufficiently high (to 17%). Simultaneously, the total Fe_2O_3 iron, magnesia, and lime are maximal for its group [34]. The ratio of ferrous iron and protochloride iron is typical for iron-rich leucobasals (8:6, oxidation ratio is 60%).

Component	Sample 528			
	Pl	Hbl	Opx	Cpx
SiO_2	46.72	48.23	51.77	52.81
TiO_2	n.d.	1.58	0.21	n.d.
Al_2O_3	33.00	6.29	0.66	0.69
Fe_2O_3*	0.66	15.15	25.82	10.18
MnO	n.d.	0.29	0.76	0.27
MgO	n.d.	15.19	22.28	14.61
CaO	17.21	11.28	0.81	22.29
Na_2O	1.95	0.55	n.d.	n.d.
K_2O	0.11	0.03	n.d.	0.05
Total	99.65	98.59	102.31	100.90
F		33	36	26

Component	Sample 645–1				Sample 645	
	Pl	Hbl	Opx	Cpx	Pl	Opx
SiO_2	51.03	50.50	52.28	52.75	52.03	52.69
TiO_2	n.d.	0.87	0.14	0.13	0.00	0..16
Al_2O_3	31.14	5.91	0.76	1.38	29.83	0.91
Fe_2O_3*	0.53	15.41	26.60	10.77	0.30	25.95
MnO	n.d.	0.36	1.07	0.35	0.06	0.91
MgO	n.d.	14.31	20.95	13.51	0.00	21.01
CaO	14.56	11.78	0.78	22.26	14.36	1.01
Na_2O	2.89	n.d.	n.d.	n.d.	3.37	n.d.
K_2O	n.d.	0.05	n.d.	n.d.	0.07	n.d.
Total	100.15	99.19	102.58	101.15	100.02	102.64
F		36	38	28		38

Note. Here and below: Ol—olivine, Opx—orthopyroxene, Cpx—clinopyroxene, Hbl—hornblende, Pl—plagioclase, Sp—spinel. Fe_2O_3* = FeO + Fe_2O_3 (as Fe_2O_3), *F* = Fe_2O_3* / (Fe_2O_3* + MgO + MnO), n.d.—the element was not detected or was not determined. Mineral analyzes were performed using a microprobe Camebax by V.V. Knauf (VSEGEI, St. Petersburg).

Table 1. Microprobe analyses of rock-forming minerals from amphibole microgabbronorites, wt. %.

The basic peculiarity of amphibole microgabbronorites is the unusually low SiO_2 content at a large amount of Al_2O_3; it is naturally explained by the reliably established fact of the early segregation of a large amount of magnetite from magma. This forms the deficiency of metals for building mafic silicates, rocks are dressed with plagioclase, and finally remains noncompensated silica, involved in forming later acid differentiates quartz gabbro and hypersthene tonalities. This route of crystallization is provided by high oxygen (or water) potential within

Structural features	
1	Idiomorphic lath-like shape of plagioclase grains indicates its early fast crystallization
2	Simple character of twins determined by their formation simultaneous to the growth of crystals; parallel location of twin planes determined by crystal reorientation in the process of subsidence
3	Direct plagioclase zoning, emerging in the course of its crystallization from the melt
4	Porphyry-like form of hornblende grains indicates its late magmatic growth under free matter access
5	Presence of chaotically oriented smaller laths of plagioclase within large hornblende isolations; testifies to successive crystal sorting from the melt
6	Reactionary relationships between hornblende and clinopyroxene associated with the longer growth of the former
7	Presence of smallest magnetite grains within plagioclase and clinopyroxene testifies to crystallization of the former preceding that of silicates
Mineral composition features	
8	Plagioclase contains 55–95% anorthite molecule (most frequently 80–85%)
9	Orthopyroxene contains less than 1% (0.66–0.91%) Al_2O_3
10	Clinopyroxene contains practically no Na_2O
11	Hornblende contains (wt. %): TiO_2–0.9–1.6, Al_2O_3–5.9–6.3, Fe_2O_3* – 15.15–15.41, Na_2O – 0.0–0.5, K_2O – 0.03–0.05; mafic index (*F*) = 33–35%

Note. The composition of minerals and symbols are shown in **Table 1**.

Table 2. Petrographic and mineralogical characteristics of amphibole Microgabbronorites.

the system, and, after pioneering works by Osborn [48], has been known as "crystallization at the constant general composition." Early magnetite segregation also explains noticeably lower mafic index of dark-colored minerals in comparison with bulk mafic index of rocks. The emergence of orthopyroxene is naturally associated with low alkalinity and high alumina of the original magma. Under these conditions, most calcium is associated within plagioclase, which explains its high alkalinity, and hypersthene is crystallized instead of some part of monocline pyroxene. Hornblende is formed on the magmatic stage with the alkaline concentration rise within the system and probably lends some calcium from plagioclase.

Thus, the main factors of specific peculiarities of microgabbronorites are high pressure of volatiles in the melt by the start of its crystallization, as well as the low alkalis and high aluminum in the parent magma. All the revealed proofs of the genetic difference between amphibole microgabbronorites and basic granulites are logically completed with the data on the general pressure value for rocks to be formed.

Since the main reason for Nekrasov to distinguish Archean rocks of the granulite facies in the northern part of the Pekulney Ridge was their amphibole-two-pyroxene mineral composition, above we have deliberately compared them with reliably Archean rocks containing analogous mineral paragenesis. Now, we would notice that, by the chemical composition, amphibole

Structural features	
1	Isometric shape of plagioclase grains with irregular blastic boundaries resulted from crystallization under pressure
2	Very fine polysynthetic twinning of plagioclase with characteristic wedging of one of twin individual systems, indicating the deformational nature of twinning; non-oriented (isotropic) location of twin planes within the rock, pointing at the lithostatic character of pressure
3	Azonal structure of plagioclase or its vague reverse zoning, determined by Na entering clinopyroxene due to the increased general pressure
4	Mostly similar sizes of all mineral grains at possible growth of any of them (metamorphic differentiation)
5	No impurities within hornblende, particularly no minerals with elements of idiomorphism
6	Stable structural (blastic) relations among all minerals without signs of reactionary relationships
7	Equidistance of magnetite grains within the rock indicating its crystallization simultaneously to that of other minerals
Mineral composition features	
8	Plagioclase contains 47–55% anorthite molecule (due to the transition of part of calcium into garnet)
9	Orthopyroxene contains over 1% (1–6) Al_2O_3
10	Clinopyroxene contains 0.2–1% Na_2O
11	Hornblende contains (wt. %): TiO_2 – 2, Al_2O_3 – 12, Fe_2O_3 – 23, Na_2O – 1.5, K_2O – 2.2; mafic index (*F*) = 58–60%

Note. These properties, including mineral compositions, refer to the amphibole-two-pyroxene crystalline schists from the Aulandzha Block of the Omolon Massif basement [49]. Their Paleoarchean age is confirmed by the latest results of U–Pb SHRIMP-RG dating of zircons [51].

Table 3. Petrographic and mineralogical characteristics of amphybole-two-pyroxene crystalline schists.

microgabbronorites of the Pekulney Ridge do not correspond to amphibole-two-pyroxene crystalline schists but to eclogite-like rocks: only for them typical is low silicic acid with high alumina and iron [47, 49]. Under high general pressure, characteristic for Archean granulite complexes, such component ratio determines crystallization of garnet, a barophilic mineral rich in alumina and iron but silica-poor. High pressure also provides including a large amount of calcium in garnet, which determines stably low alkalinity of plagioclase in eclogite-like schists [50]. Simultaneously, sodium (jadeite molecule) goes from plagioclase into diopside, but its amount is not large and does not compensate the loss of calcium. Similar composition peculiarities are typical for eclogite-like rocks of the Southern Pekulney, as well [10].

The discussion was finalized by the results obtained by Siberian geologists in the course of large-scale program works on the comparative study of ophiolite petrogenesis conditions in intracontinental folding systems and of ocean-continent transition zones (Siberia, Urals, Mongolia, Chukotka, Kamchatka and others), a few years after our works [51, 52]. Plagioclases and clinopyroxenes from the Pekulney Ridge rocks, described in [5–7] as Precambrian amphibole-two-pyroxene crystalline schists, contain melt inclusions, which is

Component	Gabbro				Veins		
	1	**2**	**3**	**4**	**5**	**6**	**7**
SiO_2	44.6	44.50	45.7	49.00	53.9	68.30	72.04
TiO_2	0.9	0.70	0.60	0.60	0.5	0.57	0.40
Al_2O_3	17.30	18.70	17.50	17.10	20.8	15.44	14.27
Fe_2O_3*	14.20	11.10	10.20	9.80	6.5	4.41	3.32
MnO	0.21	0.17	0.15	0.14	0.1	0.06	0.06
MgO	7.40	8.50	8.80	8.00	4.8	1.64	1.04
CaO	12.10	12.50	13.10	11.00	10.4	5.56	3.90
Na_2O	2.20	2.40	2.20	2.60	2.8	3.49	4.66
K_2O	0.29	0.39	0.28	0.45	0.4	0.42	0.46
P_2O_5	0.10	0.07	0.05	0.06	0.06	0.10	0.04
LOI	0.50	1.10	1.30	1.30	0.4	0.62	0.53
Total					100.06	100.61	100.72
Sr	334	318	277	269		339	314
Ca/Sr	258	284	332	298		115	87
F	49	40	37	38	57	58	63
n	9	5	2	3	1	1	1

Note. 1—amphibole microgabbronorites, 2—pyroxene-amphibole gabbro, 3—amphibole gabbro, 4—biotite-amphibole gabbro, 5—quartz gabbronorite, 6—hypersthene tonalite 7—amphibole plagiogranite. Here and in **Table 6** rock analyzes were performed using the X-ray spectrometer ARL-72000 under the direction of V.Y. Borchodoev (NEISRI, Magadan); oxide content—wt. %, Sr—pm, *n*—number of analyzes.

Table 4. The chemical composition of hornblende-rich gabbro, and the accompanying veins.

an indisputable indicator of the magmatic genesis of the rocks under discussion. The author has diagnosed them as gabbronorites and amphibole gabbronorites crystallized within the temperature interval 1250–1300°C ([52], p. 142).

Now, let us briefly describe other petrographic groups of gabbro, rich in hornblende, as well as the associated vein formations. In more or less solid blocks, it is established that amphibole microgabbronorites and *pyroxene-amphibole gabbro* are closely connected with each other within unified geological bodies. It is important that amphibole microgabbronorites are inclined to a lower hypsometric level, exposing mostly in long core outcrops along canyon-shape valley sides. In general, pyroxene-amphibole gabbro are most widely developed of all hornblende-rich gabbro.

Amphibole gabbro insignificantly differs from pyroxene-amphibole ones in samples and thin sections. From the outside, they are somewhat larger-grained and homogenous. At the same time, on the background of amphibole microgabbronorites, amphibole gabbros are mapped as independent bodies with borders sufficiently clear, because they clearly crosscut microgabbronorite banding as well as systems of parallel leucogabbro veinlets, characteristic for

microgabbronorites and pyroxene-amphibole gabbro. *Biotite-amphibole gabbro*, in turn, has a lot in common with amphibole gabbro but presents the type already normal for Russia's North-East: medium-grained basic rocks with columnar hornblende and plagioclase more acid than the one in the previous group, which is seen in the sample by its dull white (not glass-gray, as in previous groups) coloring. Biotite-amphibole gabbro composes the south-western part of the Svetlorechensky Massif and is separated from other types of amphibole gabbro by faults (**Figure 1**). A rather monotonous petrographic outlook of the "amphibole microgabbronorites-biotite gabbro" series is significantly varied in the geological sense by vein leucocratic rocks. They fall into three groups: (1) leucogabbro, (2) hypersthenic tonalities, and (3) amphibole plagiogranites.

Leucogabbro is a relatively largely grained differentiate characteristic for all types of the amphibole gabbro. However, in dark-colored microgabbro and pyroxene-amphibole gabbro, they are distinguished with more contrast than in lighter amphibole and biotite-amphibole gabbro. Irrespective of the host rock composition, in all leucogabbro, short-prismatic hornblende prevails among dark-colored minerals. In amphibole microgabbronorites and pyroxene-amphibole gabbro, it is joined by hypersthene, associated with quartz. However, plagioclase maintains its high basicity, and by their bulk chemical compositions, such variations stay within the gabbro group. *Hypersthenic tonalites* are largely grained greenish-white rocks of stroke texture; they compose veins to a few meters thick, which, on the one side, do not go beyond the pyroxene-bearing gabbro contours and, on the other side, act independently in the geological sense. At some sites, the volume of hypersthenic tonalities exceeds that of the substance, and the latter acts as xenolites with traces of dislocation and deformation. With parallel vein location, rocks generally acquire the outlook resembling layered migmatites; with chaotic substance block orientation, agmatites. *Amphibole plagiogranites* have the outlook similar to that of hypersthenic tonalities (inside large bodies, they may be linked with them by gradual transitions). In general, however, they have a much larger area of distribution. In amphibole and biotite-amphibole gabbro, plagiogranites sometimes form compound branching veins that give these rocks an agmatite-like outlook, as well. The largest volume of plagiogranites is found at the western slope of the ridge, where they are traced along its piedmont as a system of independent thick (to 20 m) and long veins.

Geological data permit to conclude that amphibole and biotite-amphibole gabbro characterize different levels of erosional exposure of the same magmatic bodies. The issue of correlations between amphibole microgabbronorites and pyroxene-amphibole gabbro is more complex. It is discussed below. Chemical compositions of rocks described in Section 3.2.2 are presented in **Table 4**.

3.2.3. Layered series

Hornblende-rich fine- and medium-grained rocks, including amphibole microgabbronorites, made a total of about two-thirds of the massif part. The rest is built from medium-, large-, and giant-grained gabbroids, which we call the "layered series" (LS). While mapping it, we have distinguished (1) plagioclase peridotites, (2) leucocratic troctolites, and (3) gabbroanorthosites. They compose unified geological bodies with well-expressed banding, from course (dozens meters) to centimeters and even millimeters. Parallel-banded packs frequently are

http://dx.doi.org/10.5772/intechopen.74994

adjacent to those deformed to different degrees, up to "isoclinally folded" ones. The series is accompanied by lode differentiates: gabbro-pegmatites, ophitic leucogabbro, magnetite gabbronorites, microferrogabbro.

For field research, the LS is relatively simple. Large sizes of mineral individuals allow to diagnose rock types through the naked eye, and banded textures, clearly expressed in various scales, facilitate drawing boundaries between distribution fields of individual facial variations. On spots of a significant erosion incision, it is systematically exposed that voluminously significant outcrops of melanocratically extreme series members (melanocratic troctolites, plagioclase peridotites) are located in the lower parts of mountain slopes and are upper replaced by leucocratic troctolites. Boundaries between large bodies of both rocks are rather sharp. Leucocratic troctolites and mesocratic olivine gabbro are interconnected by more gradual transitions. In some cases, leucocratic troctolites act toward melanocratic ones as a later active phase. Both variations of troctolites are characterized by weak (2–5 cm) crossveins of finely grained magnetite gabbronorites and even finer blind veinlets of dark-gray microferrogabbro. The largest volume in the series composition is taken by large-grained gabbroanorthosites; distinguished on their gray background are light bands to half-meter thick, build from anchimonomineral anorthosites. Of dark-colored minerals, clinopyroxene always prevails in gabbroanorthosites.

The characteristic member of the LS is made from geologically independent bodies of olivine-amphibole gabbronorites (**Figure 2**). They are highly melanocratic at the maximally complete set of dark-colored minerals in the primary magmatic paragenesis (olivine, two pyroxenes, hornblende). The simplest mineral composition distinguishes ophitic amphibole leucogabbro (further briefly referred to as leucogabbro), which build bodies of the same type as those built from olivine-amphibole gabbronorites. They differ from compositionally close amphibole leucogabbro, described above as differentiates of amphibole microgabbronorites, by reverse structural ratios of plagioclase and hornblende (large idiomorphic tablets of plagioclase are well recognized in ophitic leucogabbro even through the naked eye); but most importantly, by their geological independence. They are spatially attached to large outcrops of the LS rocks (**Figure 2**).

The question of interrelations between the LS rocks with hornblende-rich gabbroids, including amphibole microgabbronorites, is a key to the problem of the origin of basites in the northern part of the Pelkulney Ridge. At the first sight, each of the two large groups (supergroups) is so clearly petrographically specific that it should undoubtedly distinguished into an independent complex. This viewpoint seems to be supported by clearly crosscutting relations between olivine-amphibole gabbronorites and amphibole microgabbronorites, which was first pointed at by Nekrasov [5] and then confirmed by our observations. In the upstream of the Raysky Creek, in a bedrock exposure, it is clearly seen that the contact line of olivine-amphibole gabbronorites, complicated by small apophyses, crosscuts the amphibole microgabbronorite banding, emphasized by the elongated leucogabbro veinlets. In olivine-amphibole gabbronorites, in their turn, banding oriented discordantly with that of amphibole microgabbronorites is observed. Observations on body interrelations in exposures are confirmed by the general structure pattern of the area, as well. The north-northeastern spread of most mapped bodies of olivine-amphibole gabbronorites is sharply crosscutting the general northwestern orientation of the vein leucocratic phase of amphibole microgabbronorites and

pyroxene-amphibole gabbro (**Figure 2**). Besides, in gabbroanorthosites occurred small xenoliths of amphibole microgabbronorites.

Like our predecessors, we originally tended to overestimate the facts as determinants, though even then some common signs between the LS rocks and amphibole gabbronorites. For instance, in the course of the 1981 field works, it was fixed that when the two-pyroxene-plagioclase basic mass of microgabbronorites has finely or, at some spots, medium-grained structure, these rocks externally closely resemble the finest-structured variations of olivine-amphibole gabbronorites. This resemblance was the more conspicuous that both rocks are spread in one area, in the Raysky Creek upstream. It was also noticed that microgabbronorite sites containing no hornblende are similar to finely grained magnetite gabbronorites, building thin veinlets in largely grained layered gabbro bodies.

But the greatest attention was attracted by the close spatial connection of the LS rocks with hornblende-rich gabbroids. The 1981 mapping of a sufficiently large area showed that rocks exposed in the vicinities of Lake Romb could not be distinguished into a tectonically independent complex, which, according to [5, 6], has direct structural connections with the South Pekulney ophiolites, since characteristically analogous gabbroids spread far to the north, making the typomorphic components of the basite massif in the northern part of the Pekulney Ridge. It has become obvious that the close location of layered and amphibole gabbroids did not result from an occasional tectonic coincidence of different formations but had a regular character.

Petrographic variety of the LS, in general, is great, however, basically determined by variations of quantitative ratios within the unified set of minerals: olivine, orthopyroxene and clinopyroxene, hornblende, plagioclase, magnetite, spinel; their properties change insignificantly practically within the whole range of rocks, from melanocratic troctolites to olivine-amphibole gabbronorites and microferrogabbro (**Table 5**). The only (and expected) exception is plagioclase. Optical measurements showed that in most voluminous rocks, representing the LS s. stricto (largely grained melanocratic and leucocratic troctolites, gabbroanorthosites, anorthosites), plagioclase is characterized by quite high and, generally, weakly varying content of the anorthite molecule (93–97%), while in the lode series rocks, its behavior is more varied: e.g., in ophitic leucogabbro, plagioclase is extremely rich in calcium (No. 98–100), while in polymineral and highly ferruginous gabbroids (olivine-amphibole and magnetite gabbronorites, microferrogabbro) is noticeably more acid (No. 82–95).

Orthopyroxene is represented by bronzite with the general mafic index varying from 19 to 26%. Judging by the available microprobe analysis from olivine-amphibole gabbronorite, clinopyroxene refers to low-iron diopside (**Table 5**, Sample 643a). In all rocks of the series, from melanocratic troctolites to microferrogabbro, primarily magmatic hornblende is present. In most cases, it is xenomorphic. Only in finely grained olivine-amphibole and magnetite gabbronorites are large hornblende crystals of poikiloophitic texture sometimes observed. Hornblende from the LS rocks is more magnesia than that from amphibole gabbroids (**Table 5**, Sample 643a, 629-3-1). Troctolites usually contain rare fine grains of green spinel. It is referred to pleonast, has 38% mafic index, and contains no chromium (**Table 5**, Sample 629-3-2).

Rock structures within the typomorphic LS are typical cumulative. Plagioclase-enriched differences have the gabbro structure, sometimes with elements of the ophitic one. Characteristic

Component	Sample 643a							
	Pl	Hbl	Opx	Cpx	Ol			
SiO_2	44.63	45.25	52.77	51.17	37.08			
TiO_2	n.d.	0.04	0.09	0.09	н.о.			
Al_2O_3	34.85	11.88	3.37	2.70	1.47			
Fe_2O_3*	0.29	11.04	18.34	6.88	28.92			
MnO	n.d.	0.13	0.34	0.28	0.52			
MgO	0.16	16.09	25.92	15.96	34.98			
CaO	19.11	11.63	0.93	23.25	0.04			
Na_2O	0.72	1.30	n.d.	n.d.	n.d.			
K_2O	n.d.	0.03	n.d.	n.d.	n.d.			
Total	99.76	97.39	101.76	100.33	103.01			
F		26	26	18	29			
Component	**Sample 629-3-2**				**Sample 629-3-1**			
	Pl	**Opx**	**Ol**	**Sp**	**Pl**	**Hbl**	**Opx**	**Cpx**
SiO_2	44.16	53.23	38.40	0.53	45.52	44.26	52.60	51.28
TiO_2	n.d.	0.18	0.06	n.d.	0.07	1.93	0.10	0.23
Al_2O_3	35.17	3.94	1.55	63.63	34.18	11.22	2.86	3.26
Fe_2O_3*	0.37	13.62	20.31	20.20	0.43	11.74	19.06	7.61
MnO	n.d.	0.49	0.55	0.14	n.d.	0.54	1.07	0.32
MgO	0.19	29.19	41.26	16.63	n.d.	14.92	25.24	14.85
CaO	19.46	0.55	n.d.	0.05	18.45	11.60	0.86	23.06
Na_2O	0.45	n.d.	n.d.	0.29	1.15	1.36	n.d.	n.d.
K_2O	n.d.	n.d.	n.d.	n.d.	n.d.	0.05	n.d.	n.d.
Total	99.80	101.20	102.13	101.47	99.81	97.62	101.79	100.61
F		19	20	38		28	27	20

Note. 643a—Olivine-amphibole gabbronorite, 629-3-2—melanocratic troctolite, 629-3-1—microferrogabbro (vein in sample 629-3-2). A special analysis of Sp on Cr gave a negative result. Mineral analyzes were performed using a microprobe Camebax by V.V. Knauf (VSEGEI, St. Petersburg). Other symbols and notes can be found in **Table 1**.

Table 5. Microprobe analyses of rock-forming minerals from layered gabbro, wt. %.

is high freshness of rocks. More or less noticeable secondary alterations (partial development of zoisite and prehnite in plagioclase, achromatic acicular amphibole in pyroxenes, and talc in olivine and bronzite) are fixed only in most highly magnesial members of the series (plagioclase peridotites). Chemical composition peculiarities of the LS rocks confirm the legitimacy of its differentiation offered on the base of geological and petrographic data (**Table 6**). Simultaneously, calculating the average composition of the LS gabbroids, which could at least

approximately reflect the composition of the original nondifferentiated melt, appears practically insurmountable because it requires knowing volumes of single rock varieties, which is impossible. In our case, the solution of the problem is facilitated by the availability of small-volume weakly differentiated bodies of olivine-amphibole gabbronorites: their average composition, judging by the whole set of the LS minerals in their paragenesis, might be considered original for it, in a first approximation.

Certainly, evaluation of those rocks' average composition also faces problems determined by their textural heterogeneity. However, this with a purposeful approach can be overcome, since bodies of olivine-amphibole gabbronorites are often all-out revealed in base rock exposures. At our disposal, there are five analyses of this group of rocks. They are sufficiently homogeneous, and the average obtained can be considered representative (**Table 6**, column 8). Characteristic is low silica (43.3%) and alkali (12%) with high Al_2O_3 and CaO (17.5 and 13.4%, respectively). The average value of mafic index in the selection has turned out comparatively low (30%). The average value of mafic index in the selection has turned out comparatively low (30%). It is possible that, more objectively, mafic index of the original melt of these rocks as well as of the

Component	The main phase							
	Layered series							
	1	2	3	4	5	6	7	8
SiO_2	40.24	38.86	42.67	45.37	44.00	41.30	40.80	43.30
TiO_2	0.25	0.09	0.78	0.12	0.60	1.20	1.20	0.40
Al_2O_3	9.02	24.38	22.98	32.24	21.60	16.50	17.30	17.50
Fe_2O_3*	13.20	6.47	9.94	1.31	8.20	17.30	16.90	10.50
MnO	0.12	0.08	0.13	0.02	0.10	0.21	0.20	0.16
MgO	25.77	11.32	5.20	0.77	6.30	8.60	9.30	12.40
CaO	5.69	14.20	14.66	17.00	13.10	13.30	11.30	13.40
Na_2O	0.54	0.76	1.48	1.25	2.20	1.00	1.20	1.10
K_2O	0.04	n.d.	0.05	0.04	0.40	0.05	0.21	0.10
P_2O_5	0.03	0.01	0.05	0.01	0.03	0.03	0.03	0.04
LOI	5.66	3.38	2.03	1.68	3.18	0.69	2.00	1.00
Total	100.56	99.55	99.97	99.81	100.03			
Sr	167	312	355	472		258		271
Ca/Sr	238	319	289	252		362	—	352
F	20	22	49	46	39	50	48	30
n	1	1	1	1	1	4	2	5

Note. 1: Troctolite melanocratic, 2: troctolite leucocratic, 3: gabbroanorthosite, 4: anorthosite, 5: ophitic leucogabbro, 6: magnetite gabbronorites, 7: microferrogabbro, 8: olivine-amphibole gabbro.

Table 6. Chemical composition of the Svetlorechensky pluton rocks.

http://dx.doi.org/10.5772/intechopen.74994

whole LS reflects included in the selection Sample 644 (38%, collection of Zhulanova), which is a maximally homogeneous finely grained variation of olivine-amphibole gabbronorites. The LS differentiates, marginal in the mafic index value, are magnetite gabbronorites and microferrogabbro (in our analyses, 50 and 48%, respectively).

3.2.4. Discussion of nature

Empirical preconditions for choosing a theoretical model: The material presented above testifies to the fact that in each of the two internally heterogeneous basite associations, there are rocks that most completely characterize peculiarities of the parent melt. In the LS, these are, due to their weak differentiation, olivine-amphibole gabbronorites building comparatively small independent bodies (**Figure 2**). Among hornblende-rich gabbroids, amphibole microgabbronorites are the most interesting. Judging by their petrography (**Table 2**), they represent fast-crystallized facies, most precisely reflecting specificity of primary magmas. Peculiarities of structure and composition of pyroxene-amphibole gabbro were to a great extent determined by the impact of the fluid concentrated in the crystallization chamber with the melt solidification. It is even more obvious with amphibole and biotite-amphibole gabbro. The comparison of olivine-amphibole gabbronorites and amphibole microgabbronorites shows that they possess the features of both similarity and difference. It should be emphasized that their similarity is determined by the kinship of their parent magmas, while their differences are connected with different crystallization conditions. The entity of magmas, from which the LS rocks and hornblende-rich gabbroids were crystallized, is testified to by such peculiarities of chemical compositions of olivine-amphibole gabbronorites and amphibole microgabbronorites as stable low silica and alkali with large amounts of alumina and lime (**Tables 4**, **6**). The similarity of mineral parageneses also appears nonrandom. The base of both olivine-amphibole gabbronorites and amphibole microgabbronorites is high-calcium plagioclase, with which orthopyroxene and clinopyroxene as well as hornblende are associated. Olivine, typomorphic for the LS, acts as a nonequilibrium phase in olivine-amphibole gabbronorites. It is kept as relics armored by later dark-colored minerals, and is never observed contacting plagioclase in these rocks. The high share of hornblende in olivine-bearing gabbronorites should be specially emphasized. It usually dominates among dark-colored minerals and, besides, is collected in gabbro-pegmatite lodes.

Now, we will outline the most important differences between olivine-amphibole gabbronorites and amphibole microgabbronorites. First, they are detected in rock textures and structures. Olivine-amphibole gabbronorites, in most cases, are medium- to largely grained rocks with the gabbro structure, while amphibole microgabbronorites have the ophitic one. The main petrographic peculiarity of olivine-amphibole gabbronorites is a different position of magnetite in the general mineralization sequence: while in amphibole microgabbronorites, it appears the first, in olivine-amphibole gabbronorites, on the contrary, it completes magmatic crystallization. To estimate petrological similarity and difference between the two basite associations, in general, it is most efficient to compare the character of internal evolution of each. We should start with the fact that among hornblende-rich gabbroids, there are two independent intrusive phases distinguished from geological data: (1) amphibole microgabbronorites and pyroxene-amphibole gabbro and (2) amphibole and biotite-amphibole gabbro; both phases are accompanied by their acid differentiates (hypersthene tonalites and

amphibole plagiogranites, respectively). It is essential that amphibole plagiogranites act as geologically independent bodies. Their large lodes, unlike one order smaller veins of hypersthene tonalites, go far beyond the boundaries of their parent intrusions.

The LS exposes two differentiation levels. The first is the brightest, expressed in formation of banding within large unified geological bodies. The second level is represented by the severance of an autonomous lode facies from partly differentiated volumes of magma. However, inside the LS, no large independent phases of intrusion have been fixed; therefore, it appears correct to compare its evolution with that of just the first (main) phase of hornblende-rich gabbroids. In this case, the following differences seem most conspicuous: (1) direction of mafic index changes in the amphibole microgabbronorites-pyroxene-amphibole gabbro sequence, from the one hand, and within the LS, from the other hand (**Figure 5**); (2) spalling silica-enriched lode differentiates from amphibole gabbroids, while there is no such process in the LS.

The increase in general rock mafic index at the transition from olivine-amphibole gabbronorites to magnetite gabbronorites illustrates the most common trend of chemical differentiation of the LS. The same trend is clearly distinguished within the coarsely banded part of the series, as well, when comparing its two main variations: olivine-bearing (melanocratic and

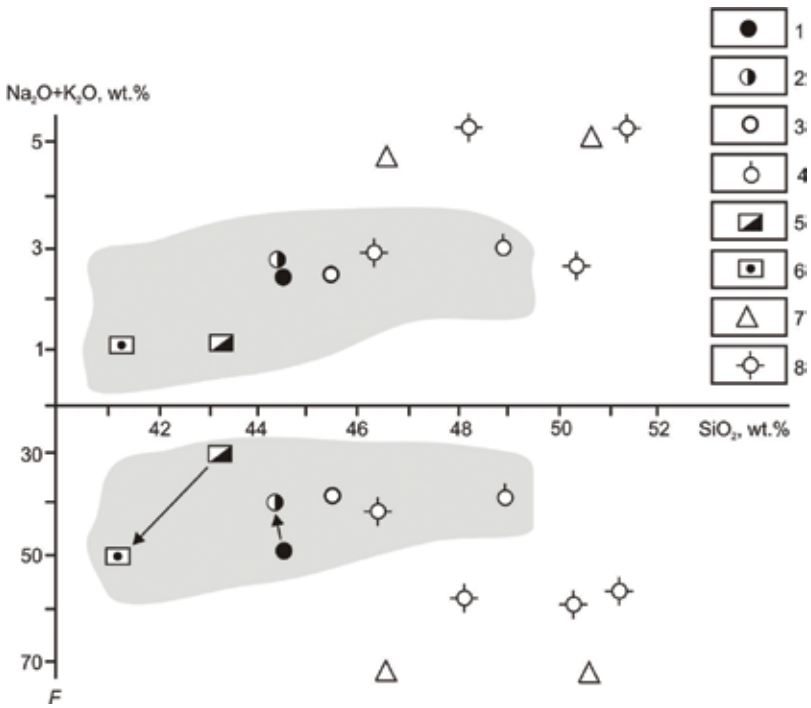

Figure 5. The SiO_2—($Na_2O + K_2O$) and SiO_2—*F* diagrams for the rocks of the Svetlorechensky complex and gabbroids of other age groups (according to **Tables 4**, **6** and [13]): 1–6—Svetlorechensky complex: 1—amphibole microgabbronorites, 2—pyroxene-amphibole gabbro, 3—amphibole gabbro, 4—biotite-amphibole gabbro, 5—olivine-amphibole gabbronorites, 6—magnetite gabbronorites; 7—pre-Cretaceous gabbronorites; 8—metadolerites of Early Cretaceous Poperechnynsky Complex. The arrows illustrate the opposite trends in the evolution of mafic index *F* in layered and marginal rock series of the main intrusive phase of the Svetlorechensky pluton. $F = Fe_2O_3^*/(Fe_2O_3^* + MgO + MnO)$, $Fe_2O_3^* = FeO + Fe_2O_3$ (as Fe_2O_3).

http://dx.doi.org/10.5772/intechopen.74994

leucocratic troctolites) and olivine-free (gabbroanorthosites, anorthosites) gabbroids (**Table 6**, columns 1–4). Highly ferruginous differentiates (magnetite gabbronorites, microferrogabbro) make one of lode branches of the LS. The second one is represented by ophitic leucogabbro. They are noticeably richer in alkali than all other rocks ($Na_2O + K_2O$ make 0.58–1.53 and 2.60%, respectively; **Table 6**), sometimes contain quartz, and, by these signs, might be considered a sort of homologs of quartz-bearing differentiates of the amphibole gabbroid group. However, by their silicic acid content, ophitic gabbro practically does not differ from anorthosites (in our analyses, 44.00 and 45.37%, respectively; **Table 6**, columns 5, 4), and by this parameter are not comparable to silicic lode derivatives of the first phase of amphibole gabbroids, quartz gabbronorites and hypersthene tonalities (53.9 and 68.3% SiO_2, respectively; **Table 4**, columns 5, 6). The analysis of differences in the direction of petrological evolution of the first phase of hornblende-rich amphibole gabbroids, from the one hand, and of the LS, on the other hand, served as a key to deciphering the essence of interrelation between two basite associations in the northern part of the Pekulney Ridge, which, finally, permitted to unite them within a unified magmatic complex. It was found that all exposed peculiarities of basites in the studied area, both similarities and differences, can be consistently correlated if interpreted in accordance with the latest theoretical views of the mechanist of forming layered intrusions.

On factors and conditions of magmatic layering phenomenon: For over a 100 years (since the first experiments of Bowen), layered intrusive massifs have served a basis for developing fundamental problems of magmatism and ore genesis. Widely discussed are the role of volatile components, liquation, assimilation, convection, and other processes in formation of magmatic stratification. Qualitative progress in understanding the mechanism of their development was accomplished due to involving the data on crystallization of metallurgic and petrurgic molds. Having generalized those, Sharkov offered the first model of layered intrusion based on the general consolidation theory [53]. Fundamental is the conclusion on the natural division of the liquor, filling the chamber of the future layered intrusion establishing, into two parts, marginal and interior, essentially different in temperature regimes; they are crystallized in principally different ways: the larger is the magmatic mass volume, the more conspicuous are the differences [54].

In *marginal* parts, consolidation occurs in the conditions of sharp supercooling. Since the temperature gradient vector is perpendicular to the heat emission surface, primary textures of marginal faces are conform to contacts. Due to sharp supercooling, in marginal zones, mineral parageneses of solidus are immediately formed. Spots with lowest temperatures may then have compositions identical to that of the parent liquor. Differences in temperature regimes of the subbottom, lateral, and upper endocontact zones determine certain differences in composition and structure of rocks building respective spots. Within bodies of lens- and blanket-like shape, the lateral series can be partly or completely reduced. Low-thickness bodies are totally crystallized according to the marginal series pattern. In *central* parts of large intrusions, separated by the marginal "crust" from cold enclosing rocks, crystallization occurs in conditions maximally close to the equilibrium. As a result, here the crystallization zone is formed: one part of it corresponds to the liquidus isotherm; another, that of solidus. At the crystallization front, highest temperature phases are distinguished. Depending on the density ratio, crystals may sink, remain suspended, or float up. The residual liquor systematically changes its

composition toward enrichment with easily fusible components. Correspondingly, the central series section, in general, reflects the succession of fractional crystallization of the parent liquor. Under the impact of the Earth gravity field, the crystallization front is always horizontally oriented, which determines autonomous inner structure of the intrusion marginal parts in respect to its marginal zones. Textures of the LS rocks are predetermined by the ratio of crystals and liquor density; structures, by interaction of minerals with the interstitial liquor.

For interpreting the nature of the Svetlorechensky pluton, the statement of mandatory presence of rapidly crystallized marginal facies in large layered bodies is of primary interest. This theoretically grounds the close spatial connection between the LS and hornblende-rich gabbroids that we established by geological mapping. The principal similarity of the North Pekulney LS with central series of classical layered intrusions is proved not only by direct structure-texture signs and commonness of chemical composition but also by the fact that minerals, which constitute the classic Bowen reaction succession, create the petrographic diversity of our LS. Of peculiarities of this LS, we should notice (1) leucocratic rocks domination, (2) extremely high plagioclase basicity in all differences, (3) small range of mafic index fluctuations in olivines and rhombic pyroxenes, (4) high-calc composition of clinopyroxene, (5) scarcity of ore minerals, and (6) no chromium in spinel. Ultrabasic members of the series, judging by their geological and petrographic characteristics, are products of the liquidus olivine accumulation in subbottom parts of the crystallization chamber. Specific characteristics of amphibole microgabbronorites are (1) finely grained structures, (2) trachytoid textures, (3) mutually parallel orientation of lens-like accumulation of hornblende and leucogabbro veinlets; this makes their outlook resemble that of granulites. All the abovementioned unequivocally indicates high velocity of crystallization of amphibole microgabbronorite parent liquor in physically, chemically, and mechanically anisotropic substance. From the viewpoint presented, one can logically explain not only all signs of petrochemical kinship between the LS and amphibole microgabbronorites but also all differences between them. Many peculiarities of the inner structure of the Svetlorechensky pluton point at the influence of the thermal shrinking process, whose role in the mechanism of layered plutons establishing is generally quite essential [55].

Uniting the LS and hornblende-rich gabbroids of the first phase into the unified Svetlorechensky pluton, based on Sharkov model [53, 54], permits to make conclusions on possible composition of the parent liquor. It is obvious that minimally differentiated, structurally homogeneous variations of marginal microgabbronorites, containing no large segregations of later hornblende, have closest similarities to the composition of the parent melt. In our collection, it is Sample 565б, characterizing the pluton marginal zone exposed to the north of the Raysky Creek (see **Figure 2**). In the selection of nine samples, characterizing amphibole microgabbronorites (**Table 4**, column 1), this rock represents the silica-richest variation. It contains 48.37%—SiO_2, 0.70%—TiO_2, 17.44%—Al_2O_3, 10.82%—(Fe_2O_3 + FeO) in the form of Fe_2O_3, 0.22%—MnO, 6.95%—MgO, 11.03%—CaO, 3.8%—Na_2O, 0.3%—K_2O, 0.09%—P_2O_5, and in these parameters corresponds to the typical basalt in the tholeiite series of island arcs [56].

Now, we will mark peculiarities that distinguish the Svetlorechensky pluton from classical layered intrusives localized in tectonically stable structures (ancient platforms, Precambrian shields) [54]. Petrologically, the most obvious difference is the wide development of hornblende-rich rocks in the Svetlorechensky pluton. They are systematically present within the

http://dx.doi.org/10.5772/intechopen.74994

LS, dominate among the marginal group formation, and, besides, build an additional intrusive phase of amphibole and biotite-amphibole gabbro. Abundance of hornblende indicates high content of volatile components in the liquor that generated Svetlorechensky pluton; this had been determined by the special geological and tectonic situation, in which the parent liquor was melted and crystallized (see below).

3.2.5. Timing of magmatism

The principal difficulty of geologically dating the Svetlorechensky gabbro complex is connected with low probability of relations between magmatic rocks and surrounding sedimentary-volcanogenic masses, not violated by faults. This, in its turn, is explained by deep erosion of the Svetlorechensky pluton in the course of great neotectonic uplift of the axis part of the ridge. Even purposefully studying contact zones, we managed to observe active relations with Barrias-Valanginian (the Tithonian-Valanginian Gruntovsky Strata [14]) only in amphibole gabbro of the additional intrusive phase (**Figure 2**). The most petrographically perfect (indisputable) hornfels, not only in aleurolites but also in basalts, have been revealed in bedrock exposures in the bottom of the trough valley of the Pekulneyveem River, at the place where it leaves the mountains. The undisturbed active contact of amphibole gabbro with enclosing deposits on this very site is causally associated with peculiarities of its position in the current structure of the Svetlorechensky pluton. The Pekulneyveem River valley is an independent narrow block, vertically taking the intermediate position between the two blocks: the northern (higher elevated) and the southern, relatively subsided (**Figure 2**). Due to a favorable combination of faults of different ages, along the youngest of which the river bed had formed with time, in the bottom of its valley, plowed by a glacier, a good intrusive contact between amphibole gabbro and Gruntovsky Strata deposits has remained.

Exposures of rocks of the LS, building the deep part of the Svetlorechensky pluton, are all along bordered by faults. However, it is characteristic that they are systematically associated by small blocks of layered metamorphic rocks. It was them, that were described as hornfels by the Pekulneyveemskaya Suite, then dated by Valanginian [4]. Our data show that these formations refer to a lower structural level than Bajocian-Hauterivian deposits in their current understanding (Pekulneyveemskaya Suite and Gruntovsky Strata [14]). Compositions of metamorphic formations are different on the eastern and the western slope (**Figure 1**). On the eastern slope, at the foot of the ridge, near Sbornoye Lake, a block built by the parametamorphic thick is mapped. At the bottom of the thick, finely grained heteroblastic garnet-biotite-hypersthene gneisses prevail, while in its upper part, garnet-sericite-graphite microschists dominate. On the western slope of the ridge, in the block to the south of the Yuzhnyy Chekogytgyn Lakes, fragments of high-temperature metamorphic complex, presented by apoterrigenous-volcanogenic schists, amphibolites, and gneisses, have been exposed. Amphibolites, with their characteristically systematic admixture in the primary paragenesis of biotite, preserve clear signs of forming due to the bedded volcanogenic formation, including bedding and crosscutting bodies of isofacially metamorphized gabbroids. In the amphibolite mass, all stages of granitization (debasification) with plagiogranitogness formation are traced. Among dark-colored minerals, in plagiogneisses, along with green hornblende of the replaced (granitized) substrate, cummingtonite is systematically present. In finely grained amphibolites, unique centimeter anatectite “nests” of zonal

structure occur, built from biotite-hypersthene plagiogneisses, where Plagioclase 64 contains 1.56% K_2O (charnokitoid trend of anatexis) ([47], Figure 59). On FGM-200/2 metasedimentary, partly metavolcanogenic, comparatively weakly altered formations are distinguished as the supposedly Middle Paleozoic Pekulneygytgyn Strata (assumedly corresponds the Middle-Upper Paleozoic-Early Mesozoic Strata, first described in [6]). Briefly outline above, high-temperature (amphibolite and granulite facies) aposedimentary and apobasalt metamorphic rocks, associated with the LS gabbroids, are referred to the conventionally Paleozoic Sbornensky Strata [14]. Metamorphic formations are intruded by sills and dykes of gabbronorites, diabases, plagiogranites, among which pre- and postmetamorphics are distinguished. On the eastern slope of the ridge, where parametamorphic rocks always contact with the LS gabbroids, both in gneisses and in intrusive bodies (including diabases identical to those of Early Cretaceous), crosscutting them, clear signs of hornfelsing by LS gabbro have been revealed. The only reliable data on the upper age border of the Svetlorechensky pluton are given by biotite plagiogranites, cutting through them: all researchers unanimously refer them to the Early Cretaceous Yanranaysky complex (**Figures 1**, **2**). To the north of Lake Pekulneygytgyn, biotite plagiogranites cut through the LS (**Figure 1**). Besides, the Yaranay complex granitoids are interesting for numerous xenoliths of basic rocks and act as their inseparable attribute (typomorphous peculiarity). Our collection contains amphibole and biotite-amphibole hornfels by volcanogenic rocks, amphibolites identical to the Sbornensky mass rocks, finely grained two-pyroxene basites—most probably, "pre-Svetlorechensky."

In the area of the Pekulney Ridge, to the south of 66°00′ N (conventional border between geologically different southern and eastern parts of the ridge, corresponding the border of FGM-200—see above), the total area of the Svetlorechensky complex rocks is estimated approximately 35 km^2 (**Figure 3**) [14]. It has been established that on the western boundary of the Pravoberezhny intrusion, on a site about 3 km long, the contact of gabbro with terrigenous-volcanogenic deposits of the Tithonian-Valanginian Gruntovsky Strata has the intrusive nature. It is expressed by the hornfelsing zone, top tens of meters thick. In its northern part, the Pravoberezhny intrusion is cut through by an intrusion of the Yanranaysky complex plagiogranites; at the contact with the intrusion, gabbro had been brecciated and overlappingly amphibolized [14]. The age of the Svetlorechensky gabbro complex on FGM-200/2 sheets has been accepted as Valanginian, with a reference to the combination of geological and geochronometric data [14]. They are critically discussed below (Part 4), with all other materials that permit to estimate the time of the Pekulney Ridge basalts formation with maximum correctness, from today's viewpoint. Obviously, without it, any advance in geological, tectonic, and geodynamical discussion on the issue would be impossible.

4. Svetlorechensky gabbro complex as a geodynamical indicator

Reconstruction of the Inner Structure of the Svetlorechensky Layered Pluton: The offered pattern of the inner structure of the Svetlorechensky pluton (**Figure 6**) is a "composite construction" with all elements observed on the contemporary erosional section of the ridge but in an offset position. The Pekulney Ridge belongs to the category of young mountain structures, where relief forms directly depend on the amplitude of the Earth crust uplift, which, as a rule, is inherited. The researched part of the ridge, located between the upper Bychya River and the

http://dx.doi.org/10.5772/intechopen.74994

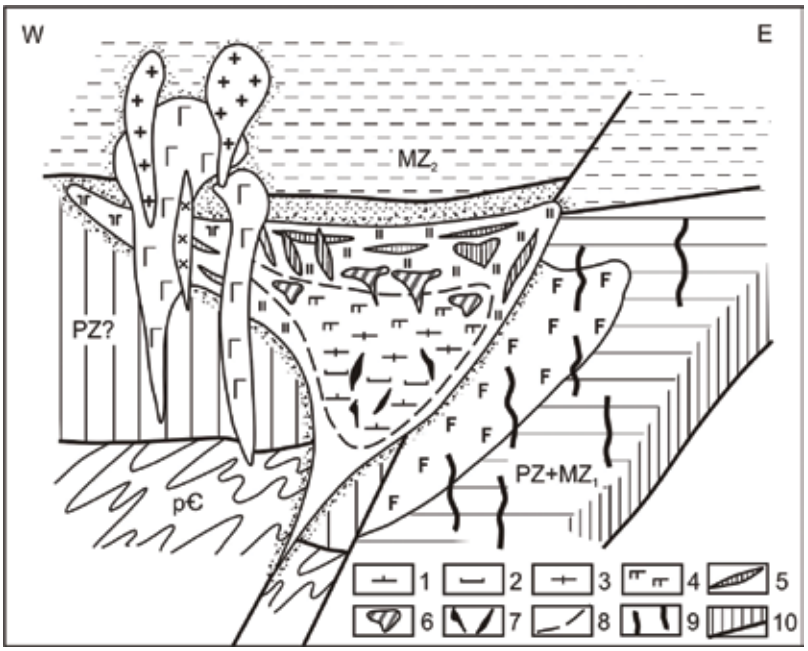

Figure 6. Reconstruction scheme of the internal structure of the Svetlorechensky layered pluton (at the latitude of the Pekulneyveem River): 1–7—stratified series: 1—plagioclase peridotites, melanocratic troctolites, 2—leucocratic troctolites, olivine gabbro, 3—gabbroanorthosites, anorthosites, 4—amphibole-olivine gabbronorites, 5–7—vein facies of a stratified series: 5—olivine-amphibole gabbronorites, 6—ophitic leucogabbro, 7—magnetite gabbronorites and microferrogabro; 8—boundary between stratified and edge series; 9—dykes and small intrusions of the Ostrozubsky and the Poperechninsky complexes; 10—general inclined fault. See **Figure 2** for the remaining symbols. Explanations are in the text.

through valley, housing the South Chekogytgyn Lakes (**Figures 1**, **3**), is the most uplifted and dissected fragment of the ridge. In its turn, it is longitudinally asymmetric: its eastern half is noticeably more uplifted than the western one. It was this fact that permitted to assume already on the first stage of the research that the successive replacement of hornblende-rich gabbro by the LS, observed on the right bank of the Pekulneyveem River from the west to the east (**Figure 2**), characterizes pluton sections differing in depth. Henceforth, a solid pro for such interpretation was the data of the parametamorphic rocks (lower parts of the conventionally Paleozoic Sbornensky Strata [14]) systematically attached to the LS.

The next item that requires a comment is the general asymmetry of the Svetlorechensky pluton. Geological mapping has established that the layered section rocks are always located more to the north than hornblende-rich gabbroids. Only on the western slope, amphibole and biotite-amphibole gabbro are observed, building the additional intrusive phase bodies and amphibole plagiogranite lodes. Only in the western part of the ridge are outcrops of granitized apoterrigenous-volcanogenic amphibolites (upper part of the Sbornensky Strata) known. In the north of the area, they build a large block cut through by small bodies of the additional phase amphibole gabbro (**Figure 1**); in the south, by xenoliths in the Yanranaysky granitoid complex.

We assume that the eastern contact of the Svetlorechensky pluton subsides to the west, and that such body morphology fixes the principal position of the canal (fault system), along which the magma of the main intrusive phase had intruded. In this case, the formation of

large volumes of layered gabbroids at the eastern edge of the pluton establishing chamber would be explained by the fact that here, due to the heat flow along the faults, the liquor was crystallized slowly, in the conditions close to the equilibrium, which is the main factor causing layering [54]. The pluton western part, built from finely grained marginal facies, appears a lopolith-like "tongue," extending rather far from the main chamber into enclosing rocks. Subhorizontal location of this part of the massif is directly witnessed by the dominating gentle sloping of such inner elements as the system of hypersthene tonalite lodes, leucogabbro veinlets, hornblende bands in amphibole microgabbronorites. Our data imply that the vertical thickness of gabbroids of the Svetlorechensky pluton marginal series in the western part of the ridge is not large. The most unbalanced facies of the Svetlorechensky gabbro complex (amphibole microgabbronorites with banded texture) are clearly drawn to the lowest hypsometric relief level, above which they transfer to much better crystallized pyroxene-amphibole gabbro. Such correlations can be explained only by the fact that in this part of the ridge, amphibole microgabbronorites build the lower endocontact.

The bottom of the body of the first-phase hornblende-rich gabbro (marginal series) is built from metamorphized basic rocks. Most completely, the bottom of the marginal series gabbroids is characterized by granitized amphibolites, building the block to the south of the Yuzhnyy Chekogytgyn Lakes. Granitization of amphibolites indicates that in the period of metamorphism, these rocks were in the uplifted (hanging) wing of the fault zone, where decompression and free fluid influx took place. Parametamorphic rocks (lower part of the Sbornenskaya Strata), spatially attached to the LS, on the contrary, correspond recrystallization products under higher general pressure by all petrological characteristics. This embarrassed melting but promoted crystallization of barophilic garnet, which is quite rare for the rocks in the northern part of the Pekulney Ridge. This kind of situation is well conformed with geologic and tectonic conditions in the lying wing of the inclined fault zone. The deep melting spot that had produced the Svetlorechensky complex was to the west relative to the crystallization chamber of the LS and connected to it with an inclined conduit while the additional phase was injected by later vertical faults. Only this can explain the spatial separation of the additional phase intrusions and the LS.

Manifestations of "pre-Svetlorechensky" magmatism are fixed to the east of the system faults bordering outcrops of the LS rocks (**Figure 2**). On FGM-200/2 sheets, they are distinguished into the Mid-Jurassic-Early Cretaceous Ostrozubsky complex, uniting bosses and dykes of metadolerites with fissure intrusions of plagiogranites (**Figure 3**); also, the Poperechninsky complex of contiguous dykes of gabbro-metadolerites-plagiogranite-porphyries, assumedly cutting through the Svetlorechensky complex gabbroids and the Yanranaysky plagiogranites and, thus, dated by the Valanginian [14]. According to our data, neither smaller bodies of the Ostrozubsky complex nor variegated Poperechninsky dykes penetrate Svetlorechensky gabbroids. Misunderstanding here originates from yet another complex of layered gabbroids, older than Ostrozubsky metadolerites (diabases) and fragmentally present in the structure of the eastern slope of the ridge. We first distinguished them on the eastern slope of the ridge to the south of Lake Romb and described them as uralitized gabbro [13]. Mapping showed that uralitized gabbro are widespread in the area as enclosing rock relics (screens) for most of genuine "parallel" dykes (**Figure 2**). The age of uralitized gabbro was originally defined as pre-Cretaceous [13]. At present, we should consider the results of SHRIMP-dating zircons from plagiogranites, which, judging by their description, refer to the Ostrozubsky metadolerite-plagiogranite complex. Zircon dates fall in two domains: Triassic (with individual Late

http://dx.doi.org/10.5772/intechopen.74994

Permian and Early Jurassic values) and Neoproterozoic-Early Paleozoic [43]. The data on relatively old layered gabbroids (uralitized gabbro complex), present on the eastern slope of the Pekulney Ridge, were a basis for reconstructing the assumed structure of the lying side of the fault-closing tectonic structure enclosing the Svetlorechensky pluton (**Figure 6**).

Thus, the materials in total permit to interpret the Svetlorechensky pluton as a highly asymmetric harpolith localized in the hanging wing of the long-developed horst-anticlinorium. The crystallization chamber must have been located in the presumably Paleozoic basement. The unconformity surface in its sole might have worked as a mechanic and thermal screen, which provided volatiles accumulation at the upper edge of the chamber and slowed its central parts cooling.

On the geodynamic nature of the Svetlorechensky gabbro complex: Materials of our Pekulney Ridge research were broadly discussed in the interested professional community. Our conclusion that there are no outcrops of Archean "granulite-basites," identical to the oldest complexes in the crystalline basement of the Siberian Platform and Omolon Massif, raised no objection. As to the Early Cretaceous age of all gabbroid variations, presented in the northern part of the ridge, at that time, this opinion was not taken unanimously. The discussion on the possibility of extrapolating our data on Early Cretaceous deposits hornfelsing by amphibole gabbro of the Svetlorechensky pluton additional phase has been completed by the results of new works in the southern part of the Pekulney Ridge [14]. These facts are more than enough to see that the whole volume of the Svetlorechensky gabbro complex had formed in the interval between the accumulation of deposits of the Tithonian-Valanginian Gruntovskaya Strata and the invasion of granitoid intrusions of the Early Cretaceous Yanranaysky complex. Today's isotopic dating results unequivocally confirm the Early Cretaceous establishing of the Svetlorechensky complex. Three quantitative $^{40}Ar/^{39}Ar$ dates of amphibole from the Svetlorechensky complex rocks [44] appear equally important. Two samples characterize the main (layered) phase; one more, the additional. The plateau calculation showed the same age, consistent with the Hauterivian and Barremian border by the International Chart (about 129.4 Ma). Thus, this result completely correlates with the conclusion made on a purely geological basis. It is especially interesting for the purpose of interpreting the geodynamical nature of the Svetlorechensky gabbro complex.

The Hauterivian age is brightly distinguished by the manifestation of facially varied basite-ultrabasite magmatism. The paleontologically characterized (remains of ammonites) Hauterivian mass (lavas, hyaloclastites, tuffs of picrites, picrobasalts, basalts; at the top, thin interbeds of tuffaceous-sedimentary rocks, limestones, ash tuffs of rhyolites) is a component of the Ostantsovogorsky volcanic-plutonic association. The latter unites two complexes of the same name: picrite-basalt-metadolerite and peridotite-gabbro-metadolerite. [14]. The comprehensive research of the rare variation of the Svetlorechensky pluton rocks, orbicular allivalite, resulted in a series of petrological arguments for the genetic kinship of the Svetlorechensky pluton and Hauterivian basite-ultrabasites in the southern part of the Pekulney Ridge, offered by Gelman (1930–2017), a prominent expert in magmatism and metamorphism of Russia's North-East. In the then absence of data on intrusions of the Svetlorechensky gabbro complex of the ridge southern part, Gelman assumed that the Svetlorechensky pluton was an intrusive analog to the picrite-basalt association, whose development band seems to continue gabbroid outcrops to the south [1]. The current picture of spatial relations between intrusives of the Svetlorechensky and of both Ostantsovogorsky complexes looks somewhat different at the first glance (**Figure 3**), but in fact does not contradict

the described model. Mapping showed that the absence of near-surface basite-ultrabasites in the northern part of the Pekulney Ridge is determined by its intensive neotectonic uplift.

The inner structure reconstruction for the Svetlorechensky pluton (**Figure 6**) permitted to conclude that its establishment took place in the hanging wing of a long-developed anticlinorium. Here, the beginning of basalt magmatism is fixed by small metamorphized bedded bodies of gabbronorites localized in the lower parts of the conventionally Paleozoic, possibly older (particularly Precambrian, considering the latest zirconometric data [43]) paragneiss-amphibolite Sbornensky Strata. In the actualistic view, the reconstructed structure can be interpreted as an island arc uplift. However, the question of the time of its appearance is still open. The problem of relations of the complexes building the western and the eastern slopes of the ridge also seems debatable. Their interpretation as autochthon and allochthon, respectively and widely acknowledged, is far from indisputable. The thick tectonic suture of the northeastern extent, dividing structures of the western and the eastern slope, comprehensively researched, turned out to be not serpentinite mélange marking the fault sole [5] but the zone controlling the Hauterivian basite-ultrabasite magmatism. According to our data, in the current structure, this suture is reconstructed as a large and, probably, sufficiently old shift, dislocated in the course of later tectonic movements. In the preserved pull-apart structures, there are erratic blocks of deep complexes on the current erosion section, including, according to our observations [10], fragments of at least three geologically independent complexes: (1) deep-seated magmatic ultramafics, uniting the magnesia-calcium (dunites, wehrlites, and clinopyroxenites) and the aluminous-ferruginous (garnet-spinel clinopyroxenites, containing orthopyroxene, pargasite, and magnetite) series; (2) fragments of the frame of aluminous-ferruginous ultramafics, represented by texturally heterogeneous eclogite-like feldspar-free hornblende-rich rocks (stratigraphically equivalent to Lower Archean amphibole eclogites of the Omolon Massif basement [47]); (3) structurally and facially various diaphthorites by rocks of the regional metamorphism granulite facies, analogous to supracrustal Lower Archean formations building the crystalline basement offsets in Verkchoyansk-Chukotka Mesozoides. The purposeful study of garnet-spinel clinopyroxenites, participating in building ultramafic massifs in the southern part of the Pekulney Ridge (Middle Jurassic-Early Cretaceous Pekulneysky dunite-peridotite-gabbro complex [14]), would greatly contribute to developing the geological aspect of the nature of the Svetlorechensky layered gabbroids. By their chemical composition (low SiO_2, high Al_2O_3 and MgO), those feldspar-free rocks with clear signs of magmatic crystallization are analogous to leucocratic troctolites of the Svetlorechensky pluton [10]. It is natural to assume that they represent the deepest seated facies of the Svetlorechensky gabbro complex.

5. Conclusions

1. The study of the northern part of the Pekulney Ridge started with the aim to identify finely grained thin-banded amphibole-two-pyroxene rocks in the Pekulneyveem River basin with Archean crystalline schists of the analogous mineral composition, brought the author to an absolutely different range of problems. Our research showed that the rocks of disputable genesis are amphibole microgabbronorites included in the composition of a large intrusive massif. It belongs to a special type, never distinguished in the region before, which has features of layered plutons and multiphase intrusions. The first (main) phase

consists of two different facies, the marginal and the layered; externally, they are sharply different. Amphibole microgabbronorites, whose nature served as a subject for discussion, are a typical component of the marginal series. Their petrographic peculiarities that make them externally similar to amphibole-two-pyroxene crystalline schists are determined by the high velocity of crystallization in the anisotropic substance of the intrusive chamber exterior. The main volume of the intrusive is the layered series differentiated from plagioclase peridotites and troctolites to olivine-amphibole gabbronorites. According to the data obtained, the parent magmatic melt was alumina-rich and alkali-poor. By the principal parameters of its chemical composition, it corresponds to the typical basalt of the tholeiite series of island arcs. The second (additional) intrusive phase is built by amphibole and biotite-amphibole gabbro. It is accompanied by a vein series of amphibole plagiogranites.

2. The researched intrusion was named the Svetlorechensky-layered pluton and is considered a petrotype of the intrusive gabbro complex of the same name. The pluton area exposed on its current section is no less than 200 km^2. By the present, the Svetlorechensky gabbro complex intrusions have been also mapped on the eastern slope of the southern part of the ridge, but here they are significantly smaller in size. Critical consideration of geological and geochronological data available today permits to conclude that the most probable time of establishing the Svetlorechensky gabbro complex was the Hauterivian. Some petrological and geological indicators support the previously published hypothesis of genetic kinship of the Svetlorechensky gabbro complex with the Ostantsovogorsky volcanic-plutonic basite-ultrabasite association, whose Hauterivian age has been paleontologically confirmed.

3. The deep structure reconstruction of the Svetlorechensky layered pluton, based on geological mapping materials, permitted to interpret it as a heavily asymmetric harpolith localized in the hanging side of a long-developed horst-anticlinorium (ancient island arc uplift). The determinant of its evolution was the system of long-lasting deep faults inclined under the Paleoasian Continent[1].

Author details

Irina L'vovna Zhulanova

Address all correspondence to: metamor@neisri.ru

North-East Interdisciplinary Scientific Research Institute of Far East Branch of the Russian Academy of Sciences (NEISRI FEB RAS), Magadan, Russia

References

[1] Gel'man ML. Orbicular allivalite from the Pekulney Ridge: Comparisons and issues of origin. Magadan: SVKNII; 1991. 107 p (Dep. in VINITI on 28.11.91, No. 4443-B91)

[1] All references are in Russian, except for [5, 8, 20, 22, 24, 25, 28, 31, 33, 36, 41–44, 49, 51, 57].

[2] State Geological Map of the USSR. 1:1,000,000. In: Titov VA, editor. Sheet Q-60 (Anadyr). Leningrad: VSEGEI; 1961 [In Russian]

[3] State Geological Map of the USSR. 1:200,000. In: Kaygorodtcev GG, editor. Anadyr Series. Sheet Q-60-XIX. Leningrad: VSEGEI; 1963

[4] State Geological Map of the USSR. 1:200,000. In: Kaygorodtcev GG, editor. Anadyr Series. Sheets Q-60-XIII, XIV. Leningrad: VSEGEI; 1964

[5] Nekrasov GE. New data on tectonic structure of Pekulney Ridge (left bank area of the Anadyr River). Doklady Akademii Nauk SSSR. 1978;**238**:1433-1436

[6] Markov MS, Nekrasov GE. Ophiolites of the rift zones of the ancient continental crust (Pekulney Ridge, Chukotka). In: Pushcharovsky YM, Janshin AL, editors. Tectonic Development of the Earth's Crust and Faults. Moscow: Nauka; 1979. pp. 81-93

[7] Markov MS, Nekrasov GE, Palandzhjan SA. Ophiolites and melanocratic basement of the Koryak Upland. In: Pushcharovsky YM, Tilman SM, editors. Notes on the Tectonic of the Koryak Upland. Moscow: Nauka; 1982. pp. 30-70

[8] Palandzhjan SA. Ophiolite belts in the Koryak Upland, Northeast Asia. Tectonophysics. 1986;**127**:341-460

[9] Zhulanova IL. Interconnection of tholeiitic and calc-alkaline magmatism at the boundary of the Inner and Outer Zones of the Pacific Belt [thesis]. Khabarovsk: Institute of Tectonics and Geophysics of Far Eastern Scientific Center of the Academy of Sciences of the USSR. 1986

[10] Zhulanova IL, Pertsev AN. On the heterogeneity of mafic-ultramafic massifs of the Pekulney Rindge (the Anadyr-Koryak Folded System). Zapisky WMO. 1988;**117**:276-293

[11] Pertsev AN. Magmatic differentiation, metamorphism and clinopyroxene-garnet associations in the deep ultramafic rocks of the Pekulney Ridge (Chukotka). Izvestya VUZov: Geologya i razvedka. 1997;**7**:36-41 (8:36-43)

[12] Shul'diner VI. Precambrian Basement of the Pacific Belt and framing platforms. Moscow: Nedra; 1982. 226 p

[13] Zhulanova IL, Pertsev AN. Basic rocks from the northern part of Pekulney Ridge: geology, petrologic features and the problem of origin. Tikhookeanskaya Geologiya. 1987;**3**:65-76

[14] State Geological Map of the Russian Federation (Second Generation). 1:200,000. In: Markovsky BA, editor. Koryak Series. Sheets Q-60-III, Q-60-XIX. St. Petersburg: VSEGEI; 2009

[15] Polevoy PI. The Anadyr region. Part I. The principal results of the Anadyr expedition. Proceedings of the Geological Committee. New episode. Issue 140. Petrograd, 1915. 138 p. With 11 plates and 2 maps. (Summary in English: 116-132)

[16] Polevoy PI. In: Orlov VP, editor. Repressed Geologists. Moscow–St. Petersburg: VSEGEI; 1999. pp. 248-249

[17] Chekhov AD. To the sources of knowledge of the Far East Asia geology. In: Proceedings of the Scientific-Practical Conference "4th Dikov Readings"; Mar 22-24, 2006; Magadan. Magadan: Svknii Dvo Ran; 2006. pp. 39-43

[18] Kaygorodtcev GG. The ophiolitic formations of the Pekulney Ridge. In: Drabkin IE, editor. Materials on Geology and Mineral Resources of the Northeast the USSR. Magadan; SVGU; 1961. pp. 93-104

[19] Kaygorodtcev GG. On the discovery of eclogite-like rocks in the Pekulney Ridge (the Anadyr River basin). Geologya i Geofizika. 1966;**4**:140-143

[20] Pinus GV, Agafonov LV, Velinsky VV. Eclogite-like rocks of the Anadyr-Koryak folded-eded system. Pacific Geology. 1970;**2**:81-91

[21] Chekhov AD. Tectonic Evolution of Northeastern Asia (Marginal-Sea Model). Moskow: Nauchny Mir; 2000. 204 p

[22] Peive AV. Ophiolites in the structure of the Earth'h crust [thesis]. Moscow: Subcomission for International Tectomic Map of the World; 1973. pp. 121-123

[23] Markov MS. Metamorphic Complexes and the "Basaltic" Layer of the Earth Crust in Island Arcs. Moscow: Nauka; 1975. 232 p

[24] Nekrasov GE. Types of ophiolites and lateral heterogeneities of the mantle and crust of the Penzhina–Anadyr region. Doklady Akademii Nauk SSSR. 1980;**250**:679-683

[25] Zimin SS, Yusim EI, Granovsky AG, Shcheka ZA. Meimechite-picrite, gabbro-diabase and picrite-diabase complexes of the Pekulney Ridge in the Northeast of the USSR. Doklady Akademii Nauk SSSR. 1979;**249**:954-957

[26] Markovsky BA, Bogdanov GV. The province of the ultramafic volcanics of the Pekulney Ridge (the Northeastern USSR). Sovetskaia Geologia. 1985;**6**:117-126

[27] Zonenshain LP, Kuzmin MI, Moralev VM. Global Tectonics, Magmatism and Metallogeny. Moscow: Nedra; 1976. 232 p

[28] Zonenshain LP, Savostin LA, Baranov BV. Plate boundaries of the USSR. Episodies. 1984;**7**:43

[29] Lev Pavlovich Zonenshain. Essays. Memories. Moscow: Nedra; 1995. 350 p

[30] Morozov OL. Geological Structure and Tectonic Evolution of Central Chukotka. Moscow: GEOS; 2001. 201 p

[31] Nekrasov GE, Liapunov SM. Melanocratic basement of the Pekulney Ridge (Chukotka) and the directivity of evolution of the Pacific-Ocean Northwest framing lithosphere paleoceanic zones. Doklady Akademii Nauk SSSR. 1987;**297**:162-166

[32] Nekrasov GE, Sumin LV. The melanocratic basement of the Pekulney Ridge and its Pb–Pb isotopic age. In: Pushcharovsky YM, editor. Essays on the Geology of the Northwestern Sector of the Pacific Tectonic Belt. Moscow: Nauka; 1987. pp. 183-199

[33] Gladenkov YuB, Oleynikov AN, Rrozorovskaya EL, Rozanov AYu, Shick SM, Zhamoida AI, editors. Stratigraphic Code of Russia. 3rd ed., 2006. St. Petersburg: VSEGEI Press; 2012. 48 p

[34] Petrographic Code of Russia. Magmatic, Metamorphic, Metasomatic, Impact Rock-Assemblages. 2nd ed. St. Petersburg: VSEGEI Press; 2008. 200 p

[35] Zhulanova IL. Ancient metamorphic rocks associated with ultramafic bodies in the ophiolite belts of the Pekulney Ridge and the Taygonos Peninsula (Northeastern Russia). In: Proceedings of the International Scientific Conference "Metamorphism and geodynamics"; Feb 16-17, 2006; Ekaterinburg. Ekaterinburg: IGG UrO RAN; 2006. pp. 29-32

[36] Nekrasov GE, Zhuravlev DZ. Sm-Nd isotope system in the lower crustal rocks of the southern Pekul'ney Ridge (Late Mesozoides of Chukotka). Doklady Earth Sciences. 2000;**372**:732-736

[37] Nekrasov GE. Crust – mantle boundary complexes of the continental and transitional structures and some questions of the continental lithosphere vertical accretion. In: Leonov MG, editor. Vertical Accretion of the Earth Crust. Factors and Mechanisms. Nauka: Moscow; 2002. pp. 237-267

[38] Nekrasov GE. Pekulney Ridge Phanerozoic granulites. In: Proceedings of the 2nd Russian Conference on Precambrian Geology and Geodynamics "Granulite complexes in the Precambrian and Phanerozoic geology development"; Oct 2-4, 2007; St. Petersburg. St. Petersburg: IGGD RAN; 2007. pp. 231-235

[39] Ledneva GV, Bazylev BA, Kononkova NN, Ishiwatari A. Ultramafic and mafic rocks in the Pekulney complex (Chukotka): high-pressure island-arc cumulates. In: Proceedings of the 3rd International Conference "Mafic–Ultramafic Complexes of Foldeded Regions and Related Deposits"; Aug 28–Sep 2, 2009; Kachkanar. Vol. 2. Ekaterinburg: IGG UrO RAN; 2009. pp. 17-20

[40] Nekrasov GE. The Pekulney ultramafic-mafic-granulite complex (Chukotka) as a fragment of mantle–crust transition in a rift zone of continental margin. In: Proceedings of the 3rd International Conference "Mafic–Ultramafic Complexes of Foldeded Regions and Related Deposits"; Aug 28–Sep 2, 2009; Kachkanar. Vol. 2. Ekaterinburg: IGG UrO RAN; 2009. pp. 72-76

[41] Bazylev BA, Ledneva GV, Kononkova NN, Ishiwatari A. High-pressure ultramafics in the lower crustal rocks of the Pekul'ney complex, Central Chukchi Peninsula. 1. Petrography and mineralogy. Petrology. 2013;**21**:221-248. DOI: 10.1134/S0869591113030028

[42] Bazylev BA, Ledneva GV, Ishiwatari A. High-pressure ultramafics in the lower crustal rocks of the Pekul'ney complex, Central Chukchi Peninsula. 2. Internal structure of blocks and ultramafic bodies, geologic and geodynamic setting of rock formation. Petrology. 2013;**21**:336-350. DOI: 10.1134/S0869591113040024

[43] Palandzhyan SA, Hayasaka I. New data on Early Mesozoic magmatism in the Pekulnei-Zologorsk island arc system (far Northeastern Asia): SHRIMP U–Pb zircon dating of the Pekulnei Ridge plagiogranite. Doklady Earth Sciences. 2015;**464**:894-897. DOI: 10.1134/S1028334X15090068

[44] Palandzhyan SA, Layer PW, Patton JWW, Khanchuk AI. Geodynamic interpretation of the $^{40}Ar/^{39}Ar$ dating of ophiolitic and arc-related mafics and metamafics of the northern part of the Anagyr-Koryak Region. Geotectonics. 2011;**45**:481-495

[45] Nekrasov GE. A new geodynamic model of the Anadyr Region of the Koryak-Kamchatka Foldeded Area. In: Proceedings of the XLIII Tectonic Meeting "Tectonics and geodynamics of folded belts and Phanerozoic platforms"; Feb 2-5, 2010; Moscow. Vol. 2. Moscow: GEOS; 2010. pp. 85-89

[46] Nekrasov GE. Transform-shear (alternative collisional) model of the Verkhoyansk-Chukchi Mesozoides tectonics. In: Proceedings of the XLIX Tectonic Meeting "Tectonics of modern and ancient oceans and their margins" Jan 31–Feb 4, 2017; Moscow. Vol. 2. Moscow: GEOS; 2017. pp. 33-36

[47] Zhulanova IL. The Earth's crust of the Northeastern Asia in the Precambrian and Phanerozoic. Moscow: Nauka; 1990. 304 p

[48] Osborn EF. Role of oxygen pressure in the crystallization and differentiation of the basaltic magma. American Journal of Science. 1959;**257**:609-647

[49] Akinin VV, Zhulanova IL. Age and geochemistry of zircon from the oldest metamorphic rocks of the Omolon Massif (Northeast Russia). Geochemistry International. 2016;**54**:651-659. DOI: 10.1134/S0016702916060021

[50] Pattison DRM. Petrogenetic significance of orthopyroxene-free garnet + clinopyroxene + plagioclase ± quarts-bearing metabasides with respect to the amphibolite and granulite facies. Journal of Metamorphic Geology. 2003;**21**:21-34. DOI: 10.1046/j.1525-1314.2003.00415.x

[51] Kuznetsov PP, Simonov VA. Ophiolites and Rifts. Novosibirsk: Nauka; 1988. 150 p

[52] Simonov VA. Petrogenesis of Ophiolites (Thermobarogeochemical Investigations). Novo sibirsk: Nauka; 1993. 247 p

[53] Sharkov EV. Petrology of Layered Intrusions. Leningrad: Nauka; 1980. 184 p

[54] Sharkov EV. Formation of Layered Intrusions and Their Mineralization. Moscow: Nauchnyi Mir; 2006. 368 p

[55] Osipov MA. Formation of Layered Plutons from Positions of Heat Shrinkage. Moscow: Nauka; 1982. 100 p

[56] Kuno H. High-alumina basalt. Journal of Petrology. 1960;**1**:121-145

Section 3

Theoretical Aspects and Numerical Modeling of Volcanoes

Chapter 7

Dynamics of Convective Heat and Mass Transfer in Permeable Parts of Seismofocal Zones of the Kamchatka Region and Conjugated Volcanic Arcs

Yury Perepechko, Victor Sharapov,
Konstantin Sorokin and Anna Mikheeva

Additional information is available at the end of the chapter

http://dx.doi.org/10.5772/intechopen.73225

Abstract

This chapter considers the dynamics of convective heating of mantle and crustal rocks in the seismic focal zone of Kamchatka region and associated volcanic arcs, which are characterized by the predominance of compressive stresses and the compaction of the heterophase medium. Features of heating, determining the dynamics of metasomatic transformations and convective melting, are studied on the basis of nonisothermal hydrodynamic model of heating of lithospheric rocks above the magmatic chambers.

Keywords: mantle wedge, convective heat and mass transfer, infiltration metasomatism, zoning, mathematical model

1. Introduction

The problem statement arose out of consideration of the nature of porphyritic deposits (porphyritic formation PF) as paleosystems [1], similar to existing fluid systems in transitional areas of the Pacific Ocean (PO) [2]. In the canonic model of these ore-forming systems, the fluid mass transfer is determined by the retrograde boiling of magma in mesoabyssal intrusive cameras. The analysis of time characteristics of formation [3, 4] and the cyclic nature of porphyritic deposits of active margins of PO have showed that more than 70% of the described

deposits are formed with the participation of mantle-crustal ore-magmatic systems [5]. Building quantitative models, it is necessary to rely on the data on tectonophysical characteristics of mantle-crust systems of modern volcanic arcs. This chapter takes into account the data on the dynamics and structure of the seismic focal zone (SFZ) of Kamchatka and the Kuril Island arc, and data on the nature of the volcanic groups of the Japan Islands, their spatial structure, and time cycles of formation [6, 7]. Physical models of convective heat and mass transfer in the fluid mantle-crust systems associated with magmatic chambers are discussed taking into account the already developed schemes of convective heat transfer in the earth's crust for tensile phases [1, 8] as well as the specifics of regions of the SFZ, where the conditions of compression prevail [9, 10].

2. On tectonophysical conditions of development of the magmatogene fluid systems under terrestrial and submarine volcanoes of Kamchatka and the Kuril Islands

The considered problems of convective heat and mass transfer in the mantle wedge beneath volcanic arcs of the Japanese Islands, the Kuril Island arc, the Kamchatka region, and the Aleutian Island arc result from tectonophysical developments, distinguishing regions of SFZ with a predominance of conditions of compression and extension [11–14]. Problems of existing models of the mechanics of development of morphostructures of active marginal continents are discussed in the review of works on canonic models of subduction [15]. New geological and geophysical information about the structures of northwest part of PO, which appeared in the last two decades [16–24], contains the actual data, which has not received explanation in the framework of the discussion in the above review. Among them are research data that are not considered within the canonic model of subduction: (1) before the frontal part and in the rear area of the coastal stripe of volcanoes in the linear and arc permeable zones, there are cyclically occurring and ongoing processes of magmatism with certain geochemical trends [1, 5–7, 18, 25–28]; (2) in the northern and southern sectors of the Kuril-Kamchatka volcanic arc in the upper part of the lithosphere, there is a fixed splitting of the SFZ into the western and eastern branches with orthogonal drop of fracture zones [17, 29] in the area of development of grouping (swarm) earthquakes [12, 30–31]; (3) central parts of volcanic arcs of the northern and northwest areas of PO fall into segments with different structural characteristics of transition zones and back-arc basins; (4) time harmonics of development of tectonic and magmatic processes [5, 17] and stages of formation of PF deposits [2–4] allow assuming that within the seismic focal regions in the continental lithosphere, there have been previously and there are now permeable zones with periodically functioning mantle-crustal ore-magmatic systems. No correct physical models of heat-mass transfer have been proposed for such zones yet; (5) in these segments, there is no "frontal" volcanic zone, since magmatic and hydrothermal events have developed and still occur in the faults that are longitudinal and transverse to the axis of the ocean trench, in the strip of the modern subaerial volcanoes, considered to be the "frontal" volcanic area above the lithospheric wedge; and (6) there are latitudinal fault zones, in which all dated magmatic events in the interval 0–75 million years are recorded [6, 18, 26, 28].

The last point is significant: the analysis of time harmonics of PF formation in the PO margins has found several characteristic dynamic features: (1) the existence of multistage mono- and polycyclic deposits [2–4] and (2) the duration of the formation of individual deposits ranges from a few tens of thousands of years to tens of millions of years, while maintaining thermodynamically close conditions of ore formation [1, 5]. Over the observed period of less than 100 years within the SFZ of the Kamchatka region, the significant seismic activity has a cycle with a period of about 10–12 years [17]. From this, we can conclude that since the formation of deep ocean trenches in the northern half of PO, the tectonophysical characteristics of the SFZ did not remain stationary [18, 22, 25] that is similar to the position of permeable zones in the lithosphere section. As a consequence, it is necessary to clarify the direction of the evolution of tectonophysical characteristics of the structure of the SFZ in the Kamchatka region and the conditions for the development of fluid magmatic systems associated with magmatic chambers under the morphological structures typical for the transition region of "ocean continent."

3. On the structure of the ocean: Continent transition zones of the Kamchatka region and associated volcanic arcs

The structure of the earth's crust to the west of the axis of ocean trenches of the continental sector of the N-W margins of PO is considered in detail in the above-cited works. The most detailed discussion of the crustal structure of the transition area of the Kamchatka region (in its submarine part) may be found in [32]. At that, the structure of the jointing region (ocean trench), as a rule, is beyond the scope of the description of its geophysical characteristics and a real form and distribution of lineaments, submarine volcanic structures and configuration of magma bodies in the crust.

These data may be found using the GIS complex GIS-ENDDB [33], in particular, to clarify the distribution of volcanic bodies in lineaments in the lithosphere structure of the Kamchatka region for the "ocean-continent" transition region (**Figure 1**), and the distribution of density and magnetization of rocks (**Figures 2** and **3**), to correlate earthquake epicenters with the gravimetric map of inhomogeneities in the crust (**Figure 4**), and to determine heat flow values (**Figure 5**) and positions of compression and extension in SFZ on the basis of modern catalogs of seismic events (**Figure 6**).

The most important factor of the development of magmatogene fluid systems is a fixed blocky structure of the Kamchatka lithosphere [27, 34] and its compliance with the current blocky structure of SFZ. The blocky structure of the lithosphere within the SFZ of the Kamchatka region was determined by two methods: (1) estimating the size and shape of areas with similar characteristics of strains, separated by bands of unstable seismicity [11, 35] and (2) monitoring the bands of seismic activity with changing ratios of velocities of longitudinal and transverse waves [30–31]. The development of the first approach using laboratory simulation of stress fields of optically anisotropic media allowed simulating the "restored" continuous stress fields for the relevant mechanisms of earthquakes in the selected region of the energy spectrum [12]. The development of the second approach allowed investigating the structure of SFZ in the depth interval of 0–70 km, where about 90% of seismic events take place and define the

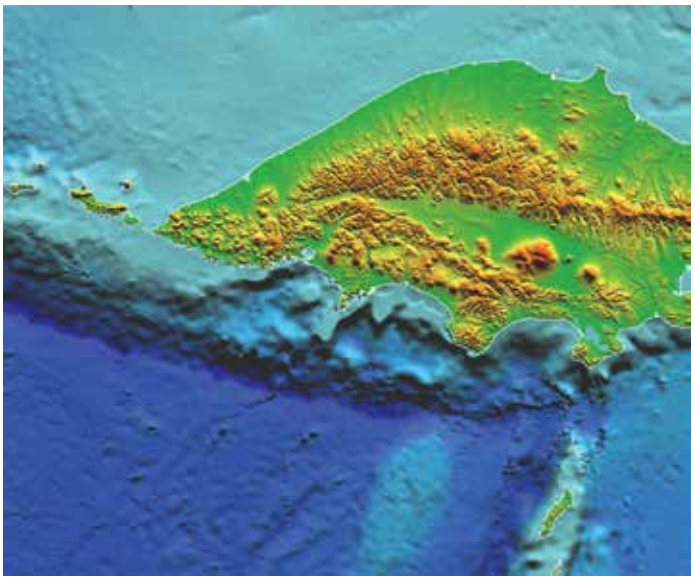

Figure 1. The morphological structures and lineaments of the "ocean-continent" transition zone in the Kamchatka region.

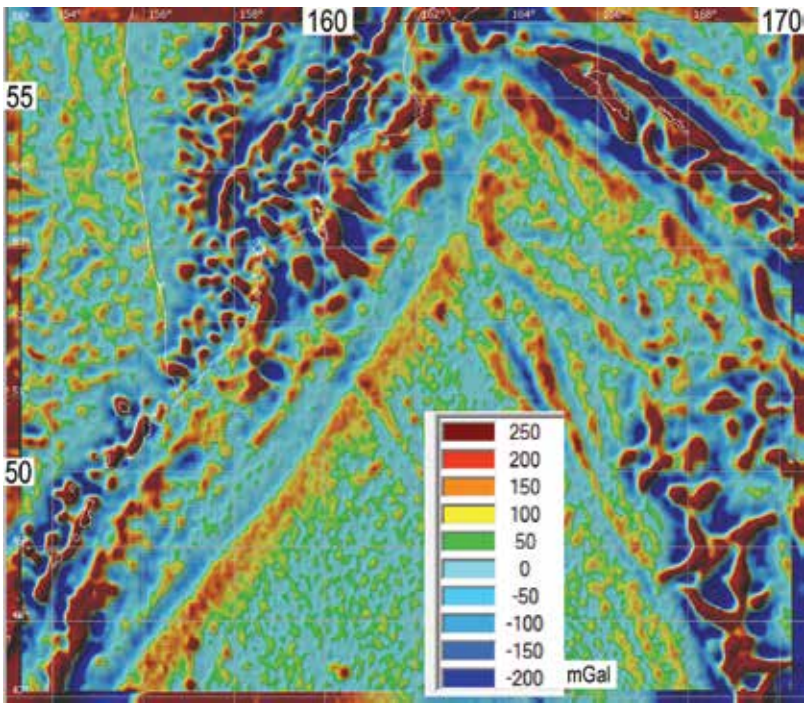

Figure 2. The structure of local variations in the density of the crust of the Kamchatka region and associated volcanic arcs.

http://dx.doi.org/10.5772/intechopen.73225

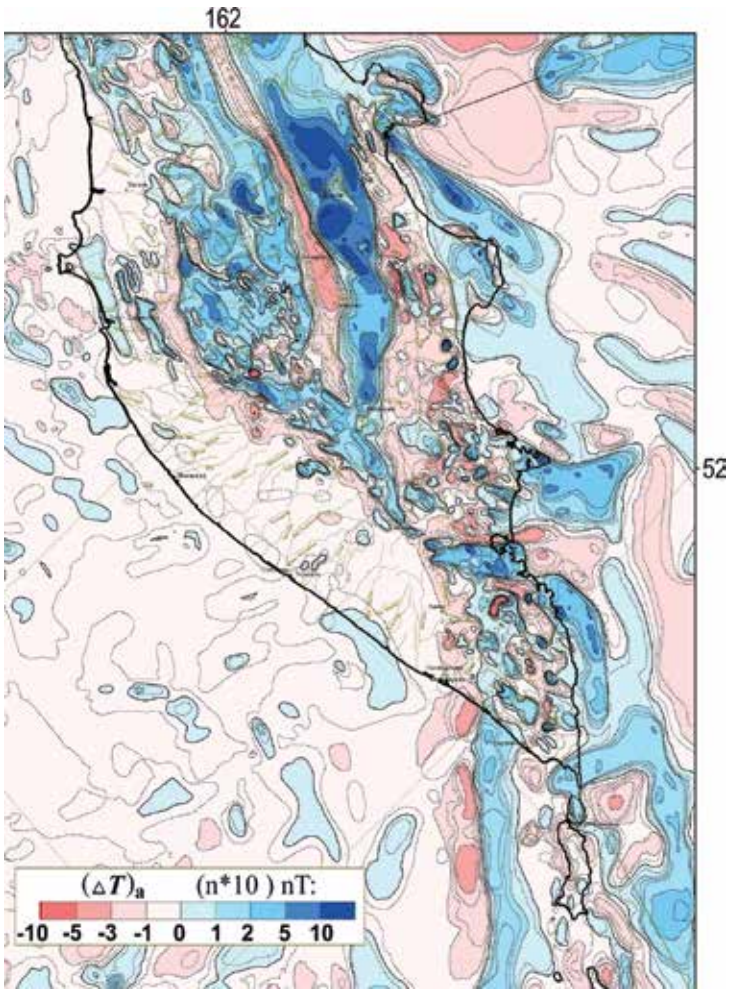

Figure 3. Sequences of positively (basite) and negatively (granite) magnetized asynchronous (Cretaceous—Present) magmatic bodies, part of which has higher density (basite intrusions). (Litvinova TP, editor. Map of anomalous magnetic field of Russia. Scale 1:2500000. Moscow: VSEGEI; 2010).

tectonic appearance of the volcanic zones, the surface morphology of the earth's crust, and its lineament system [17]. It should be noted that under active volcanoes, the morphology of permeable zones in the crust is distinguished experimentally. Thus, according to the study of the crust structure under the Avacha volcano [36], they represent linear fracture zones with a width of 2–4 km. Such zones are conductors of melts and magmatogene fluids, originating from the magma chambers [19, 37].

The distribution of subaerial and submarine volcanic structures of Kamchatka region may be added with the known scheme of structural control of volcanism in Kamchatka [27, 38], built on the basis of tectonophysical data [39], and a structural scheme of satellite data interpreting for the area under consideration [40–41]. This allowed obtaining data on the junction of

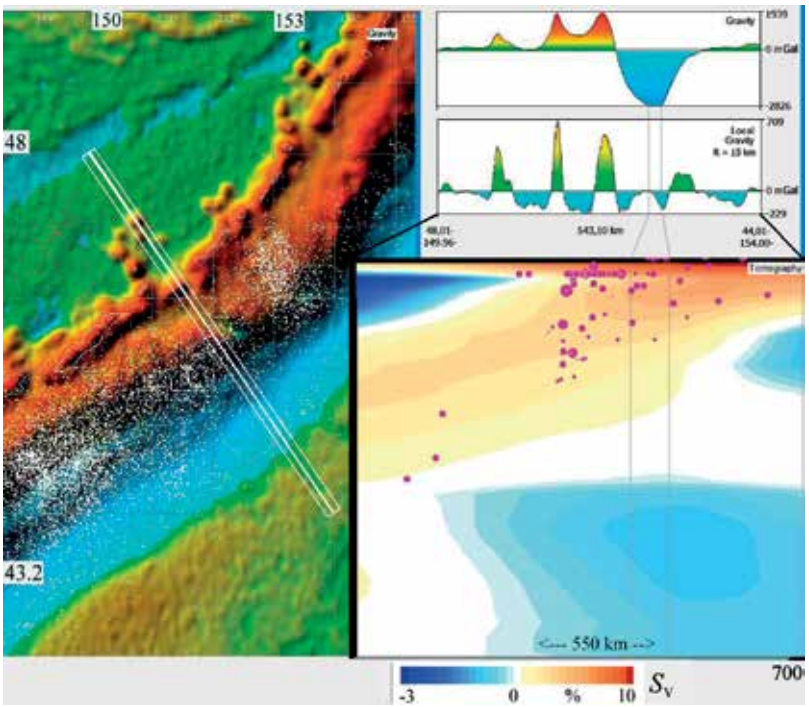

Figure 4. Distribution of epicenters of earthquakes (white dots) in the Kurile region and adjacent volcanic arcs, rendered on the regional map of the gravitational field of the earth's crust. The axial region of the trench is characterized by low seismicity. In the inserted picture: The gravitational cross section, its local part, and tomographic cross section are shown. The axial region of the trench is marked by vertical lines.

lineaments of ground surface and seabed. These data on structural elements, when compared with variations of parameters of different geophysical fields based on the results of satellite observations and ground measurements, serve to correlate the appearance of faults, deformations of the earth's crust and formation of magmatic bodies in the permeable zones. This greatly increases the reliability of geological-genetic schemes of the above-cited papers when compared with the results of the structural analysis and tectonophysical schemes from [12, 17, 19–20, 30–31, 37, 40–41].

The analysis of morphology and position of volcanic structures, location, and extent of tectonic and geomorphic elements in the Kamchatka region (**Figure 1**) suggests that: (1) linear volcanic ridges may cross the structural elements from the edge of the continental shelf to the area of occurrence of volcanic ridges of the oceanic plate, parallel to the axis of the deep trench, (2) these transverse ridges may cross some arc volcanic ridges on the shelf of the continental slope and oceanic plates, (3) the mentioned ridges may cross tectonic terraces of the continental slope up to the limits of the shelf, and (4) linear submarine ridges may be located on the continuation of arc and line faults, controlling the volcanic groups of terrestrial volcanoes of Eastern and Southern Kamchatka.

Based on the found values of tectonic cycles of development and manifestation of magmatic systems of the Okhotsk Sea basin and the Kuril Island arc [18, 22] and the data of Kamchatka

http://dx.doi.org/10.5772/intechopen.73225

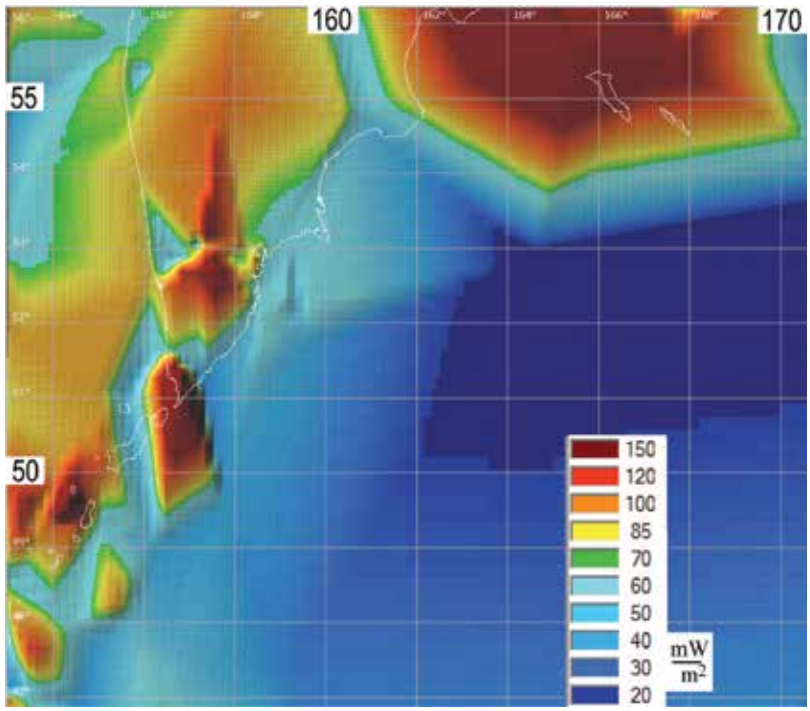

Figure 5. The regional thermal field in the morphostructures of the Kamchatka region and associated volcanic arcs.

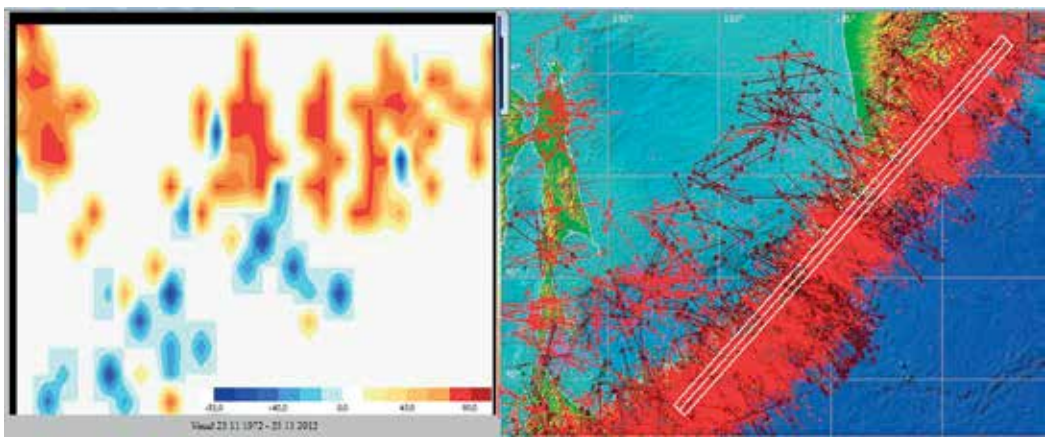

Figure 6. Distribution of compression and stretching regions along the continental slope in the seismic focal zone of Kamchatka region and the southeastern part of the Okhotsk Sea. The structure of vertical and inclined destruction zones of mantle rocks in the lithosphere and in the upper mantle appears above the perovskite transition.

terrestrial magmatic systems dating [26, 28, 42], it is possible to make some assumptions about the sequence of magmatic events, recorded in **Figures 1-3**. After forming the ocean trench offspur, in the "ocean-continent" transition region, there were cyclic processes of tension and shear with their development over arc and line faults of volcanic structures. In the grabens of the bays, in the direction from the trench axis to the volcanic groups of Eastern and Southern

Kamchatka, from about 8 to 14 tectonic and tectonic-magmatic events were detected. With regard to the fixed scale of magmatic events in the vicinity of deep-sea trenches and submarine conditions, the most significant is thought to be the latest magmatic phase [28], which developed within the boundaries and geodynamic conditions of the actual SFZ. Therefore, the model of heat and mass transfer dynamics for mantle-crust magmatic systems should be built taking into account tectonic and physical data, as shown in **Figures 4-6**, and tomographic data of the work [19].

4. Problem statement and mathematical model

Note the main structural and mineralogical and thermo-dynamic effects that may be assumed in the fields of compaction of heterophase media under volcanoes. The correct model of heat and mass transfer dynamics in orthomagmatic systems under volcanoes was developed [5, 8], assuming the predominance of tension conditions in such systems [12]. This assumption was based on then available statistical data on the identified mechanisms of earthquakes [11–12]. Results of processing of seismic data of Kuril-Kamchatka SFZ accumulated since then and shown in **Figures 5** and **6** give reason to significantly adjust the specified assumption. As can be seen from **Figures 5** and **6**, in the section of the earth's crust of Kamchatka, the condition of tension prevails in the western and eastern parts of the SFZ, whereas in the vertical section of the central region of SFZ, there are alternating regions of compression and tension. At that, at the junction of blocks, there are regions with changing configuration, characterized by the conditions of compression. It is obvious that for such areas, the developed hydrodynamic model of magmatic fluid filtering [5, 8] is not quite correct. Therefore, we are developing a more correct model of heat and mass transfer in compressible heterophase media as discussed below.

It should be noted that for mantle rocks, we have already seen experimental evidence of the complexity of such "fluid-rock" interactions. So in mantle rocks, in the field of compression predominance, processes of percolation are assumed in the formation of recrystallization margins along the boundaries of the rock matrix crystals in the presence of a fluid phase [43]. On the other hand, in the models of catastrophic eruptions of andesite volcanoes, it was discovered that heating of the heterophase medium might occur in the zone of tension in the volcanic channel in a heterophase flow in the presence of mechanical interaction of phases [44]. Considering the interaction of compressible phases when filtering fluids in the fractured media [10] apparently can detect a similar effect. Note that under crustal tectonophysical conditions in metasomatic debasification of ultrabasites of Kamchatka, there is the effect of rodingite melting in the areas of ophiolite plate protrusion [32]. Similar effects of local heating in compacted heterophase medium should be expected when filtering the fluid in terms of compaction of the heterophase medium in permeable zones of the lithospheric mantle.

Keeping in mind the above, the physical model of heat and mass transfer in the lithosphere under continental and submarine volcanoes in its governing equations will take into account the main effects of interfacial interaction in the compacted heterophase medium in permeable zones above the magmatic source of fluids. Equations of the mathematical model of such fluid system evolution in the lithosphere were obtained in the framework of the laws of conservation, which

is based on the compliance of the first principles of thermodynamics, conservation laws, and group invariance of the equations [45]. The used phenomenological method ensures thermodynamic consistency of equations of the nonlinear mathematical model of the heterophase medium dynamics. In the framework of this approach, different models were obtained for saturated porous media [46] and two-phase media under the assumption of phase equilibrium in pressure and temperature [47]. The nonlinear model of two-phase media is based on the assumption of the lack of phase equilibrium in pressure, but with phase equilibrium in temperature.

The unit volume of the heterophase medium is characterized by density ρ, velocity $\mathbf{v}$, mass density of the entropy s, and mass content of one of the phases c. The relative motion of phases in such a heterophase medium is characterized by velocity $\mathbf{w}$. The selected parameters of the heterophase medium are connected with parameters of the phases: partial densities and velocities of the phases ρ_s, ρ_f, $\mathbf{u}_s$, $\mathbf{u}_f$ by ratios: $\rho = \rho_s + \rho_f$, $\mathbf{v} = c\,\mathbf{u}_s + (1-c)\mathbf{u}_f$, $\mathbf{w} = \mathbf{u}_s - \mathbf{u}_f$. Thermodynamics of such a medium is fixed by the choice of the functional dependence of energy $E = E(\rho, c, \mathbf{v}, \mathbf{w}, s)$. Governing equations of two-velocity hydrodynamics of heterophase medium with two pressures include the laws of conservation of total mass and mass of one of the phases:

$$\frac{\partial \rho}{\partial t} + \operatorname{div}(\rho \mathbf{v}) = 0,\ \frac{\partial \rho c}{\partial t} + \operatorname{div}\left(\rho c \mathbf{v} + \rho\left(c - c^2\right)\mathbf{w}\right) = 0, \tag{1}$$

the entropy transfer equation

$$\begin{aligned} &T\frac{\partial \rho s}{\partial t} + T\operatorname{div}(\rho s \mathbf{v}) = \operatorname{div}(\kappa \nabla T) + \operatorname{div}(\nu \mathbf{w}) + , \\ &+\rho(1-c)b\,\mathbf{w}^2 + \eta_v v_{ik}^2 + \eta_m v_{ik} w_{ik} + \eta_w w_{ik}^2 \end{aligned} \tag{2}$$

transferred with an average velocity of the two-phase flow $\mathbf{v}$, satisfying the conservation law

$$\frac{\partial \rho v_i}{\partial t} + \partial_k\left(\rho v_i v_k + \rho\left(c - c^2\right) w_i w_k + p\delta_{ik}\right) = \partial_k\left(\eta_v v_{1ik}\right) - \partial_k\left(\eta_w w_{1ik}\right) + \rho g_i, \tag{3}$$

and the equation describing the relative motion

$$\begin{aligned} &\frac{\partial w_i}{\partial t} + (\mathbf{v}, \nabla) w_i + (\mathbf{w}, \nabla) v_i + (1-2c)(\mathbf{w}, \nabla) w_i = -\partial_i q + (\mathbf{w}, \mathbf{w})\partial_i c + \\ &+ \nu\left(c - c^2\right)^{-1} \nabla T - bc^{-1} w_i + c^{-1}\partial_k\left(\mu_v v_{1ik}\right) - (1-c)^{-1}\partial_k\left(\mu_w w_{ik}\right) \end{aligned} \tag{4}$$

Here, $v_{ik} = \frac{1}{2}\left(\partial_k v_i + \partial_i v_k - \frac{2}{3}\delta_{ik}\operatorname{div}\mathbf{v}\right)$, $w_{ik} = \frac{1}{2}\left(\partial_k w_i + \partial_i w_k - \frac{2}{3}\delta_{ik}\operatorname{div}\mathbf{w}\right)$ are tensors of deformation rates, $\mathbf{g}$ is the acceleration, T is the temperature, p is the pressure, and q is the parameter of interfacial interaction, introducing a second pressure in the two-phase medium. Kinetic coefficients of interfacial friction b, dynamic viscosity η_i, thermal conductivity of the medium κ, and the coefficient ν are functions of thermodynamic parameters. Effects of bulk viscosity in this model are not taken into account.

The equation of state and closing dynamic equations (1–4) in the linear approximation [48] are taken as follows:

$$\frac{\delta\rho}{\rho} = \alpha\,\delta p - \beta\,\delta T,\ \ \delta s = c_p\frac{\delta T}{T} - \beta\frac{\delta p}{\rho},\ \ \frac{\rho_0}{\rho}\frac{\delta c}{c} = \rho(1-c)\alpha_q\,\delta q. \tag{5}$$

Coefficients of volumetric compression α, α_q, and thermal expansion β, as well as the specific heat c_p of the heterophase medium introduced here are additive on subsystems. Full density of the heterophase medium and density of entropy are, assumingly, associated with temperature and pressure and do not depend on the second pressure.

The constructed model was analyzed numerically. The difference approximation of the equations (1–4) of nonlinear two-velocity model was realized in the framework of the method of control volume [49–50], whose essential advantage for solving the hydrodynamic problem is that discrete analogs of differential equations satisfy exact integral balance relationships even on rough grids. Application of the control volume method to nonlinear nonstationary equations (1–4) features the choice of assumptions, concerning the change in the dependent variables at a time step, determining the appropriate method to discretize the convective terms at the faces of control volumes, building the algorithm for calculating the pressure field and the consistent velocity field, and satisfying the continuity equation. To determine the values of dependent variables at a new time layer, we have chosen a fully implicit scheme in time, which allows eliminating restrictions on the time step [51–52] and enables making calculations on large time scales characteristic of the problem under consideration. For discretizing the convective terms to determine the values of dependent variables on the faces of control volumes, the nonlinear scheme of the second order HLPA was implemented [53–54]. This scheme

Parameters	**Values**
Fluid viscosity, η_f (Pa · s)	4.5×10^{-5}
Fluid density, ρ_f (kg/m^3)	120
Fluid thermal conductivity, κ (W/m K)	32
Fluid specific heat capacity, c_p (J/kg K)	0.17
Fluid initial temperature in source, T_0 (°C)	1000–1200
Fluid compressibility, β_f (m^2/N)	8.07×10^{-5}
Density of crust rocks, ρ_f (kg/m^3)	2600
Density of lithospheric rocks, ρ_f (kg/m^3)	3000
Specific heat capacity of lithospheric mantle rocks, c_p (J/kg K)	1000
Thermal conductivity of lithospheric mantle rocks, κ (W/m K)	2.4
Fluid heat transfer coefficient on the side of the fluid conductor (W/m^2 K)	0.005–0.05
Fluid conductor length, L	50–150
Fluid conductor width, L_2	4
Effective porosity along the fluid conductor	0.01–0.03
Effective permeability along the fluid conductor, (m^2)	10^{-16}–10^{-13}

Table 1. Physical parameters.

Medium	Composition
Earth's crust rocks, H_1 (0–10 km)	Basalts
Earth's crust rocks, H_2 (10–40 km)	Andesites
Lithospheric mantle rocks, H_3 (40–150 km)	Harzburgites
Magmatogenic fluid in the reservoir (source), R_0 (mol)	C: 0.01-1, H: 0.02-2, O: 0.03-3, N: 0.01, S: 0.003-0.01, Cl: 0.01-0.5, F: 0.003-0.1, Si: 0.125-0.8, Ca: 0.01-0.3, K: 0.001-0.02, Na: 0.01-0.03, Al: 0.01-0.3, Fe: 0-0.2, Ti: 0-0.01
Gas in the reservoir, average content, R_1 (%)	Gas: 0.5-5
Rock in the reservoir, initial composition, $R_{1,\ldots,40}$ (mol)	Si: 6.248, Ca: 0.112, K: 0.006, Na: 0.019, Al: 0.082, Fe: 0.583, Ti: 0.006, Mg: 10.705, Mn: 0.023, Cr: 0.034, P: 0.004, O: 25.52

Table 2. Mineralogical composition.

ensures the monotonicity and the required accuracy of the solutions and meets the convective boundedness criterion (CBC).

The feature of this model is the presence of two pressures in a heterophase medium. For the calculation of consistent velocity fields and pressure fields, the iterative algorithm SIMPLE was adapted [50, 55]. The general iterative approach to the construction of the computational algorithm, based on the method of simple iteration that includes local iterations at solving

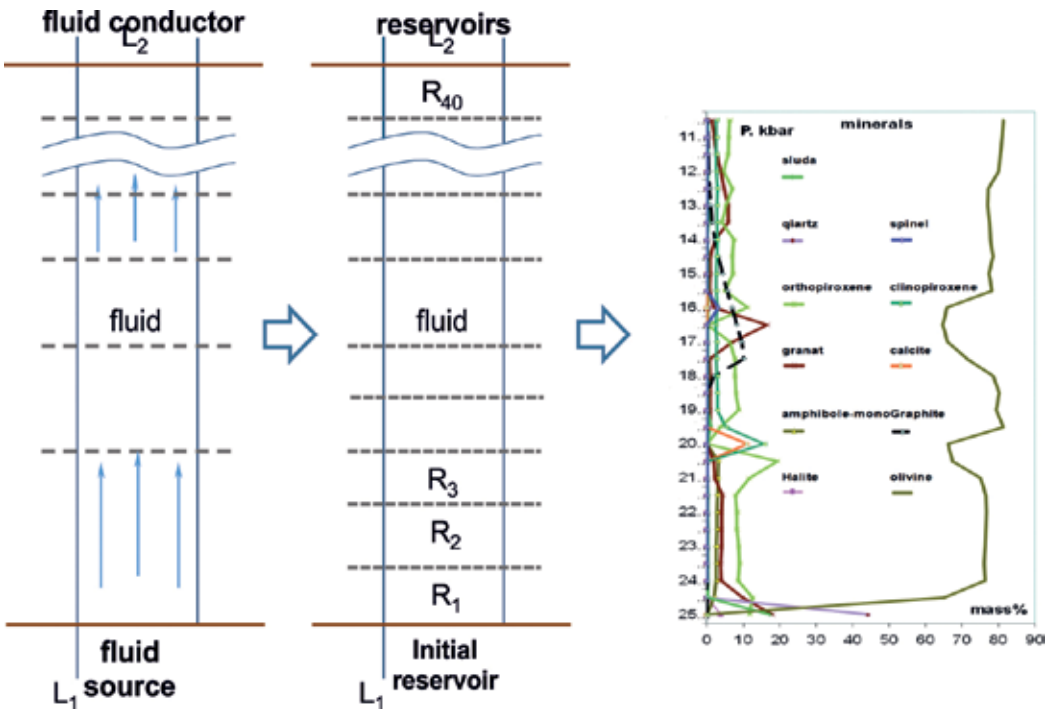

Figure 7. Model of convective heating of lithosphere rocks over a deep chamber of basite magma by the fluid flow over the permeable zone (left), general scheme of a multireservoir thermodynamic model, and distributions of minerals in metasomatic columns (right).

each of the equations and closes with global iterative procedure SIMPLE with recalculation of thermodynamic parameters at each step, takes into account the nonlinearity of the model. All numerical calculations are performed on uniform rectangular grids with a staggered arrangement of nodes. To solve the discrete analogs of differential equations (1–4) obtained by the method of control volume, the following is used: a combination of the direct method of three-point sweep with the iterative method of Gauss-Seidel method of variable directions [50]; direct and iterative methods, optimized to account for the matrix sparsity and implemented in the IMSL and IMKL libraries, used for numerical solution of the system of linear algebraic equations, arising in the calculation of pressure correction [56]. Physical values used in numerical calculations are given in **Tables 1** and **2**, and the problem geometry is shown in **Figure 7**.

5. Numerical modeling of heat exchange dynamics at compacting the heterophase medium

The general structural and geological scheme of mantle-crustal magmatic and local fluid systems under the Avacha group of volcanoes is built on the basis of seismotectonic data; for each of them, the dynamic model of flow-through many-vessel reactor is presented. The physical and chemical analyses of the emergence of substrates, whose convective melting may lead to the formation of carbonatite, basite, and other magmas, are based on the coordinated use of the model of nonstationary nonlinear dynamics of heat and mass transfer in heterophase media and the nonisothermal model of a flow-through many-vessel reactor, describing processes of equilibrium metasomatic transformation of depleted ultrabasic rocks. The problem geometry is shown in **Figure 7**. Pressure in the magma source is taken to be equal to a lithostatic one. Pressure distribution in the field of fluid filtration is set consistently with the distribution of porosity and permeability. According to the study of anisotropy of rocks in the lithosphere [16, 57] and tectonic conditions of formation of volcano-plutonic deposits, one of the main petrophysical characteristics of fluid systems is significant variation in the permeability over the section of the mantle wedge. In the problem, it is assumed that permeability (k_p) and porosity (m_p) decrease with depth (Z = 0–100 km) according to the power law from k_p (Z_0) = 10^{-15} m^2, m_p = 2%, or are set piecewise constant for individual layers in the range 10^{-13}–10^{-17} m^2. Temperature over the border of the mantle magmatic source at lithosphere thickness of 100 km changes from T_0 = 1330 to 1100°C.

The results of numerical simulation of convective heat and mass transfer, taken into account when modeling the dynamics of equilibrium infiltration metasomatism, not accompanied by partial or complete melting of some of the zones in the metasomatic column, show that in the quasi-stationary stage of the fluid system evolution, the temperature distribution in the lower part of the conductor is always higher than in the fluid source by tens of degrees. The magnitude of this effect depends on the values of effective permeability. When considering the dynamics of metasomatic processes, it is possible to explore the temperature range, in which melting in some areas of the emerging column is not expected.

We investigated the types of metasomatic columns at fluid temperature variation in magmatic source from 1330 to 1100°C for constant and variable content of petrogenic components and at the following ratio of molar contents of independent components in the source fluid: C (1),

http://dx.doi.org/10.5772/intechopen.73225

O (2), H (2), Cl (0.25–0.5), F (0.1–0.25), S (0.01), N (0.01). The variation of molar quantities of petrogenic components in the fluid was consistent with the previously defined area of harzburgites' wehrlitization. The differences in the dynamics of metasomatic zoning development for single- and two-speed models in the fluid systems of the lithospheric mantle come to a much longer duration of the metasomatic zone formation at realized compaction, and to facies differences in the composition and ratios of mineral assemblages, involving pressure increase in the fluid system at compaction of heterophase media. Furthermore, at pressures above 20 kbar for temperatures below 1150°C, the rate of synthesis of clinopyroxene at the same intensity of olivine decomposition is about two times larger than that of orthopyroxene. Thus, in the fluid system at wehrlitization in high temperature zones, the content of orthopyroxene in associations is higher than in the upper part of emerging metasomatic columns. When a quasi-steady-state temperature distribution is not reached, differences in the mineral associations of the metasomatic zones, formed with and without compaction of heterophase media, are minimum. If $T_0 \leq 1300°C$, there are a number of detected mineralogical effects, related to variations of fluid composition in the source: at different ratios of Si/Ca in the fluid debasification of ultrabasites is implemented with the lines of compositions of metasomatites from carbonatite to grospydites; and complete replacement of olivine by orthopyroxene is realized at ≈975°C. At compaction of heterophase medium with $T \geq 1330°C$, an anomalous development of wehrlitization is realized for a range of ratios in the fluid $1 \leq Si/Ca \leq 5$. At abnormal wehrlitization, the content of petrogenic components significantly changes, which is reflected in the mineral composition of zones of a metasomatic column.

Simulating the dynamics of metasomatic transformation of mantle ultrabasites on the basis of the hydrodynamic model of compaction of heterophase media reveals complete dissolution of olivine in the external front of temperature growth in the range 1326–1330°C with the formation of clinopyroxene and carbonate, as well as with the formation of a zone of garnet lherzolites above the column section. In realizing such a " transformation column of originally homogeneous depleted ultrabasic rocks," there may be up to three formed regions of melting of simultaneously existing magma chambers, meeting virtually the entire spectrum of mantle magmatic melts in the "ocean-continent" transition zone in the volcanic arcs of the Pacific Ocean. This allows understanding the reason for the existence of the above-mentioned magma chambers at different depths in areas of SFZ compression.

That is, there may appear three levels of changes in the mineral composition of the initial depleted ultrabasite substrate, where melting zones may show up with the formation of basite liquids. In the lower part of the earth's crust, the heating temperature may reach values that are necessary for melting of granitoid magmas.

6. Applying the obtained results to the description of the isothermal dynamics of metasomatic processes in the mantle wedge at compacting the heterophase medium

Numerical simulation of the equilibrium dynamics of nonisothermal fluid systems beneath the volcanoes of the frontal zone of Kamchatka using single-velocity hydrodynamics in the area of

predominance of tensile stresses is considered in [58]. As shown in **Figure 8** in SFZ, in the zones of the meridional shear (at a depth of fluid sources ≥ 100 km for initial temperatures of magmatic fluids 1000 ÷ 1200°C) in metasomatic zoning of altered ultrabasites, there are facies variations in the ratios of minerals of wehrlite rocks [1, 58].

In the mantle wedge of the geodynamic northwestern margin of the Pacific Ocean, over which epicontinental volcanic arcs developed at postmiocene stage, products of asynchronal and multilevel magmatic systems may be combined in the same permeable zones in the "crust-lithospheric mantle" transition area. So, geodynamics of consistently developed types of ore-magmatic systems (from back-arc basin of the Manus type to the formation of the epicontinental volcanic structures of bimodal series) is described in ore deposits of porphyritic formation of one of the Aleutian Islands. Temperature values of the melting centers of the lithospheric mantle in the presence of ultrabasite matrix wehrlitization must be at least 1300°C for this kind of systems [59]. According to the model [25, 36], "cratonization" of the main volcanic sections of the continental earth's crust in such systems, typical for post-Cretaceous geodynamic history of Kamchatka, has to be realized according to the scheme of "metasomatic granitization," the initial element of which is wherlitization of ultrabasic rocks of the mantle wedge. This is why in the framework of the model of compaction in the fluid systems associated with compression and tension areas, we have simulated processes of equilibrium metasomatic

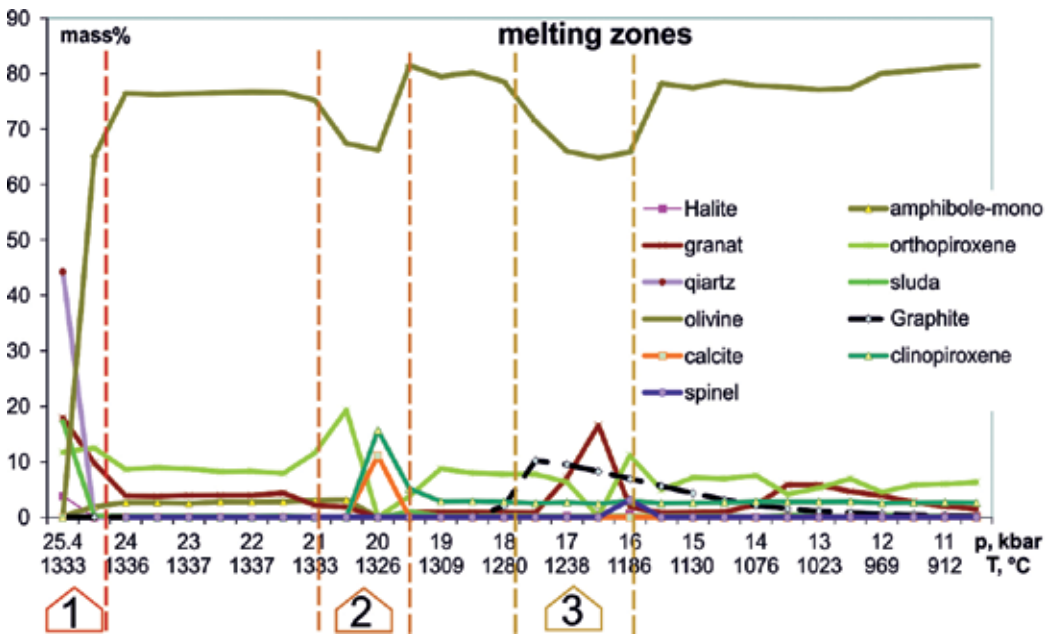

Figure 8. The formation of complex metasomatic columns, which may be the cause of appearance of mantle magma chambers with different levels [59]. (1) Alkaline magma formation area, (2) carbonatite melting area, and (3) basic magma melting area.

http://dx.doi.org/10.5772/intechopen.73225

debasification of rocks of the mantle wedge, using the approximation of the flow-through many-vessel reactor [60, 1]. The hydrodynamic basis for the numerical description of the dynamics of convective heat and mass transfer in this report are the results given in the previous section.

It should be noted that the value of "thermal effect" obtained in the calculations meets some reasonable assumptions, but cannot be experimentally verified in respect of possible maximum values. However, even the obtained underestimated value of temperature growth of about 30°C leads to a very significant physical and chemical "reactivation" of fluids at the exit of the secondary zone of basification, which results in a fundamental change in the nature of dynamics in the metasomatic column (**Figure 8**). Further in the modeling of volcanic ore-magmatic systems in terms of heat and mass transfer in the zones of active seismicity, we should move from the analysis of steady motion of the melts and gas mixtures over permeable zones in the areas of compression dominance and associated areas of the predominance of tension in the seismic focal zone to solving problems of multispeed dynamics of heterophase media. This also applies to hydrodynamic models of nonisothermal motion of heterophase media in flat [8] and tubular [44] channels. Such hydrodynamic models of mantle-crust magmatic systems should be applied to the areas with predominance of compressive stresses within the continental slope of Kamchatka or under volcanoes of the Southern Kuril Islands [12]. The presence of "asthenospheric layer" under the continental slope of Kamchatka [19, 35], of volcanic linear and arc ridges, and the discharge of submarine thermal systems [15] indicate the necessity of using multivelocity hydrodynamics in the description of the dynamics of ore-forming fluid systems of Kamchatka and Kurile volcanic arc.

7. Conclusion

Hydrodynamics of heat and mass transfer in heterophase systems with and without the account for compaction may vary significantly. In seismically active areas of the lithosphere of the transition zone of PO, the presence of the depth zone with compaction should lead to the emergence of specific conditions of heating over the mantle magmatic sources of fluids. Metasomatic columns in such fluid systems can have at least three possible levels of convective melting of metasomatized substrates of the mantle wedge, and the region of high-temperature "fluid" processing of basite intrusions in the crust. This chapter shows some of the reported effects in the implementation of metasomatic processing of the rocks of the mantle wedge. Some mineralogical primitivity of obtained mineral associations is determined by the insufficiency of the used database of thermodynamic characteristics of minerals in the solid phase (rocks of the lithospheric mantle) for a more complete description of metasomatic processing of the depleted ultrabasites of the mantle wedge. The broadening of this information will allow us to proceed (with diagrams of state of obtained mineralogical associations) to the description of a rather complete picture of the formation of magma chambers in the lithospheric mantle and the related ore-forming systems of PF.

Author details

Yury Perepechko[1]*, Victor Sharapov[1], Konstantin Sorokin[1] and Anna Mikheeva[2]

*Address all correspondence to: perep@igm.nsc.ru

1 V.S. Sobolev Institute Geology and Geophysics SB RAS, Novosibirsk, Russia

2 Institute of Computational Mathematics and Mathematical Geophysics SB RAS, Novosibirsk, Russia

References

[1] Sharapov VN, Lapukhov AS, Guzman BV, Cherepanova VK. The influence of the structure of fluid-conductors on the dynamics of phase boundaries in the magmatogene fluid in the formation of deposits in the southern Kamchatka. Russian Geology and Geophysics. 2012; **53**(9):837-852. DOI: 10.1016/j.rgg.2012.07.001

[2] Sillitoe RH. Porphyry copper systems. Economic Geology. 2010;**105**:3-41. DOI: 10.2113/gsecongeo.105.1.3

[3] Singer BS, Jicha BR, Harper MA, Naranjo JA, Lara LE, Moreno-Roa H. Eruptive history, geochronology, and magmatic evolution of the Puyehue-Cordon Caulle volcanic complex, Chile. Geological Society of America Bulletin. 2008;**120**(506):559-618. DOI: 10.1130/B26276.1

[4] Sincair WD. Geological Survey of Canada. Mineral Deposits of Canada: Porphyry Deposits. Open-File: http://mollymarieprospect.com/textfiles/sinclair_porphyry_ synthesis.pdf [Accessed: 2017–08-29]

[5] Sharapov VN, Lapukhov AS, Smolyaninova LG. Time patterns of magmatic ore systems in circum-Pacific volcanoplutonic belts. Russian Geology and Geophysics. 2013;**54**(11): 1352-1368. DOI: 10.1016/j.rgg.2013.10.004

[6] Kondo H, Kaneko K, Tanaka K. Characterization of spatial and temporal distribution of volcanoes since 14 Ma in the northeast Japan Arc. Bulletin of the Volcanological Society of Japan. 1998;**43**(4):173-180. DOI: 10.18940/kazan.43. 4_173

[7] Umeda K, Ban M, Hayashi S, Kusano T. Tectonic shortening and coeval volcanism during the quaternary, Northeast Japan arc. Journal of Earth System Science. 2013;**122**(1):137-147. DOI: 10.1007/s12040-012-0245-z

[8] Polyakov GV, editor. Model Analysis of the Development of the Continental Mantle-Crustal Ore-Forming Systems. Novosibirsk: RAS Publication; 2009. 399 p (in Russian)

[9] Nikolaevskii VN. Geomechanics and Fluidodynamics. London: Kluwer academic publishers; 1996. p. 349

[10] Belikov VT. Basic equations of fluid filtration in deformable cracking porous media. Russian Geology and Geophysics. 1989;**5**:59

[11] Sharapov VN, Simbireva IG, Bondarenko PM. Structure and Geodynamics of the Seismic Focal Zone of the Kuril–Kamchatka Region. Novosibirsk: Nauka; 1984. 199 p (in Russian)

[12] Sharapov VN, Simbireva IG, Bondarenko PM. Seismotectonics of the Kuril-Kamchatka region and its junction with the Aleutian arc. Seismological and Tectonophysical Models. Novosibirsk: IGG: 1992. 138 p. (in Russian)

[13] Christova C. Depth distribution of stresses in the Kamchatka Wadati-Benioff zone inferred by inversion of earthquake focal mechanisms. Journal of Geodynamics. 2001;**31**(4):355-372. DOI: 10.1016/S0264-3707(01)00005-9

[14] Christova C. Spatial distribution of the contemporary stress field in the Kurile Wadati-Benioff zone by inversion of earthquake focal mechanisms. Journal of Geodynamics. 2015;**83**:1-17. DOI: 10.1016/j.jog.2014.11.001

[15] Stern RJ. Subduction zones. Reviews of Geophysics. 1012;**40**(4):1-38. DOI:10.1029/2001RG000108, 2002

[16] Astakhova NV, Lelikov EP. The specifics of ferromanganese ore formation on the submarine Vityaz' ridge (Pacific slope of the Kuril island arc). Russian Geology and Geophysics. 2013;**54**(5):518-525. DOI: 10.1016/j.rgg.2013.04.004

[17] Boldyrev SA. The effect of the lithospheric structure and properties on the seismic field of the Kamchatka region. Izvestiya. Physics of the Solid Earth. 2002;**38**(6):447-468

[18] Emelyanova TA, Kostitsyn YA, Lelikov EP. Geochemistry of volcanic rocks of the submarine Vityaz ridge on the Pacific slope of the Kuril Island arc. Geochemistry International. 2012;**50**(3):289-303. DOI: 10.1134/S0016702912030056

[19] Koloskov AV, Gontovaya LI, Popruzhenko SV. The upper mantle of Kamchatka in isotopic-geochemical and geophysical anomalies: The role of asthenospheric diapirism. Russian Journal of Pacific Geology. 2014;**8**(3):151-162. DOI: 10.1134/S1819

[20] Kulinich RG, Karp BYa., Baranov BV, Lelikov EP, Karnaukh VN, Valitov MG, Nikolaev SM, Kolpakschikov TN, Tsoy IB. Structural and geological characteristics of a "seismic gap" in the central part of the Kuril Island Arc. Russian Journal of Pacific Geology. 2007;**1**(1):3-14. DOI: 10.1134/S181971400

[21] Lelikov EP, Emel'yanova TA, Baranov BV. Magmatism of the submarine Vityaz ridge (Pacific slope of the Kurile Island arc). Oceanology 2008;**48**(2):239-249. DOI: 10.1134/S000143700

[22] Lomtev VL. Structure features and history of development of the northwestern part of the Pacific Ocean bottom. Geomorphology RAS. 2016;**2**:59-71 (in Russian)

[23] Taylor CD, Johnson CA, editors. Geology, geochemistry, and genesis of the Greens Creek massive sulfide deposit, Admiralty Island, southeastern Alaska. U.S. Geological Survey Professional Paper 1763; 2010. 429 p

[24] Tamura Y, Tatsumi Y, Zhao DP, Kido Y, Shukuno H. Hot fingers in the mantle wedge: New insights into magma genesis in subduction zones. Earth and Planetary Science Letters. 2002;**197**(1–2):105-116. DOI: 10.1016/S0012-821X(02)00465-X

[25] Goryachev AV. The Main Regularities of the Tectonic Development of the Kurile–Kamchatka Zone. Moscow: Nauka; 1966. 253 p (in Russian)

[26] Koloskov AV, Kovalenko DV. New age data for Cainozoic magmatism in Kamchatka. Bulletin of Kamchatka regional association "educational-scientific center". Earth Sciences. 2009;**1**(13):231-236 (in Russian)

[27] Erlich EN. Modern Structure and Quaternary Volcanism of the Western Part of the Pacific Ring. Novosibirsk: Nauka; 1973. 232 p (in Russian)

[28] Bindeman IN, Leonov VL, Izbekov PE, et al. Large-volume silicic volcanism in Kamchatka: Ar–Ar and U–Pb ages, isotopic, and geochemical characteristics of major pre-Holocene caldera-forming eruptions. Journal of Volcanology and Geothermal Research. 2010;**189**(1–2):57-80. DOI: 10.1016/j.jvolgeores.2009.10.009

[29] Lomtev VL, Nagornykh TA, Safonov DA. On the structure and seismotectonics of the Kuril arc-trench system. Seismic Instruments. 2013;**49**(4):327-342. DOI: 10.3103/S074792391304004X

[30] Slavina LB, Pivovarova NB, Babanova DN, Levina VI. A Study of Structure for the Benioff Zone of Kamchatka: The Avacha Bay — Cape Lopatka Segment. In: Geofizicheskie issledovaniya (Geophysical Investigations). Moscow: IFZ RAN. 2007;**8**:117-126 (in Russian)

[31] Slavina LB, Levina VI, Babanov DN. Features of occurrence and distribution of swarm sequences of earthquakes in the seismic focal zone in the waters of the Pacific coast of Kamchatka. In: Proceedings of the 2nd Scientific and Technical Conference "Problems of Complex Geophysical Monitoring of the Far East of Russia"; 11–17 October 2009; Petropavlovsk-Kamchatsky: GS RAS; 2009. p. 151-155 (in Russian)

[32] Seliverstov NI. Structure of Kamchatkian Water Area Bottom and Geodynamic of a Junction Zone between the Kuril-Kamchatka and Aleutian Island Arcs. Nauchnyi Mir: Moscow; 1998. 164 p (in Russian)

[33] Mikheeva AV, Marchuk AG, Dyadkov PG. Geoinformation systems for studying seismicity and impact cratering using remote sensing data. In: Nielso D, editor. Geographic Information Systems (GIS): Techniques, Applications and Technologies. France: Nantes University. 2014. pp. 151-216

[34] Aprelkov SE, Popruzhenko SV, Bogdan PS, Kasyanyuk EE. Structures of the Foundation and Localization of Volcanism in Southern Kamchatka. Geodynamics and Volcanism of Kuril-Kamchatka Island Arc System. IMGG FEB RAS: Petropavlovsk-Kamchatskiy; 2001 (in Russian)

[35] Simbireva IG, Fedotov FS, Feofilaktov VD. Inhomogeneities of the stress field of the Kuril-Kamchatka Island arc according to seismic data. Russian Geology and Geophysics. 1976;**1**:70-85

[36] Koulakov I, Jaxybulatov K, Shapiro N, Abkadyrov I, Deev E, Jakovlev A, Kuznetsov P, Gordeev E, Chebrov V. Asymmetric caldera-related structures in the area of the Avacha group of volcanoes in Kamchatka as revealed by ambient noise tomography and deep

seismic sounding. Journal of Volcanology and Geothermal Research. 2014;**28**:36-46. DOI: 10.1016/j.jvolgeores.2014.08.012

[37] Gontovaya LI, Popruzhenko SV, Nizkous IV. Upper mantle beneath Kamchatka: The depth model and its relation to tectonics. Russian Journal of Pacific Geology. 2008;**2**(2): 165-174. DOI: 10.1134/S1819714008020073

[38] Ehrlich EN, Kuzmin YD. De rerum atura and Grand Theory. 2016. 43 p (in Russian)

[39] Averyanova VM. Deep Seismotectonics of Volcanic Arcs of the North-West Part of the Pacific Ocean. Moscow: Nauka; 1975. 220 p (in Russian)

[40] Sharapov VN, Bondarenko PM, Pyatkin VP. Identifying with instrumental methods the patter of faults of Central Kamchatka and deciphering their genesis. Earth Observation and Remote Sensing. 1980;**2**:44-50

[41] Sharapov VN, Simbireva IG, Bondarenko PM, Gnibedenko GS. On the structure of the earth's crust at the junction of ocean: Continent in the area of the Kamchatka trench. Russian Geology and Geophysics. 1981;**1**:15-19

[42] Sheimovich VS, Puzankov YM, Puzankov MY, Golovin DI, Bobrov VA, Moskleva SV. Manifestation of alkaline magmatism in the vicinity of the Avacha Bay. Journal of Volcanology and Seismology. 2005;**4**:36-46

[43] Soustelle V, Tommasi A, Demouchy S, Ionov DA. Deformation and fluid–rock interaction in the supra-subduction mantle: microstructures and water contents in peridotite xenoliths from the Avacha Volcano, Kamchatka. Journal of Petrology, 2010;**51**(1–2):363-394. DOI: 10.1093/petrology/egp085

[44] Barmin AA, Melnik OE, Skulsky OI. Model of a non-isothermal stationary magma flow in a volcanic conduit taking into account slip boundary conditions at the conduit wall. Computational Continuum Mechanics. 2012;**5**(3):354-358. DOI: 10.7242/1999-6691/2012. 5.3.42

[45] Khalatnikov IM. An Introduction to the Theory of Superfluidity. New York: W.A. Benjamin; 1965. p. 206

[46] Dorovsky VN. Mathematical models of two-velocity media. Mathematical and Computer Modelling. 1995;**21**(7):17-28

[47] Dorovsky VN, Perepechko YV. Mathematical models of two-velocity media. Part II. Mathematical and Computer Modelling. 1996;**24**(10):69-80. DOI: 10.1016/S0895-7177(96) 00165-3

[48] Perepechko YV, Sorokin KE, Imomnazarov KK. Numerical simulation of the free convection in a viscous compressible fluid. Bulletin of the Novosibirsk Computing Center. Series: Mathematical Modeling in **Geophysics**. 2011;**14**:59-64

[49] Samarskiy AA. The Theory of Difference Schemes (Pure & Applied Mathematics). New York: Marcel Dekker, Inc.; 2001. p. 788

[50] Patankar SV. Numerical Heat Transfer and Fluid Flow. Washington: Hemisphere Publishing Corporation; 1980. p. 197

[51] Fletcher C. Computational Techniques for Fluid Dynamics. Berlin Heidelberg: Springer-Verlag; 1988. p. 552

[52] Randall JL. Finite Volume Methods for Hyperbolic Problems. Cambridge: Cambridge University Press; 2004. p. 553

[53] Zho J, Rodi W. Zonal finite-volume computations of incompressible flows. Computers Fluids. 1991;**20**(4):411-420. DOI: 10.1016/0045-7930(91)90082-S

[54] Wang JP, Zhang JF, Qu ZG, He YL, Tao WQ. Comparison of robustness and efficiency for SIMPLE and CLEAR algorithms with 13 high-resolution convection schemes in compressible flows. Numerical Heat Transfer. Part B. 2014;**66**(2):133-161. DOI: 10.1080/10407790.2014.894451

[55] Moukalled F, Darwish M. A unified formulation of the segregated class of algorithms for fluid flow at all speeds. Numerical Heat Transfer. Part B. 2000;**37**(1):103-139. DOI: 10.1080/104077900275576

[56] Kuzmin A, Luisier M, Schenk O. Fast methods for computing selected elements of the Greens function in massively parallel nanoelectronic device simulations. In: Proceedings of the 19th International Conference on Parallel Processing (Euro-Par 2013); 26-30 August, 2013; Aachen, Germany: Lecture Notes in Computer Science. 2013;**8097**:533-544. DOI: 10.1007/978-3-642-40047-6_54

[57] Park J, Levin V, Brandon MT, Lees JM, Peyton V, Gordeev E, Ozerov A. A dangling slab, amplified arc volcanism, mantle flow and seismic anisotropy near the Kamchatka plate corner. In: Stein S, Freymueller J, editors. Plate Boundary Zones. AGU Geodynamics Series, Washington DC. 2002;**30**:295-324

[58] Sharapov VN, Kuznetsov GV, Timina TY, Tomilenko AA, Chudnenko KV. **S**imulation of nonisothermal metasomatism of peridotite from mantle wedge beneath the Avacha group of volcanoes (Kamchatka). Russian Geology and Geophysics. 2017;**58**(5):674-700. DOI: 10.15372/GiG20170502

[59] Green D, Eggins S. Primary magmas and mantle temperatures. European Journal of Mineralogy. 2001;**13**:437-451. DOI: 10.1127/0935-1221/2001/0013-0437

[60] Chudnenko KV. Thermodynamic modeling in geochemistry: Theory, algorithms, software, appendices. Novosibirsk: Geo. 2010. 287 p (In Russian)

Chapter 8

Finite Element Models of Elastic Volcano Deformation

Timothy Masterlark and Sui Tung

Additional information is available at the end of the chapter

http://dx.doi.org/10.5772/intechopen.71156

Abstract

The migration of magma within a volcano produces a deformation signature at the Earth's surface. Inverse models of geodetic data estimate parameters that characterize the magma migration. These characterizations are tied to the specific model that relates migration to the observed deformation. A model is a simplified representation of a natural system. A modeler is tasked with the challenge of designing a model that represents the system, in the context of the available data and purpose of the model. This chapter presents a systematic approach to quantitatively simulate geodetic data with finite element models (FEMs) in the framework of a deformation modeling protocol. This chapter will (1) address the design and execution of FEMs that can account for the geophysical complexity of a volcano deformational system and (2) define techniques for including FEMs in both linear and nonlinear inverse methods to characterize a magmatic system based on observed geodetic data. With these techniques, researchers can estimate magmatic migration within active volcanoes and understand how uncertainties in the data propagate into predictions. These estimates comprise some measure of central tendency, a sense of uncertainty, and a quantification of biases.

Keywords: FEM, InSAR, deformation, inverse model

1. Introduction

The upward migration of magma controls the eruption cycle of an active volcano. The specific characteristics of this migration (the impulse) and surrounding structure of the volcano produce a specific deformation signature (the response) at the Earth's surface. Forward models of such a system, with given magma migration characteristics and host domain configurations, predict the surface deformation. However, in practice we are faced with the much more challenging problem of using inverse models of geodetic data to estimate key controlling parameters that characterize the inaccessible magma migration at depth. The resulting estimates are

strongly controlled by the geometric configuration and distribution of materials that host the migration and modulate how the magma migration impulse translates to the deformational response of the Earth's surface. This impulse-response perspective underpins the concepts presented in this chapter.

A model is a simplified representation of a natural system. The degree of simplification depends on the desired accuracy of predictions, the available constraining information and its uncertainty, and the limitations of the modeling device and methods [1]. Model design is an assembly of decisions that a modeler makes to represent the natural system. Each decision must be justified with sensitivity analyses –some may be formal quantitative assessments, while others may be simple Boolean logic. Ultimately, the reliability of the model depends on how well model predictions compare to observations of the natural system [2]. This chapter focuses on applications of finite element models (FEMs) for simulating quasi-static volcano deformation. Such models are useful for explaining how magma flux, the migration and storage of magma at depth, translates to geodetic observations. With FEMs, this translation can simultaneously account for the complex geometric configurations and distributions of material properties of an active volcano. Thus, FEMs are key to advancing multidisciplinary understanding of active volcanoes.

A given model prediction may be thought of as an estimate, which requires two components (1) a measure of central tendency and (2) an expression of uncertainty. Quantitative confrontations between model predictions and observations must account for both central tendency and uncertainty. Because model predictions are a function of the model design components, a modeler must examine how variations in model design propagate into model predictions. It is important to include the uncertainties in the constraining information that guides the model design. With experience, a modeler will begin to intuitively identify and understand which model design component variations most strongly influence or bias prediction variations.

The volcano deformation protocol described in this chapter is a formalized process developed from general methods for mathematic modeling [3]; protocol methods for other Earth science fields [2]; and the authors' experience specific to applications of FEMs for simulating quasi-static deformation to explain geodetic observations. The protocol includes a systematic guide to multidisciplinary quantitative assessments and interpretations for volcano deformation.

Concepts are presented in this chapter using a case study of Okmok volcano, Alaska (**Figure 1**), because this volcano is the target of the most sophisticated FEM analyses, to date. The remainder of this chapter is divided into three sections. Section 2 summarizes different types of geodetic data and introduces other types of data that influence the translation between magma flux (impulse) and deformation (response). Section 3 describes the volcano deformation modeling protocol. This protocol may be viewed as a checklist for conducting analyses of volcano deformation. Section 4 describes the necessary components for reporting quantitative numerical modeling analyses of volcano deformation.

http://dx.doi.org/10.5772/intechopen.71156

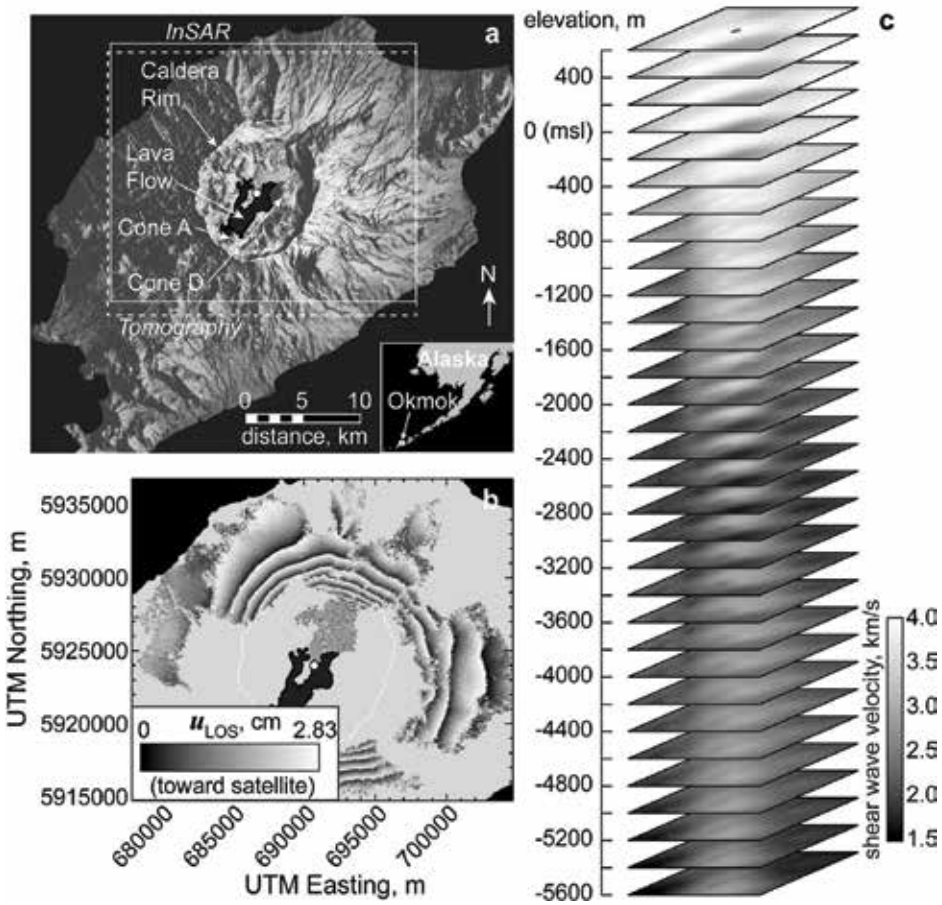

Figure 1. Example study site. (a) Shaded relief image of Okmok volcano, Alaska. White boxes outline footprints for InSAR (solid) and tomography (dashed). White circle near center of the caldera denotes the horizontal reference position of a magma chamber. Inset at bottom right shows location of Okmok. (b) InSAR data show deflation during the 1997 eruption. Coordinates are given for UTM zone 2. (c) Tomography model. Each slice represents the velocity structure for the elevation with respect to mean sea level. The horizontal positions of the caldera rim and horizontal reference position overlay the top-most slice for reference. Note spatial variation in seismic velocities. Modified from Masterlark et al. [10].

2. Data

2.1. Geodetic data

Deformation of the Earth's surface is driven by an array of processes that span deep-seated mantle convection, lithospheric stresses, magma migration and storage, surface loading process, and anthropogenic activities, such as reservoir impoundment and fluid extraction and injection. This paper will focus on deformation of earthquakes and active volcanoes. Geodetic data precisely define point positions, $\mathbf{x}$, for the Earth's surface. Displacement, u, is

defined as the incremental, or discrete, change in position of a point over a given increment of time. In Cartesian coordinates, the displacement of a point p over an increment having initial and final times, t_0 and t_1 respectively, is the vector $u_p = [\mathbf{x}_{t1} - \mathbf{x}_{t0}]_p$. An assembly of displacements gives a spatial sampling of deformation over a given increment of time. Displacement data were historically collected with various field-based methods, such as leveling and line-length measurements. Over the past few decades, space-borne instruments revolutionized the precision and spatial resolution of Earth's deformation. These instruments provide two very different, but complementary types of deformation data.

2.1.1. GPS data

First, position time series are collected for thousands of global positioning system (GPS) stations using data from the constellations of global positioning system (GPS) satellites. These data provide three-component position estimates with uncertainties approaching 1 mm. Some GPS stations provide continuously sampled position records, while others are re-occupied periodically for campaign-style measurements. Continuously sampled sites provide systematic position samplings for time intervals that are limited only by the instrument or infrastructure, but have relatively expensive power and telemetry or data logging requirements. Alternatively, campaign-style measurements rely on less expensive, but more labor-intensive re-occupation strategies having relatively long time intervals separating sequential occupations. The technical aspects of GPS data processing are far beyond the scope of this work. For our purposes, however, it is suffice to say that GPS data provide three component displacements with known uncertainties at time t for a given GPS station having location $\mathbf{x}$.

2.1.2. InSAR data

Interferometric synthetic aperture radar (InSAR) imagery characterizes changes in the phase distribution of radar scenes acquired for a given target from two separate satellite passes. Because the radar wavelength is constant and the initial phase of radar wave and positioning of a satellite are known for both passes, the distribution of phase changes can be related to the displacements parallel to the look direction of the satellite in unwrapped InSAR images. The technical aspects of InSAR processing are far beyond the scope of this paper, but aspects relevant to modeling are given here. Unwrapping refers to the process of spatially integrating the phase data to achieve a map of line-of-sight (LOS) displacements and for our purposes, InSAR implies the unwrapped image. We will note, however, that techniques exist to directly analyze the unwrapped phase data [4]. LOS displacements may be cast as either relative to the satellite or ground position. For the remainder of this paper, LOS displacement refers to ground displacement in the direction of the satellite. An InSAR image provides a map of incremental LOS displacement that represents the difference between the positions of the pixels at the time of the second and first satellite passes, respectively. That is, an InSAR image provides incremental displacement and provides no information about the displacement between the image acquisition times. InSAR images are susceptible to artifacts caused by spatial variations in atmospheric moisture and orbital uncertainties [5]. The former can be identified via pair-wise inspection or stacking techniques [6] and the latter can be accounted for with linear inverse methods, as discussed below. The pixels of an InSAR image are not independent for a

variety of reasons. An InSAR image may be processed with a variety of quadtree [7] or other reduction techniques to provide an LOS deformation map with corresponding uncertainties [8]. Alternatively one may examine model residuals to estimate uncertainties [9–11].

2.2. Seismic data

Energy from a seismic source propagates through the Earth and is recorded as motion with seismometers or geophones at or near the Earth's surface. The resulting seismic data may be used to estimate the distribution of internal rock properties based on well-established relationships between seismic velocities and elastic moduli [12] and the propagation and storage characteristics of magma, all of which are generally time-dependent, within an active volcano.

2.2.1. Tomography

Seismic wave propagation is a function of the specific material properties of the rock that hosts the waves. More specifically, these material properties describe the p and s wave propagation velocities, *Vp* and *Vs*, respectively, both of which are related to elastic moduli. Thus, the estimated distribution of a tomography model may be expressed as a distribution of elastic moduli. Note that homogeneous elastic half-space (HEHS) assumptions, which are commonly used in models of volcano deformation [13], imply that these moduli are constant in space and generally conflict with seismic tomography. Masterlark et al. [11] quantified the implications of ignoring seismic tomography in volcano deformation models for Okmok volcano, Alaska (**Figure 1**). In this example, ignoring the relatively weak caldera materials translated to significant underestimation of the magma chamber depth. This result may be illustrated conceptually by assuming that the stiffness of the weak rock is zero. In this case, the weak layer may be removed from consideration to give an effective free-surface that lies at the base of the weak materials filling the caldera.

2.2.2. Seismicity

Magma processes may serve as a source of seismic energy. The propagation of fluid-filled cracks perturbs the local stress field and produces microseismicity. We can use microseismicity to track magma migration. The case of a propagating dike is precisely analogous to tracking hydrofracture propagation in energy application. Alternatively, the viscous flow of magma produces VLF seismic signals that reveal episodic dike breakout [14].

2.3. Auxiliary data

2.3.1. Topography and bathymetry

For deformation studies, the land or seafloor of a volcano is represented as a stress-free surface because we assume that the shear resistance of the low viscosity atmosphere or water column is zero and that the normal stress variations are also small. This latter assumption may require consideration for seafloor deformation studies having substantial overlying water columns. Not surprisingly, the shape of the free surface will influence deformation predictions. We can visualize this effect by considering how the deformation field would be influenced by the extreme

case of a vertical cliff. In this case, the true free surface would be orthogonal to the customary flat surface of an HEHS domain. Thus, an irregular free surface estimated from topography and bathymetry data, both of which are readily available for the entire surface of the Earth, will influence deformation predictions. Cayol and Cornet [15] demonstrated that topographic gradients less than 20° are well approximated by a flat free surface. Because the nonuniform internal structure of an active volcano implies a nonuniform land surface, deformation models should generally address the irregular free surface of topography or bathymetry.

2.3.2. Thermal data

Rock rheology is strongly temperature-dependent [16]. Not surprisingly, heat from an active magma chamber propagates into and weakens the surrounding country rock. Temperature, T, measurements at the land surface can constrain the thermal system of an active volcano, which can be simulated with relatively simple numerical models to estimate the thermal regime due to conductive heat flow. The governing equations are $\nabla^2 T = c$, where $c = 0$ for steady state conditions or internal heat source. The resulting temperature distribution can explicitly constrain the rheology of the rock. For example, Masterlark et al. [17] used thermal models to identify a discrete viscoelastic rind surrounding an active magma chamber. Del Negro et al. [18] used similar thermal models to estimate a domain having a temperature-dependent viscoelastic behavior.

2.3.3. Petrologic data

Petrologic analyses of frozen lava sampled at or near the land surface reveals the pressure and temperature history of material when it was at depth [19]. For example, the presence of volatiles can be studied to infer the pressure of crystallization, and hence depth of a magma system [20]. Alternatively, plagioclase zoning records episodic perturbations to the pressure or temperature conditions within a magma chamber [21]. Such episodes can be interpreted as variations in magma flux, which in turn, can be used to account for episodic deformation.

3. Protocol

The deformation modeling protocol [22] provides a framework that subjects the modeling effort to a rigorous system of checks to ensure self-consistency, repeatability, and reliability. An innovational aspect of the protocol is that it requires a dynamic modeling process that iteratively updates and improves model configurations with new information and evaluations of prediction misfit. Adherence to such a protocol maximizes the effectiveness of FEM applications and is essential for quantitative analyses, parameter estimations, and interpretations of geodetic data for active volcanoes.

3.1. Purpose

The first step in the protocol is to identity the purpose of the modeling, which will include a precise definition of the scientific problem and statement of objectives in mathematical terms.

This step includes a literature review and the assembly and visual (qualitative) inspection of geodetic and auxiliary data. Based on this information, the modeler will formulate scientific questions regarding the relationship between magma flux (what we cannot directly observe) and the observed geodetic data and identify goals that will answer these questions. The modeler will then devise strategic testable hypotheses to address these goals. These tests will use statistical hypothesis testing (SHyT) to ensure that quantitative estimates and interpretations include the propagation of prediction uncertainties. A typical SHyT analysis comprises competing null (H_0) and alternative (H_A) hypotheses, respectively, and a means to accept or reject hypotheses with a defined level of confidence. For example, a typical study of geodetic data for a volcano will include rudimentary modeling and an unsupported statement of "…good fit to the data…". We call on the modeling community to require that any statement of goodness-of-fit be supported with quantitative evidence. For example, we can readily test whether a model well predicts an assembly of geodetic data for an active volcano with, say, a 95% confidence level. The SHyT could be formulated as follows:

H_0: Model predictions are the same as the geodetic data.

H_A: Model predictions are different from the geodetic data.

Based on an F-ratio (F) test, which explicitly accounts for the uncertainty in both data and model predictions [23], and the critical value appropriate for the 95% confidence level (F_{crit}), we would accept H_0 if $F < F_{crit}$ value or reject H_0 and accept H_A if $F \geq F_{crit}$. Such a test provides a powerful quantitative basis to interpret geodetic data. The F-ratio is only one of many powerful tools available for SHyT analyses, but is particularly convenient for calculating the performance of predictions from two competing reference (*ref*) and alternative (*alt*) models in a way that accounts for the data uncertainties and number of model parameters:

$$F = \frac{\chi^2_{alt}/dof_{alt}}{\chi^2_{ref}/dof_{ref}} \geq 1.0 \quad \text{with} \quad \chi^2 = \sum_{i=1}^{N} \frac{e_i^2}{\sigma_i^2} \tag{1}$$

where *dof* represents the degrees of freedom, which may be calculated as the difference between the number of data and the number of adjustable parameters, N and M, respectively; e_i and σ_i are the prediction error and data uncertainty for the i^{th} datum. Note that Eq. (1) is readily amenable to SHyT analyses. Every statement regarding model predictions and interpretations should be supported by a quantitative assessment and, ideally, expressed as a probability density function (PDF). For the example given by the F-ratio test, the PDF is expressed in terms of an F-distribution [24]. Other methods for comparing competing model performance include the Akaike information criterion [25] or Bayesian techniques [26, 27].

3.2. Conceptual model

The conceptual model is a qualitative representation of the deformational system. A suitable conceptual model of a volcano deformational system requires a domain configuration comprising the geometry, governing equations, boundary conditions, initial conditions, and loading conditions or mechanisms. Some or all of these components may be a function of time.

3.2.1. Domain configuration

The initial decisions of the conceptual model include the choice of units and coordinate system. For scientific investigations, the units will be Système International (SI). Modelers are strongly cautioned against using any other system in an effort to ensure consistency. The modeler must then establish a global coordinate system, which generally approximates the local volcanic system in Cartesian coordinates [east, north, up]. This approximation, which neglects the curvature of the Geoid, is justified for the relatively small near-field regions of an active volcano. The UTM coordinate system is a particularly convenient choice for a global coordinate system. Some models may require local coordinate systems to formulate directional aspects, such as directionally-dependent material properties, fault-slip, or dike and sill openings. The modeler will document all coordinate system transformations. The geometry of the model domain is a representation of the model space. The top of the domain represents the land surface or seafloor. The nearfield geometry may include local geometric complexities, such as a high-resolution representation of the topography. The far-field represents how the domain extends beyond the nearfield region in both horizontal and depth dimensions.

While the actual spatial system of an active volcano is a 3D entity, the modeler is tasked with choosing the simplest dimensional configuration that adequately represents the system. While lower dimensionality configurations are computationally simpler, the modeler must remember that this simplicity has precise meanings for the higher dimensions. For example, a 1D domain implies that the domain is constant and extends to infinity in the two dimensions that are not explicitly simulated. Likewise, a 2D domain implies that the system is constant and extends to infinity in the third dimension. A full 3D domain may be recovered by sweeping a 2D axisymmetric domain about an axis of symmetry. Sensitivity analyses are necessary to justify the choice of dimensionality. For example, justification is satisfied for a 2D domain if results from a 3D domain are sufficiently similar. The free surface should generally reflect topography or bathymetry, unless the goals of the modeling are qualitative. This implies the general need for 3D systems, except for special cases where topography and bathymetry are effectively flat. However, as near-field deformation becomes less sensitive to topography and bathymetry with distance, a modeler may design a domain having fidelity to topography and bathymetry that decays with distance from the near-field. Such a strategy is aligned with mesh design considerations discussed later.

3.2.2. Governing equations

The governing equations specify the physical behavior of the system. The equations of static elasticity are expressed here in index notation for a heterogeneous and isotropic material, using Einstein summation:

$$\frac{\partial}{\partial x_j}\left[G(\mathbf{x})\left(\frac{\partial u_i}{\partial x_j}+\frac{\partial u_j}{\partial x_i}\right)\right]+\frac{\partial}{\partial x_j}\left[\lambda(\mathbf{x})\left(\frac{\partial u_k}{\partial x_k}\right)\right]\delta_{ij}=0 \tag{2}$$

where u is displacement; x is a spatial component of coordinate axes $\mathbf{x}$; G is the shear modulus; λ is Lame's parameter; δ is the Kronecker delta; and indices i and j span orthogonal spatial coordinates 1, 2, and 3. The subscript k implies summation over i and j. In this formulation, x_1, x_2, and x_3 are equivalent to Cartesian coordinates x, y, and z. These equations describe elastic behavior in a 3D domain comprising a spatial distribution of isotropic elastic properties and no body forces [28]. For anisotropic materials, the scalar elastic moduli are replaced with tensors. FEMs are the best tool for approximations that satisfy these equations over arbitrary geometric domains. Note that the quality of an FEM approximation to a solution that satisfies Eq. (2), and thus quality of predictions, depend on the model design and configuration described in the next section.

If the elastic properties are taken outside of the spatial derivatives, then Eq. (2) reduces to the Navier formulation Sadd [29] and; with the appropriate loading, boundary, and initial conditions; describes the behavior of an HEHS domain that is commonly assumed in deformation models of point [13] (**Figure 2**) and dislocation [30] deformation sources. However, the fundamental existence of an active volcano requires localized complexity, or a distribution of material properties, $G(\mathbf{x})$ and $\lambda(\mathbf{x})$. If the properties are spatially uniform, then a volcano would not be present. Furthermore, because an elastic system is linear, transient deformation of an elastic system may be achieved by casting the state variables as velocities, rather than displacements, via a time-dependent loading scheme.

These governing equations can be adapted to account for more complicated transient viscoelastic quasi-static behavior. For example, the strain rate ($d\varepsilon/dt$) for a Maxell viscoelastic material is a function of the viscosity (μ), which is in turn a function of temperature:

$$\frac{d\varepsilon}{dt} = \frac{1}{2\mu}\sigma_d^n \quad \text{and} \quad \mu = A\exp\left(\frac{E}{R_B T}\right) \tag{3}$$

where σ_d is the deviatoric stress, A is a constant, E is the activation energy, and R_B is the Boltzmann constant. Because strain is defined as a displacement derivative, it is easy to visualize how the strain rate in Eq. (3) propagates into Eq. (2). The strain rate increases as a nonlinear function of increasing T. It is important to note that the system converges to static elastic behavior with $T|_{x,y,z,t} \to 0$, which conflicts with the presence of an active magma chamber. Alternatively, the governing equations (Eq. (2)) can be augmented to account for transient poroelastic or thermoelastic behavior due to coupling of stress with fluid or thermal diffusion, respectively [31]. FEMs satisfy this critical need to account for such complexities.

3.2.3. Boundary conditions

Boundary conditions constrain the constants of integration resulting from solutions to the governing equations (Eq. (2)) and define how the domain behaves along the domain boundaries. HEHS domains require a flat, stress-free surface and lateral and depth boundaries extending to infinity and having zero displacement (**Figure 2**). On the other hand, FEMs allow for great flexibility in boundary specifications. All external FEM boundaries (and internal boundaries, if they exist) require boundary condition specifications to constrain the displacement

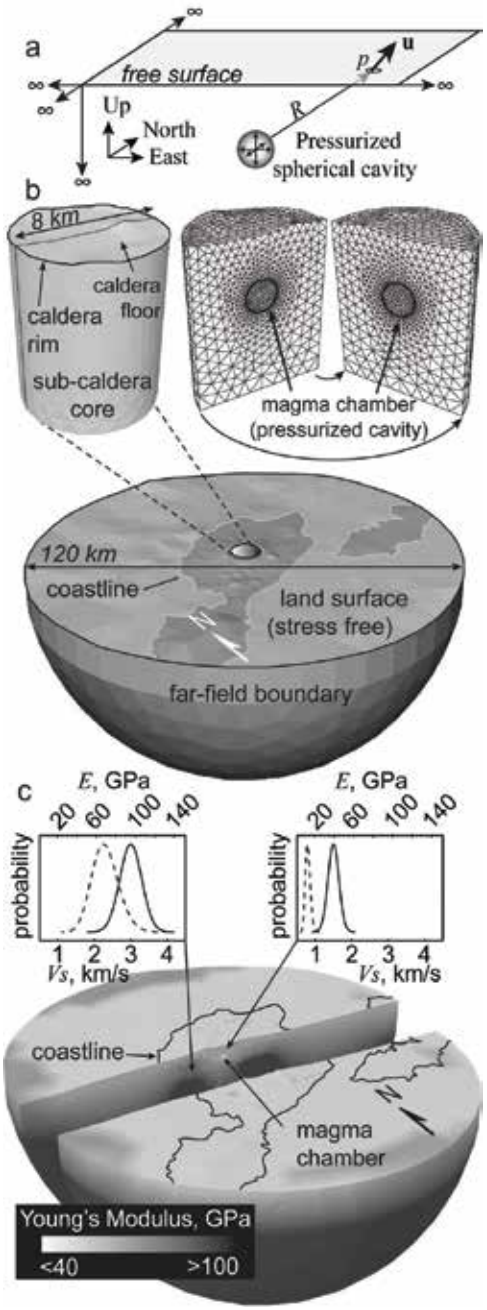

Figure 2. Model configuration for Okmok volcano, Alaska. (a) Homogeneous elastic half-space (HEHS). Analytical solutions predict the displacement of point p in response to the pressurized spherical cavity embedded in an HEHS domain (uniform elastic properties). The point, p, and cavity are separated by the Euclidean distance R. (b) FEM domain. Exploded views reveal the subcaldera core, pressurized magma chamber, and mesh. (c) Distribution of material properties for. Probability distributions for Young's modulus, E, (dashed curves) calculated from shear wave, V_s, distributions (solid curves) are shown for two example locations. The domain is shown in exploded view to reveal the internal structure. Modified from Masterlark et al. [10].

solution over the domain. These specifications include displacements, displacement derivatives, stress, or stress-dependent displacements. The default boundary condition of the FEM formulation is stress-free, which is appropriate for the land surface of seafloor. The lateral and depth spatial extents of the domain are generally represented as zero displacement, $u_{1,2,3} = 0$ (pinned). Such boundaries can be further constrained to zero displacement and rotation, $u_i = du_i/dx_i = 0$ (encastre). Alternatively, boundaries may be cast as specified strain, stress, or stress-dependent displacement. Overly constrained boundaries will adversely propagate into the domain solution, while insufficient constraints lead to arbitrary solid body motion. Therefore, the choice of an appropriate configuration of boundary conditions is an important challenge that requires sensitivity analyses. A common goal is to have far-field boundaries that do not adversely propagate unwanted artifacts into the near field. Sensitivity analyses that investigate a variety of boundary condition domain far-field configurations are necessary to ensure that this goal is achieved.

3.2.4. Initial conditions

The governing equations express displacement with respect to the initial conditions. For volcano deformation, the initial conditions are usually steady state. These conditions should not be interpreted as zero stress, strain, or displacement. Instead, steady state condition implies time independence. The initial conditions for elastic systems are always steady state, as is self-evident by the absence of time in Eq. (2).

3.2.5. Loading conditions

The loading conditions can be interpreted as the impulse that causes the model to respond or deform. Alternatively, without loading, the model will remain in the state of defined by the initial conditions. Loading may take the form of elastic dislocations that can be implemented in FEMs via kinematic constraint equations [1]. These dislocations are useful for simulating fault parallel modes of earthquakes or opening modes of dikes and sills. Pressurized magma chambers may be simulated with an applied pressure, P_0, to the cavity walls or as mass flux of magma, the latter of which results in a changing magma pressure and volume that depends on the choice of fluid properties [17]. Surface loads may be applied as specified pressure along the free surface to simulate loading of glaciers or lava flows [6]. For all of these examples, the response of an elastic domain is a linear function of the load. More sophisticated models may include poroelastic or thermoelastic loads. For the remainder of this chapter, we will focus on pressure loads that are common in models of volcano deformation.

3.2.6. Calibration targets

Some data are used to constrain the model configuration. For example, a distribution of material properties may be estimated from a seismic tomography model of the volcano. However, other data, such as geodetic data that sample the surface deformation of a volcano, may be used to quantify some process of interest, such as the location and pressurization caused by an episode of magma intrusion. The magma intrusion is characterized by calibration parameters that are adjusted in a way that produces predictions that best account for the

calibration targets. Rather than use all relevant data for calibration, it is important that the modeler reserve some of the data for the verification analyses discussed below. A pitfall of many inverse (calibration) analyses of geodetic data is that all the geodetic data are used in the inversion to estimate the calibration parameters. Consequently, modelers may report that the model with the calibrated parameters well-predicts these data. However, this method is faulty because the inverse analysis forces the suite of parameters that best fit the data. Thus it should be no surprise that the model well-predicts the data. However, the reliability of such a model is unknown because the model is not tested against information that is independent of the inverted data. Verification data are reserved for this independent test and are necessary to demonstrate a model's reliability.

3.2.7. Calibration parameters

Calibration (adjustable) parameters are identified as part of the conceptual model. These parameters will be calibrated to the data that are identified as calibration targets. Decisions regarding the choice of calibration parameters are strongly controlled by the availability of the constraining information. Well-studied volcanoes having more data warrant more calibration parameters, whereas volcanoes having relatively sparse information are best simulated with fewer parameters.

An equally important consideration for defining the number of parameters is whether the model response is a linear or nonlinear response to a given parameter. A model having numerous linear calibration parameters may be much easier to calibrate via matrix inversion methods that a model having a few nonlinear calibration parameters that require sampling of a multidimensional nonlinear parameter space. For example, a single execution of an FEM is necessary to characterize the model response to each linear parameter. For linear parameters, the resulting response is a linear function of the parameter impulse –doubling the impulse doubles the response. This is a convenient property of linear systems. However, numerous samples are required to adequately characterize the model response to a single nonlinear parameter. For example, doubling the depth of a magma chamber having a given pressurization does not double the resulting surface deformation. The number of samples required to characterize nonlinear parameters depends on the degree of nonlinearity, which is generally poorly known for sophisticated FEM domains. While experience plays a role in deciding on the specific suite of calibration parameters, the calibration process itself will quantitatively reveal the resolution and precision of the calibration parameters. Furthermore, testing and sensitivity analyses may be needed to guide the identification of calibration parameters.

3.2.8. Sensitivity analyses

Some conceptual model components are specified a priori and justified based on analogous published studies or based on the modeler's experience. However, other components may have multiple options for which the implications are not clearly understood. Sensitivity analyses are identified that will be conducted to test how the model predictions will respond to variations in model design. Almost any question regarding the model design, construction, execution, and interpretation posed during any phase of the protocol may be addressed with

sensitivity analyses. Modelers should expect to conduct an exhaustive array of sensitivity analyses over the protocol. Alternatively, if all the answers are known, then modeling is not necessary and purpose must be re-defined.

3.3. Model assembly and execution

3.3.1. Solution method

The modeler identifies the specific mathematical method and precisely explains components. The components of a mathematical model are governing equations, boundary conditions, loading specifications, and initial conditions. The mathematical methods used for analyses of deformation are separated into two distinct classes. First, analytical solutions are closed form equations. These equations are solutions to boundary value problems. A rich panoply of analytical solutions are available to simulate a variety of volcano deformation scenarios for the Earth's lithosphere [32]. Likewise, analytical solutions are available for static deformation due to surface loads applied to lithospheric plates [16, 33, 34]. However, these analytical solutions require simplifying assumptions that cannot account for known complexities of an active volcano. These assumptions may include some combination of half space domains having either homogeneous or layered isotropic material properties. While such analytical solutions are attractive because of their low computational requirements, their true cost lies in their inability to account for the known complexity of an actively deforming volcano. It is well known that such complexities strongly influence predictions of volcano deformation (For example, see [10] and references therein).

This chapter is concerned with FEMs, which allow for a broad flexibility in model design and simulation. A vast body of literature documents the capabilities and limitations of the finite element method methods [35, 36], which was first proposed by [37]. Accordingly, the formulation of FEMs is far beyond the scope of this chapter and we refer the reader to the availability of thorough textbook treatments of FEM formulation. Instead our focus is on how to implement FEMs rather than formulate them. While there are some initiatives to provide finite element code for deformation studies in Earth science (e.g., Computational Infrastructure for Geodynamics, https://geodynamics.org), there are some excellent proprietary general purpose FEM codes, such as Abaqus and COMSOL. Such codes may be used to build FEMs that honor the conceptual model devised as described above in Section 3.2.

The FEM method divides the geometry of the simulated domain into an assembly of discrete elements. The mechanical behavior is defined piecewise over each element using constitutive mechanical relationships and the resulting assembly is simultaneously integrated over the domain to minimize global energy constraints in the context of specified initial, boundary, and loading conditions. It is this piecewise formulation that bestows FEM with powerful capabilities to simulate the deformational behavior (satisfy Eq. (2)) over distributions of material properties in arbitrary geometric domains that simulate the complex systems of active volcanoes (e.g., **Figure 3**). The solution for an FEM approximation is a matrix problem, for which a greater number of elements translates to a bigger matrix and consequently, greater computing requirements. Therefore, an FEM is inherently a matrix formulation having a size

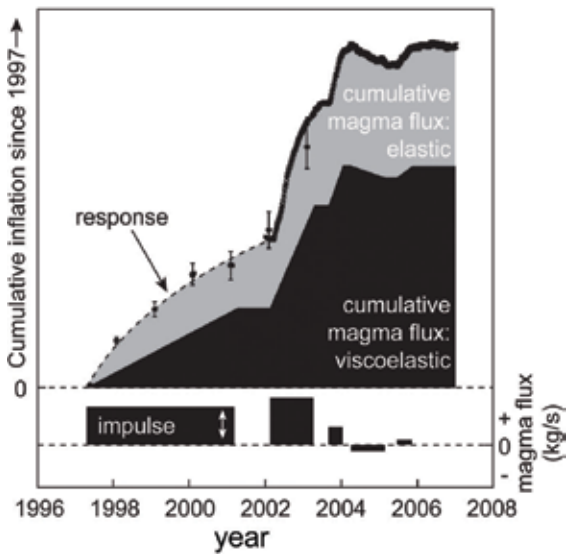

Figure 3. Influence of rheology on interpretations of transient deformation. InSAR and GPS data reveal the transient deformation between the 1997 and 2008 eruptions of Okmok. 1σ error bars are given for InSAR and GPS results, shown as closely-space black stars, span 2002–2007. The estimated magma re-supply, depends on the rheology of the system. The cumulative magma flux for an elastic system (gray + black polygon) linearly tracks the response curve. The response curve for a viscoelastic rheology is a function of magma flux impulses convolved with the viscoelastic response, the latter of which may contribute an additional ~50% to the deformation signal [17]. Modified from Masterlark et al. [10].

that depends on the number of elements that comprise the domain mesh. The quality of the FEM solution is a function of the quality of the mesh, the latter of which is a function of the shape and size of the elements. The FEM approximation converges to an exact solution as the characteristic element size converges to zero.

This leads the modeler to the fundamental problem of a trade-off between the quality of the FEM approximation and the limitations of the available computing resources. For a given domain space, a larger number of smaller elements translates to a larger matrix problem that may become unfeasible. Alternatively, a smaller number of large elements yields a smaller matrix problem that requires nominal computing resources, but with a cost of a relatively poor approximation to a solution to Eq. (2). The design of a suitable mesh is a fundamental challenge for designing FEM simulations. A common approach is to tessellate the near field region of the domain with relatively small element sizes that become larger toward the far-field boundaries. This strategy accounts for the need for a more refined mesh in areas having a relatively higher strain gradient (c.f. Eq. (2)), such as near the deformation source compared to the far-field boundaries that experience relatively low strain gradients.

3.3.2. Validation

Validation ensures a numerical model is working properly and model design is functioning. We can validate the FEM configurations (e.g., mesh, boundary conditions, and loading conditions) by comparing model predictions to known benchmarks, which ideally come from exact

analytical solutions. Available analytical solutions for displacement due to various loading strategies are limited to very specialized configurations, such as dislocations and pressurized cavities embedded in HEHS domains [13, 30]. It is because of these limitations that we turn to FEMs in the first place.

However, once we define our working FEM configuration, we can often simplify the configuration so that it is not too different from the more complicated working FEM counterpart, but are sufficiently similar to an HEHS configuration. For example, consider an FEM that simulates a pressurized sphere embedded in a domain having a distribution of material properties, a free surface having the geometric irregularity of topography, far-field boundary conditions of zero displacement, and initial conditions of equilibrium. We can modify the domain to have spatially constant elastic properties and a flat free surface. Such a model reasonably approximates the configuration of Mogi [13] and if FEM prediction errors are small, say <5%, then the FEM may be considered to be validated. If prediction errors are too large, then the FEM configuration is problematic. Ideally, any FEM of volcano deformation should be validated.

For cases where the FEM configuration is not amenable to reconfigurations that adequately resemble the configuration of an analytical solution configuration, the modeler must rely on sensitivity analyses to demonstrate the adequacy of the FEM approximation. For example, how do we know if a mesh is adequately refined for a model that cannot be validated with an analytical solution? First, we must benchmark the FEM formulation, if it has not already been done so. Second, we can then compare predictions from models having increasing refined mesh configurations. Once the modeler determines that increased mesh refinement does not change the predictions, then the mesh is adequate. We can devise such strategies of sensitivity analyses to examine the influence of a wide range of FEM configuration aspects, with the goal of demonstrating that the model is performing correctly. Predictions, estimations, and interpretations based on FEMs that are either not validated or lack sufficient sensitivity analyses of the domain configuration are suspect.

3.4. Calibration

3.4.1. Forward model

The predicted three-component displacement, $\mathbf{u}_{p,i}$, for location i due to a magma chamber pressurized by ΔP is:

$$\mathbf{u}_{p,i} = P_s \mathbf{u}_i \tag{4}$$

where $\Delta P = P_s \cdot P_0$; and $\mathbf{u}_i$ is a three-component displacement vector $[u_{x,i}, u_{y,i}, u_{z,i}]$ predicted by the FEM having applied load P_0 and a magma chamber having a specified location and shape embedded in a domain having a specified distribution of material properties. Note that the deformation is a linear function of pressurization and nonlinear functions of the magma chamber location or shape and distribution of domain materials. The LOS displacement, u_L, for the i^{th} InSAR pixel is a linear combination of contributions from the pressurized magma chamber and plane-shift:

$$u_{L,i} = P_s \mathbf{u}_i \mathbf{L}^T + a_1 x_i + a_2 y_i + a_3 \tag{5}$$

where L is the LOS unit vector; a_i are coefficients of a plane to account for the displacement at an arbitrary reference location and horizontal components of the range gradients attributed to errors in modeling orbital effects [5]; and the superscript T denotes the matrix transpose operator. The matrix formulations for Eqs. (4) and (5), respectively, are:

$$\mathbf{d}_p = \mathbf{G}\,\mathbf{m} = [\mathbf{u}][Ps] \quad \text{and} \quad \mathbf{d}_L = G\,m = \left[\mathbf{u}\mathbf{L}^T, \mathbf{x}, \mathbf{y}, \mathbf{1}\right]\left[P_s, a_1, a_2, a_3\right]^T \tag{6}$$

where **G** is a matrix of Greens functions, **m** is the parameter vector, **d** is the column vector of data, and **1** is a unity vector. The InSAR data, $\mathbf{d}_L$, have locations given by column vectors **x** and **y**. The complete data vector that includes both GPS and InSAR data may be constructed by appending the relationships given in Eq. (6). The matrix representation for an assembly of calibration data and parameters is:

$$\mathbf{Gm} = \mathbf{d} \quad \text{and} \quad \mathbf{e} = \mathbf{d} - \mathbf{Gm} \tag{7}$$

where **G** is a matrix of Green's functions, **m** is a vector of linear calibration parameters, **d** is a column vector of the data, and **e** is a vector of prediction errors for the corresponding data [23]. The forward model predicts the displacements for a given **G** matrix and vector **m**.

3.4.2. Inverse model

The inverse model estimates the calibration parameters based on the data. These estimates include both a central tendency and sense of variability or uncertainty for each calibration parameter (**Figure 3**). The matrix **G** depends on the specific model configuration that may include nonlinear calibration parameters. Variations in the nonlinear calibration parameters will impose an asystematic influence on the G matrix, whereas the vector of linear calibration parameters may be readily estimated with linear inverse methods [9, 23, 38]. We emphasize the importance of recognizing that a forward model is the linkage between the calibration data and the calibration parameters. SHyT techniques that implement, for example, F-tests (Eq. (1)), provide relatively simple, but powerful methods to establish the suitability of a particular model or compare the performance of competing models to account for observed deformation data based on assessment of bulk misfit.

3.4.2.1. Linear calibration parameters

Linear calibration parameters comprise the vector **m**. We can find a least-squares estimate (minimizing $\mathbf{e}^T\mathbf{e}$) for **m**, by pre-multiplying both sides of Eq. (7) with the inverse of the data covariance matrix, $\mathbf{C}_d$, and then inverting to estimate **m** is a way that accounts for the propagation of geodetic data uncertainties:

$$\mathbf{C}_d^{-1}\mathbf{Gm} = \mathbf{C}_d^{-1}\mathbf{d} = \mathbf{G}_c\mathbf{m} = \mathbf{d}_c \quad \text{and} \quad \mathbf{m} = \left(\mathbf{G}_c{}^T\mathbf{G}_c\right)^{-1}\mathbf{G}_c{}^T\mathbf{d}_c \tag{8}$$

where σ_j is the uncertainty of the j^{th} element of **d**. Neglecting the data uncertainties implies that $\mathbf{C}_d$ is an identity matrix, for which the uncertainties are unity for all data. The uncertainty of the parameters is characterized by the parameter covariance matrix, $\mathbf{C}_m$:

$$\mathbf{C}_m = \left(\mathbf{G}_c^T \mathbf{G}_c\right)^{-1} \mathbf{G}_c^T \mathbf{d}_c \mathbf{C}_d \mathbf{G}_c \left(\mathbf{G}_c^T \mathbf{G}_c\right)^{-1} \quad (9)$$

Eqs. (8) and (9) provide a mechanism for providing estimates of central tendency and uncertainties for linear calibration parameters, in a way that accounts for the uncertainties of the data. For linear inverse methods, the parameter PDFs are Gaussian distributions that are conveniently characterized with 95% intervals $\mathbf{m} \pm 1.96\ \mathrm{diag}(\mathbf{C}_m)^{1/2}$. Model performance and comparisons from linear inverse methods are readily amenable to ShyT analyses (e.g., Eq. (1)) that may be used to address the scientific questions specified in Section 3.1.

3.4.2.2. Nonlinear calibration parameters

Nonlinear calibration parameters are embedded in the structure of **G** rather than in **m**, the latter of which is the case for linear parameters. The nonlinear inverse method involves perturbing a nonlinear parameter and examining its influence on **G** and the forward model predictions. A simple strategy is to conduct a predefined grid search of nonlinear parameters to find an optimal solution. However, such a strategy is biased by the modeler's expectations of the best solution. Furthermore, the PDF of the parameters will have a resolution that is biased by the grid design. Monte Carlo sampling of a nonlinear parameter space involves random perturbations of a nonlinear parameters and investigating model predictions. An infinite sampling of the parameter space will precisely define nonlinear parameter PDFs. However, as each sampling requires an FEM re-compute, pure Monte Carlo methods are only useful for models having few calibration parameters because the necessary number of FEM executions necessary to characterize PDF of the parameter space is n_s^M, where n_s is the number of samples per nonlinear parameter and M is the number of nonlinear parameters [39]. Directed Monte Carlo sampling methods, such as Markov Chain Monte Carlo and Simulated Annealing [39], combine the efficiency of gradient methods with the benefits of random sampling to calibrate nonlinear parameters. Masterlark et al. [10] used directed Monte Carlo methods to calibrate a few hundreds of nonlinear parameters in FEM-based models of volcano deformation (e.g., **Figure 4**).

3.5. Verification

The calibration process identifies the model and suite of calibrated adjustable parameters that best predict the calibration data. Thus, it is a circular argument to suggest a model is reliable if the calibrated model well-predicts the data, because the calibration process forces the model to do so. Instead, verification addresses the reliability of a model by confronting predictions with data that are independent of the calibration process. For example, an active volcano may have both InSAR and GPS data that characterize the deformation of the volcano. Instead of using both InSAR and GPS in the calibration process, one might calibrate to the InSAR and then quantitatively assess the calibrated model's ability to predict the GPS data. A validated, calibrated, and verified model is necessary to provide reliable predictions.

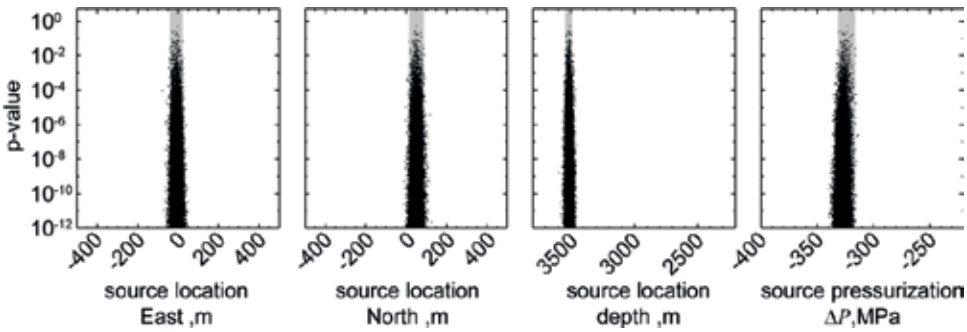

Figure 4. Parameter estimate PDFs, cast as p-values. The geometric location of the spherical source requires three nonlinear parameters (first three panels). The fourth panel is the linear pressurization parameter. Each black dot represents results from sampling a single parameter suite. This example includes 130,000 normal sample suites. Vertical gray bars are 99% confidence intervals. Note the logarithmic scale for the p-values. Modified from Masterlark et al. [10].

3.6. Post-audit

A well-crafted hypothesis provides an explanation of some phenomenon, predicts the outcome of future observations, and must include a chance of showing the hypothesis to be wrong. We give an analogous treatment to a model of volcano deformation –A reliable model provides an explanation of volcano deformation, predicts the outcome of future observations, and must include a chance of showing the model predictions to be wrong. The post-audit addresses the latter two requirements. A deformation model should be confronted with new geodetic or other relevant information as it becomes available. This confrontation should take the form of SHyT analyses. If the model fails, the modeler must re-visit an earlier stage of the protocol, as appropriate. The post-audit requirement recognizes that all models are wrong and require continuous evaluation in an effort to converge on the truth.

4. Reporting

The protocol discussed above outlines the components that should be included in a written modeling report. Section 3 is intended for use as a checklist for both authors and reviewers of modeling analyses for volcano deformation. While all components of the protocol are necessary, the validation step is particularly important because it is a mechanism that demonstrates the adequacy of numerous model design aspects. Unfortunately, validation is often missing from written reports of FEM-based analyses of volcano deformation. This oversight undermines the reliability of any estimates, results, interpretations, discussions, and conclusions based on FEM analyses. Furthermore, few FEMs of volcano deformation include verification. This problem undermines the reliability of model predictions. The general lack of validation and verification in reported FEM-based analyses of volcano deformation is sufficiently severe that we recommend that authors who conduct FEM-based analyses of volcano deformation neither submit manuscripts without validation and that editors and reviewers reject any manuscript having FEM analyses of volcano deformation that lack validation, verification, and a mechanism to confront a model with a post-audit.

Acknowledgements

This work is funded, in part, by NSF EAR 1316082 and NASA ESI 16-ESI16-0037.

Author details

Timothy Masterlark* and Sui Tung

*Address all correspondence to: masterlark@sdsmt.edu

South Dakota School of Mines, Rapid City, SD, USA

References

[1] Masterlark T. Finite element model predictions of static deformation from dislocation sources in a subduction zone: Sensitivities to homogeneous, isotropic, Poisson-solid, and half-space assumptions. Journal of Geophysical Research. 2003;**108**:17

[2] Anderson MP, Woessner WW. Applied Groundwater Modeling: Simulation of Flow and Advective Transport. 1st ed. San Diego: Elsevier; 1991. p. 381

[3] Meerschaert MM. Mathematical Modeling. 4th ed. Amsterdam: Associated Press; 2013. p. 365

[4] Feigl K, Thurber CH. A method for modelling radar interferograms without phase unwrapping: Application to the M 5 Fawnskin, California earthquake of 1992 December 4. Geophysical Journal International. 2009;**176**:491-504

[5] Massonnet D, Feigl K. Radar interferometry and its application to changes in the Earth's surface. Reviews of GeophysicsReviews of Geophysics. 1998;**36**:441-500

[6] Lu Z, Masterlark T, Dzurisin D. Interferometric synthetic aperture study of Okmok volcano, Alaska: Magma supply dynamics and post-emplacement lava flow deformation. Journal of Geophysical Research. 2005;**110**:18

[7] Masterlark T, Lu Z. Transient volcano deformation sources imaged with interferometric synthetic aperture radar: Application to Seguam Island, Alaska. Journal of Geophysical Research. 2004;**109**:16

[8] Lohman RB, Simons M. Some thoughts on the use of InSAR data to constrain models of surface deformation: Noise structure and data downsampling. Geochemistry, Geophysics, Geosystems. 2005;**6**:12

[9] Gubbins D. Time Series Analysis and Inverse Theory for Geophysicists. Cambridge: Cambridge University Press; 2004. p. 272

[10] Masterlark T, Donovan T, Feigl KL, Haney M, Thurber C, Tung S. Volcano deformation source parameters estimated from InSAR: Sensitivities to uncertainties in seismic tomography. Journal of Geophysical Research. 2016;**121**:3002-3016

[11] Masterlark T, Feigl KL, Haney MM, Stone J, Thurber CH, Ronchin E. Nonlinear estimation of geometric parameters in FEMs of volcano deformation: Integrating tomography models and geodetic data for Okmok volcano, Alaska. Journal of Geophysical Research. 2012;**117**:17

[12] Simmons G, Brace WF. Comparison of static and dynamic measurements of compressibility of rock. Journal of Geophysical Research. 1965;**70**

[13] Mogi K. Relations between the eruptions of various volcanoes and the deformations of the ground surface around them. Bulletin Earthquake Research Institute, University of Tokyo. 1958;**36**:99-134

[14] Haney MM, Nies A, Masterlark T, Needy S, Pedersen R. Interpretation of Rayleigh-wave ellipticity observed with multicomponent passive seismic interferometry at Hekla volcano, Iceland. The Leading Edge. 2011;**30**:526-531

[15] Cayol V, Cornet FH. Effects of topography on the interpretation of the deformation field of prominent volcanoes-application to Etna. Geophysical Research Letters. 1998;**25**: 1979-1982

[16] Turcotte DL, Schubert G. Geodynamics. 2nd ed. Cambridge: Cambridge University Press; 2001. p. 456

[17] Masterlark T, Haney M, Dickinson H, Fournier T, Searcy C. Rheologic and structural controls on the deformation of Okmok volcano, Alaska: FEMS, InSAR and ambient noise tomography. Journal of Geophysical Research. 2010;**115**:22

[18] Del Negro C, Currenti G, Scandura D. Temperature-dependent viscoelastic modeling of ground deformation: Application to Etna volcano during the 1993-1997 inflation period. Physics of the Earth and Planetary Interiors. 2009;**172**:299-309

[19] Finney B, Turner S, Hawkesworth C, Larsen J, Nye C, Grorge R, et al. Magmatic differentiation at an island-arc caldera: Okmok volcano, Aleutian islands, Alaska. Journal of PetrologyJournal of Petrology. 2008;**49**(5):857-884

[20] Masterlark T, Eichelberger J, Freymeuller J, Haney M, Hurwitz S, Izbekov P, Larsen J, Nakada S, Neal C, Roggenthen W, Thurber C. Sampling and in-situ Observations of Okmok (SINOOK). National Science Foundation (NSF) Workshop: Drilling Active Tectonics and Magmatism. Park City, UT; 2013. p. 5

[21] Ustunisik G, Kilinc A, Nielsen RL. New insights into the processes controlling compositional zoning in plagioclase. Lithos. 2014;**200-201**:80-93

[22] Masterlark T, Hughes KLH. The next generation of deformation models for the 2004 M9 Sumatra-Andaman earthquake. Geophysical Research Letters. 2008;**38**:45

[23] Menke W. Geophysical Data Analysis: Discrete Inverse Theory. 3rd ed. Amsterdam: Elsevier; 2012. p. 293

[24] Davis JC. Statistics and Data Analysis in Geology. 3rd ed. New York: John Wiley & Sons; 2002. p. 638

[25] Burnham KP, Anderson DR. Understanding AIC and BIC in model selection. Sociological Methods & Research. 2004;**33**:261-304

[26] Simons M, Minson SE, Sladen A, Ortega F, Jiang J, Owen SE, et al. The 2011 magnitude 9.0 Tohoku-Oki earthquake: Mosaicking the megathrust from seconds to centuries. Science. 2011;**332**:1421-1425

[27] Kruschke JK. Doing Bayesian Data Analysis: A Tutorial with R, Jags, and Stan. 2nd ed. San Diego: Academic Press Inc; 2014. p. 776

[28] Vasco DW, Charles W Jr, Karasaki K, Marques O. Geodetic imaging: Reservoir monitoring using satellite interferometry. Geophysical Journal International. 2002;**149**:555-571

[29] Sadd MH. Elasticity–Theory, Applications, and Numerics. 3rd ed. Amsterdam: Elsevier; 2014. p. 582

[30] Okada Y. Internal deformation due to shear and tensile faults in a half-space. Bulletin of the Seismological Society of America. 1992;**82**:1018-1040

[31] Wang HF. Theory of Linear Poroelasticity: With Applications to Geomechanics. Princeton University Press: Princeton; 2000. p. 297

[32] Segall P. Earthquake and Volcano Deformation. Princeton University Press: Princeton; 2010. p. 432

[33] Brotchie JF, Silvester R. On crustal flexure. Journal of Geophysical Research. 1969;**74**(22): 5240-5252

[34] Grapenthin R, Sigmundsson F, Geirsson H, Arnadottir T, Pinel V. Icelandic rhythmics: Annual modulation of land elevation and platespreading by snow load. Geophysical Research Letters. 2006;**33**:5

[35] Huebner KH, Dewhirst DL, Smith DE, Bryan TG. The Finite Element Method for Engineers. 4th ed. New York: John Wiley & Sons, Inc; 2001. p. 720

[36] Zeinkiewicz OC, Taylor RL. The Finite Element Method for Solid and Structural Mechanics. Oxford: Elsevier, Ltd; 2005. p. 631

[37] Courant R. Variational methods for the solution of problems of equilibrium and vibrations. Bulletin of the American Mathematical Society. 1943;**49**:1-23

[38] Aster RC, Borchers B, Thurber CH. Parameter Estimation and Inverse Problems. San Diego: Elsevier Academic Press; 2005. p. 301

[39] Press WH, Teukolsky SA, Vetterling WT, Flannery BP, editors. Numerical Recipes: The Art of Scientific Computing. 3rd ed. New York: Cambridge University Press; 2007. p. 1235

Chapter 9

Mechanics of Magma Chamber with the Implication of the Effect of CO_2 Fluxing

Simakin Alexander G. and Ghassemi Ahmad

Additional information is available at the end of the chapter

http://dx.doi.org/10.5772/intechopen.71655

Abstract

The rheological contrast between the viscous magma in the magmatic chambers and the surrounding rocks, having an elastic behavior, has allowed for a disturbance of the stress field, which, at a magmatic pressure unequal to the lithostatic one, can give rise to various modes of rock failure, leading to an eruption. In this context, one of the most important problems is represented by the mechanical stability of both large and extra-large magmatic chambers, such as the Yellowstone magmatic chamber. Due to its large volume, the critical overpressure necessary to start the volcanic eruption requires large added volumes of magma and fluids. The viscous relaxation of deviatoric stresses in the thermal areole of large chambers on a time scale of more than few years increases the critical volumetric flow rate of magma to 0.1–1 km^3/yr. In this chapter, we have demonstrated that the deep CO_2 flux related with the underplating of basaltic magma has significantly enhanced the expansion of the magmatic chamber. In Yellowstone, the CO_2 fluxing can be the driver of its cyclic uplift and subsidence having a period of several decades. The extraction of water from the silicic melt by CO_2 increases the volume of the fluid up to 4 times, thus multiplying the pumping effect of the fluid. In a long term, simple estimates have also indicated that the CO_2 flux can significantly contribute to the heat balance, which can be up to the half one with respect to the value associated with the basaltic magma. The integrated stability index of a magma chamber has been tested during the beginning of the interglacial periods, when the rate of generation of the basaltic magma in a plume setting is of an order of magnitude higher than the normal one. The spikes of rhyolitic magmatism in some periods of the last Quaternary interglacials have been weakened for the Yellowstone case history. The last Pleistocene glaciation activated only strong hydrothermal eruptions, which may imply that at present, the level of CO_2 and basalt supply rate is not high enough to cause a major eruption in Yellowstone in the near future.

Keywords: magma chamber, viscoelasticity, CO_2, eruption, Yellowstone

1. Introduction

1.1. Basic relations

In a first approximation, a magmatic chamber can be regarded as the inclusion of a liquid in deformed elastic solid rocks. As a rule, viscous deviatoric stresses within this inclusion can be neglected and the stress state can be represented by hydrostatic pressure. The boundary between the enclosing rocks and magma can be approximately regarded as discrete. On this boundary, the continuity of the normal and zero tangential stress conditions are valid (e.g., [1]) or in vector notation:

$$\sigma \cdot n = P_m(t,x,y,z) \cdot n, \tag{1}$$

where n is normal to the chamber wall in point (x,y,z), P_m(t,x,y,z) is the magma pressure. The pressure of the magma depends on the deformation of the walls of the chamber, and also on the mass and state of the magma inside it [1]:

$$M(t) = \int_{V(P(t))} \rho(P_m(t,x,y,z))dV \tag{2}$$

Differentiating the r.h.s. and l.h.s. of Eq.(2) with respect to time while using the space averaged pressure $P_m(t) = P_0 + dP_m(t)$ and expressing $V_{ch} = V_{ch,0} + dV(t)$, $M(t) = M_0 + q_m t$ and $\rho = \rho_0(1 + dP_m(t))$ yields another form of Eq. (2) which is used, for example, in Ref. [2]:

$$\frac{dV_{\text{ch}}}{V_{\text{ch},0}} = -\frac{dP_m(t)}{K_m} + q_m dt / V_{\text{ch},0}\rho_0 \tag{3}$$

where K_m is effective bulk modulus of the multi-phase magma, $V_{ch,0}$ and ρ_0 are reference magma chamber volume and magma density, q_m is mass flux of magma. When magma contains fluid bubbles its compressibility increases significantly [2]. Change of the magma chamber volume at the hosting rocks deformation can be expressed in effective form used in theoretical analysis as equation of state (dependence of the volume from the magma pressure P_m, which is a reference pressure in the apical part of chamber boundary when hydrostatic pressure gradient is included)

$$dV_{\text{ch}}/V_{\text{ch},0} \quad = \quad dP_m(t)/K_{\text{ch}} \tag{4}$$

A chamber volume at the rising pressure increases not only due to the rocks compression as suggested, for example, in Ref. [2] but also due to the uplift of the surface and roof buckling. Therefore effective chamber bulk modulus K_{ch} can be at least order of magnitude smaller than that of the host rocks. Roof faulting reduces K_{ch} several times more [1]. In the correct numerical models boundary condition (1) and EOS of magma (2 or 3) are applied simultaneously (fully coupled system of equations) and pressure is determined iteratively at each time step.

The mechanical modeling of the magma chambers is mainly aimed at:

1. Prediction of localization and mode of the failure of the host rocks including chamber roof, volcano cone or in more general term magmatic—tectonic coupling;
2. Localization of the transport of magma out and into the chamber by dykes;
3. Simulation of processes during a volcanic eruption or on the way to an eruption, including the mechanical effects of filling the chamber with melts and fluids, the magma outflow through dykes, the magma crystallization and the degassing.

1.2. Tectonic-magmatic coupling

A strong rheological contrast between the magma and the rocks leads to the localization of the strains around the magmatic chamber, so that the rock deformation (and failure) is coupled with the magma emplacement on a global scale, especially in an extensional regime [3]. In a compressional tectonic setting, the magma chamber attracts thrusts, as shown in analog experiments and explained with an analytical solution for a circular hole in a compressed solid [4]. Simakin and Ghassemi [5] have studied numerically in 2D the effect of an elliptical magma chamber at shearing and showed that when interacting with the magmatic chamber, the strike-slip faults have experienced offset, similar to the step-over pattern.

In some situations, the influence of a pressurized magma chamber on a regional stress field can be represented by the solution of the problem of a pressurized circular hole in an elastic plate subjected to uniaxial stress at infinity [6]. The calculated directions of the maximum compressive main stress (s1) are initially perpendicular to the chamber walls and, with an increasing distance from the chamber, rotate to the far-field stress direction. The dykes propagate through magma fracturing along the s1 directions and perpendicular to the least compressive main stress (s2 in 2D) [7]. Taking into account the influence of dykes on the stress field makes theoretical prediction of the dyke directions almost identical to those observed for the West Peak intrusion, Colorado [6].

1.3. Influence of shape

The mechanical properties of the magmatic chambers beneath the volcanoes depend on the shape of chamber, its relative depth (ratio depth to width), the gravitational load of the volcanic cone over the chamber. In general, magma chambers are horizontally elongated, as can be judged by the shape of solidified intrusions [8]. However, small shallow chambers under volcanoes often have an isometric shape close to a spherical. There are several theoretical studies in which the interaction of such spherical chambers with the surface is analyzed.

1.3.1. Spherical and cylindrical chambers

A closed-form analysis (improving classic Mogi [9] solution) of the stresses around a spherical inclusion (3D) in an elastic half-space was presented by McTigue [10]. The model predicts that the conic dykes (magma fracturing) can be expected to initiate on a ring of maximum $\sigma_{\phi\phi}$ on the sphere's surface. The ring is delineated by planes (lines) drawn tangent to the sphere

through a point on the symmetry axis at the surface. An accurate analytical solution for cylindrical chamber (circular in 2D) in the elastic half space was presented in Ref. [11]. Based on their solution for direction of the most compressive principle stress, authors developed conception of the capture zone for the ascending magma. They suggested that the magma ascending from the generation level in the zone of the differential stress above 1 MPa, caused by the presence of magma chamber, moves along s1 directions toward it. Overpressurized spherical magma chamber redistributes s1 directions in its vicinity normal to its surface and thus attracts ascending magma.

1.3.2. Elliptic chamber

The distribution of stresses around elliptical chambers near the surface has been numerically studied by many researchers (see in Ref. [12]). The main features of such solutions (in 2D) are shown in **Figures 1** and **2**. Both the overpressurized (**Figure 1a**) and underpressurized (**Figure 1b**) elliptic chambers when interacting with a free surface create an arch pattern of the maximum differential stress (s1-s2). This parameter is twice larger than the maximum tensional principle deviatoric stress used in Ref. [11]). At the overpressure (**Figure 1a**), the preferred paths of dykes start at the edges of the chamber. Only a small part of the s1

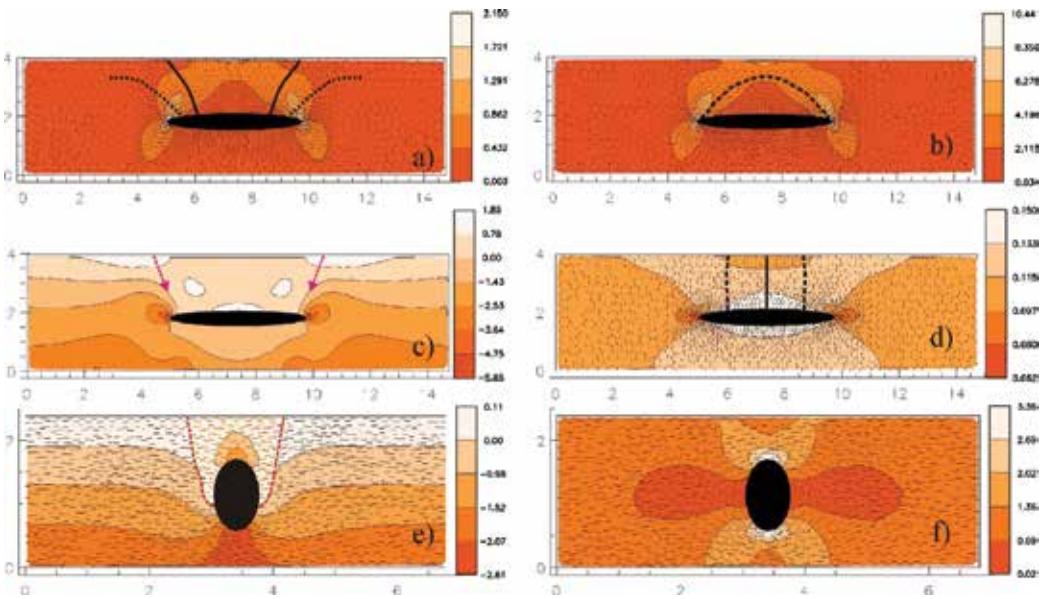

Figure 1. Examples of the calculated numerically in 2D elastic approximation of the stress fields around magma chambers without edifice. Spatial unit l_0 is arbitrarily chosen. Stress units are scaled with $\rho g l_0$, nondimensional Young modulus is 500 (at l_0 = 2500 m, ρ = 2500 kg/m^3, E = 30 GPa), Poisson's ratio ν is 0.2. Density of the magma and rocks are equal. Short dashes map s1 directions. (a) s1-s2, overpressurized chamber potential dykes trajectories are localized near the roof edges, (b) s1-s2 in the underpressurized magma chamber, reference pressure in the apical point is zero, hydrostatic gradient exists, (c) s2 in the underpressurized magma chamber, arrows depict normal faults starting on the surface, (d) s1-s2 at extension, lines show potential trajectories of dykes out of magma chamber, (e) s2, overpressurized vertical chamber, potentially rocks within red dashed line can be ejected with diatreme formation, (f) s1-s2, underpressurized vertical chamber.

http://dx.doi.org/10.5772/intechopen.71655

trajectories leads to the surface, while the other ones form the "saucer edges" known for shallow sills [13]. For the underpressurized chamber, the arch zone of the maximum shear stress (**Figure 1b**) can cause the detachment of the apical roof zone into the chamber. On the map of s2 values (**Figure 1c**), one can note zones of the tensile stress on the surface above the edges of the chamber. Many researchers [12, 14, 15] suggest an essential role in normal inward dipping ring faults in the roof collapse and caldera formation. When the regional fault crossed the roof of the chamber in a position parallel to the arch of maximum s1-s2, the stress is amplified and this configuration can initiate the trap-door caldera formation at an enough overpressure [1]. During the extension, the conjugate normal faults tend to develop in the roof. The magma transport directions are vertical, and they all lead to the surface (see **Figure 1d**). A vertical chamber with excess pressure creates a stress field (**Figure 1e**), which can potentially lead to diatreme formation. The underpressurized vertical chamber only slightly disturbs the stress field (**Figure 1f**).

1.3.3. Elliptic chamber with cone

A perfect volcanic cone is often formed with the repeated effusive eruptions from the magma chamber. The cone loading significantly modifies the stress field. Without overpressure, the cone focuses the trajectories of the magma toward the apex of the cone (see **Figure 2a**). This theoretical prediction looks reasonable, since the huge perfect cones of Fujiyama and Klyuchevskoi volcanoes have a height of about 4 km above the base and were formed in hundreds of the repeated eruptions with magma outflow through the central crater at the top.

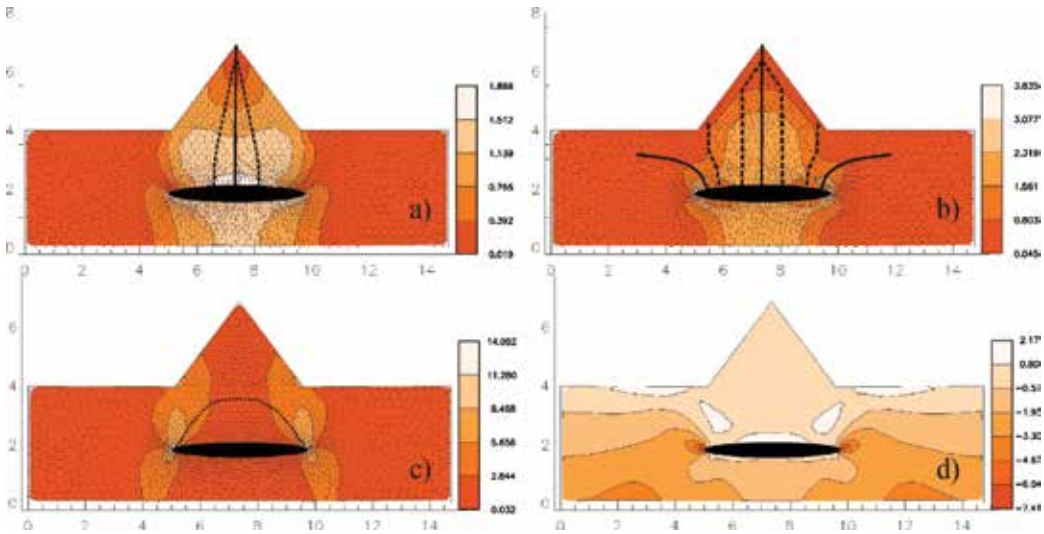

Figure 2. Calculated elastic stress field for magma chamber with edifice (calculations details as in Figure) (a) s1-s2 uncompensated and unrelaxed respond on the large edifice load, magma is focused toward cone top, (b) s1-s2 magma chamber is overpressurized, dykes trajectory toward the slope of cone appear, (c) s1-s2, reference $P_m = 0$, edifice slope instability is expected, (d) s2, reference $P_m = 0$, inward dipping normal faults formation is dictated by the extended linear zones with positive (tension) s2 in the roof.

However, at a strong overpressure, focusing is weakened, and some trajectories can lead to the slope and to the base of the volcano (see **Figure 2b**). At the same time, Pinel and Jaupart [16] predicted that the dykes propagating vertically are pushed out from the edifice edges, probably because they did not include the magma chamber in their model. At the underpressure, the extensional zones develop on the surface and in the roof. Outward dipping zones of shear fractures also arise including the cone slope bottom (see **Figure 2c**). The failure of the bases of the cone can lead to the instability of the slopes of the volcanic edifice and to the consequent emplacement of debris avalanches, followed by an explosive eruption and by the formation of a horseshoe-shaped caldera. In this case, another failure mode is represented by extensional fissures dipping inwards (**Figure 2d**).

1.4. Effect of viscous relaxation of the deviatoric stresses

All the shown modes of the interactions of the magma chambers with the hosting rocks have been obtained in an elastic approach as an immediate reaction on the magma arrival or its evacuation. The long-term deformations around the magma chambers should be treated with accounting for the stress relaxation. The viscoelastic Maxwell rheology is appropriate for the modeling of the rocks with temperature above c.a. 400°C at enough long times. The characteristic time scale of a viscous relaxation is a ratio of the viscosity to Young modulus of the heated rocks $\tau_{ve} = \eta/E$, that is, 1–30 years at η =1–10 $\times$ 10^{18} Pas, E = 10–30 GPa. For example, geodetic data on the unrest in the in Long Valley caldera in 1998 in the shorter time scale of several months were well interpreted accounting heated zones with viscosity $\eta = (1–100) \times 10^{16}$ Pa s [17].

In the two-dimensional numerical model by Simakin and Ghassemi [1], the viscosity of the rocks was calculated for the quasi-steady-state temperature field around an elliptic magma chamber. It was shown that at the constant influx rate (without magma loss into the dykes and at the eruptions), the magmatic overpressure (and corresponding deviatoric stresses in the hosting rocks) soon approaches an asymptotic value depending on the current magma chamber volume. This model is incomplete, since the paths leading to the probed current state of a chamber of a given size are not taken into account. Karlstrom et al. [18] have included the transient temperature field and the dyking in their complex model of magma chamber evolution. The mechanics was modeled with a rather complicated analytical solution for the circular inclusion in the viscoelastic half-space [18]. Obviously, many provisional features of viscoelastic shell were introduced due to the formal symmetry requirements. The model is not fully consistent, since the undefined initial chamber size has been used as a parameter in the evolutionary model. Melting and assimilation description is crude in comparison with special studies. Viscosity used in the calculations is not explicitly shown. Nevertheless by the order of magnitude results of both studies are quite close. According to Ref. [18], flux of about 0.004 km^3/y is required for a chamber with volume 37 km^3 to initiate eruption, similar parameters are obtained for the reference viscosity of the rocks in thermal aureole of $\eta = 5 \times 10^{19}$ Pa s at T = 400°C [1]. This value is within a range of the typical magma supply rates for continental silicic magmatic centers of 4.4 $\pm$ 0.8e-03 km^3/y. [19].

Both the models predict that for a large magma chamber, the magma fluxes as high as 0.1–1 km^3/a are required to reach an overpressure capable to cause roof failures and caldera-forming

eruptions. In this chapter, we will consider additional factors that can influence the thermal and mechanical state of large magmatic chambers.

2. Deep fluid flux as an important mechanical factor

There is an increased interest in the giant silicic magma chambers, which in their life can become a batholith or a supervolcano, or both. Since in historical time, there were no supereruptions with a volume of 1000 km^3 and more, judgments about the mechanisms of this phenomenon remain essentially theoretical. However, some aspects of this problem are almost completely clear. A huge volume of silicic magma can be formed by melting a silicic crust at the underplating with basaltic magma, which may include remelting of former rhyolitic volcanic rocks and granites. For the volcanic complex, Altiplano-Puna of the central Andes, including the caldera of La Pacana, with size 65 × 35 km, this mechanism is convincingly shown by geologic and geochemical data [20]. The Altiplano-Puna complex was formed at a thickening of the continental crust and intensive basalts generation in the mantle wedge at the steepening of the subduction angle and probably delamination of the crust [21]. For Bishop Tuff rhyolites (Long Valley, California), the composition of radiogenic isotope indicates a significant mantle contribution, which is interpreted as the consequence of the mid-crustal melting of amphibolites with basaltic protolith of mantle origin [22]. Another possible explanation for these observations may be the contamination of the silicic melts by REE, Pb and Sr, transferred by the CO_2-CO fluid from the underplating basalts. Below, we will consider some of the already established geochemical consequences of the fluxing of rhyolitic magma with deep CO_2. In any case, a sufficiently high rate of basalts generation is an essential condition for the production of a large volume of rhyolites. This requirement can be fulfilled in deep mantle plumes or in smaller upper mantle plumes (ascending flows) caused by the crustal delamination or breakage off the oceanic plate in the collision zones. The mechanics of assembling large volumes of silicic magma from small portions is analyzed in [23, 24]. In a long-term, magma in giant chambers is in a state of mush.

2.1. Why mush

2.1.1. Theoretical view

The melt in the partially molten zones of the Earth tends to separate from the solid phase when their densities are different. A two-phase melt-crystals homogeneous system is gravitationally unstable. At low concentration of the solid phase, the crystals separated from the magma by Stokes settling. When the solid-phase content becomes close to 40–45 vol.%, the crystals begin to interact mechanically and form a coherent matrix. At the melt density lower than that of matrix, melt separation takes place in the form of a compaction. The physics of compaction is quite complex and deserves special consideration, which is beyond the scope of this chapter. For the subjects considered below, it is important to know the stable content of the melt in the mushes of basic and silicic compositions. The effectiveness of the compaction is characterized by the compaction length δ_c [25]:

$$\delta_c = \left[\frac{\varsigma + \frac{4}{3}\eta_s}{\eta_m} k(\varepsilon)\right]^{1/2} \quad (5)$$

where ζ and η_s are the bulk and shear viscosity of the matrix, respectively, η_m is magma viscosity, k is a permeability of the matrix with porosity ε. When the thickness of the mush layer is less than δ_c, the compaction is fast. In a detailed analysis of the matrix viscosity and permeability, Tegner et al. [26] estimated the compaction length for olivine-plagioclase cumulates of Skaergaard intrusion at an initial porosity of 22 vol.% at δ_c = 870 m. Due to the fast compaction in the geologic sense with the mush thickness < δ_c, the volume fraction of the residual melt in the olivine-plagioclase orthocumulates of the Skergaard reduced to several volume percent [26]. This estimate is consistent with McKenzie's [25] conclusion that in the regions of basalt generation in plumes and in Mid-Ocean Ridges, the volume contents of the melt is no more than a few percent due to the rapid compaction and segregation of the melt into the veins and dykes. In silicic systems, compaction is less effective because of the low viscosity of a wet mush with a high quartz content and relatively high viscosity of the rhyolite melt. The corresponding meter-decimeter scale of δ_c and nonlinear rhyological effects lead to local phase separation with the formation of a migmatite-like texture [27]. It is usually believed that additional tectonic deformations are involved in the separation of granitic magma and the formation of displaced granite plutons [28]. Thus, while in the basaltic system, partial melts with a volume fraction of melt greater than a few percent exist only temporarily [25], silicic mush, probably locally heterogeneous, with melt content of 10–20 vol.%, can persist for long time, limited by the rate of cooling and solidification.

The erupted Yellowstone intracaldera rhyolites are fairly homogeneous [23]. Periodic intrusion at different levels in the mush zone of superheated rhyolites from contact with underplating basalts can be a physical mechanism that wipes the mush heterogeneities and provides mixing on a large scale. The direct invasion of basaltic magma into the mush was hardly massive, since in Yellowstone only traces of clots of mafic minerals were identified in erupted intracaldera rhyolites [29], in contrast to the mixing textures well expressed in the extracaldera rhyolites [30].

2.1.2. Geophysical observations

A geophysical insight into the state of large silicic magma chambers requires a sufficiently large volume of observations. The seismic tomographic model of the Yellowstone volcanic system with two magmatic columns under resurgent domes merging at depth was proposed by Husen et al. [31]. It was significantly improved when data were combined from the dense seismic arrays of the Yellowstone, Teton and Snake River Plain (SRP) regional seismic networks, the NOISY array and the wide-aperture EarthScope Transportable Array ([32] and refs. in it). A continuous layer of a partial melt under the caldera at depths of about 6–12 km was clearly identified with a separate, presumably basaltic magma accumulation zone at depths 20–50 km. In this study, the volume fraction of the melt in the upper crustal body was estimated at 9%, and in the lower zone - 2 vol.%. Another independent source of information is provided by the magnetotelluric method. For the Yellowstone upper crust, the highly conductive zone of the hydrous partial melt is localized at approximately the same depths

6–12 km under the caldera [33, 34], as envisaged by seismic tomography. In fact, the interpretation of MT data is not absolutely unambiguous. High conductivity can be interpreted as a manifestation of a partial silicate melt or carbonatitic melt [35], aqueous or carbonic fluids and graphite. MT and seismic data may be complementary since the same volume fractions of carbonatitic and silicate melts will have a similar effect on the seismic velocity, while the conductivity of carbonatite melt will be at least two orders of magnitude higher [35]. Therefore, a very small volume fraction of carbonatites (or CO_2-CO-based solutions) will be detectable by MT and not visible in seismic data. The observed low resistance layer (seismically practically undistinguishable) under all SRP to the west of the Yellowstone caldera at depths of about 50–70 km can be a residual carbonatite melt with a low melting temperature or concentrated solution in carbonic fluid, rather than a basaltic partial melt.

In this chapter, we will focused on analyzing the large magma chambers created in some way such as the chamber under Yellowstone volcanic field which is one of the most studied (see e.g., review [36]). A generalized scheme of such a silicic chamber formed above the hot spot is shown in **Figure 3**. The possible role of volatiles in the heat budget and the mechanics of large silicic magma chambers is the least studied and will become the main subject of the following paragraphs.

2.2. High emission of deep CO_2

CO_2 is the main component that is released during degassing of basalts, especially from dry basalt formed during decompression melting in plumes. It was also assumed that in the lower crust there are reservoirs of the supercritical CO_2 derived in the mantle at 2–3 GPa [37]. A direct observation of the CO_2 mantle reservoir (at c.a. P = 1.8 GPa) sampled in the xenoliths from paleovolcanoes in the Pannonian basin is reported in Ref. [38]. In these xenoliths, CO_2/

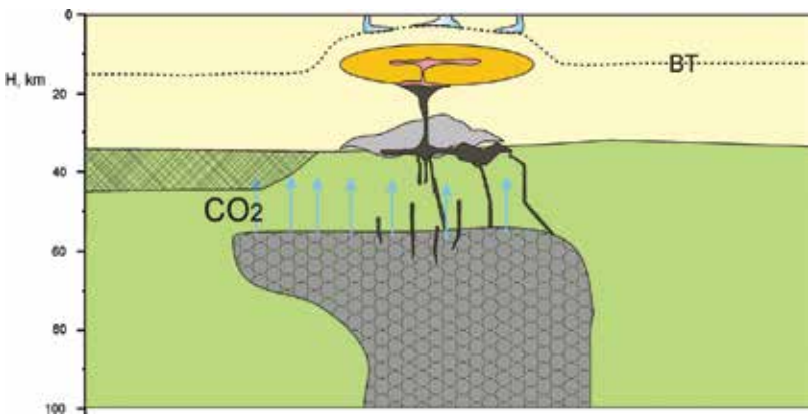

Figure 3. Cartoon schematically displays large silicious magma chamber in the continental hotspot setting. Basaltic magma originated in plume underplates crust (black) and where it partially solidifies to form mafic intrusions and partially rise to mush zone. At the lower contact of the mush zone, superheated rhyolite is formed and invades into mush. Hydrothermal system operates in the upper crust above brittle-ductile transition level. CO_2 infiltrates through the zone of magmatic activity and accumulates near the Moho away of this zone (crosshatched).

magmatic glass mass ratio is estimated of up to 0.25. The carbonated silicate melt with such CO_2 a content releases CO_2 at P = 2–3 GPa and later at their ascend, the basaltic magma and the CO_2 can move independently. Where deep sources of CO_2 exist, the magma chambers will be subjected to high fluxes of volatiles, which can play a significant role in keeping long-term heat balance [39], in modifying the composition of magma and in influencing the deformation of the magma chamber. Bachmann and Bergantz [40] attempted to model the essential water fluid Darcy's flow through the partial rhyolitic melt. In the model, water fluid was released from the basalt magma with 4–6 wt.% of dissolved H_2O. They found that possible fluid contribution in the instant mobilization of several 1000 km^3 of mushes immediately before eruption is negligible. Their conclusion is mainly determined by slow Darcy's filtration rate while faster mechanisms can exist.

In the following section, we will consider the effect of CO_2 fluxing on the example of Yellowstone caldera since the total CO_2 flux through Yellowstone caldera is among the largest and is about an order of magnitude greater than across the entire rift zone of Iceland [41]. Werner and Brantley [42] found that the largest flux of 456 $kg/m^2/yr$ in average is registered in the areas of the acid geotherms with surface 145 km^2. Average CO_2 flux in the hydrothermal activity zones is about 40 $kg/m^2/yr$, while in inactive forestry area background flux is 3.5 $kg/m^2/yr$. Authors ascribe isotope composition of carbon and helium to 70% of CO_2 from the mantle source and the rest from sediments (Mammoth limestones). An analysis of CO_2 flux value showed that it is significantly larger than expected at the basalts magma degassing one at the rate of basalts generation in plume 0.03–0.05 km^3/yr [42]. Extraordinary CO_2 generation can be linked with interaction of the mantle plume and Farallon pate. Part of subducted slab slides along 400–600 km phase boundary under SRP [43]. It is separated by lateral tear from the older part of the slab intersecting this boundary. Plume crosses Farallon plate trough the tear. Presumably, oceanic slab contains carbonates that are mobilized by hot plume material and release CO_2 at pressure below 2–3 GPa (see e.g., in Ref. [44]).

2.3. Heat budget with CO_2

The heat supply by deep fluids may be important in order to prevent from cooling the large volumes of the partial melts in the large and super-large magma chambers (such as the Yellowstone In the most general form, the heat budget of the mush layer can be estimated adding the heat supplied by the different contributions of the carbonic fluid and basaltic magmas. The dissipation of heat depending on the specific physical mechanism can reduce the positive part of the balance. The heat lost is assumed to be essentially vertical, equal to the observed average heat flux, while the horizontal thermal loss is neglected. At the positive heat balance, the silicic melt will be generated and probably erupted, while at the negative balance the magma will solidify approaching a scenario of formation of batholiths.

The amount of the advective heat transfer by the ascending fluid depends on the mechanism of transport. If the fluid has passed the interval from contact with the basaltic magma to the layer of the partial rhyolitic melt along the fractures rather than by the Darcy's flow, then the heat losses through the crack walls will be small, and we can assume that the heat flux is approximately equal to

$$Q_{adv} = c_{p,fl}(1200 - 850)q_{co2} = 0.22e08\ J/m^2/yr\ (0.70\ W/m^2), \quad (6)$$

where qCO2 is mass flux of CO_2 in kg/m^2/yr, the specific heat of the fluid $c_{p,fl}$ is taken equal to 1.4 Kj/kg/o, the temperatures of basaltic magma and rhyolitic mush are 1200 and 850°C, respectively. As the first proxy, q_{CO2} = 40 kg/m^2/yr is taken equal to the average value of flux observed in the geothermal regions of Yellowstone [42]. Below we consider the effect of the variation in q_{CO2} over a wide range on the heat balance.

In fact, the carbonic fluid exsolving from the underplated basalts and stored in the mantle reservoirs is a reduced. At P = 2–3 kbar, the mole fraction of CO in such a fluid at f_{O2} around QFM-0.5 is in the range 0.1–0.2 depending on the temperature [45]. At the oxidation of CO heat is released:

$$CO + 1/2O_2 = CO_2 \quad (7)$$

The enthalpy ΔH_T of the oxidation reaction (7) at T = 700°C is −198870.4 J/mol. Volume effect of the reaction (7) is negative, so the heat effect is somewhat larger than ΔH_T at a pressure P = 2 Kbar corresponding to a chamber depth of 7 km. However, not pure oxygen can be involved in the reaction, so we use the value of ΔH_T as the maximum estimate. If we take q_{CO2} equal to 40 kg/m^2/yr., as above, and set X_{CO} = 0.1, then the heat of CO oxidation will be equal to

$$Q_{CO} \approx -0.1\,\Delta H\, q_{co2}1000/44 = 0.18e08\ J/m^2/yr\ (0.57\ W/m^2) \quad (8)$$

The main source of heat in Yellowstone is associated with the flow of basaltic magma. The simple arrival of q_b = 0.05 km^3 of magma annually means advective heat flux

$$Q_b = q_b\left(\rho_b c_{p,b}(1200 - 850) + \Delta H_{m,b}\right)/S_0 \quad = 0.51e08\ J/m^2/yr\ (1.62\ W/m^2) \quad (9)$$

where the surface of the active part of the caldera is roughly estimated at 2000 km^2, the density of basaltic magma is set 2700 kg/m^3, the specific heat $c_{p,b}$ is 1 kJ/kg/o and the latent heat of fusion, absorbed at melting of rhyolites is $\Delta H_{m,b}$ = 400 kJ/kg. With these values of the parameters, the value of the advective heat flux Q_b is comparable in order of magnitude with the heat flux associated with CO_2.

Basalts generally do not intersect partial rhyolite layer serving a density filter. Their heat content is transferred to the superheated rhyolites formed on the lower boundary of mush zone that can penetrate in the partial melt. While fluid is not accumulated in the crust and rise through partial melt transferring heat and dissolved components into and out of the mush zone. Purely conductive heat transfer through partial melt and upper thermal aureole of magma chamber is limited by the stationary heat flux through mush layer in the absence of convection of the order

$$Q_{cond} = \lambda\Delta T/H_{mush} \quad (10)$$

where λ = 2.5 W/m/o, H_{mush} = 6 km. With these parameters values, the conductive heat flux will be only 0.145 W/m^2 or 0.05e08 J/m^2/yr. The average heat flux through Yellowstone caldera is significantly larger than this conductive estimate.

The dense basaltic magma interacting with the lower contact of the mush zone transfers its heat content to the superheated rhyolites formed during this interaction. The superheated rhyolite penetrates into the mush zone and indirectly transfers Q_b. The low density fluid moves directly through the lower contact into a partial melt and transfers heat and dissolved components.

2.4. Thermal profile through the mush zone

The above global estimates are valid regardless of the real physical mechanism of fluid transport. A self-consistent mechanical model of fluid transport through a partial melt should include the coupled magma and fluid flow through a deformable viscoelastic matrix that extends the viscous [25] and visco-pastic [27] compaction models. With a sufficiently comprehensive model one can consider complex flow regimes similar to a self-organized critical transport observed experimentally [46]. Below, we consider the simplest estimate of the spatial temperature distribution in a mush with a pervasive fluid flow as a solution of the general advection problem in a porous media. The mass flux of the fluid will not be found as a part of the solution (e.g., as a solution of Darcy's equation, as in Ref. [40]) but is specified on the basis of observations. In the general form, 1-D equation of advective heat transfer through a porous medium is

$$\rho_s c_{\mathrm{ps}} \frac{\partial}{\partial t} T(z,t) = \lambda \frac{\partial^2 T(z,t)}{\partial z^2} + c_{\mathrm{pf}} Q_f \frac{\partial}{\partial z} T(z,t) \tag{11}$$

or in nondimesional form

$$\frac{\partial}{\partial t} \overline{T}(z,t) = \frac{\partial^2 \overline{T}(z,t)}{\partial z^2} + \mathrm{Pe} \frac{\partial}{\partial z} \overline{T}(z,t) \tag{12}$$

where Peclet number is $Pe = l_0 c_{pf} Q_f / k_T \rho_s c_{ps}$. Substituting l_0 = 200 m, k_T = 1.0e-06 m^2/s, c_{pf} = 1.4 kJ/kg/o, c_{ps} = 0.84 kJ/kg/o, ρ_s = 2500 kg/m^3, we get the time scale 1300 yrs, Pe = 0.013–0.4 with q_f in the range 4–100 $kg/m^2/yr$. At this time and spatial scales problem is weakly to moderately advective (Pe < 1). It is important to set proper boundary conditions for temperature.

At the lower boundary, the temperature of basaltic magma T_b = 1200°C is prescribed. The heat flux from the mush layer supports the heat flux in the geothermal system and in the quasi-steady state their values should be close in average by area and time (as used in 1D models). In our calculations, a heat flux Q_h of 4.6 GW/2000km^2 = 2.3 W/m^2 at the upper boundary is set, equal to the average estimates for Yellowstone [36].

We calculated the transient solutions for different Pe values. At Pe = 0.13, corresponding to a mass flux of CO_2 of 40 $kg/m^2/yr$ in a geologically short time of 13 Kyrs, the temperature at the top of the mush layer drops to 200°C and continues to decrease and the thickness of the mush layer is halved (see **Figure 4a**). With a stronger fluid flow Pe = 0.5 in time equal to 56 Kyrs, the boundary temperature still increased to c.a. 500°C, but did not reach a steady-state value (see **Figure 4b**).

In our formulation, in steady state, there is relationship between Pe(q_{fl}) and the maximum admissible heat flux $Q_{h,max}$. This is determined by the fact that temperature at the outer

http://dx.doi.org/10.5772/intechopen.71655

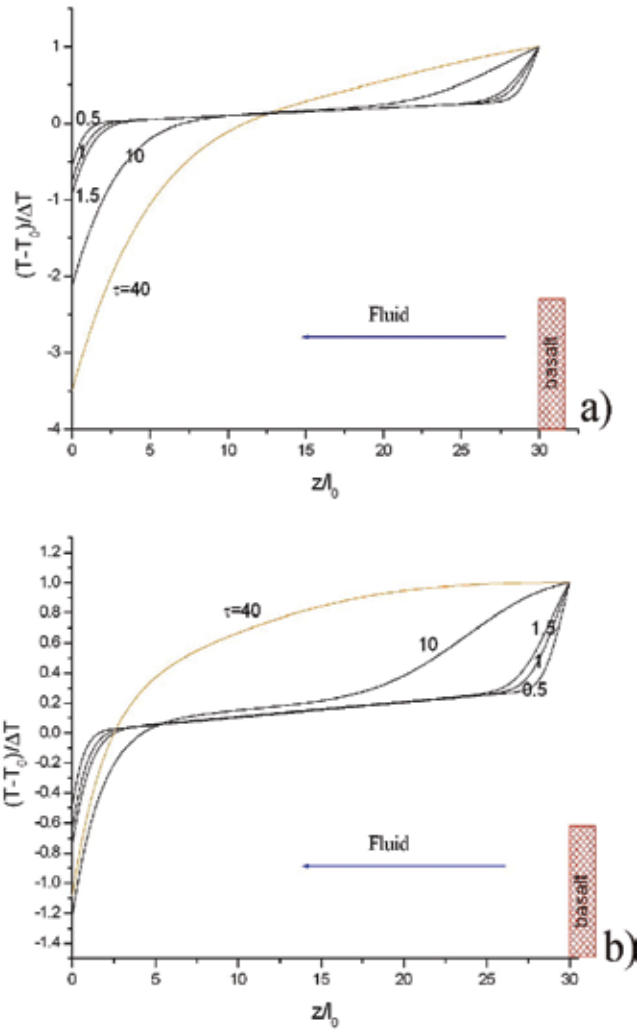

Figure 4. Calculated temperature profiles in the mush zone in nondimentional form in the moments of time τ = 0.5, 1.0, 1.5, 10 and 40. Length scale scale l_0 = 200 m, time scale t_0 = 1300 years. Right boundary is at T = T_b = 1200°C, left boundary is subjected to the constant heat flux of 2.3 W, initial temperature of mush T0 = 850°C, (a) Pe = 0.13 (corresponds to q_{CO2} = 40 kg/m^2/yr, (b) Pe = 0.5. In (a) at τ = 40 temperature at left boundary is physically meaningless, since constant heat flux boundary condition does not guarantee even positive absolute temperature. At Pe = 0.5, left boundary temperature stabilizes around reasonable T = 500°C, however then almost one third of the mush zone asymptotically is heated to T_b.

boundary (closer to surface) is part of solution. We fix a reasonable value of T(0) = −0.7 (about 600°C in physical dimension) and get

$$Q_h = 1.7\mathrm{Pe}/\left(1 - \exp\left(-30.0Pe\right)\right) \tag{13}$$

The numerical solution agrees with Eq. (13), at Pe = 0.13 the maximum $Q_{h,max}$ = 0.226 (Eq.13) is less than 0.73, used in the numerical solution, and at Pe = 0.5 $Q_{h,max}$ = 0.85 > 0.73. As expected the mush layer solidifies in the first and melts in the second case, respectively.

The heat flux is measured directly only on a small part of caldera. The measurements of the heat flow at the bottom of Yellowstone Lake [47] gave values 100–300 mW/m^2 near the caldera boundary and up to 1600 mW/m^2 in Mary Bay. Fournier [48] obtained an estimate of 2.65 W/m^2 (with an active surface 2000 km^2) on the basis of the correlation of the chlorine content and the enthalpy of the geothermal fluid. A later inventory of the chlorine balance in the Yellowstone river system [49] gives an average heat flux of 2.3–3.3 W/m^2 (when recalculated to an active caldera area S = 2000 km^2). The CO_2 flux was measured in geothermal areas at a quiet stage of the caldera evolution. The amount of CO_2 accumulated and periodically released is unknown. In fact, deep CO_2 is partially redistributed horizontally, accumulated underground and transferred as an HCO_3^- ion by geothermal waters. The rate of basaltic magma supply (q_b) is also known with low accuracy. In view of all these uncertainties, we are considering the heat budget in a wide range of variation of the parameters involved and display the results in **Figure 5**.

The zero heat balance conditions in the mush zone for different q_b are indicated by solid lines in the coordinates q_{CO2} - Q_h (surface heat flux). In general, the system is close to the global balance at q_b = 0.05 km^3/yr. Doubling of this rate shifts it to the rhyolite magma generation. Variations in the flux of CO_2 can lead to the transitions from solidification to melting in a state close to thermal equilibrium. The dashed line shows the dependence of the heat and CO_2 fluxes calculated using Eq. (13). Evidently, when basalt is passively underplating the mush zone, providing T = T_b (boundary condition in the advection model) only an extremely high CO_2 flux can ensure the long-term existence of the mush layer. This analysis emphasizes the importance of the interaction of mush with superheated dry rhyolites (see **Figure 3**). In fact,

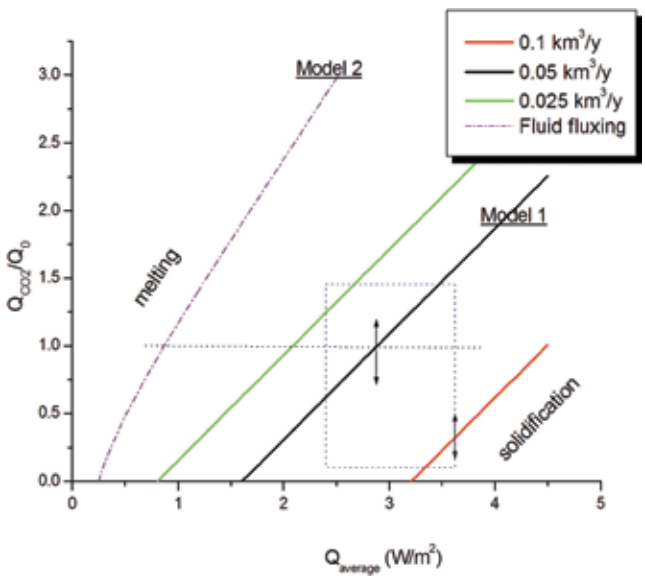

Figure 5. Zero heat balance condition for rhyolitic mush zone of Yellowstone volcano in the coordinates average surface heat and CO_2 fluxes (a) continuous lines correspond to the different basalt magma supply rates and mechanisms providing full heat transfer of basalt magma and deep CO_2 fluid to the mush, (b) dash-dot line plots relationship for advective fluid heat transfer through the mush and passive basalt underplating setting low boundary constant temperature T = T_b condition. CO_2 flux is normalized on the Q_0 = 40 kg/m^2/yr. At the heat flux larger than zero-balance value mush is solidified at the smaller heat flux or larger CO_2 flux mush is melted.

convective melting and mixing is fairly fast process [50], so that zircon crystals from melted mush will survive. Mineral thermometers will record crystallization temperatures at a solids content of about 40 vol.%, when convective melting stops, well below the initial temperature of the superheated rhyolites.

2.5. Volatiles in the melt at CO_2 fluxing

Our analysis demonstrates that the flux of CO_2 in a reasonable range can make a significant contribution to the heat budget of the mush layer. When crossing a layer of mush, the fluid should create petrologic signs of interaction with hydrous rhyolitic magma, for example, by transferring water from the melt to the CO_2 bubbles. During ascent and eruption, volatiles escape from the bulk melt, information about the pre and sin-eruptive conditions is retained in the melt inclusions in magmatic minerals. In the equilibrium with the fluid, the contents of H_2O and CO_2 in the melt depend on the PT conditions and the composition of the fluid. We approximate the mutual solubility of CO_2 and H_2O in the rhyolitic melt, using the compilation of experimental data from Ref. [51]. The solubilities in the melt are expressed through the pressure (in Kbar) and the mole fraction of CO_2 (z) in the fluid as:

$$C_{H2O} = 4.1\sqrt{P(1-z)^{1.35}},\ \ C_{CO2} = 0.0499\text{kP}z^{0.75},\ \ k = -0.54013 + 0.0164T, \tag{14}$$

where C is in wt.%, temperature in °C. The widely used model of the mutual CO_2-H_2O solubility [52] in the rhyolitic melt is more accurate, but also more complicated and can not be incorporated in numerical codes, such as a two-phase magma flow simulator. Our short expressions are for these numerical applications.

To model the melt and fluid equilibria, we solve the equations of mass balances for CO_2 and H_2O along with Eqs. (15). In the **Figure 6a**, the isobar for P = 2 Kbar for the composition of the rhyolite melt in coordinates C_{H2O}–C_{CO2} is plotted, the maximum concentration of water and CO_2 are for the pure water and CO_2 fluid, respectively. Various processes affecting volatiles in magma have been modeled and are depicted in **Figure 6a**. When the melt is depressurized during the eruption, degassing begins with the shift of the melt composition along the trajectories of degassing under the open (when all exsolved fluid is removed) or close system. Trajectories are shaped by the early loss of CO_2, followed by the release of H_2O (more on this in Ref. [52]). Melting of the mush as a close system leads to dilution of the melt with respect volatiles (movement of the composition from the initial point to the origin of coordinates in **Figure 6a**). Crystallization at constant pressure leads to a shift to more water-rich compositions along the isobar. If the fluid exsolved during crystallization remains in the mush, the pressure rises. The result of mixing with superheated rhyolite depends on the composition of the later. A transition to water poor, fluid undersaturated compositions is expected in general. At CO_2 fluxing at constant pressure, the composition follows isobar from the water-rich to water-poor melt. During CO_2 flushing, the pressure of the magma can increase due to the expansion of the chamber being constrained by the host rocks. Then the trajectory of the melt composition in H_2O-CO_2 space will deviate from the isobar (see **Figure 6a**). A significant vertical size of the magma chamber can also cause deviations of the MIs compositions from the isobar [53].

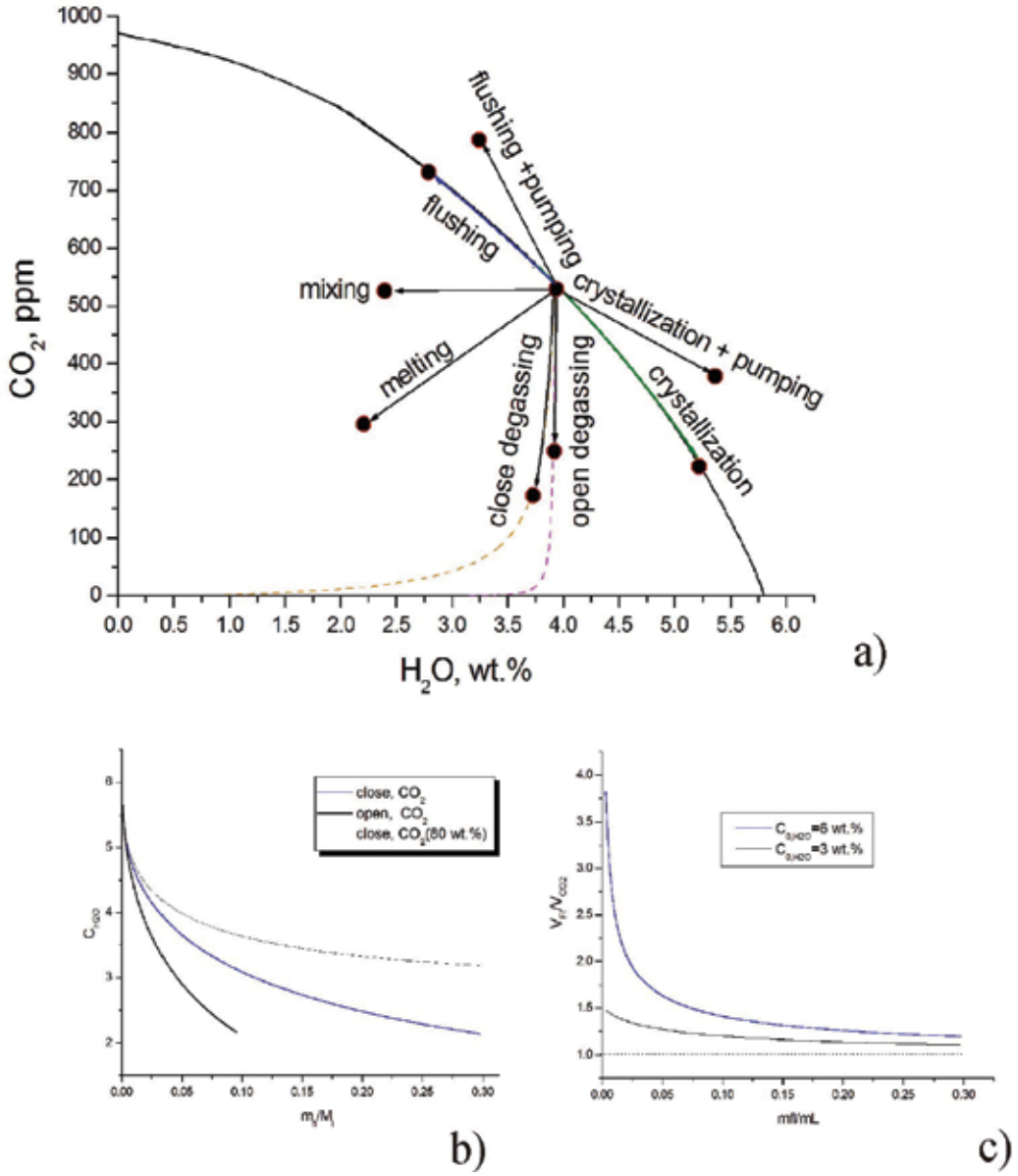

Figure 6. Results of modeling (a) different factors affecting volatiles content in the melt, (b) dependence of the water content in the magma at the flushing with CO_2 on the mass ratio of the reacted CO_2 and melt. Style of the interaction and content of CO_2 in the incoming fluid are shown in the legend (c) ratio of the volume of CO_2-H_2O composition fluid to the initial volume of CO_2 as function of the mass ratio of the reacted CO_2 and melt. In the legend initial water contents in the melt are shown.

The parameters of the CO_2 flushing process require more detailed consideration, since they are necessary for further mechanical analysis. The modeling of the closed system flushing was carried out by increasing of the total contents of CO_2 and H_2O in the system in small

increments in the proportion of the fluid composition. To evaluate the volume of a fluid in an equilibrium two-phase system, we use EOS for a CO_2-H_2O mixture from Ref. [54]. In **Figure 6b**, one can see that added mass of the fluid increases, the concentration of water in the melt gradually drops. Pure CO_2 eventually will extract all the water from the melt. With a starting content of 6 wt.%, it is sufficient to add about 30% of CO_2 by mass to reduce the water content to 2 wt.%. In the open system approximation, after every step, all the fluid is removed, and a new portion of carbonic fluid reacts with the pure melt. In this case, approximately 10 wt.% of CO_2 is sufficient to achieve the same effect. When the incoming fluid contains 20 wt.% of H_2O, it is equilibrated with the melt with c.a. 3 wt.% of H_2O and cannot reduce the water content below this value. This implies that in the SRP system, carbonic fluid penetrating the rhyolite mush contains less than 20 wt.% of water to produce melts with a lower content. The transfer of water from the melt to the fluid changes the composition of the fluid and enlarges its volume. In **Figure 6c**, the volume ratio of the final fluid and the incoming pure CO_2 at P = 2 kbar is plotted with the two initial water contents. A strong volume increase of 1.5–4 times has place at the lowest mass ratio of the added fluid to the melt. As the mass ratio increases, the volume expansion becomes less significant. Extraction of water and CO_2 dissolution in the melt at the constant temperature induces crystallization due to an increase in the liquidus temperature. Crystallization caused by water loss will release heat of fusion and heat the melt, so that the integral effect should be more precisely evaluated with numerical modeling, which is beyond the scope of this chapter.

2.5.1. Melt inclusions data supporting the concept of CO_2 flushed mush

Figure 7 shows the results of the studies of melt inclusions in quartz phenocrysts from various large-volume rhyolites from Snake River Plain (SRP) and Long Valley calderas (Western USA). Lava Creek Tuff (LCT, Yellowstone 0.64 Ma) [55] decompression sequence is rooted in a 2 kbar isobar with an initial relatively high water content of 3 wt.%. The post caldera Tuffs of Bluff Point (Yellowstone, TBP 175–180 kyr) [56] sequence corresponds to degassing at the decompression from a pressure slightly higher than 1.5 kbar with a starting water content of 2 wt.%. Early Arbon Valley Tuff (AVT) [57] represents the products of the Picabo caldera eruption (10.44 Ma) with the highest water content of 6.5 wt.%. The AVT-LCT-TBP sequence illustrates a gradual decrease in water and an increase in the CO_2 content. Bishop Tuff (BT) MIs [53] demonstrate a highly variable set starting in CO_2 free compositions with c.a. 6 wt.% of H_2O. Some points follow approximately an isobar of 2 kbar, while others lie on the open system degassing path. One exceptional point with the highest CO_2 content reaches an equilibration pressure of more than 2.5 kbar. In general, the BT data are consistent with the fact that the magma was flushed with CO_2 followed by an eruption. Alternatively, the observed CO_2 enrichment and H_2O loss process can be explained by mixing superheated rhyolites with a high CO_2 content and hydrous partial melts (see **Figure 6a**). It is likely that AVT data with a simple shift of compositional points along the H_2O axis may correspond to such a mixing process that creates a fluid undersaturated melt. For comparison, we plotted in **Figure 7**, the MIs in quartz data for the Toba volcano [58] located in the subduction zone. Obviously, in a subduction setting with much lower CO_2 fluxes and a shorter residence time, the magma contains much less CO_2. However, even in this case, one can expect a CO_2 fluxing with the

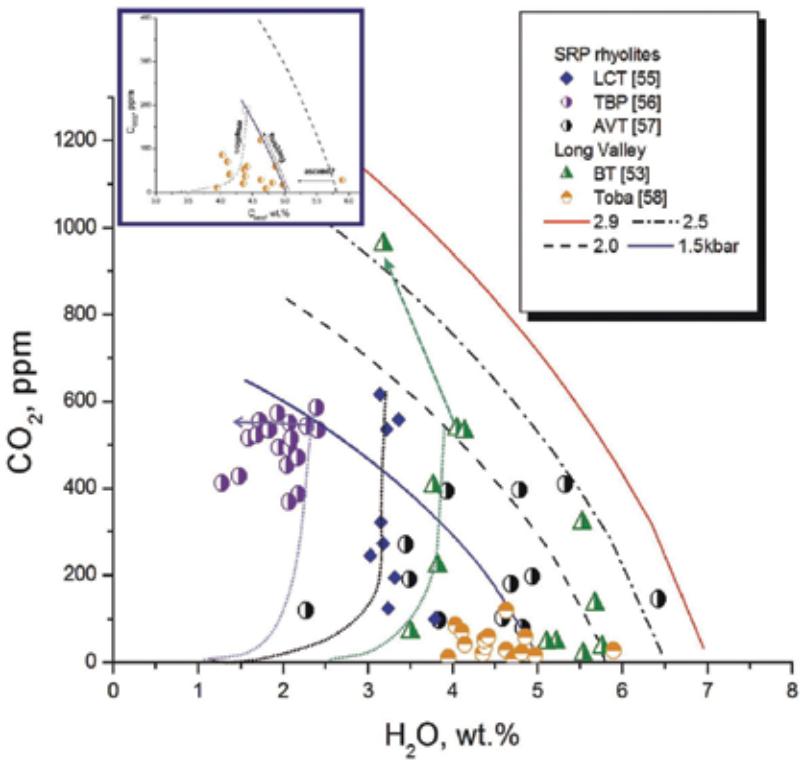

Figure 7. Contents of CO_2 and H_2O in MIs in quartz from silicic volcanic rocks from western USA and Toba. Line show equilibrium mutual solubilities of CO_2 and H_2O at the different pressures. Points located along isobars may correspond to the CO_2 fluxing of the hydrous silicic magma. Pyroclastics from the bishop tuff eruption (Long Valley caldera) experienced more strong interaction with CO_2 than Yellowstone system. In the Toba volcano localized in the subduction system this interaction is weakest.

alignment of some compositional points along the 1.5 kbar isobar. Other points may be located on the close system degassing trajectories, starting with an isobar of 1.5 kbar (see in the inset in **Figure 7**).

3. The "heavy breath" of the Yellowstone

3.1. Yellowstone breathes because it is alive

The "heavy breath" of the Yellowstone caldera with periodic (time scale of decades) uplift and subsidence with total amplitude of about 0.5 m (see references in Ref. [36]) was attributed to the exsolved water-rich fluid at the solidification [48] or accumulation of two-phase CO_2-H_2O fluid in the upper 4 km subsurface layer [39]. Recent episode of the fast uplift in 2004–2007 was studied in detail [59] and interpreted as a result of the deep fluid and magma intrusion at the depths of about 7–12 km (horizontal size of expanding object was about 20 km). Pure fluid invasion was also anticipated near Norris Geyser Basin.

Probable connection with CO_2 fluxing as a cause of the slow Yellowstone chamber deformations is confirmed by the approximately fivefold increase in 1978 in the content of "magmatic carbon" in the annual rings of pines from Mud volcano thermal area [60] associated with earthquakes swarm and transition to the subsidence phase of the caldera surface. Certainly to reach shallow geothermal level CO_2 must pass through the mush zone. We will consider mechanical respond of this deep zone on CO_2 pumping that should have inertia larger than shallow reservoirs that can be in pace with several decades period of deformations. Similar mechanical disturbances of the surficial geothermal system (depth 2–3 km) caused by invasion of the fluid from intruded magma in Campi Flegri geothermal field (Italy) dissipate in the time scale of several years [61] by spreading excess fluid horizontally in Darcy's flow.

If deep CO_2 enters the mush zone by a mechanism more efficient than Darcy's filtration (e.g., with superheated rhyolites or through fracture zones), one can expect mush zone to expand. A rule of thumb estimate of the maximum value of the overpressure which can be reached in Δt years is $\Delta P = K_{ch}\left(\gamma q_{co2} S\Delta t/\rho_{fl} V_{ch}\right)$, where γ is correction factor accounting water extraction from the melt (here 1.2), Δt is time interval of pumping (here 50 years), S – caldera area (2000 km^2, we use active area less than maximum one delineated by circular fault), V_{ch} is magma chamber volume that can be taken for Yellowstone as 3000 km^3/0.3, K is bulk modulus of 20 GPa, ρ_{fl} is density of fluid at P = 2 kbar and T = 850°C it is 600–500 kg/m^3. At Δt = 50 yrs this order of magnitude estimate is 18 MPa. The coefficient γ characterizes incoming fluid volume increase due to water extraction from the melt. As discussed above, its value depends on the actual volume of the melt that reacted with fluid. If interaction is efficient enough and the mass ratio of fluid/reacted melt is small this coefficient can be up to 4, otherwise it is in the range 1.1–1.2.

3.2. Viscoelastic model of flushing

It follows that at the used parameters values overpressure and associated deviatoric stresses can be high enough for mechanical failure and fluid release followed by the caldera subsidence and beginning of the new cycle. Considering the periodic expansion and contraction of the magma chamber in the time scale of decades, it is important to take into account the viscoelastic properties of heated surrounding rocks. As a first approximation of this problem, the formulation in the form of a viscoelastic spherical shell (approach used in Ref. [62]) can be analyzed. With an increase of the relative shell thickness (the heated and damaged rocks aureole), this approximation at small times approaches the conventional equation for a spherical inclusion in an infinite elastic medium. Because of the spherical symmetry, this problem reduces to 1-D and has a simple analytical solution (see in the textbooks). The geometry of the shell is determined by the outer R_1 and the inner R_0 radii. On the external surface, pressure (radial stress) p_1 and p_0 is applied on the inner surface. It is easy to show that the stress distribution does not depend on the material parameters (elastic, viscous or viscoelastic) and depends only on the shell geometry:

$$s_2 = \frac{-P_1R_1^3\left(R^3+R_0^3\right)+P_0R_0^3\left(R_1^3+2R^3\right)}{2R^3\left(R_1^3-R_0^3\right)},\quad s_{\mathrm{rr}} = -\frac{p_1R_1^3\left(R^3-R_0^3\right)+P_0R_0^3\left(R_1^3-R^3\right)}{R^3\left(R_1^3-R_0^3\right)} \tag{15}$$

here s_2 are angle components of stress tensor in spherical coordinates $s_{\phi\phi}$=$s_{\tau\tau}$. The radial displacement in an elastic solution is

$$u(R) = -P_1\left(\frac{R^3}{3} + \frac{3K}{4\mu}R_0^3\right)R_1^3 + P_0\left(\frac{R^3}{3} + \frac{K}{4\mu}R_1^3\right)R_0^3/K\left(R_1^3 - R_0^3\right)R^2 \tag{16}$$

With a confining pressure P_1 equal to the internal P_0, the displacement field is reduces to a uniform displacement field corresponding to the volume deformation and all components of the stress tensor (σ_{rr}, $\sigma_{\phi\phi}$,$\sigma_{\theta\theta}$) becomes—P. In the expression for the tangential stress (s_{rr}), the first term, proportional to the confining pressure, is compressive, while the term proportional to the internal pressure is tensile so that $s_{rr} > 0$ for the thin shell and high overpressure. The solution for the radial distribution of displacements u(R) depends on the material parameters and can be used to calculate the deformation of the magma volume due to internal processes. The general viscoelastic solution is easily derived from elastic one through its Laplace transform, obtained by replacing the shear modulus with the complex shear modulus and the boundary pressures on their Laplace transforms. With an instantaneous onset of the pressures P_1 and P_0 (dP = P_0-P_1), the expression for the transient displacements u(R_1,t) at the outer boundary is a sum of

$$\begin{aligned} u_1(R_1,t) &= dP\frac{\alpha^3 R_1 t}{4(1-\alpha^3)\eta}, \quad u_2(R_1,t) = dP\frac{R_1(1+\nu)}{3E\nu}\frac{(2-\nu)\alpha^3}{2(1-\alpha^3)}, \quad u_3(R_1,t) \\ &= -dP\frac{R_1(1-2\nu)^2\alpha^3}{3E\nu(1-\alpha^3)}\exp\left(-\frac{3E\nu}{2(1+\nu)^2\eta}t\right), \end{aligned} \tag{17}$$

where the first term (Eq. (17)) describes viscous deformations of the shell at the applied overpressure dP and two next terms describe viscoelastic deformations. Sum of u_3 and u_2 corresponds to some expansion due to exponential relaxation. Term u_2 corresponds to the residual displacement at the full relaxation. Elastic displacements $u_2 + u_3(t = 0)$ (equivalent to the surface uplift at dP > 0) are proportional to dPR_1/E. By setting R_1 = 3000 m, dP = 30 MPa and E = 30 GPa, we get u = 0.9 m initial deformations and 1.2 m residual uplift (at dP = const = 30 MPa). Viscosity $\eta = 10^{19}$ Pas can be considered as typical for the weak lower crust below brittle-ductile transition boundary. This boundary arises above active magma chambers. Viscosities $\eta \le 10^{18}$ Pas delineate zone the closest thermal aureole. One can distinguish between this zone and magma mush only in a short time scale deformations. By setting effective viscosity of the shell of $\eta = 10^{19}$ Pas we get viscous uplift (expansion) rate of 2 cm/y. At time interval 60 years viscous and elastic deformations equated in magnitude. Relaxation time scale at these parameters will be 44 years.

3.3. Solution for magma pressure variation

For the general dependence of the internal pressure P_0 + dP(t) on time, the expression for radial displacements is formulated with viscoelastic and viscous terms (retaining terms depending on the overpressure dP(t)) as:

$$u_{ve}(R_1,t)=\frac{R_1\alpha^3}{(1-\alpha^3)}\left(dP(t)\frac{3(1-\nu)}{2E}-\frac{(1-2\nu)^2}{2\eta(1+\nu)^2}\int_0^t\exp\left(-\frac{3E\nu(t-\xi)}{2(1+\nu)^2\eta}\right)dP(\xi)d\xi\right) \tag{18a}$$

$$u_{ve}(R_0,t)=\frac{R_0\alpha^3}{(1-\alpha^3)}\left(dP(t)\frac{1+\nu+2\alpha^3(1-2\nu)}{2E\alpha^3}-\frac{(1-2\nu)^2}{2\eta(1+\nu)^2}\int_0^t\exp\left(-\frac{3E\nu(t-\xi)}{2(1+\nu)^2\eta}\right)dP(\xi)d\xi\right) \tag{18b}$$

$$u_{visc}(R_1,t)=\frac{R_1\alpha^3}{4\eta(1-\alpha^3)}\int_0^t dP(\xi)d\xi,\quad u_{visc}(R_0,t)=\frac{R_0}{4\eta(1-\alpha^3)}\int_0^t dP(\xi)d\xi \tag{18c}$$

Relative volume increment (dV/V) in time t then can be expressed through displacement of the inner surface as $dV/V = 3(u_{ve}(R_0,t) + u_{visc}(R_0,t))/R_0$. Eqs. (18) is transformed into nondimentional form with pressure scale P_{sc} (50 MPa) and time scale t_0 (10 years):

$$\frac{dV}{V}=\frac{3u(R_0)}{R_0}=\frac{3\alpha^3}{(1-\alpha^3)}\left(c_1dP(\tau)-c2\int_0^\tau e^{c3(\tau-\xi)}dP(\xi)d\xi+\frac{3c4}{(1-\alpha^3)}\int_0^\tau dP(\xi)d\xi\right), \tag{19}$$

where coefficients are:

$$c_1=\frac{1+\nu+2\alpha^3(1-2\nu)P_{sc}}{2E\alpha^3},\ c_2=\frac{P_{sc}t_0(1-2\nu)^2}{2\eta(1+\nu)^2},\ c_3=\frac{3E\nu t_0}{2(1+\nu)^2\eta},\ c_4=\frac{P_{sc}t_0}{4\eta} \tag{20}$$

and can be expressed through two independent physical parameters namely, the Deborah number, $De = Et_0/\eta$, and nondimensional Young modulus, E/P_{sc}. A geometric factor $\alpha = R_0/R_1$ is another independent variable. Poisson's ratio, ν, is in the range 0.2–0.25. We use the physical parameters values as in the examples considered above, that is, Young's modulus E = 30 GPa, viscosity $\eta = 10^{19}$ Pas, Poisson's ratio $\nu = 0.25$, $\alpha = 0.5$. To get the simplest solution, we take a polynomial representation of the overpressure in nondimentional time:

$$dP(\tau)=\sum\nolimits_{i=1}^{3}a_i\tau^i \tag{21}$$

Upon substituting $dp(\tau)$ in Eq. (19), it takes a closed form. Then, it becomes easy to find an approximation that produces close to linear in time volume growth at a constant fluid flux $dV/V(\tau)$ in the interval $0<\tau<5$ by minimizing $\int_0^\tau\left(dV(dp(\xi))/V_{ch}-\gamma q_{f\,l}\xi/V_{ch}\right)^2d\xi$. This is easy to do in Maple, and the order of magnitude of the deviation of mean integral square deviation for the third-order polynomial is 10^{-12}.

Relative magma chamber expansion dV/V at $\tau = 5$ (t = 50 years) is the controlling parameter depending on the multiplication coefficient γ and CO_2 flux. Indeed, even the chamber volume V_{ch} is not well constrained. We take V_{ch} in the range (2–3) $\times$ 10^4 km^3, γ = 1.2–4, S = 1000–2000 km^2, $qCO_2 = 40$ $kg/m^2/yr$. and get at $\tau = 5$

$$dV/V=\frac{\gamma\tau q_{CO_2}S}{V_{ch}\rho_{fl}}=0.5\times10^{-4}-0.002 \tag{22}$$

With variation of q_{CO2} in the range 0–100 kg/m^2/yr., the relative volume increase is within 0–0.005. We calculate the variation of overpressure with time for different parameters values (see **Figure 8a**). For a fixed set of mechanical parameters and different CO_2 fluxes ($dV/V = (0.3–3) \times 10^{-3}$), the overpressure is 1–11 MPa. Hydraulic fracturing with accumulated CO_2 starts at an overpressure that exceeds the tensile strength of rocks, which is realistically estimated to be around 6 MPa [63]. It means that in 10–50 years, CO_2 will be released into the upper crust and after uplift the caldera will subside. Indeed, mechanical parameters and relative shell thickness also influence the pressurization rate (see **Figure 8b**), and the given calculations cannot be considered as an irrefutable proof for the discussed mechanism of "heavy breath". Nevertheless, results of these calculations show that for a certain range of parameters values the mechanism can correctly explain the observations. More field data are required to unambiguously distinguish between accumulation of residual fluid at the solidification [48], and CO_2 infilling. The first mode corresponds to the fast reduction of the magma volume while second to its growth or thermal equilibrium.

4. Acceleration of basaltic magma supply rate due to deglaciation

Large caldera-forming eruptions (LCFE) require a special eruptive mechanism, since normally overpressure in the chamber reaches zero when evacuating a very small fraction of the magma volume [63]. Dunson [63] has suggested that if an eruption occurs while the roof simultaneously subsides along outward dipping faults, then the overpressure can remain on a significant level. Indeed, it has been shown [1] that it is enough to have one outside dipping fault crossing the roof of the magmatic chamber to form a caldera with a trap-door configuration, which can later evolve into a full scale piston-like subsidence of the roof. At the early stage of an eruption, a strong overpressure is required to cause a critical failure of the roof of the magma chamber or the activation of a regional fault. Then, the integrity of the entire structure can be lost and pieces of the roof will literally float in the magma pool below. This will cause an abrupt drop in the magma pressure. When all the volume of the magma (or partial melt) is saturated with respect to the H_2O-CO_2 fluid (which is possible with a CO_2 fluxing), vesciculation will start throughout the magma volume and a reduced magma density will have a feedback effect on the pressure. In this scheme, the factor that creates a sharp increase in the rate of magma generation becomes a trigger capable of initiating LCFE.

4.1. Effect of deglaciation on the melting rate

Deglaciation is a factor, accelerating the rate of magma generation and strongly affecting the stress state of the crust. Glaciation in the Northern Hemisphere was initiated c.a. 3 Myr ago (e.g., [64]). Since then, periodically large ice caps of up to several kilometers thickness were formed and melted in the high latitudes. Ice is similar to low density sedimentary rocks however, at the onset of the interglacial, ice melting rate exceeds normal denudation rates thus creating geologically unprecedentedly high unloading rates. Recently, it was shown that deglaciation locally accelerates erosion rate that enhances net unloading effect [65]. In the areas of magma generation caused by decompressional melting in the ascending mantle flows

http://dx.doi.org/10.5772/intechopen.71655

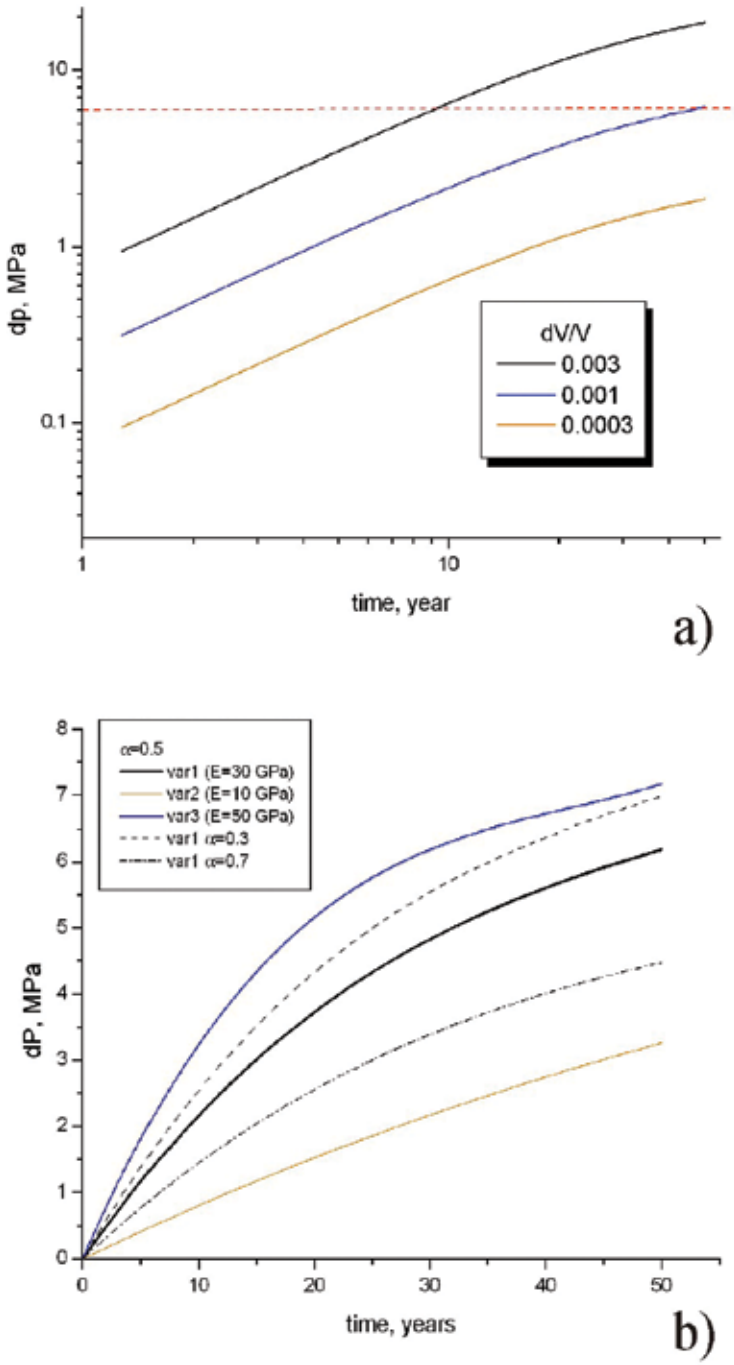

Figure 8. Calculated pressure increase dP at the infilling of magma chamber with CO_2 at P = 2 kbar. Simplified model of a spherical viscoelastic shell filled with magma is used (see text). Different inflation rates are applied overpressure is calculated. In 50 years, the magma volume is increased by dV/V (a) dV/V is in the range 0.0003–0.003 (b) dV/V = 0.001 and different values of Young's modulus, E, and relative thickness of the shell ($\alpha = (R_1/R_0)^3 - 1$) are used.

(mantle plumes, compensatory flows at the delamination, back arc setting in subduction related mantle upwelling) fast decrease of the glacial load produces significant increase in the melting rate. Decompression melting in the ascending mantle flow occurs at a characteristic pressure decrease rate of (3–5) $\times$ 10^{-4} MPa/yr at a flow velocity of 1.0–1.5 cm/yr. [66]. Thus, it appears that when the glacier melting time is about 1000 years, the associated decompression rate is 0.01 MPa/a. That is, the expected increase in melting rate is 20–30 times. In accordance with this estimate, the volumetric eruption rate in Iceland increased 20 times in the Holocene [67]. The effect of deglaciation on the Yellowstone giant magmatic chamber will be considered next.

4.2. Quaternary glaciations in Yellowstone

Geologic observations in the north-central United States (Iowa, Nebraska, Kansas and Missouri) [68] reveal that some of the tills that marked termination of major glaciation episodes were covered by ashes from the last Yellowstone eruptions (2.1, 1.2 and 0.64 Myr ago). Geographically studied region is are far away from Yellowstone but great advance of the ice cap from Canada recorded there probably was in phase with development of glaciation in the highlands in western United States including Yellowstone. Probably multiplicity of caldera-forming eruptions at this location of the mantle plume contrasted with single major eruptions in other calderas of Snake River plain is related to the influence of deglaciation. The last young post-LCT rhyolites eruptions of Central Plateau started in c.a. 260, 176, 124, 79 Kyr [69]. All of them are well correlated with beginning of the global interglacials (see **Figure 9**) after a maximum of 262, 182, 132, 93 Kyr as recorded in the ice core of Vostok site of Antarctica ice shield [70]. Obviously, glacial state of the Yellowstone can differ from the global average reflected in the ice core. Delay of about 14 Kyr for the last event can partially be linked with deviation from the integrated climate variation record. It is also unclear why not all global interglacials have paired rhyolitic eruptions episodes. Christiansen [71] presented arguments that some Central Plateau Member rhyolites were emplaced against glacial ice that may imply that not all eruptions were initiated by deglaciation. These estimates are very preliminary and need extensive field studies to search glacial and postglacial signatures onsite.

4.2.1. Last Pleistocene glaciation in Yellowstone

More is known about the last phase of Pleistocene glaciation in Yellowstone. Based on the fluid inclusions study [48], it has been concluded that Yellowstone plateau was covered with ice sheet with thickness 450–750 m. However, there were no eruptions that can be expected in connection with at least 10-fold increase of the generation rate of basaltic magma. Only hydrothermal explosions producing craters at most 2 $\times$ 3 km in size occurred in early Holocene [72]. First moment after ice load removal is characterized by the largest differential stresses at depths close to the half-width of a glacier. In Holocene, strong earthquakes with magnitude larger than 6 were recognized even in the tectonically passive platforms [73]. Such tectonic events can produce new fractures changing the stress state of the hydrothermal reservoir and provide paths for the deep fluid, thus increasing heat transfer. Hydrothermal explosions are commonly explained by the pressure drop in the water-dominated hydrothermal system with temperature close to boiling [74]. For example, abrupt decrease of the water table due to drainage of glacially dammed lakes [72] will induce deep boiling, reservoir expansion and mechanical disruption with boiling front

http://dx.doi.org/10.5772/intechopen.71655

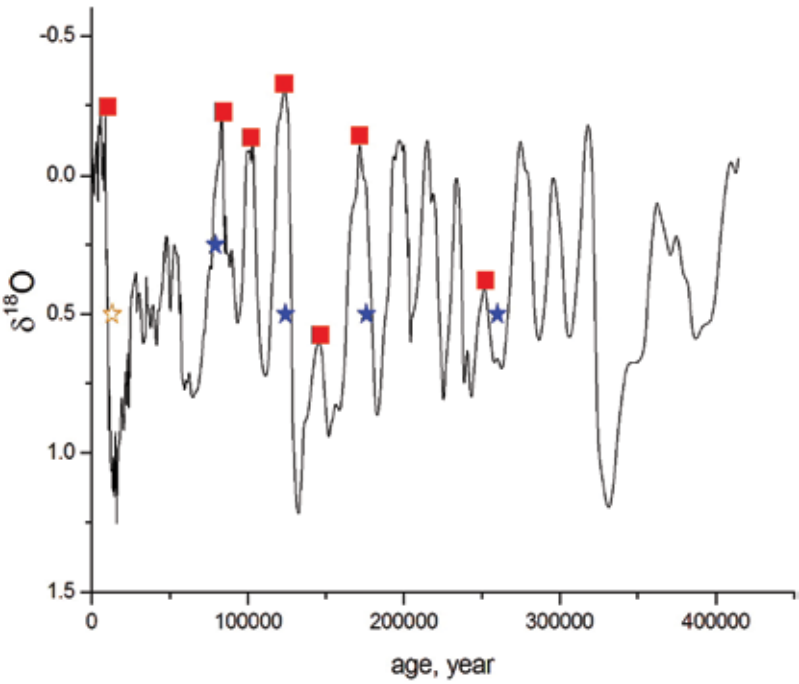

Figure 9. Isotope composition $\delta^{18}O$ of the oxygen from air in ice the core from the Vostok station, in East Antarctica [70] is plotted as global glaciation index, red squares are at the total ice mass minima (interglacials). Blue stars indicate time of the beginning of the recent volcanic activity in Yellowstone [69]. Semi-filled circle corresponds to the burst of the hydrothermal explosions in Holocene [72].

propagating downwards. In their review Browne, Lawless [74] noted that accumulation of gaseous CO_2 near the surface may enlarge the effect of hydrothermal explosion in classic mode. Similar effects can be produced by the fast invasion of the CO_2-rich hot fluid into water-dominated hydrothermal reservoir. A similar mechanism was proposed by Hedenquist and Henley [75], suggesting that Waiotapu (New Zealand) geothermal system was under stress when injected by magmatic gases that induced strong hydrothermal explosion (crater diameter 5 km, maximum depth of ejected clasts 350 m).

4.2.1.1. Some geochemical evidences for CO_2 fluxing in Yellowstone

Reduced carbonic fluid is a good solvent not only for Pt but for Sr as well as other elements [76]. Thus, one can expect that CO_2 fluid passing through the mush zone would transfer light rare earth elements (LREE), Sr from the basalt magma to rhyolitic magma and extract Ba, Sr and some other elements from it, carrying them to the near-surface hydrothermal system.

Our suggestions are consistent with the geochemical data on hydrothermally altered rhyolites from Mary Bay (Yellowstone Lake) [72]. These altered rocks are enriched in Ba (up to 18 times) and especially Sr (up to 80 times) in comparison with intracaldera rhyolites, as expected if their transfer by deep CO_2 is significant. The Sr concentrations in the altered pyroclastics are much higher than in the extracaldera basalts [23]. More interestingly, these rocks (former rhyolites)

have a high Ni content up to 1600 ppm. A close positive correlation between the content of Ni and Co, Ni and Cr and Ni and V was encountered. These observations suggest that some organometallic-compounds of these siderophilic elements were present in the fluid. A detailed hydrological study [77] revealed a clear outflow of Ba and Sr (extracted from the rhyolite mush) into the Yellowstone Lake with geothermal fluids.

4.2.1.2. Current state of Yellowstone magma chamber

In the view of the high uncertainties in the estimates of the heat and CO_2 fluxes and basaltic magma supply rate, results of the glacial probes which reflect the integrated state of the magma chamber under Yellowstone are of exceptional importance. Mechanical test of the last glaciation demonstrated that currently, the magmatic system of Yellowstone is far from the impending catastrophic eruption. Impulse of the basaltic magmatism inevitably accompanying last deglaciation was dumped in the massive mush zone with low partial melt content. It is noteworthy that the time interval of rhyolite eruptions in the post LCT series [69] monotonously decreased with time, which can be interpreted as manifestation of the decay in the basaltic magma generation under the caldera. Moreover "periodic deglaciation forced evacuation" of magma from Yellowstone magma chamber might prevent it from a major eruption.

5. Conclusions

Since extra-large magma chambers require extra-large volumes of the added magma in a short time to erupt, eruptions have an extremely low frequency. Some large magma chambers, such as Yellowstone, are located in areas not only of exceptional magma generation rate, but also of very high CO_2 inflow which can significantly affect the mechanical stability of the chamber.

Deep CO_2 flux in the measured range alone cannot prevent the cooling and solidification of the Yellowstone mush zone. In combination with the thermal energy of basaltic magma, a temporary increase in the flow of CO_2 can switch the thermal state from the thermal equilibrium to the mush melting.

Based on the analysis of melt inclusions, it is possible to estimate the current integrated mass flux of CO_2 to be at least 0.1–0.3 of the total melt mass in the mush zone of Yellowstone. The geochemical consequence of the long CO_2 fluxing can be averaging the magma composition and reducing of the content of Sr and Ba extracted into the geothermal system.

Simple modeling of deformations of viscoelastic rocks of the thermal aureole of Yellowstone magma chamber herein, shows that deep CO_2 fluxing in a reasonable range of flow rate and mechanical parameters can lead to slow uplift and subsidence cycles with a full amplitude of about 1 m and a period of several decades.

The main triggering mechanisms of the eruption are spikes in the rate of generation of basaltic magma caused by internal processes in the mantle plume underlying Yellowstone. In the Quaternary, repeated glaciation in the Northern Hemisphere became another factor that periodically increased magma generation rate 10–30 times in early interglacials. The last Pleistocene

glaciation in Yellowstone caused only hydrothermal and not magmatic eruptions in the Holocene. Since the previous interglacials were marked by voluminous post-LCT rhyolite eruptions, the result of Holocene glacial probing may imply that the current state of the Yellowstone magma system is in a stable or decaying thermal regime.

Author details

Simakin Alexander G.[1,2]* and Ghassemi Ahmad[3]

*Address all correspondence to: simakin@iem.ac.ru

1 Institute of Experimental Mineralogy, RAS, Chernogolovka, Russia

2 Institute of Physics of the Earth, RAS, Moscow, Russia

3 Reservoir Geomechanics & Seismicity Research Group, The University of Oklahoma, USA

References

[1] Simakin AG, Ghassemi A. The role of magma chamber-fault interaction in caldera forming eruptions. Bulletin of Volcanology. 2010;**72**:85-101

[2] Huppert HE, Woods AW. The role of volatiles in magma chamber dynamics. Nature. 2002;**420**:493-495

[3] Corti G, Bonini M, Conticelli S, Innocenti F, Manetti P, Sokoutis D. Analogue modelling of continental extension: A review focused on the relations between the patterns of deformation and the presence of magma. Earth-Science Reviews. 2003;**63**:169-247

[4] Montanari D, Corti G, Simakin A. Magma chambers and localization of deformation during thrusting. Terra Nova. 2010;**22**:390-395

[5] Simakin AG, Ghassemi A. The mechanics of a magma chamber-fault system in transtension with application to Coso. Journal of Structural Geology. 2007;**29**:1971-1983

[6] Meriaux C, Lister JR. Calculation of dike trajectories from volcanic centers. Journal of Geophysical Research. 2002;**107**(B4):2077. DOI: 10.1029/2001JB000436

[7] Muller OH, Pollard DD. Stress state near Spanish Peaks. Pure and Applied Geophysics. 1977;**115**:69-86

[8] Petford N, Cruden AR, McCaffrey KJW, Vigneresse J-L. Granite magma formation, transport and emplacement in the Earth's crust. Nature. 2000;**408**:669-673

[9] Mogi K. Relations between eruptions of various volcanoes and the deformations of the ground surfaces around them. Bulletin of Earth-quake Research Institute. 1958;**36**:99-134

[10] McTigue DF. Elastic stress and deformations near a finite spherical magma body: Resolution of the point source paradox. Journal of Geophysical Research. 1987;**92**(B12):12931-12940

[11] Karlstrom L, Dufek J, Manga M. Organization of volcanic plumbing through magmatic lensing by magma chambers and volcanic loads. Journal of Geophysical Research. 2009;**114**:B10204. DOI: 10.1029/2009JB006339

[12] Folch A, Marti J. Geometrical and mechanical constrains on the formation of ring fault calderas. Earth and Planetary Science Letters. 2004;**221**:215-225

[13] Polteau S, Mazzini A, Galland O, Planke S, Malthe-Sorenssen A. Saucer-shaped intrusions: Occurrences, emplacement and implications. Earth and Planetary Science Letters. 2008;**266**:195-204. DOI: 10.1016/j.epsl.2007.11.015

[14] Gudmundsson A. Conceptual and numerical models of ring-fault formation. Journal of Volcanology and Geothermal Research. 2007;**164**:142-160

[15] Geyer A, Bindeman I. Glacial influence on caldera-forming eruptions. Journal of Volcanology and Geothermal Research. 2011;**202**:127-142

[16] Pinel V, Jaupart C. Magma storage and horizontal dyke injection beneath a volcanic edifice. Earth and Planetary Science Letters. 2004;**221**:245-262

[17] Newman AV, Dixon TH, Gourmelen N. A four-dimensional viscoelastic deformation model for Long Valley Caldera, California, between 1995 and 2000. Journal of Volcanology and Geothermal Research. 2006;**150**:244-269

[18] Karlstrom L, Dufek J, Manga M. Magma chamber stability in arc and continental crust. Journal of Volcanology and Geothermal Research. 2010;**190**:249-270

[19] White SM, Crisp JA, Spera FJ. Long-term volumetric eruption rates and magma budgets. G3. 2006;**7**:Q03010. DOI: 10.1029/2005GC001002

[20] de Silva SL. Altiplano-Puna volcanic complex of the central Andes. Geology. 1989;**17**:1102-1106. DOI: 10.1130/0091-7613(1989)017<1102:APVCOT>2.3.CO;2

[21] Kay SM, Coira BL. Shallowing and steepening subduction zones, continental lithospheric loss, magmatism, and crustal flow under the central Andean Altiplano-Puna Plateau. In: Kay SM, Ramos VA, Dickinson WR, editors. Backbone of the Americas: Shallow Subduction, Plateau Uplift, and Ridge and Terrane Collision. Geological Society of America Memoir ed. GSA; 2009. pp. 229-260. DOI: 10.1130/2009.1204(11)

[22] Hildreth W, Wilson CJN. Compositional zoning of the bishop tuff. Journal of Petrology. 2007;**48**(5):951-999. DOI: 10.1093/petrology/egm007

[23] Bindeman IN, Simakin AG. Rhyolites—Hard to produce, but easy to recycle and sequester: Integrating microgeochemical observations and numerical models. Geosphere. 2014;**10**(5): 1-27. DOI: 10.1130/GES00969.1

[24] Michaut C, Jaupart C. Two models for the formation of magma reservoirs by small increments. Tectonophysics. 2011;**500**:34-49

[25] McKenzie D. The generation and compaction of partially molten rock. Journal of Petrology. 1984;**25**(3):713-765

[26] Tegner C, Thy P, Holness MB, Jakobsen JK, Lesher CE. Differentiation and compaction in the Skaergaard intrusion. Journal of Petrology. 2009;**50**(5):813-840

[27] Veveakis E, Regenauer-Lieb K, Weinberg RF. Ductile compaction of partially molten rocks: The effect of non-linear viscous rheology on instability and segregation. Geophysical Journal International. 2015;**200**:519-523

[28] Rabinowicz M, Vigneresse J-L. Melt segregation under compaction and shear channeling: Application to granitic magma segregation in a continental crust. Journal of Geophysical Research. 2004;**109**(B4). DOI: 10.1029/2002JB002372

[29] Troch J, Ellis BS, Mark DF, Bindeman IN, Kent AJR, Guillong M, Bachmann O. Rhyolite generation prior to a Yellowstone Supereruption: Insights from the Island Park–Mount Jackson rhyolite series. Journal of Petrology. 2017;**58**:29-52. DOI: 10.1093/petrology/egw071

[30] Pritchard CJ, Larson PB, Spell TL, Tarbert KD. Eruption-triggered mixing of extra-caldera basalt and rhyolite complexes along the East Gallatin–Washburn fault zone, Yellowstone National Park, WY, USA. Lithos. 2013;**175–176**:163-177

[31] Husen S, Smith RB, Waite GP. Evidence for gas and magmatic sources beneath the Yellowstone volcanic field from seismic tomographic imaging. Journal of Volcanology and Geothermal Research. 2004;**131**:397-410

[32] Huang H-H, Lin F-C, Schmandt B, Farrell J, Smith RB, Tsai VC. The Yellowstone magmatic system from the mantle plume to the upper crust. Science. 2015;**348**(6236):773-776. DOI: 10.1126/science.aaa5648

[33] Kelbert A, Egbert GD, deGroot-Hedlin C. Crust and upper mantle electrical conductivity beneath the Yellowstone hotspot track. Geology. 2012;**40**(5):447-450. DOI: 10.1130/G32655.1

[34] IRIS. Yellowstone Hotspot: Insights from Magnetotelluric Data [Internet]. 2010. Available from: https://www.iris.edu/gallery3/research/2010proposal/upper_mantle/Yellowstone2_50km_wprofiles

[35] Gaillard F, Malki M, Iacono-Marziano G, Pichavant M, Scaillet B. Carbonatite melts and electrical conductivity in the asthenosphere. Science. 2008;**322**:1363-1365

[36] Smith RB, Jordan M, Steinberger B, Puskas CM, Farrell J, Waite GP, Husen S, Chang W-L, O'Connell RJ. Geodynamics of the Yellowstone hotspot and mantle plume: Seismic and GPS imaging, kinematics, and mantle flow. Journal of Volcanology and Geothermal Research. 2009;**188**:26-56

[37] Frezzotti ML, Peccerillo A, Panza G. Carbonate metasomatism and CO2 lithosphere-astenosphere degassing beneath the western mediterranean: An integrated model arising from petrological and geophysical data. Chemical Geology. 2009;**262**:108-120

[38] Creon L, Rouchon V, Youssef S, Rosenberg E, Delpech G, Szabo C, Remusat L, Mostefaoui S, Asimow PD, Antoshechkina PM, Ghiorso MS, Boller E, Guyot F. Highly CO_2-supersaturated melts in the Pannonian lithospheric mantle – A transient carbon reservoir? Lithos. 2016;**4170**. DOI: 10.1016/j.lithos.2016.12.009

[39] Lowenstern JB, Hurwitz S. Monitoring a Supervolcano in repose: Heat and volatile flux at the Yellowstone caldera. Elements. 2008;**4**:35-40

[40] Bachmann O, Bergantz GW. Gas percolation in upper-crustal silicic crystal mushes as a mechanism for upward heat advection and rejuvenation of near-solidus magma bodies. Journal of Volcanology and Geothermal Research. 2006;**149**:85-102

[41] Barry PH, Hilton DR, Furi E, Halldorsson SA, Gronvold K. Carbon isotope and abundance systematics of Icelandic geothermal gases, fluids and subglacial basalts with implications for mantle plume-related CO_2 fluxes. Geochimica et Cosmochimica Acta. 2014;**134**:74-99

[42] Werner C, Brantley S. CO_2 emissions from the Yellowstone volcanic system. G3. 2003;**4**(7): 1061. DOI: 10.1029/2002GC000473

[43] Sigloch K, McQuarrie N, Nolet G. Two-stage subduction history under North America inferred from finite-frequency tomography. Nature Geoscience. 2008;**1**:458-462

[44] Luth RW. Experimental study of the $CaMgSi_2O_6$–CO_2 system at 3–8 GPa. Contributions to Mineralogy and Petrology. 2006;**151**:141-157

[45] Simakin AG. Peculiarities of the fluid composition in the dry C-O-S system at PT parameters of the low crust by the data of the thermodynamic modeling. Petrology. 2014;**22**(1):50-59

[46] Bons PD, van Milligen BP. New experiment to model self-organized critical transport and accumulation of melt and hydrocarbons from their source rocks. Geology. 2001;**29**(10): 919-922

[47] Morgan P, Blackwell DD, Spafford RE, Smith RB. Heat flow measurements in Yellowstone Lake and the thermal structure of the Yellowstone caldera. Journal of Geophysical Research. 1977;**82**(26):3719-3732

[48] Fournier RO. Geochemistry and dynamics of the Yellowstone National Park hydrothermal system. Annual Review of Earth and Planetary Sciences. 1989;**17**:13-53

[49] Friedman I, Norton DRI. Yellowstone losing its steam?— Chloride flux out of Yellowstone National Park. In: Morgan LA, editor. Integrated Geoscience Studies in the Greater Yellowstone Area—Volcanic, Tectonic, and Hydrothermal Processes in the Yellowstone Geoecosystem. Professional Paper 1717 ed. U.S. Department of the Interior U.S. Geological Survey; 2007. pp. 275-293

[50] Simakin AG, Bindeman IN. Remelting in caldera and rift environments and the genesis of hot, "recycled" rhyolites. Earth and Planetary Science Letters. 2012;**337–338**:224-235

[51] Botcharnikov R, Freise M, Holtz F, Behrens H. Solubility of C-O-H mixtures in natural melts: New experimental data and application range of recent models. Annals of Geophysics. 2005;**48**(4/5):633-646

[52] Newmana S, Lowenstern JB. VolatileCalc: A silicate melt–H_2O–CO_2 solution model written in visual basic for excel. Computers & Geosciences. 2002;**28**:597-604

[53] Anderson AT, Davis AM, Lu F. Evolution of bishop tuff Rhyolitic magma based on melt and magnetite inclusions and zoned phenocrysts. Journal of Petrology. 2000;**41**(3):449-473

[54] Kerrick DM, Jacobs GK. A modified Redlich-Kwong equation of state for H_2O, CO_2, and H_2O-CO_2 mixtures at elevated pressures and temperatures. American Journal of Science. 1981;**281**:735-767

[55] Befus KS, Gardner JE, Zinke RW. Analyzing water contents in unexposed glass inclusions in quartz crystals. American Mineralogist. 2012;**97**:1898-1904

[56] Befus KS, Gardner JE. Magma storage and evolution of the most recent effusive and explosive eruptions from Yellowstone caldera. Contributions to Mineralogy and Petrology. 2016;**171**:30. DOI: 10.1007/s00410-016-1244-x

[57] Drew DL, Bindeman IN, Loewen MW, Wallace PJ. Initiation of large-volume silicic centers in the Yellowstone hotspot track: Insights from H_2O- and F-rich quartz-hosted rhyolitic melt inclusions in the Arbon Valley tuff of the Snake River plain. Contributions to Mineralogy and Petrology. 2016;**171**:10. DOI: 10.1007/s00410-015-1210-z

[58] Chesner CA, Luhr JF. A melt inclusion study of the Toba tuffs, Sumatra, Indonesia. Journal of Volcanology and Geothermal Research. 2010;**197**:259-278

[59] Chang W, Smith RB, Wicks C, Puskas C, Farrell J. Accelerated uplift and source models of the Yellowstone caldera, 2004–2006, from GPS and InSAR observations. Science. 2007;**318** (5852):952-956

[60] Evans WC, Bergfeld D, McGeehin JP, King JC, Heasler H. Tree-ring 14C links seismic swarm to CO_2 spike at Yellowstone, USA. Geology. 2010;**38**:1075-1078

[61] Battaglia M, Troise C, Obrizzo F, Pingue F, De Natale G. Evidence for fluid migration as the source of deformation at Campi Flegrei caldera (Italy). Geophysical Research Letters. 2006;**33**. DOI: L01307, 10.1029/2005GL024904

[62] Dragoni M, Magnanensi C. Displacement and stress produced by a pressurized, spherical magma chamber, surrounded by a viscoelastic shell. Physics of the Earth and Planetary Interiors. 1989;**56**:316-328

[63] Gudmundsson A. The mechanics of large volcanic eruptions. Earth-Science Reviews. 2016;**163**:72-93

[64] Mudelsee M, Raymo ME. Slow dynamics of the northern hemisphere glaciation. Paleoceanography. 2005;**20**. DOI: PA4022, 10.1029/2005PA001153

[65] Sternai P, Caricchi L, Castelltort S, Champagnac J-D. Deglaciation and glacial erosion: A joint control on magma productivity by continental unloading. Geophysical Research Letters. 2016;**43**. DOI: 10.1002/2015GL067285

[66] Ligi M, Cuffaro M, Chierici F, Calafato A. Three-dimensional passive mantle flow beneath midocean ridges: An analytical approach. Geophysical Journal International. 2008;**175**:783-805

[67] Maclennan J, Jull M, McKenzie D, Slater L, Gronvold K. The link between volcanism and deglaciation in Iceland. G3. 2002;**3**:1062. DOI: 10.1029/2001GC000282

[68] Roy M, Clark PU, Barendregt RW, Glasmann JR, Enkin RJ. Glacial stratigraphy and paleomagnetism of late Cenozoic deposits of the north-central United States. GSA Bulletin. 2004;**116**(1/2):30-41

[69] Loewen MW, Bindeman IN. Oxygen isotope and trace element evidence for three-stage petrogenesis of the youngest episode (260-79 ka) of Yellowstone rhyolitic volcanism. Contributions to Mineralogy. 2015;**170**:39

[70] Petit JR, Jouzel J, Raynaud D, Barkov NI, Barnola JM, Basile I, Bender M, Chappellaz J, Davis J, Delaygue G, Delmotte M, Kotlyakov VM, Legrand M, Lipenkov V, Lorius C, Pe'pin L, Ritz C, Saltzman E, Stievenard M. Climate and atmospheric history of the past 420,000 years from the Vostok ice Core, Antarctica. Nature. 1999;**399**:429-436

[71] Christiansen RL. The Quaternary and Pliocene Yellowstone Plateau Volcanic Field of Wyoming, Idaho, and Montana. Professional Paper 729-G Ed. U.S. Geological Survey: Reston, Virginia; 2001. 146 p

[72] Morgan LA, Shanks WCP III, Pierce KL. Hydrothermal Processes above the Yellowstone Magma Chamber: Large Hydrothermal Systems and Large Hydrothermal Explosions. Special Paper 459 ed. The Geological Society of America; 2009. 95 p. DOI: 10.1130/2009.2459

[73] Wu P. Intraplate earthquakes and postglacial rebound in Eastern Canada and northern Europe. In: Wu P, editor. Dynamics of the Ice Age Earth: A Modern Perspective. Uetikon-Zurich, Switzerland: Trans Tech Publications; 1998. pp. 603-628

[74] Browne PRL, Lawless JV. Characteristics of hydrothermal eruptions, with examples from New Zealand and elsewhere. Science Reviews. 2001;**52**:299-331

[75] Hedenquist JW, Henley RW. Hydrothermal eruptions in the Waiotapu geothermal system, New Zealand: Their origin, associated breccias and relation to precious metal mineralization. Economic Geology. 1985;**80**:1640-1668

[76] Simakin AG, Salova TP, Gabitov RI, Isaenko SI. Dry CO2–CO fluid as an important potential deep earth solvent. Geofluids. 2016;**16**:1043-1057

[77] Balistrieri LS, Shanks WC, Cuhel RL, Aguilar C, Val Klump J. The influence of sublacustrine hydrothermal vent fluids on the geochemistry of Yellowstone Lake. In: Morgan LA, editor. Integrated Geoscience Studies in the Greater Yellowstone Area—Volcanic, Tectonic, and Hydrothermal Processes in the Yellowstone Geoecosystem. Professional Paper 1717 ed. U.S. Geological Survey; 2009. pp. 173-199

Section 4

Application of Volcanoes to Industry

Chapter 10

Volcanic Scoria as Cement Replacement

Aref M. al-Swaidani

Additional information is available at the end of the chapter

http://dx.doi.org/10.5772/intechopen.77970

Abstract

Numerous volcanic scoria (VS) cones are found in many places of the world. Many of them have not yet been investigated, although few have been used as binders for a very long time. The use of natural pozzolans as cement replacement could be considered as a common practice in the construction industry due to the related economic, ecologic and performance benefits. This chapter highlights the advantages and disadvantages of the use of volcanic scoria as cement replacement in concrete mixes in terms of fresh and hardened concrete properties. The chemical and mineralogical composition of volcanic scoria samples collected from 36 countries is presented in this chapter, with some further analysis. The effects of using volcanic scoria as cement replacement on some paste, mortar and concrete properties, such as the setting times, the heat of hydration, the compressive strength, the water permeability and the chloride penetrability, have been studied. The improvement in resistance against the chemical attack of volcanic scoria-based cement mortar has also been highlighted. Some estimation equations depending on the data available in literature have also been derived from the analyzed data. The modification of the microstructure of VS-based cement paste has been confirmed, as well.

Keywords: volcanic scoria, blended cement, compressive strength, concrete durability, pozzolan

1. Introduction

Concrete is the most widely used construction material around the world, because of the economic and widespread availability of its constituents, its versatility, its durability and its adaptability [1]. In the year 2000, more than 1.5 billion tons of cement were produced to make, on average, nearly 1 m^3 of concrete per capita [2].

Ordinary Portland cement concrete (OPC) is a composite material and its constituents are cement mixed with water, fine-grained aggregate (sand) and coarse-grained aggregate consisting of natural gravel or crushed stones [3]. Cement is a finely pulverized, dry material that by itself is not a binder but develops the binding property as a result of hydration (i.e., from chemical reactions between cement minerals and water) [4]. The considerable amount of carbon dioxide (CO_2) liberated during the production of Portland cement, the most commonly used hydraulic cement, is of a greater concern. On average, about 1 ton of CO_2 is liberated per ton of Portland cement produced [1].

The use of mineral admixtures such as pozzolans (materials containing reactive silica) in concrete is now widespread due to many economic, ecological and performance-related benefits [4, 5]. Pozzolanic material is "a siliceous or siliceous-aluminous material that in itself possesses little or no cementitious value but will, in finely divided form and in the presence of water, chemically react with calcium hydroxide at ordinary temperatures to form compounds possessing cementitious properties" [6]. Pozzolanic supplementary cementitious materials (SCMs) differ from hydraulic SCMs in that hydraulic SCMs can form cementitious products in water, without the presence of calcium hydroxide [6]. The term "pozzolan" comes from the town of Pozzuoli, northeast of Naples in Italy, where red pozzolanic deposits from the volcano Vesuvius were found [7].

Pozzolanic materials can be divided into natural and artificial pozzolans. Natural pozzolans could be considered the first cementing materials used for the production of artificial stones, ancient mortars and concretes, 3000 years ago [8]. For example, according to Jackson et al. [9], the binding pozzolanic mortars of 2000-year-old concretes in the monuments of imperial age Rome contained 40–50 vol. % of scoriaceous volcanic ash. The natural pozzolans may be further divided into two main groups: (1) those derived from volcanic rocks (volcanic scorias, ashes, tuffs, pumices and obsidians) and (2) others derived from rocks and earths, such as the diatomaceous earths (cherts, opaline silica), clays which have been naturally calcined by heat from flowing lava [10].

Volcanic scoria is loose, rubbly, basaltic to andesitic (40–60% SiO_2) ejecta that accumulates around Strombolian eruptive volcanic vents, eventually building up as a scoria cone, whose height may range from a few tens of meters to 300 m. The scoria clasts range widely in size, from millimeters to centimeters in size, and have a light, frothy texture, being full of vesicles (**Figure 1e**). The vesicular nature of scoria is due to the escape of volcanic gases during eruption. Sometimes these vesicles are refilled with minerals like zeolite, calcite and quartz that form from hot water-rich fluids. The scoria clasts are mainly dark gray in color, although when fresh they may be iridescent, but often the scoria oxidizes by reaction with steam escaping from the vent, when it becomes a deep reddish brown [11–13]. The most economically valuable volcanic scoria deposits are late tertiary or quaternary in age [14]. Most of the scorias are composed of glassy fragments and may contain phenocrysts. The word scoria comes from the Greek *skōria*, rust. An old name for scoria is cinder [15].

With respect to pumice, typical scoria has larger and more interconnected vesicles, is characterized by lower silica content and displays a darker, brown, reddish or black color [16]. Volcanic scoria can be utilized, other than as cement replacement, in several industrial applications including the manufacturing of lightweight concrete, as a heat-insulating material, in addition to other uses such as fillers, filter materials, absorbents and other architectural applications [17].

http://dx.doi.org/10.5772/intechopen.77970

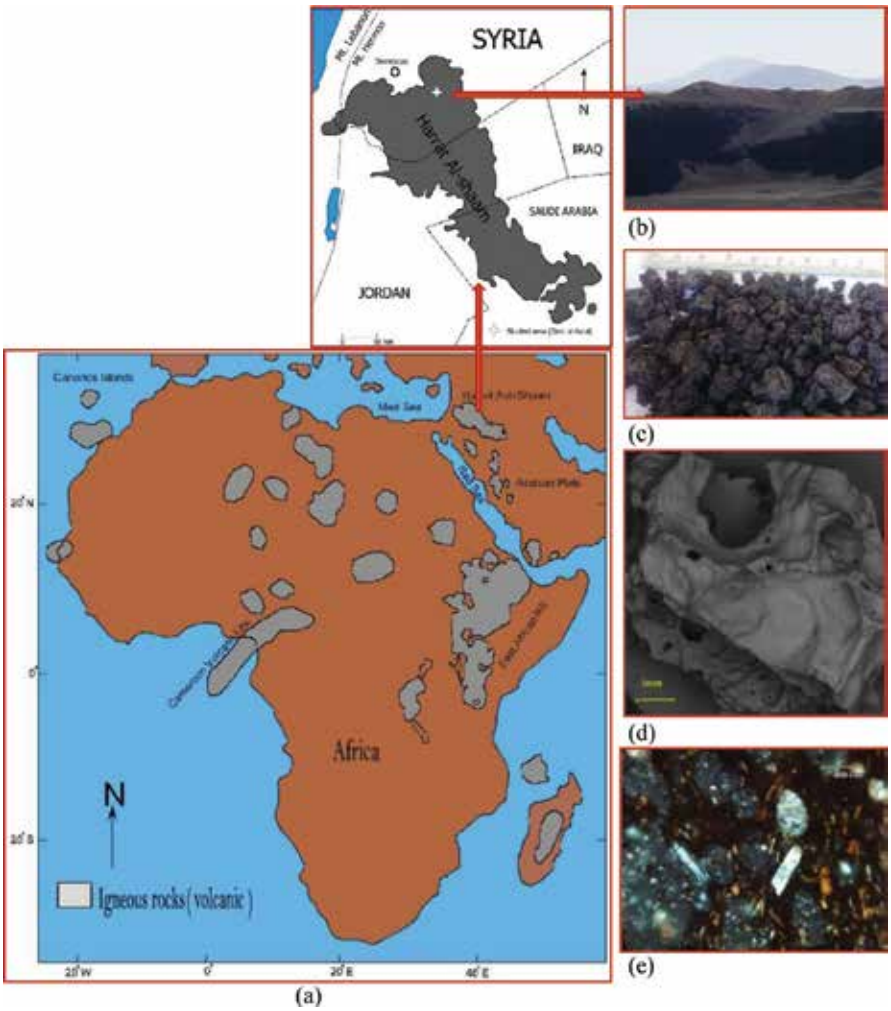

Figure 1. (a) Map of African and Arabian plate with a clearer map of Harrat al-Shaam in the upper part of the figure, (b) Photo of Syrian volcanic scoria cones, (c) Macrograph of volcanic scoria aggregates, (d) SEM of volcanic scoria particle with clear vesicles, (e) Thin section in a Syrian volcanic scoria sample.

Although there are numerous studies on using natural pozzolan as cement replacement, few works on studying volcanic scoria were reported in the literature. The present chapter highlights some characteristics of volcanic scoria and their effects on performance-related properties of paste, mortar and concrete. The importance of this chapter is to encourage countries having ample sources of volcanic scoria cones to further investigate the possibility of using it as cement replacement and thus making a greener concrete.

2. Chemical and mineralogical composition of volcanic scoria

The chemical composition of volcanic scoria varies within wide ranges and depends on its sources. Various scoria cones are abundant in many parts of the world, such as Syria, Turkey,

Source	SiO_2	Al_2O_3	Fe_2O_3	CaO	MgO	K_2O	Na_2O	TiO_2	P_2O_5	LOI	SO_3	R_1	R_2	Detected phases	Ref.
Algeria	45.9–47.2	16.6–18.9	8.4–10.6	9.0–10.8	2.8–4.4	0.2–1.5	0.8–4.3	4.1	n.a.	3.9–5.8	0.4–1.0	63–66.1	72.4–76.1	Gl, Ca, Pl, Py, Qz, Co, Hm, Ac, Ax, Mm, Il	[18–21]
Argentina	47.6	15.4	10.0	10.8	9.8	1.3	3.4	1.4	0.5	n.a.	n.a.	63.0	73.0	Gl, Ol, Pl, CPy, Op	[22]
Armenia	53.6	19.6	7.5		13	4		n.a.	n.a.	n.a.	n.a.	73.2	80.7	n.a.	[23]
Cameroon	41.4–46.9	15.0–16.2	12.8–14.5	7.9–10.5	5.3–8.7	0.9–1.6	2.2–4.5	2.1–3.4	0.4–0.6	0–9.3	0.01	56.8–62.3	69.7–75.9	Gl, Pl, CPy, Py, Ol, Qz, Hm, Mg, An, Ma, Mc, SCAS	[24–30]
Canada	45.7–54.3	12.7–16.0	11.3–12.2	7.1–8.7	4.1–12.5	1.2–1.9	3.2–4.0	1.6–2.2	0.74	0.43	n.a.	58.4–70.3	70.6–81.6	Gl, Pl, Ol, CPy	[31, 32]
Chile	46.4	18.5	12.9	6.5	3.0	1.1	3.5	1.8	0.4	6.4	n.a.	64.9	77.8	Gl, CPy, Pl, Mn, Kn	[33]
China	45.1	14.7	12.4	9.3	9.2	1.8	3.6	2.0	1.8	1.5	n.a.	59.8	72.1	Gl, Ol, Mn, Pl, Py	[34]
Congo	46.7	15.3	13.4	11.3	8.1	3.3	2.1	3.5	0.3	n.a.	n.a.	62.0	75.1	Gl, Ol, CPy, Pl, Mn, Le	[35]
Costa Rica	53.3	19.7	8.1	9.8	5.0	0.6	2.9	0.7	0.2	n.a.	n.a.	72.9	81.1	Gl, CPy, Pl, Ho	[36]
Ethiopia	47.2–49.0	16.1–16.5	12.4–13.7	8.2–10.8	5.4–6.2	0.6–0.9	3.0–3.3	2.4	0.5	0.7	n.a.	63.7–65.1	76.1–78.8	n.a.	[37, 38]
France	45.1–56.8	15.2–17.7	7.0–8.2	7.8–12.6	3.7–8.8	0.9–1.8	3.2–3.6	0.7–3.0		n.a.	n.a.	60.3–74.5	68.5–81.5	Gl, CPy, Py, Pl, Ol, Mn, Am,	[39, 40]
Germany	45.5–47.9	6.4–15.4	7.4–14.8	8.2–23.7	6.5–12.6	0.03–0.5	0.6–1.2	3.0–3.1	1.2	6.05	n.a.	51.9–63.3	59.2–78.1	Gl, Ol, Pl, CPy, Py, Am, Mi	[41, 42]
Indonesia	55.1–56.7	18.0–18.5	8.2–8.8	8.1–9.2	3.7	0.8–1.4	2.9–3.1	0.6–0.8	0.2	0.0–0.3	n.a.	73.6–74.7	82.4–82.9	Gl, Pl, Py, CPy, Mn	[43, 44]
Iran	48.0–48.3	12.3–16.4	9.4–11.4	9.6–9.8	4.4–7.7	1.3–2.7	3.3–5.6	1.8–2.6	1.1–1.6	1.1	n.a.	60.3–64.7	69.7–76.1	Gl, Py, Ol, Mn, CPy	[45, 46]
Italy	50.6	19.7	9.1	6.2	3.8	2.3	0.7	1.0	0.3	7.2	n.a.	70.3	79.3	n.a.	[47]
Japan	54.3	15.6	13.7	9.5	3.9	0.5	2.0	1.2	0.1	n.a.	n.a.	70.0	83.7	Gl, Ol, CPy, Pl	[48]
Jordan	41.7	10.6	8.9	12.8	6.3	1.4	1.1	2.3	0.4	n.a.	n.a.	52.3	61.2	n.a.	[49]
Madagascar	44.6	13.0	12.5	12.1	9.6	1.3	2.4	2.3	0.7	n.a.	0.02	57.7	70.2	Gl, Pl, Mn, CPy, Ol	[50]
Mexico	54.2–56.0	15.5–18.0	7.1–14.7	7.1–7.7	5.3–9.5	0.9–1.1	3.4–4.8	0.8–1.0	0.2–0.3	0.01	n.a.	69.7–73.9	81.0–84.5	Gl, Pl, Ol, Py, CPy	[51, 52]

Source	SiO_2	Al_2O_3	Fe_2O_3	CaO	MgO	K_2O	Na_2O	TiO_2	P_2O_5	LOI	SO_3	R_1	R_2	Detected phases	Ref.
New Zealand	46.3–47.3	11.5–13.7	10.8–13.0	8.4–9.4	9.2–16.7	0.8–1.3	2.9–3.3	2.8	0.6	n.a.	n.a.	58.8–59.9	69.6–73.0	Gl, Ol, CPy, Pl, Fe-Ti oxides	[53, 54]
Nicaragua	56.4	18.0	7.8	7.3	2.2	1.2	3.0	0.8	0.6	n.a.	n.a.	74.5	82.3	Gl, Pl, Ol, CPy, Mn	[55]
Papua New Guinea	47.5	14	3.5	6.5	5	5.0		n.a.	n.a.	1.4	0.02	61.5	65.0	n.a.	[56]
Peru	57.4	17.9	6.2	4.6	n.a.	n.a.	n.a.	n.a.	n.a.	n.a.	n.a.	75.3	81.5	n.a.	[57]
Philippines	53.2	18.5	8.9	8.5	4.4	0.95	3.4	0.7	0.3	0.2	n.a.	71.7	80.6	n.a.	[58]
Romania	46.1	18.8	9.9	10.4	7.2	1.7	3.2	1.6	1.1	n.a.	n.a.	64.9	74.8	n.a.	[59]
Russia	52.6	14.4	9.7	8.0	4.2	2.1	3.7	1.5	0.5	n.a.	n.a.	70.0	79.7	Gl, Ol, Py, Pl	[60]
Saudi Arabia	42.0–46.5	13.1–16.6	11.1–15.8	7.8–10.0	2.5–11.4	0.6–1.5	0.2–3.5	2.1–2.8	0.3–0.6	0.9–4.9	0.02–0.27	58.0–61.2	69.4–74.4	Gl, Pl, Ol, CPy, Py, Qz	[61–65]
Southern Pacific Ocean	43.9	10.8	12.6	13.1	12.9	1.5	1.4	3.1	0.5	n.a.	n.a.	54.7	67.3	n.a.	[66]
South Africa	47.3	15.7	13.1	8.7	5.5	1.0	4.2	3.7	0.7	n.a.	n.a.	62.9	76.0	Gl, Ol, CPy, Pl	[67]
Spain	44.3–46.3	14.2–17.1	10.0–12.2	8.8–9.5	4.5–9.0	1.7–2.1	2.7–4.9	2.4–3.3	0.7–1.3	n.a.	n.a.	59.2–63.4	70.9–73.4	Gl, Ol, CPy, Mn, Pl, Le	[68–70]
Syria	44.9–46.5	13.0–17.0	8.6–11.4	9.4–10.1	8.9–9.1	0.8–1.8	2.1–2.8	0.9	n.a.	0.4–2.6	0.01–0.27	59.5–61.9	70.5–70.9	Gl, Ol, Pl, Ca, CPy, Fu	[71, 72]
Tanzania	40.0	13.0	13.9	9.6	4.6	n.a.	n.a.	n.a.	n.a.	10.8	n.a.	53	66.9	n.a	[73]
Taiwan	51.5	18.8	11.1	10.0	4.7	0.4	2.8	0.9	0.1	1.4	n.a.	n.a.	n.a.	Gl, Ol, Pl, Py	[74]
Turkey	54.9–55.6	16.9–17.7	6.6–10.3	6.5–8.1	2.0–5.1	1.2–1.9	2.2–3.5	1.1–2.6	0.3–0.4	0.3–0.9	0.29	71.8–73.2	79.8–82.2	Gl, Pl, Py, CPy, Qz, Ho,	[75–77]
USA	48.0	16.7	11.8	8.6	5.9	1.8	3.5	2.0	1.2	n.a.	n.a.	64.8	76.6	Gl, Ol, Pl	[78]
Yemen	48.5	16.5	12.2	8.6	5.7	1.0	3.6	1.9	0.4	1.8	n.a.	65.1	77.3	n.a.	[79]

LOI: Loss On Ignition; n.a.: Not available.

Gl: Glass; Pl: Plagioclase; Ol: Olivine; Py: Pyroxene; CPy: Clinopyroxene, Mu: Muscovite; Qz: Quartz; Ma: Managocalcite; An: Anatase; Mc: Microcline, SCAS: Sodium calcium aluminum silicate; Co: Cordierite; Ac: Analcime; Ax: Axinite; Mn: Magnetite; Ca: Calcite; Hm: Hematite; Il: Illite; Mm: Montmorillonite; Ho: Hornblend; Mg: Maghemite; Fu: Fujasite; Am: Amphibole; OP: Opaque minerals; Mi: Mica; Kn: Kaolinite; Le: Leucite

Table 1. Chemical composition of some different scoria samples quarried from 36 countries.

http://dx.doi.org/10.5772/intechopen.77970

Saudi Arabia, Cameroon, Ethiopia, Jordan, Libya, Algeria, Spain and others [18–79]. Harrat Al-Shaam volcanic field, for example (**Figure 1a**), is a basaltic province, extends widely at the Arabian plate (over 50,000 km^2), covers the south of Syria, northeast of Jordan, north of Saudi Arabia and contains hundreds of volcanic scoria cones [80, 81]. The chemical analysis of some volcanic scoria reported for 36 countries [18–79] is presented in **Table 1**.

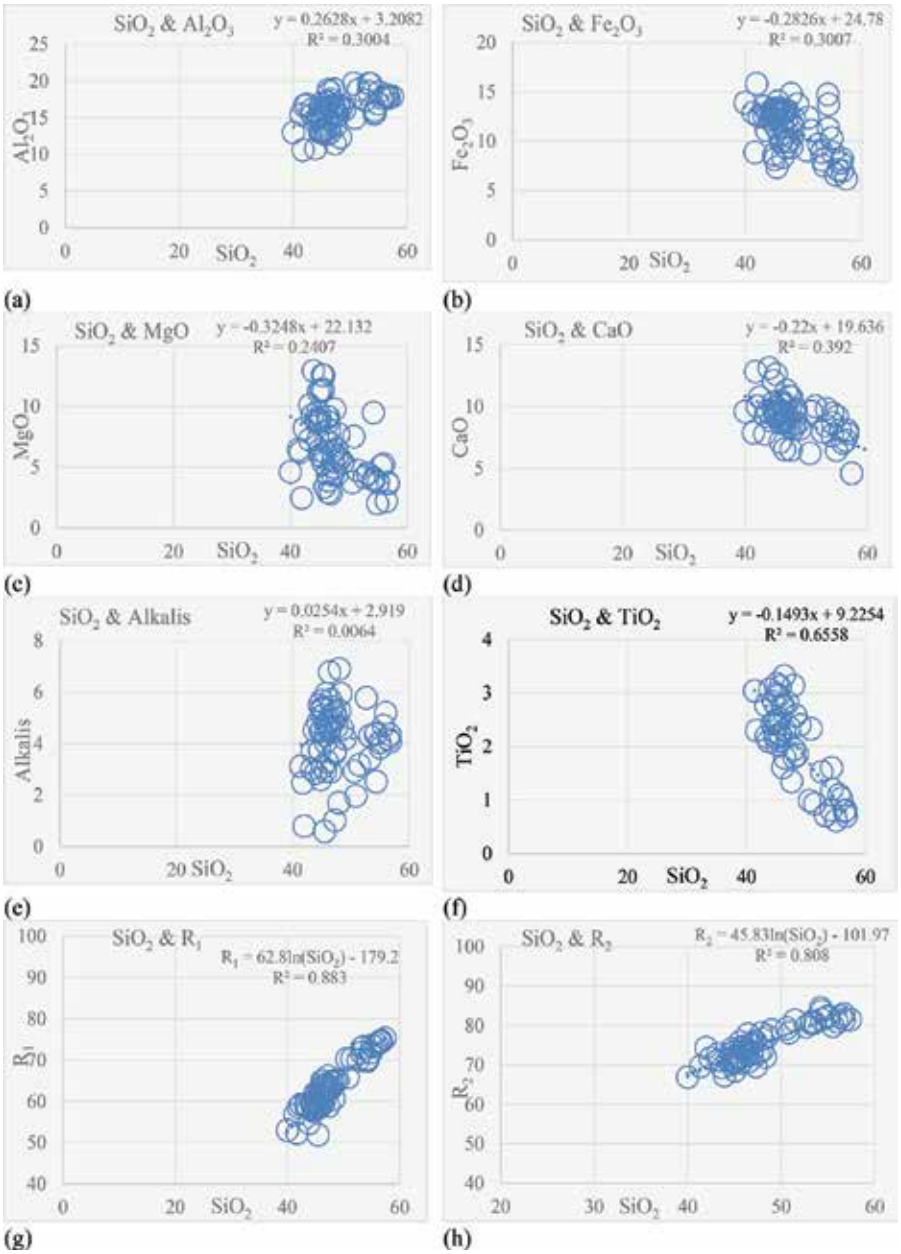

Figure 2. Different oxides versus silica content in the volcanic scoria (R_1: sum of SiO_2 and Al_2O_3; R_2: sum of SiO_2, Al_2O_3 and Fe_2O_3) [18–79].

Table 1 shows that most of the volcanic scoria samples are relatively rich in silica (40–60%) and alumina (10–20%). The next oxides are iron (5–16%), calcium (5–13%) and magnesium (2–13%) oxides. The alkali content is not high but may vary between 1 and 7%. Loss on ignition is generally low but may reach 10% in some pozzolans. Harker variation diagrams (**Figure 2**), using SiO_2, show a general increase of Al_2O_3 and alkalis with increasing SiO_2. However, the elements such as Fe_2O_3, MgO, CaO and TiO_2 display inverse relationships with SiO_2. The author attempted to derive an equation in order to estimate R_1 (sum of SiO_2, Al_2O_3 and Fe_2O_3) and R_2 (sum of SiO_2, Al_2O_3 and Fe_2O_3) from the knowledge of SiO_2 content (**Figure 2**).

The mineralogical composition of volcanic scoria also varies depending upon their sources. Owing to their formation process, volcanic scoria consists of crystalline and noncrystalline particles as glassy particles. The most detected minerals are plagioclase, olivine, pyroxene and clinopyroxene.

3. Reactivity of volcanic scoria

Volcanic scoria as a pozzolanic material has high silica (SiO_2) and alumina (Al_2O_3) content with a glassy/amorphous structure for reactivity with lime or cement [82]. Reactive silica content can react with portlandite (CH) liberated from the hydration of C_3S and C_2S in cement. This reaction forms additional calcium silicate hydrates (C-S-H). The principal reaction is.

$$\text{CH (Portlanite)} + \text{S (reactive silica)} + \text{H (Water)} \rightarrow \text{C} - \text{S} - \text{H}\left(\text{Calcium silicate hydrates}\right) \quad (1)$$

The composition of C-S-H is not very different from that formed in regular hydration, although generally the C/S molar ratio is slightly lower [83]. Analogously to reactive silica, reactive alumina present in volcanic scoria can react with CH to form calcium aluminate hydrates (C-A-H) [83]. This reaction which is frequently called the pozzolanic reaction is slow, portlandite consuming and very efficient in filling up capillary spaces [4]. It depends on several factors, such as the glassy phase content in volcanic scoria and the fineness of volcanic scoria.

3.1. Glassy phase in volcanic scoria

ASTM designation C618 (2012) [84] requires that for a material to be accepted as a natural pozzolan, the sum of SiO_2, Al_2O_3 and Fe_2O_3 should have a minimum value of 70% and the strength activity index should exceed 75% of the control mortar's compressive strength at either 7 or 28 days. The strength activity index (SAI) gives an indication of the reactivity of volcanic scoria by comparing the compressive strength of mortar cubes made with 80 wt.% cement and 20 wt.% volcanic scoria to the compressive strength of the control mortar cubes made with only cement. In addition, EN 197–1(2000) [85] requires a reactive silica content of more than 25% for volcanic scoria to be accepted as natural pozzolan.

3.2. Fineness of volcanic scoria

An increase in fineness that exposes more surface area of the volcanic scoria may accelerate the early pozzolanic reactivity [86, 87]. The specific surface area of volcanic scoria, which is the area

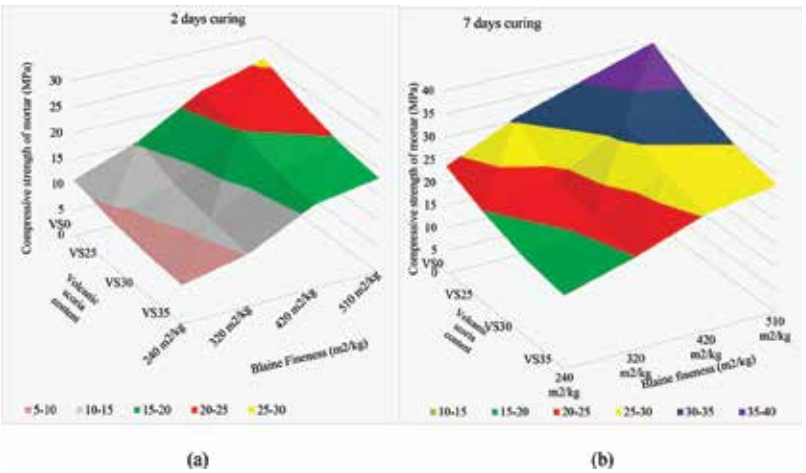

Figure 3. Effect of fineness on compressive strength of VS-based cement mortars cured for 2 (a) and 7 (b) days [89].

of a unit mass, is measurable by different techniques. The most common is the Blaine-specific surface area technique, which measures the resistance of compacted particles to an air flow. A laser particle size analyzer can also be used for the determination of the specific surface area of volcanic scoria [88, 89]. Al-Swaidani et al. [89] reported an increase of about 145% in the early compressive strength when the Blaine fineness of 2-day-cured volcanic scoria (VS)-based cement increased from 240 to 510 m^2/kg at replacement levels ranging from 25 to 35% by mass, as shown in **Figure 3**. The authors also concluded that an increase of about 5 MPa can be expected for every 1000 cm^2/g increase in Blaine fineness for VS-based binder mortars at all curing times [89]. Similar results were obtained by other researchers [90, 91]. This reactivity enhancement was explained by the effect of grinding which breaks the vitreous body, decreases the particle size and increases dissolution rate and solubility of volcanic scoria, which will accelerate pozzolanic reaction rate and the strength development of mortar containing volcanic scoria [89, 90, 92].

4. Properties of VS-based cement paste

4.1. Setting times

Most of the studied scoria samples showed an increase, ranging from slight to significant, in setting times of the VS-based cement paste with the increase in volcanic scoria content. This can be explained by the reduction of hydration heat on the binder system with the presence of VS [91]. A significant relationship ($R^2 \approx 0.9$) between initial and final setting times was obtained by the author depending on data collected from other papers [20, 62, 71, 72, 75, 79, 89, 91], as clearly shown in **Figure 4**. So, knowing initial setting time, the final setting time of the VS-based cement paste can be predicted by using the equation shown in **Figure 4**. It is worth to note that among all the investigated volcanic scoria compiled with the standard requirements in terms of the initial setting time, most of them met the requirements in terms of final setting times (i.e., initial setting time ≥ 45 min and final setting time ≤ 420 min), according to ASTM C595 [93].

4.2. Heat of hydration

The hydration of cement paste is accompanied by the liberation of heat that raises the temperature of the concrete mix. Because of the slower pozzolanic reaction, the partial replacement of cement by volcanic action results in a release of heat over a longer period of time enabling the heat to dissipate and the overall concrete temperature to remain lower. This is of great importance in mass concrete where cooling, following a large temperature rise, can lead to cracking. As shown in **Figure 5**, a volcanic scoria from Syria reduced the heat of hydration [94]. Similar results were also reported by Alhozaimy et al. [95] who concluded that the heat of hydration of VS-based cement pastes liberated in the first 72 h was, on average, 85% of the control mix.

4.3. Microstructure

The presence of volcanic scoria leads to the disappearance of portlandite crystals and the appearance of the condensed type of C-S-H crystals, as shown in **Figure 6**. This type of condensed C-S-H results from the interaction of pozzolanic material with portlandite. Condensed

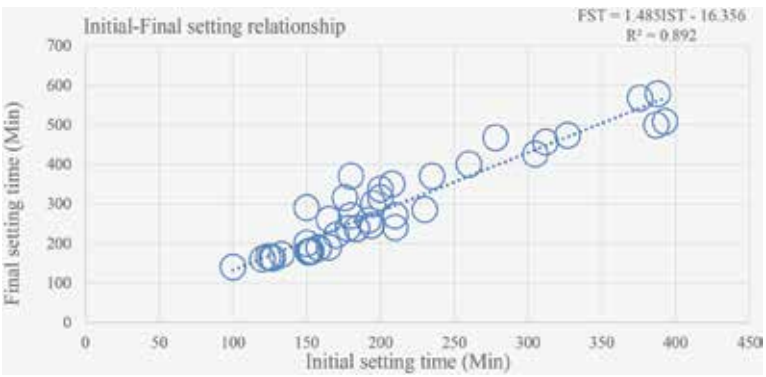

Figure 4. Relationship between initial and final setting times.

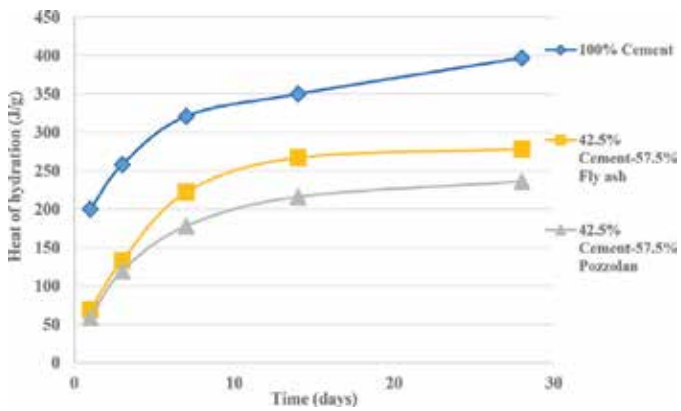

Figure 5. Influence of different SCMs on the heat of hydration of the mixtures [94].

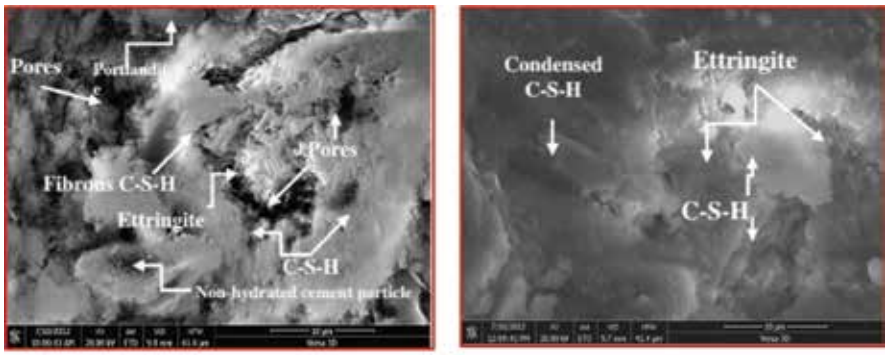

Figure 6. SEM of (a) control cement paste; (b) 20% VS-based cement paste [63].

C-S-H fills the micropores, reduces the porosity and consequently improves the impermeability and the compressive strength. The enhancement in the microstructure in the mixtures with volcanic scoria can be attributed to the formation of additional C-S-H, which generally fills in the pores, creates denser hydration products and accordingly reduces the permeability [63]. Similar observations were also reported in the literature [71, 72].

5. Properties of VS-based cement mortar/concrete

5.1. Compressive and flexural strength

All the results reported in the literature [18–20, 30, 56, 62, 63, 71, 72, 75, 79, 89, 91, 96, 97] show that the compressive strength of VS-based cement mortars/concretes increases with the curing age and decreases with the replacement level of volcanic scoria content (**Figure 7**). This reduction in the compressive strength is attributed mainly to slower pozzolanic activity at room temperature of volcanic scoria as natural pozzolan [71, 83]. This ascertainment is explained by the interaction between the reactive silica which is in the glassy portion of the addition and the $Ca(OH)_2$ released by the hydration of the cement. It has also been noted that the mortars containing volcanic scorias exhibit compressive strength comparable to those of the control mortar starting from the period of 90 days.

The author attempted to derive an equation in order to reasonably estimate the relative compressive strength of VS-based mortars. This prediction equation could be written as follows:

$$RCS = (0.176\ln t - 1.343)\,VS + 1.01 \quad (R^2=0.81) \tag{2}$$

where RCS is the relative compressive strength, t is the curing age (day) and VS is the volcanic scoria content (%). This prediction equation having a relatively high coefficient of determination ($R^2 = 0.81$) was obtained through the regression analysis of literature data (**Figure 8**). The variants in the equation are the curing age and the volcanic scoria content. So, knowing the

http://dx.doi.org/10.5772/intechopen.77970

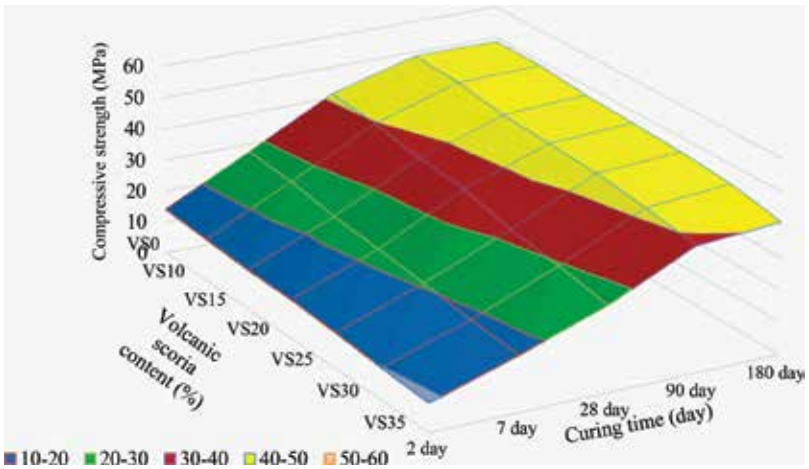

Figure 7. Compressive strength of VS-based cement concrete at different curing times [98].

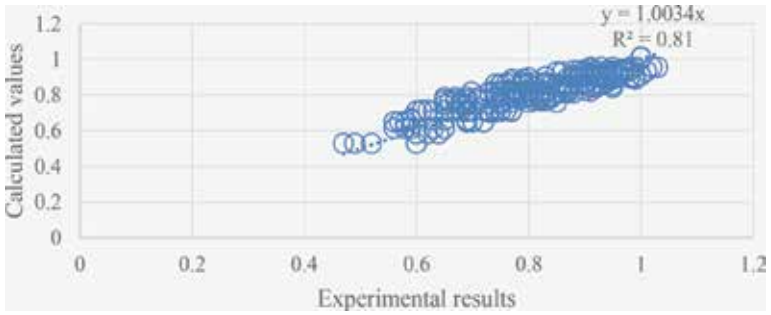

Figure 8. Experimental results versus calculated values for relative compressive strength of volcanic scoria cement-based mortars.

curing age and the volcanic scoria content and the compressive strength of the control sample (i.e., without volcanic scoria), the compressive strength of VS-based cement and mortar could be reasonably estimated.

It is worth to mention that, in contrast to previous literature, studying the effect of total alkali content (Na_2O and K_2O) and K_2O on the compressive strength of VS-based cement mortars did not give definite correlations (**Figure 9**).

A similar behavior was observed by many researchers in terms of flexural tensile strength of VS-based cement mortars. An attempt to predict the flexural strength based on the compressive strength, with a reasonable coefficient of determination ($R^2 = 0.83$), is clearly shown in **Figure 10**.

5.2. Drying shrinkage

Drying shrinkage represents the strain caused by the loss of water from the hardened material. The shrinkage is believed to originate in the C-S-H and its associated porosity [83].

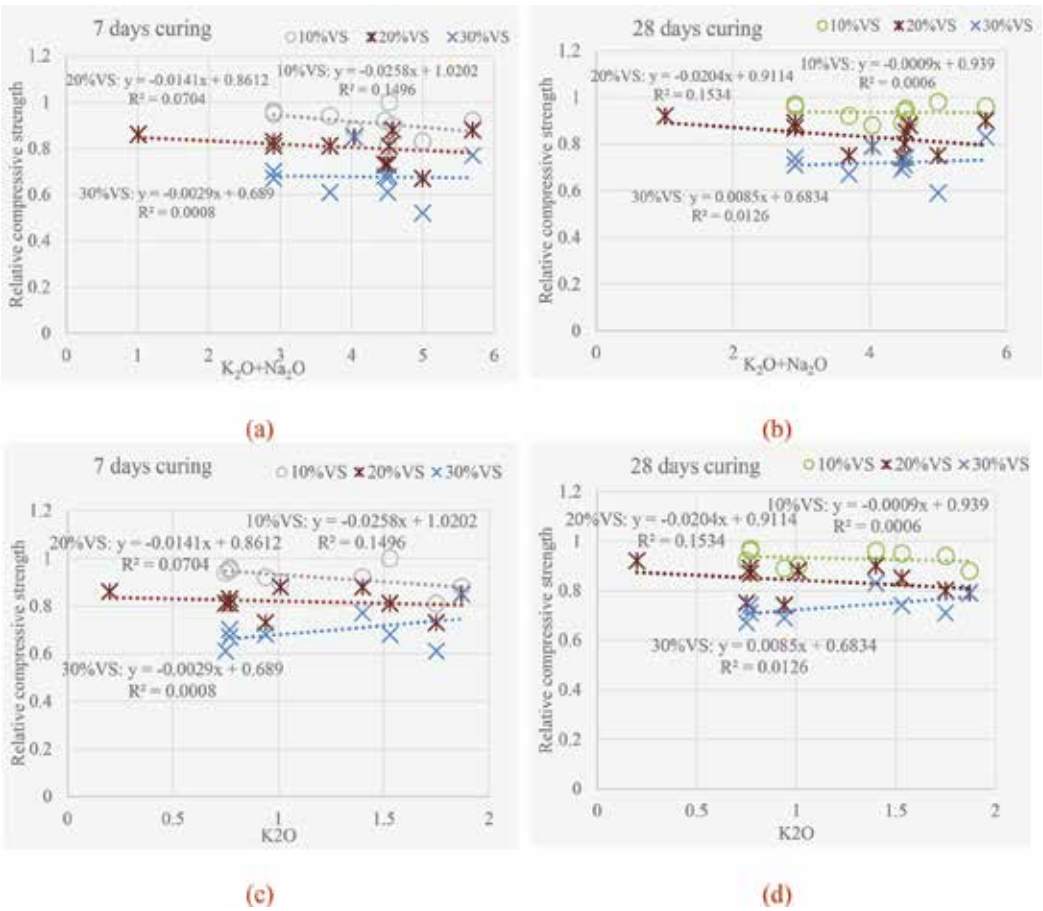

Figure 9. Effect of total alkali content (a and b) and K_2O content (c and d) on compressive strength of VS-based cement mortars at 7 and 28 days curing.

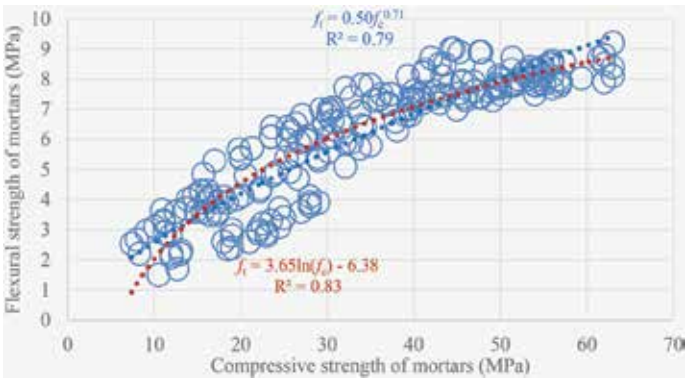

Figure 10. Relationship between compressive and flexural strengths of VS-based cement mortars.

http://dx.doi.org/10.5772/intechopen.77970

The increase of drying shrinkage with the cement replacement level [99] might be due to: (1) the pozzolanic reaction, generating an additional CSH, resulting in the decrease in spacing of CSH particles; (2) the transportation of large pores into fine pores (pore size refinement) increasing capillary tension [99–103]; (3) the higher water demand of scoria-based cements [99, 102]; (4) the porous microstructure of scoria [104] (**Figure 1d**). However, this increase was lower than the maximum 0.03% allowed by ASTM C618 (**Figure 11**) [99].

Figure 11 shows the results of drying shrinkage of VS-based cement mortars.

5.3. Sulfate attack

The sulfate attack on the cement mortar is a complex process involving the hydration products produced by Portland cement. The damage caused by sulfate attack may involve cracking and expansion of mortar as a whole, as well as softening and disintegration of cement paste [83]. Cements with a high C_3A content will be subject to sulfoaluminate corrosion in which ettringite is formed, as displayed in Eq. (3) [83, 105].

$$C_4A\check{S}H_{12}\ (\text{Monosulfate}) + 2C\check{S}H_2\ (\text{Gypsum}) + 16H\ (\text{Water}) \rightarrow C_6A\check{S}_3H_{32}\ (\text{Ettringite}) \quad (3)$$

This type of corrosion is initiated by the reaction between sulfate ions and calcium hydroxide (CH):

$$CH\ (\text{Calcium hydroxide}) + SO_4^{2-}(aq)\ (\text{Sulfate ion}) \rightarrow C\check{S}H_2\ (\text{Gypsum}) + 2OH^-\ (aq) \quad (4)$$

This reaction can be described as gypsum corrosion. Both reactions are accompanied by an expansion in solid volume causing internal stresses and ultimately lead to cracking [83].

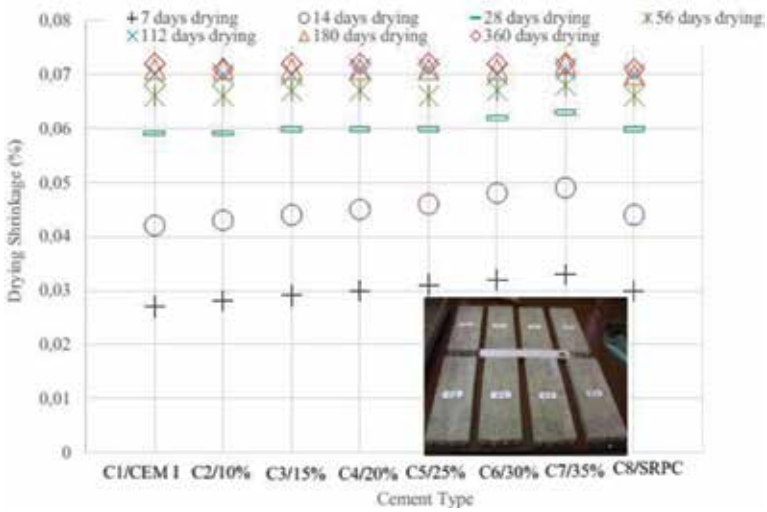

Figure 11. Drying shrinkage values of prismatic mortar specimens [99].

The beneficial effects of using volcanic scoria on the sulfate resistance of mortar as reported by many authors [5], **Figure 12**, may be ascribed to a number of mechanisms [5, 106–108], including:

- reduced permeability,
- dilution of the C_3A phases and CH (both participants in reactions with sulfates) as a result of the partial replacement of Portland cement,
- consumption of CH by pozzolanic reaction and
- alteration of hydrated aluminate phases, making them more resistant, for example, the presence of reactive silica may favor the formation of strätlingite (C-A-S-H).

5.4. Acidic attack

Sulfuric acid, among other aggressive acids such as HCl, HNO_3 and CH_3COOH, is very damaging to mortar as it combines an acid attack and a sulfate attack [109]. At the first stage, deterioration of $Ca(OH)_2$ results in an expansive gypsum formation. The gypsum then reacts with C_3A in the aqueous environment and forms a more expansive product called ettringite. These very expansive compounds cause internal pressure in the mortar, which leads to the formation of cracks [110] and the transformation of the mortar into a mushy or a noncohesive mass [111]. Sulfuric acid may also cause the decalcification of calcium silicate hydrates C-S-H and will ultimately transform the C-S-H into amorphous hydrous silica. The following equations express these reactions [110]:

$$Ca(OH)_2 + H_2SO_4 \rightarrow CaSO_4.2H_2O \text{ (Gypsum)} \tag{5}$$

$$3(CaSO_4.2H_2O) + 3CaO.Al_2O_3.12\,H_2O + 14\,H_2O \rightarrow 3CaO.Al_2O_3.3CaSO_4.32\,H_2O_3 \text{ (Ettringite)} \tag{6}$$

$$CaO.SiO_2.2H_2O + H_2SO_4 \rightarrow CaSO_4 + Si(OH)_4 \text{ (Hydrous silica)} + H_2O \tag{7}$$

The white gypsum, which covers the surface of mortar, can potentially lead to the blocking of pores on the surface, leading to a slower rate of attack initially. However, this effect lasts only temporarily [112].

The better performance of VS-based cement mortars in terms of the acid attack, as shown in **Figure 13** [99], can be due to the pozzolanic reaction [5, 113, 114]. This reaction between scoria and calcium hydroxide liberated during the hydration of cement [5, 114] leads to a refinement of the pore structure resulting in a highly impermeable matrix [5, 113]. The pozzolanic reaction also fixes $Ca(OH)_2$, which is usually the most vulnerable product of the hydration of cement insofar as the acid attack is concerned [115]. In the study by al-Swaidani and Aliyan [5],

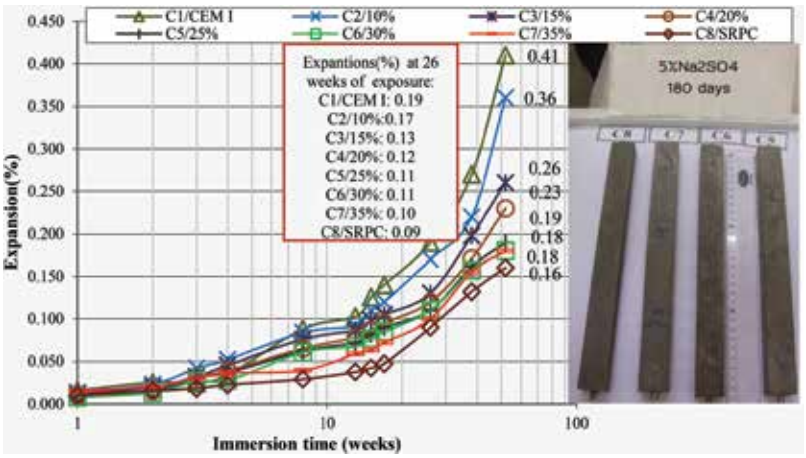

Figure 12. Length changes over time of prismatic mortars immersed in 5% Na_2SO_4 [5].

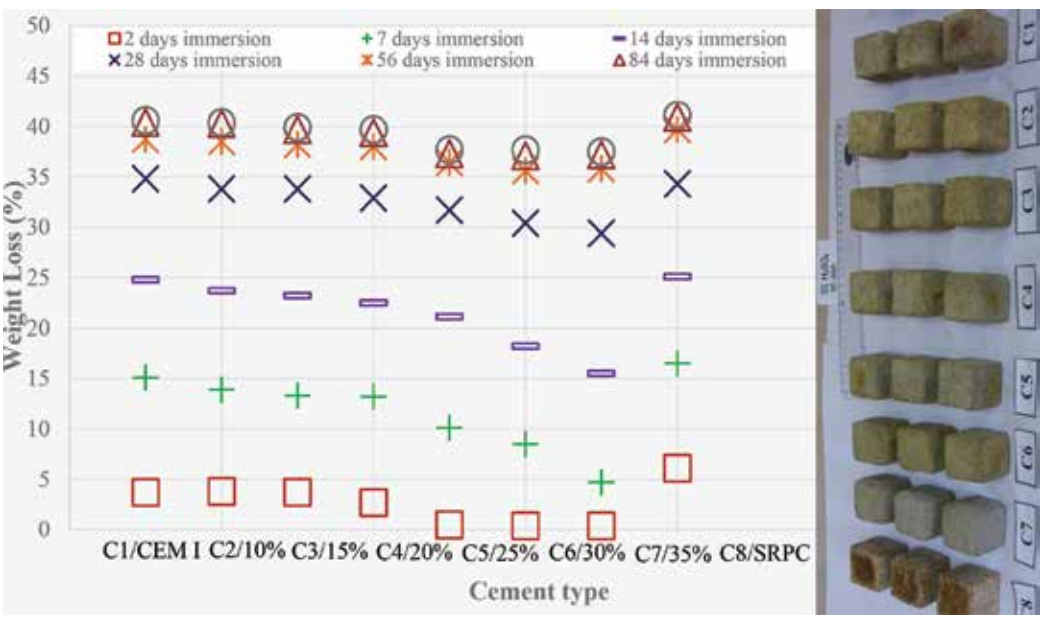

Figure 13. Weight losses over time of 90 days-cured mortars exposed to 5% H_2SO_4 [99].

the number of days needed to register a 10% loss in weight was considered in their evaluation. As shown in **Table 2**, the 10% weight loss was obtained with 35% VS-based cement mortars up to 6.2 and 6.70 days of exposure to sulfuric acid and 4.6 and 5.2 days of exposure to hydrochloric acid at 28 and 90 days curing, respectively. In addition, none of the mixtures containing 25% volcanic scoria and more lost 10% weight even after 100 days of exposure to nitric and acetic acids.

Cement type	Number of days to register 10% weight loss							
	5% H_2SO_4		10% HCl		5% HNO_3		10% CH_3COOH	
	28 days curing	90 days curing	28 days curing	90 days curing	28 days curing	90 days curing	28 days curing	90 days curing
C1/CEMI	3.5	3.5	3.7	3.2	22.5	25.9	NR	NR
C2/10%	3.7	3.7	3.7	3.1	25.4	22.8	NR	NR
C3/15%	3.8	3.8	3.8	3.6	55.5	48.9	NR	NR
C4/20%	4.0	4.1	3.9	3.7	79.1	97.3	NR	NR
C5/25%	4.7	5.1	4.1	4.3	NR	NR	NR	NR
C6/30%	5.2	5.8	4.4	4.9	NR	NR	NR	NR
C7/35%	6.2	6.7	4.6	5.2	NR	NR	NR	NR
C8/SRPC	3.0	3.0	3.2	2.9	20.1	18.8	NR	NR

NR 10% weight loss was not reached.

Table 2. Number of days needed to register a 10% weight loss of mortar cubes [5].

5.5. Permeability

Permeability of concrete to water is closely related to the durability of concrete. Permeability is the rate at which aggressive agents penetrate through concrete [115].

5.5.1. Water permeability

Water penetration depth can be considered as an indication of permeable and impermeable concrete [115]. A depth of less than 50 mm classifies the concrete as impermeable and a depth of less than 30 mm as impermeable under aggressive conditions [115]. The water penetration depth test results for concretes containing VS-based cement concretes show their lower permeability when compared with plain Portland cement, particularly at late ages (**Figure 14**) [98].

5.5.2. Chloride penetrability

Although chloride ions in concrete do not directly cause severe damage to the concrete, they contribute to the corrosion of steel bars embedded in concrete that is considered as the factor causing most premature deterioration of reinforced concrete (RC) structures worldwide, especially in the marine environments. Therefore, the study of chloride penetrability is important for evaluating reinforcing steel corrosion in RC structures. This has prompted the search for economic methods of extending the service life of structures. One of these methods was the use of pozzolan such as volcanic scoria [5].

The improvement in resistance of volcanic scoria-based cement concretes to chloride penetration which was frequently noted in the literature may be related to their refined pore structure and their reduced electrical conductivity [71]. This refinement in pore structure is due to the

secondary-contributing pozzolanic reaction that makes the microstructure of concrete denser [71]. **Figure 15** clearly shows such improvement with the increase of volcanic scoria content and curing age.

Analyzing the results of chloride penetrability gathered from different works [19, 62, 63, 98, 116, 117], an estimation equation with strong correlation ($R^2 \approx 0.86$) can be derived (**Figure 16**). The estimation equation is.

$$RCP = (-0.3\ln t - 0.68) \times VS + 1.06 \quad (8)$$

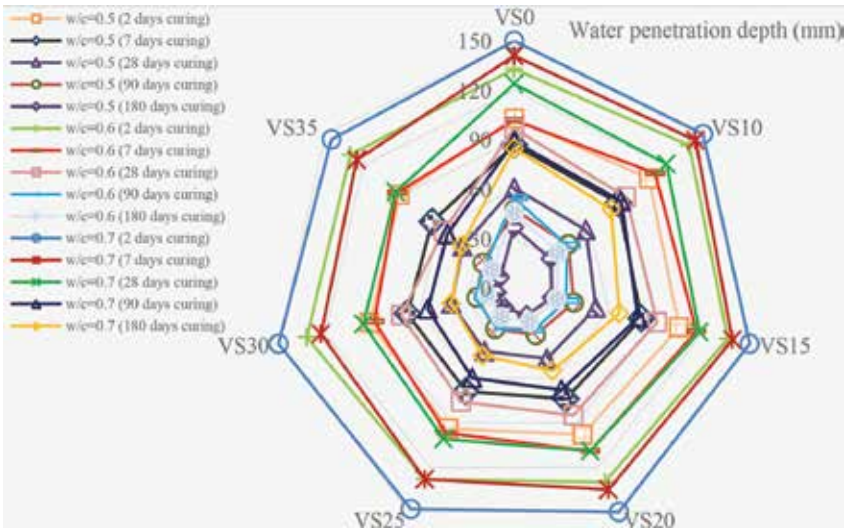

Figure 14. Water penetration depths of VS-based cement concretes prepared with different w/c ratios and cured for different ages [98].

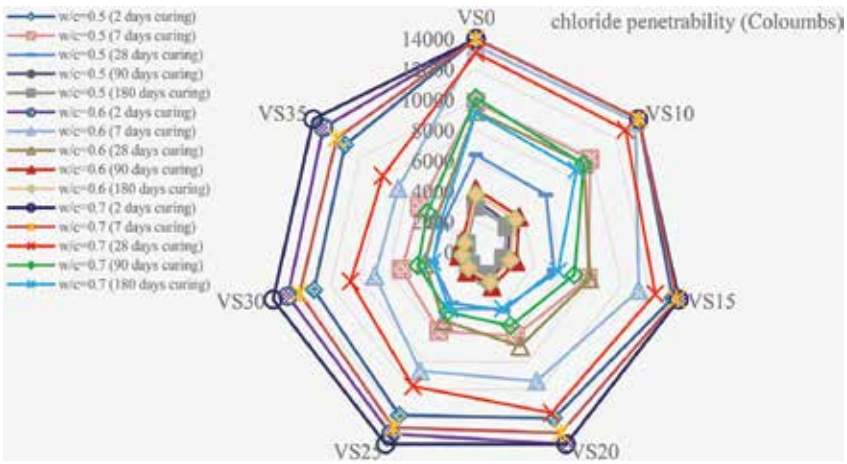

Figure 15. Chloride ion penetrability of VS-based cement concretes as reported by al-Swaidani [98].

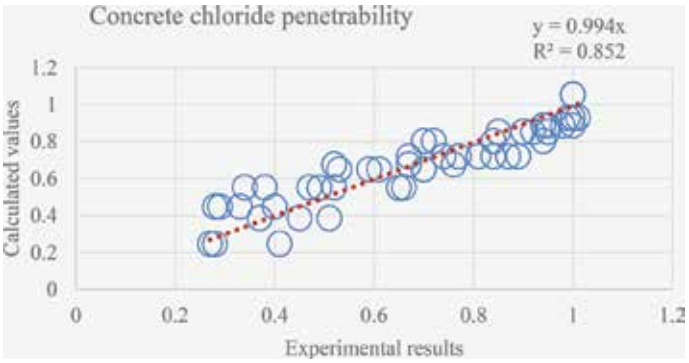

Figure 16. Experimental results versus calculated values of chloride penetrability.

where, RCP is relative chloride penetrability, t is curing age and VS is volcanic scoria content (% by mass). So, the chloride penetrability of VS-based cement concrete can be predicted from knowledge of curing time and volcanic scoria content.

6. Conclusion

- Volcanic scoria has been used in construction since ancient times in pozzolan-lime concrete providing durable structures that survived over 2000 years.
- The SiO_2 content for all sources are within the range of 40–60%; Al_2O_3 and Fe_2O_3 are within the ranges from 10 to 20% and from 5 to 16%, respectively.
- Incorporation of volcanic scoria in concrete has significant effects on the properties of concrete, particularly durability-related properties.
- The chloride permeability of VS-based cement concrete demonstrated better performance as compared to plain concrete, especially at the curing age of 28 days and longer.
- The wide availability of volcanic scoria in many countries, its low cost and the drive toward more sustainable construction have resulted in renewed interest in volcanic scoria as natural pozzolan for concrete. Historically, various types of volcanic scoria were successfully used in dams and aqueducts, where the strength demand is not high but the durability and thermal cracking control are of major concerns.
- Estimation equations for predicting the investigated concrete properties (i.e., compressive strength, water penetration depth and chloride penetration) incorporating the effect of curing time and the replacement level of volcanic scoria were derived. These equations permit the concrete properties of VS-based cement concretes to be predicted with a relatively high degree of accuracy ($R^2 \geq 0.8$).
- Investigating the volcanic scoria cones that have not been yet invested is highly recommended. In addition, making more sustainable and durable concrete using volcanic scoria is highly encouraged.

Author details

Aref M. al-Swaidani

Address all correspondence to: a-swaidan@gmail.com; a-swaidani@aiu.edu.sy

Faculty of Architectural Engineering, Arab International (Formerly European) University (AIU), Damascus, Syria

References

[1] Aitcin PC, Mindess S. Sustainability of Concrete. 1st ed. London, UK: Spon Press; 2011

[2] Aïtcin PC. Binders for Durable and Sustainable Concrete. London, UK: Taylor & Francis; 2008

[3] Brandt AM. Cement-Based Composites: Materials, Mechanical Properties and Performance. 2nd ed. London, UK: Taylor & Francis; 2009

[4] Mehta PK, Monteiro PJM. Concrete: Microstructure, Properties and Materials. 3rd ed: New York, USA: McGraw-Hill; 2006

[5] al-Swaidani AM, Aliyan SD. International Journal of Concrete Structures and Materials. 2015;**9**:241. DOI: https://doi.org/10.1007/s40069-015-0101-z

[6] ASTM C125. Standard Terminology Relating to Concrete and Concrete Aggregates. West Conshohocken, Pennsylvania, United States: American Society for Testing and Materials; 2007

[7] Jahren P, Sui T. Concrete and Sustainability. Boca Raton, Florida, USA: CRC Press; 2014

[8] Dedeloudis C, Zervaki M, Sideris K, Juenger M, Alderete N, Kamali-Bernard S, Villagrán Y, Snellings R. Natural pozzolans. De Belie N et al, editors. In: Properties of Fresh and Hardened Concrete Containing Supplementary Cementitious Materials. 2018. RILEM State-of-the-Art Reports 25. https://doi.org/10.1007/978-3-319-70606-1_6

[9] Jackson M, Deocampo D, Marra F, Scheetz B. Mid-Pleistocene pozzolanic volcanic ash in ancient roman concretes. Geoarchaeology. 2010;**25**(1):36-74

[10] Hammond AA. Pozzolana Cements for Low Cost Housing. Japan: Building and road research institute; 1983

[11] Dictionary of Earth Sciences. A Dictionary Edited by Michael Allaby. 3rd ed. Oxford, UK: Oxford University Press; 2008

[12] Lefond SJ. Industrial Minerals and Rocks. Society of Mining Engineers. New York: American Institute of Mining, Metallurgical and Petroleum Engineers, Inc. Vol. 2; 1983:723-1446

[13] Sen G. Petrology: Principles and Practice. Berlin Heidelberg: Springer-Verlag; 2014

[14] Mathers SJ, Harrison DJ, Mitchell CJ, Evans EJ. Exploration, Evaluation and Testing of Volcanic Raw Materials for Use in Construction, British Geological Survey; 2000. 116p

[15] Jackson JA, Mehl J, Neuendorf K. Glossary of Geology. Alexandria, Virginia: American Geological Institute; 2005. 800 pp

[16] Taddeucci J, Edmonds M, Houghton B, James MR, Vergniolle S. Hawaiian and Strombolian Eruptionsthe encyclopedia of volcanoes. Elsevier Inc; 2015. DOI: 10.1016/B978-0-12-385938-9.00027-4

[17] Hossain AKM. Resistance of Scoria-based blended cement concrete against deterioration and corrosion in mixed sulfate environment. Journal of Material Civil Engineering. 2009:299-308. 10.1061/(ASCE)0899-1561(2009)21,7(299)

[18] Senhadji Y, Escadeillas G, Mouli M, Khelafi H, Benosman. Influence of natural pozzolan, silica fume and limestone fine on strength, acid resistance and microstructure of mortar. Powder Technology. 2014;**254**:314-323

[19] Ghrici M, Kenai S, Meziane E. Mechanical and durability properties of cement mortar with Algerian natural pozzolana. Journal of Materials Science. 2006;**41**:6965-6972

[20] Mebrouki A, Cyr M, Belaribi NB. Enhancing value of local materials in developing countries, case of an Algerian pozzolan. European Journal of Environmental and Civil Engineering. 2009;**13**(10):1263-1278

[21] Laoufi L, Senhadji Y, Benazzouk A, Langlet T, Mouli M, Laoufi I, Benosman AS. Evaluation de la durabilité de mortiers pouzzolaniques exposés à une attaque chimique (Assessment of pozzolanic mortars sustainability exposed to chemical attack). Journal of Material Environmental Science. 2016;**7**(5):1835-1845

[22] Bertotto GW, Hirch MH, Ponce AD, Orihashi Y, Sumino H. Petrology and geochemistry of Toscales basaltic eruptive center. Extra-Andean back-arc zone of Mendoza province. Revista de la Asociation Geologica Argentina. 2016;**73**(3):330-340

[23] Kuperman AM, Gorbatkina YA, Gorenberg AY, Ivanova-Mumzhieva VG, Zakharova TY, Lebedeva OV, Solodilov VI, Petrosyan GK. Physical-mechanical properties of fibers made from scoria and materials based on them. Glass and Ceramics. 2009;**66**(7-8)

[24] Juimo WT, Cherrad LA, Oliveira L. Characterisation of natural pozzolan of :Djoungo (Cameroon) as lightweight aggregate for lightweight concrete. International Journal of GEOMATE. 2016;**11**(27):2782-2789

[25] Billong N, Melo UC, Njopwouo D, Louvet F, Bonnet JP. Physicochemical characteristics of some Cameroonian Pozzolans for use in sustainable cement like materials. Materials Sciences and Applications. 2013;**4**:14-21

[26] Tchakouté HK, Kong S, Djobo JNY, Tchadjié LN, Njopwouo D. A comparative study of two methods to produce geopolymer composites from volcanic scoria and the role of structural water contained in the volcanic scoria on its reactivity. Ceramics International. 2015;**41**(10):12568-12577. DOI: 10.1016/j.ceramint.2015.06.073

[27] Djobo JNY, Tchadjie LN, Tchakoute HK, Kenne BBD, Elimbi A. Synthesis of geopolymer composites from a mixture of volcanic scoria and metakaolin. Journal of Asian Ceramics Societies. 2014;**2**(4):387-398

[28] Tchamdjoua WHJ, Grigolettoc S, Michelc F, Courardc L, Abidia ML, Cherradia T. An investigation on the use of coarse volcanic scoria as sand in Portland cement mortar. Case Studies in Construction Materials. 2017;**7**:191-206

[29] Bidjocka C. Conception de bétons légers isolant s porteurs. Applications aux pouzzolanes naturelles du Cameroun, Thèse de doctorat. Vol. 1990. INSA de Lyon; 1990 167p

[30] Tchamdjou WHJ, Cherradi T, Abidi ML, Pereira de Oliveira LA. Influence of different amounts of natural pozzolan from volcanic scoria on the rheological properties of Portland cement pastes. Energy Procedia. 2017;**139**:696-702

[31] Wong LJ, Larsen JF. The middle scoria sequence: A Holocene violent strombolian, subplinian and phreatomagmatic eruption of Okmok volcano, Alaska. Bulletin of Volcanology. 2010;**72**:17-31. DOI: 10.1007/s00445-009-0301-y

[32] Eiche GE, Francis DM, Ludden JN. Primary alkaline magmas associated with the quaternary alligator Lake volcanic complex, Yukon territory, Canada. Contributions to Mineralogy and Petrology. 1987;**95**:191-201

[33] Amigo Á, Lara L, Smith V. Holocene record of large explosive eruptions from Chaitén and Michinmahuida volcanoes, Chile. Andean Geology. 2013;**40**(2):227-248. DOI: 10.5027/andgeoV40n2-a03

[34] Ogura T. Volcanoes in Manchuria. In: Ogura T, editor. Geology and Mineralogy of the Far East. University of Tokyo Press; 1969. pp. 373-413

[35] Smets B, Kervyn M, d'Oreye N, Kervyn F. Spatio-temporal dynamics of eruptions in a youthful extensional setting: Insights from Nyamulagira volcano (D.R. Congo), in the western branch of the east African rift. Earth-Science Reviews. 2015;**150**:305-328. http://dx.doi.org/10.1016/j.earscirev.2015.08.008

[36] Parat F, Streck MJ, Holtz F, Almeev R. Experimental study into the petrogenesis of crystal-rich basaltic to andesitic magmas at Arenal Volcano. Contributions to Mineralogy and Petrology. 2014;**168**:1040. DOI: 10.1007/s00410-014-1040-4

[37] Siegbug M, Gernon TM, Bull JM, Keir D, Barfod DN, Taylor RN, et al. Geological evolution of the Boset-Bericha volcanic complex, main Ethiopian rift: 40Ar/39Ar evidence for episodic Pleistocene to Holocene volcanism. Journal of Volcanology and Geothermal Research. 2018;**351**:115-133. DOI: 10.1016/j.volgeores.2017.12.014

[38] Tessema AET. Concrete Production and Quality Control in Building Construction Industry of Ethiopia: Addis Ababa, November 2005, Master of Science in Construction Technology and Management, pp. 148

[39] Bourdier JL, Gouragaud A, Vincent PM. Magma mixing in a main stage of formation of Montagne Pelee: The Saint Vincent-type scoria flow sequence (Martinique, F.W.I.). Journal of Volcanology and Geothermal Research. 1985;**25**(1985):309-332

[40] Jannot S, Schiano P, Boivin P. Melt inclusions in scoria and associated mantle xenoliths of Puy Beaunit volcano, Chaine des Puys, massif central, France. Contributions to Mineralogy and Petrology. 2005;**149**:600-612. DOI: 10.1007/s00410-005-0670-y

[41] Cools S, Juvigne E, Pouclet A. Composition of tephra of the Goldberg volcano (west Eifel, Germany) and search for its dispersion. International Journal of French Quaternary Association. 2011;**22**(1):47-60

[42] Büchner J, Tietz O, Viereck L, Suhr P, Abratis M. Volcanology, geochemistry and age of the Lausitz volcanic field. International Journal of Earth Sciences. 2015;**104**:2057-2083. DOI: 10.1007/s00531-015-1165-3

[43] Bourdier JL, Pratomo I, Thouret JC, Boudon G, Vincent PM. Observations, stratigraphy and eruptive processes of the 1990 eruption of Kelut volcano, Indonesia. Journal of Volcanology and Geothermal Research. 1997;**79**:181-203

[44] Handley HK, Macpherson CG, Davidson JP. Geochemical and Sr–O isotopic constraints on magmatic differentiation at Gede volcanic complex, west java, Indonesia. Contributions to Mineralogy and Petrology. 2010;**159**:885-908. DOI: 10.1007/s00410-009-0460-z

[45] Seyfi S, Azadmehr AR, Gharabaghi M, Maghsoudi A. Usage of Iranian scoria for copper and cadmium removal from aqueous solutions. Journal of Central South University. 2015;**22**:3760–3769. DOI: 10.1007/s11771-015-2920-0

[46] Asiabanha A, Bardintzeff JM, Sara Veysi S. North Qorveh volcanic field, western Iran: Eruption styles, petrology and geological setting. Mineral and Petrology. 2017:**20**. DOI: 10.1007/s00710-017-0541-z

[47] Marra F, Deocampo D, Jackson MD, Ventura G. The Alban Hills and Monti Sabatini volcanic products used in ancient roman masonry (Italy): An integrated stratigraphic, archaeological, environmental and geochemical approach. Earth-Science Reviews. 2011;**108**:115-136. DOI: 10.1016/j.earscirev.2011.06.005

[48] Nakano S, Yamamoto T. Chemical variations of magmas at Izu-Oshima volcano, Japan: Plagioclase-controlled and differentiated magmas. Bulletin of Volcanology. 1991;**53**: 112-120

[49] Al-Zboon KK, Al-Zou'by J. Effect of volcanic tuff on the characteristics of cement mortar. European Journal of Environmental and Civil Engineering. 2015. http://dx.doi.org/10.1080/19648189.2015.1053151

[50] Rajaonarison EF, Gacoin A, Randrianja R, Ranaivoniarivo VG, Bam Haja Nirina Razafindrabe BHN. Effect of scoria on various specific aspects of lightweight concrete. International Journal of Concrete Structures and Materials. 2017;**11**(3):541-555. DOI: 10.1007/s40069-017-0204-9

[51] Erlund EJ, Cashman KV, Wallace PJ, Pioli L, Rosi M, Johnson E, Granados HD. Compositional Evolution of Magma from Paricutin Volcano. Mexico: The tephra record, Journal of Volcanology and Geothermal Research; 2009. DOI: 10.1016/j.jvolgeores.2009.09.015

[52] Siebe MNGC, Agustín-Flores J. Eruptive style of the young high-mg basaltic-andesite Pelagatos scoria cone, southeast of México City. Bulletin of Volcanology. 2009, 2009;**71**:859-880. DOI: 10.1007/s00445-009-0271-0

[53] McGee. New Zealand, Lucy Emma McGee, Melting Processes in Small Basaltic Systems: The Auckland Volcanic Field. New Zealand, PhD thesis: University of Auckland; 2012. p. 210

[54] Smith IEM, Blake S, Wilson CJN, Houghton BF. Deep-seated fractionation during the rise of a small-volume basalt magma batch: Crater Hill, Auckland, New Zealand. Contributions to Mineralogy and Petrology. 2008;**155**:511-527

[55] Hradecky P, Rapprich V. Historical tephra-Tratigraphy of the Cosiguina volcano (western Nicaragua). Revista Geológica de América Central. 2008;**38**:65-79

[56] Hossain KMA, Julkarnine KMY, Anwar MS. Evolution of strength and durability of scoria concrete in sea environment. Journal of Multidisciplinary Engineering Science and Technology. 2015;**2**(6):1268

[57] Lechtman H, Moseley ME. The scoria at CHAN CHAN; non-metallurgical deposits, Ñawpa Pacha. Journal of Andean Archaeology. 1972;**10**(1):135-170. DOI: https://doi.org/10.1179/naw.1972.10-12.1.008

[58] Castillo PR, Newhall CG. Geochemical constraints on possible subduction components in lavas of Mayon and Taal volcanoes, southern Luzon, Philippines. Journal of Petrology. 2004;**45**(6):1089-1108. DOI: 10.1093/petrology/egh005

[59] Halmagyi T, Mosonyi E, Fazekas J, Spataru M, Goga F. Characterization of cements from Dominantly volcanic raw materials of the Carpathian bend zone. Hungarian Journal of Industry and Chemistry. 2016;**44**(2):135-139. DOI: 10.1515/hjic-2016-0017

[60] Ermakov VA, Gontovaya LI, Senyukov SL. Tectonics and magma chambers of the recent Tolbachik fissure eruption (Kamchatka peninsula). Atmospheric and Oceanic Physics. 2014;**50**(8):745-765

[61] Celik K, Meral C, Mancio M, Mehta PK, Monteiro PJM. A comparative study of self-consolidating concretes incorporating high-volume natural pozzolan or high-volume fly ash. Construction and Building Materials. 2014. DOI: 10.1016/j.conbuildmat.2013.11.065

[62] Khan MI, Alhozaimy. Properties of natural pozzolan and its potential utilization in environmental friendly concrete. Canadian Journal of Civil Engineers. 2011;**38**:71-78. DOI: 10.1139/L10-112

[63] Fares G, Alhozaimy A, Abdalla Alawad O, Al-Negheimish A. Evaluation of powdered scoria rocks from various volcanic lava fields as cementitious material. Journal of Materials in Civil Engineering. 2016;**28**(3):9. Paper nr. 04015139. DOI: 10.1061/(ASCE)MT.1943-5533.0001428

[64] Surour AA, Moufti MR, Nassief MO, Abu Saeda Y. Chemical characteristics of black scoria and their influence on economic use as industrial rock: A case study from harrat Rahat, Saudi Arabia, ISESCO Journal of Science and Technology, Nr. 23. 2017;**13**(23): 48-59

[65] Bakhsh RA. The Harrat Al-Birk basalts in southwest Saudi Arabia: Characteristic alkali mafic magmatism related to Red Sea rifting. Acta Geochimica. 2017;**36**(1):74-88. DOI: 10.1007/s11631-016-0126-2

[66] Thompson GM, Malpas J, Smith IEM. Volcanic geology of Rarotonga, southern Pacific Ocean. New Zealand Journal of Geology and Geophysics. 1998;**41**(1):95-104. DOI: 10.1080/00288306.1998.9514793

[67] le Roux AP, Chevallier L, Verwoerd WJ, Barends R. Petrology and geochemistry of Marion and Prince Edward Island, Southern Ocean: Magma chamber process and source region characteristics. Journal of Volcanology and Geothermal Research. 2012;**223-224**:11-20

[68] Traglia FD, Cimarelli C, de Rita D, Torrente DG. Changing eruptive styles in basaltic explosive volcanism: Examples from Croscat complex scoria cone, Garrotxa volcanic field (NE Iberian peninsula), Journal of Volcanology and Geothermal Research. 2009;**180**:89-109. DOI:10.1016/j.jvolgeores.2008.10.020

[69] Krochert J, Buchner E. Age distribution of cinder cones within the Bandas del Sur Formation, southern Tenerife, Canary Islands. 2009;**146**(2):161-172. DOI: https://doi.org/10.1017/S001675680800544X

[70] Albert H, Perugini D, Joanmarti. Fractal analysis of enclaves as a new tool for estimating rheological properties of magmas during mixing: The case of Montana Reventada (Tenerife, Canary Islands). Pure and Applied Geophysics. 2015;**172**(2015):1803-1814

[71] al-Swaidani AM. Production of more durable and sustainable concretes using volcanic scoria as cement replacement. Materiales De Construccion. 2017;**67**(326):e118. DOI: 10.3989/mc.2017.00716

[72] al-Swaidani et al. Improvement of the early-age compressive strength, water permeability, and sulfuric acid resistance of scoria-based mortars/concrete using limestone filler. Advances in Materials Science and Engineering. 2017;**2017**. article ID 8373518, 17 pages. https://doi.org/10.1155/2017/8373518

[73] Amboya HA, King'ondu CK, Njau KN, Mrema AL. Measurement of pozzolanic activity index of scoria, pumice, and rice husk as potential supplementary cementitious materials for Portland cement. Advances in Civil Engineering. 2017. p. 15. ID 6952645, DOI: 10.1155/2017/6952645

[74] Wang KL, Chung SL, O'reilly SY, Sun SS, Shinjo R, Chen CH. Geochemical constraints for the genesis of post-collisional magmatism and the geodynamic evolution of the northern Taiwan region. Journal of Petrology. 2004;**45**(5):975-1011. DOI: 10.1093/petrology/egh001

[75] Depci T, Efe T, Tapan M, Ozvan A, Aclan M, Uner T. Chemical characterization of Patnos Scoria (Agri, Turkey) and its usability for production of blended cement. Physicochemical Problems of Mineral Processing. 2011;**48**(1):303-315

[76] Ozvan A, Tapan M, Erik O, Efe T, Depci T. Compressive strength of scoria added Portland cement. Gazi University Journal of Science. 2012;**25**(3):769-775

[77] Gonca Gencalioglu-Kuscu G. Geochemical characterization of a quaternary monogenetic volcano in Erciyes volcanic complex: Cora maar (central Anatolian Volcanic Province, Turkey). International Journal of Earth Science (Geol Rundsch). 2011;**100**:1967-1985. DOI: 10.1007/s00531-010-0620-4

[78] Perry FV, Straub KT. Geochemistry of the Lathrop Wells Volcanic Center, Los Alamos, New Mexico, UC-8021996. p. 19

[79] Al Naaymi TA. Assessment of pumice and scoria deposites in Dhamar-Rada' volcanic field SW- Yemen, as a pozzolanic material and lightweight aggregates. International Journal of Innovative Science, Engineering & Technology. 2015;**2**(9):386

[80] al-Kwatli MA, Gillot PY. A New Method in Volcano-Morphology to Investigate the Tectonic Constraints on the Volcanism, Case Study of Harrat Al Sham Volcanic Field, Arabia Plate: The Interest of GIS and Relational Database, COM. Geo, June 21-23. Washington, DC, USA; 2010. p. 2010

[81] Ilani S, Harlavan Y, Tarawneh K, Rabba I, Weinberger R, Ibrahim K, Peltz S, Steinitz G. New K–Ar ages of basalts from the Harrat ash Shaam volcanic field in Jordan: Implications for the span and duration of the upper-mantle upwelling beneath the western Arabian plate. Geology. 2001;**29**:171-174

[82] Swamy RN. Design for durability and strength through the use of fly ash and slag in concrete. ACI Special Publication. 1987;**171**

[83] Mindess S, Young JF, Darwin D. Concrete. 2nd ed. USA: Prentice Hall; 2003. NY 07458

[84] ASTM C618. Standard Specification for Coal Fly Ash and Raw or Calcined Natural Pozzolan for Use in Concrete. West Conshohocken, Pennsylvania, United States: American Society for Testing and Materials; 2012

[85] EN 197-1 (2000). Cement. Part 1: Composition, Specifications and Conformity Criteria for Common Cements. European Standards

[86] ACI 232.1R-12, Report on the Use of Raw or Processed Natural Pozzolans in Concrete, American Concrete Institute

[87] Lea FM, Hewlett PC, editors. Lea's Chemistry of Cement and Concrete. 4th ed. Oxford, UK: Butterworth-Heinemann, Elsevier ltd.; 1998

[88] Ramezanianpour AK. Cement Replacement Materials: Properties, Durability, Sustainability. Springer-Verlag Berlin Heidelberg; 2014. p. 345. DOI: 10.1007/978-3-642-36721-2

[89] al-Swaidani A, Aliyan S, Adarnaly N. Mechanical strength development of mortars containing volcanic scoria-based binders with different fineness. Engineering Science and Technology, An International Journal. 2016;**19**:970-979

[90] Shi C. An overview on the activation of the reactivity of natural pozzolans. Canadian Journal of Civil Engineers. 2001;**28**(2001):778-786

[91] Tchamdjou WHJ, Cherradi T, Abidi ML, Pereira-de-Oliveira LA. The use of volcanic scoria from Djoungo (Cameroon) as cement replacement and fine aggregate by sand substitution in mortar for masonry. European Journal of Environmental and Civil Engineering. 2017. DOI: 10.1080/19648189.2017.1364298

[92] Chen W. Hydration of Slag Cement, Ph.D. Thesis. Netherland: University of Twente; 2007

[93] ASTM C 595. Standard specification for blended hydraulic cements. West Conshohocken, Pennsylvania, United States: American Society for Testing and Materials; 2002

[94] Al-Chaar GK, Yaksic DA, Kallemeyn LA. The Use of Natural Pozzolan in Concrete as an Additive or Substitute for Cement. 2011. ERDC/CERL TR-11-46

[95] Alhozaimy A, Fares G, Alawad OA, Al-Negheimish A. Heat of hydration of concrete containing powdered scoria rock as a natural pozzolanic material. Construction and Building Materials. 2015;**81**:113-119. DOI: 10.1016/j.conbuildmat.2015.02.011

[96] Moufti et al. Assessment of the industrial utilization of scoria materials in central Harrat Rahat, Saudi Arabia. Engineering Geology. 2000;**57**:155-162

[97] Fares G, Alhozaimy A, Alawad OA, Al-Negheimish A. Evaluation of powdered scoria rocks from various volcanic lava fields as cementitious material. Journal of Materials in Civil Engineering. 2015. DOI: 10.1061/(ASCE)MT.1943-5533.0001428

[98] Al-Swaidani. Prediction of compressive strength and some permeability-related properties of concretes containing volcanic scoria as cement replacement. Romanian Journal of Materials. 2016;**46**(4):505-514

[99] al-Swaidani A, Aliyan S, Adarnaly N, Hanna B, Dyab E. Influence of volcanic scoria on mechanical strength, chemical resistance and drying shrinkage of mortars. Building Research Journal. 2014;**61**(3):pp. 143-150

[100] Meddah MS, Tagnit-Hamou A. Effect of mineral admixtures on shrinkage measured on massive concrete elements. In: Tanabe et al., editors. Creep, Shrinkage and Durability Mechanics of Concrete and Concrete Structures. London: Taylor & Francis Group; 2009

[101] Rao GA. Long-term drying shrinkage of mortar—Influence of silica fume and size of fine aggregate. Cement and Concrete Research. 2001;**31**:171-175

[102] South W. A study of the compressive strength and drying shrinkage of cementitious binders prepared using natural pozzolans, PhD Thesis. Australia: University of Wollongong; 2009

[103] Touttanji HA, Bayasi Z. Effect of curing procedures on the properties of silica fume concrete. Cement and Concrete Research. 1999;**29**:497-501

[104] Massazza F. Pozzolanic cements. Cement and Concrete Composites. 1993;**15**:185-214

[105] Marchand J, Odler I, Skalny JP. Sulfate Attack on Concrete. CRC Press; 2002

[106] Thomas M. Supplementary Cementing Materials in Concrete. Taylor & Francis Group; 2013. p. 195

[107] Irassar EF, Gonzalez MA, Rahhal V. Sulfate resistance of type V cements with limestone filler and natural pozzolan. Cement & Concrete Composites. 2000;**22**(5):361-368

[108] al-Amoudi OSB. Attack on plain and blended cements exposed to aggressive sulfate environments. Cement & Concrete Composites. 2002;**24**:304-316

[109] Attiogbe EK, Rizkalla SH. Response of concrete to sulfuric acid attack. ACI Materials Journal. 1988;**85**:481-488

[110] Monteny JE, Vincke A, Beeldens A, De Belie N, Taerwe L, Van Gemert D. Chemical, microbiological, and in situ test methods for biogenic sulfuric acid corrosion of concrete. Cement and Concrete Research. 2000;**30**:623-634

[111] Al-Dulaijan SU, Maslehuddin M, Al-Zahrani MM, Sharif AM, Shameem M, Ibrahim M. Sulfate resistance of plain and blended cements exposed to varying concentrations of sodium sulfate. Cement & Concrete Composites. 2003;**25**:429-437

[112] Biczok I. Concrete Corrosion and Concrete Protection, Chemical Publishing Co. Inc. New York; 1967

[113] Cao HT, Bucea I, Ray A, Yozghatlian S. The effect of cement composition and pH of environment on sulfate resistance of Portland cements and blended cements. Cement & Concrete Composites. 1997;**19**(2):161-171

[114] Aydın S, Yazıcı H, Yigiter H, Baradan B. Sulfuric acid resistance of high-volume fly ash concrete. Building and Environment. 2007;**24**:717-721

[115] Neville AM. Properties of Concrete. 5th ed. London, UK: Pearson Education; 2011

[116] Hossain KMA. Blended cement and lightweight concrete using scoria: Mix design, strength, durability and heat insulation characteristics. International Journal of Physical Sciences. 2006;**1**(1):005-016

[117] Ghrici M, Kenai S, Said-Mansour M, Kadr EH. Some engineering properties of concrete containing natural pozzolana and silica fume. Journal of Asian Architecture and Building Engineering. 2006;**5**(2):349-354

Chapter 11

Volcanic Glass and its Uses as Adsorbent

Juan Antonio Cecilia, Miguel Armando Autie-Pérez,
Juan Manuel Labadie-Suarez,
Enrique Rodríguez Castellón and
Antonia Infantes Molina

Additional information is available at the end of the chapter

http://dx.doi.org/10.5772/intechopen.75063

Abstract

Volcanic glasses are an amorphous phyllosilicates formed by the fast cooling of the magma. The physicochemical properties of volcanic glasses are directly related to their chemical composition. Thus, the rhyolitic magma, which presents the highest SiO_2 percentage, displays a high viscosity, which leads to explosive eruptions by the ex-solution of H_2O, CO_2, and SO_2, when the pressure diminishes generates a macroporous structure with interesting applications in construction, as abrasive, acoustic, filter as well as in the agriculture field. The macroporosity of volcanic glass allows to host large molecules as biomolecules, tensoactives, or dyes. On the other hand, the existence of hydroxyl groups in this amorphous aluminosilicate also favors the adsorption of cations and anions, so the volcanic glass is an economical adsorbent to retain heavy metals or radioactive cations.

Keywords: perlite, volcanic glass, metal adsorption, dyes adsorption

1. Genesis of the volcanic glass

Volcanic glass, also named as obsidian, is formed when the magma cools suddenly. This fact difficults the formation of an ordered structure, leading to an amorphous structure denoted as "*mineraloid*" [1]. Volcanic glasses are commonly dark or black, although these structures can also be brown, tan, green even blue, red, orange, or yellow depending on the trace elements or inclusions [2]. Like any crystal, volcanic glasses are chemically metastable, that is, with the passage of time, the volcanic glasses can crystallize. However, this process does not happen

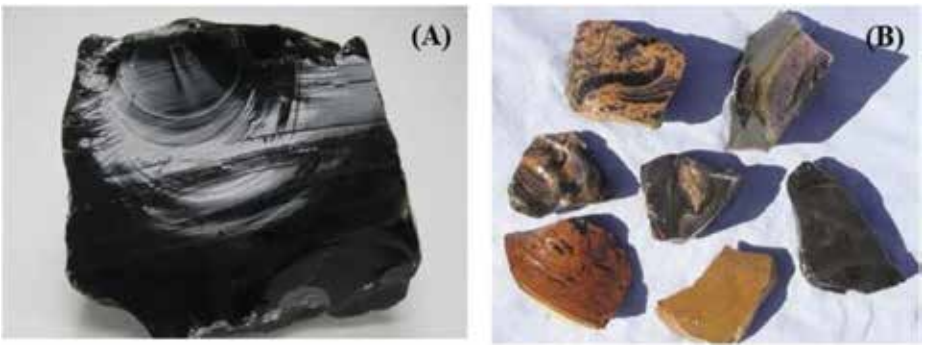

Figure 1. Images of a typical volcanic glass (A) and volcanic glasses with inclusions (B).

at a uniform rate throughout the rock. The cracks are vulnerable zones to suffer devitrification (**Figure 1**). Another zone very sensitive to the devitrification is the edges of grain of the volcanic glass. In both cases, the volcanic glass tends to evolve to crystalline phases such as quartz, tridymite, and alkali feldspar [3].

2. Chemical composition of the volcanic glass

According to their chemical composition, magmas can be classified into basaltic magma (SiO_2 45–55%), andesitic magma (SiO_2 55–65%), and rhyolitic magma (SiO_2 65–75%) (**Table 1**). The amount of gas occurring in a magma is genetically related with its chemical composition, that is, a rhyolitic magma has a higher gas content than a basaltic one.

The temperature of magmas is difficult to measure (due to the involved danger). However, the laboratory measurements coupled with the field observations have indicated that the temperature of eruption ranges from 1000 and 1200°C in a basaltic magma, from 800 and 1000°C in an andesitic magma and from 650 and 800°C in a rhyolitic magma [4–7].

The viscosity mainly depends on the magmatic composition and temperature. Thus, the magmas having a higher SiO_2 content have a higher viscosity than the magmas having a lower SiO_2 content. Moreover, low-temperature magmas have a higher viscosity than high-temperature magmas [7, 8].

The cooling of the magma depends on the viscosity of the lava, which is directly related with its chemical composition, as was indicated previously. The lava with lower viscosity, that is, the basaltic lava, cools down quickly, obtaining thin glasses with a thick below 1 cm. However, the viscous rhyolitic lava, which erupts on dry land, cooling with a low rate leading to volcanic glass with larger dimensions [7, 9].

Generally, the rhyolitic magmas (SiO_2) higher than 60% give rise to explosive eruptions, resulting in large volume of pyroclastics and related to the ex-solution of volatiles, mainly H_2O, CO_2 and SO_2 as the pressure is reduced [7, 10, 11]. Because high viscosity inhibits crystallization, a sudden cooling and loss of volatiles, as when lava extrudes from a volcanic vent, tends to chill the material to a glass rather than to crystallize it, leading to the volcanic glass [12].

Magma type	Basaltic	Andesitic	Rhyolitic
Solidified rock	Basalt	Andesite	Rhyolite
Silica content	45–55%	55–65%	65–75%
Gas content	Least	Intermediate	Most
Viscosity	Least	Intermediate	Most
Type or eruption	Effusive	Sometimes explosive	Usually explosive
Melting temperature	1000–1200°C	800–1000°C	650–800°C
Location	Rifts, oceanic hotspots	Subduction boundaries	Continental hotspots

Table 1. Characteristics of magma.

The main volcanic glass is the obsidian; however, the sudden cooling of the magma can form other glasses.

Pumice is formed when the magma erupts violently. This volcanic rock is commonly obtained from rhyolitic and andesitic magmas, although the pumice form basaltic magma is also known. Pumice presents a foaming structure due to a sudden depressurization and cooling of the magma, which causes a decrease of the solubility of various gases (CO_2 and H_2O) that are trapped inside the matrix. These materials are used for construction (mortars and concretes), cosmetics (exfoliant) or as abrasive [13].

Apache tears are dark volcanic glass with spherical structure, which are frequently associated with perlite. These rocks are formed from rhyolitic magmas with high H_2O and alkali content, leading to pebbles after the sudden cooling [14].

Tachylite is a dark volcanic glass obtained from the rapid cooling of basaltic magma so its chemical composition differs to that shown by obsidian since rhyolitic magma displays a higher SiO_2 content. These rocks appear mixed with other basaltic rocks such as feldspars or olivines, which have a stronger tendency to crystallize, because they have more freedom to arrange themselves in a crystalline order [15].

Sideromelane is an unusual glass obtained from a basaltic magma. This rock is formed at higher temperature and with more rapid chilling than tachylite. This rock is frequently formed during explosions of subglacial or submarine volcanoes. Sideromelane is usually embedded in a palagonite matrix forming hyaloclastite deposits [15].

Palagonite is also a glass obtained from basaltic magma, which is formed by the interaction between the basalt melt and water to form colored palagonite tuff cones. This tuff is composed of fragments of sideromelane and thicker basaltic rocks, which are embedded in a palagonite matrix to form hyaloclastite deposits [15].

3. Locations of the volcanic glass

The volcanic glasses are distributed in areas of recent volcanic activity throughout the world. These materials are not observed in zones where there was volcanic activity millions of years

Figure 2. Volcanic glass by country [16].

ago since obsidian is metastable material and is susceptible to geological and environmental effects, evolving mainly to smectites or zeolites [12].

As indicated, obsidian is distributed throughout the five continents. Thus, obsidian is found in several nations of America (Argentina, Chile, Peru, Colombia, Ecuador, Guatemala, Mexico, United States or Canada), Europe (France, Italy, Hungary, Greece, Iceland or Russia), Africa (Kenya, Tanzania or Ethiopia), Asia (Turkey, Iran, Indonesia or Japan) and Oceania (Australia and New Zealand) (**Figure 2**).

4. Perlite (a surprising material)

Perlite is also an amorphous volcanic glass with water retained in its structure [17]. The thermal treatment of the volcanic glass favors the removal of the structural water as well as an unusual expansion of its structure when the temperature reaches 850–900°C. The water trapped in the structure of the material vaporizes and escapes, leading to an expansion of the material to 7–20 times its original volume, acquiring a foam-like cellular structure (**Figures 3** and **4**) and obtaining a versatile and sustainable mineral that is mined and processed with a negligible impact on the environment. Thus, unexpanded ("raw") perlite has a bulk density around 1.1 g cm^{-3}, while typical expanded perlite has a bulk density of about 0.03–0.150 g cm^{-3} [18]. The main uses and applications of perlite are indicated below.

Raw perlite can be used as sandblasting, slag coagulant or silica source. In addition, perlite has interesting applications in the field of foundry, steel industries or metal finishing (**Figure 5**). However, once the perlite structure is expanded, the number of uses and applications of this material is infinitely higher. Thus, the expanded perlite can be used as insulation in a wide range of temperatures, oil well treatment, flame resistant, acoustic

http://dx.doi.org/10.5772/intechopen.75063

insulation, filtration, adsorbent, agriculture and horticulture, lightweight aggregate construction, among other applications as indicated in **Figure 6**.

The wide variety of applications that exhibits the expanded perlite would lead to a monograph about this material. This chapter is only focused on some applications of the volcanic glass related with adsorption and separation processes.

Figure 3. Morphology of perlite in its rock, crushed and expanded form.

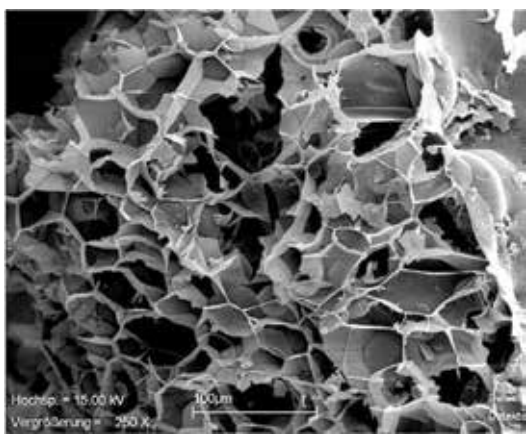

Figure 4. SEM image of expanded perlite.

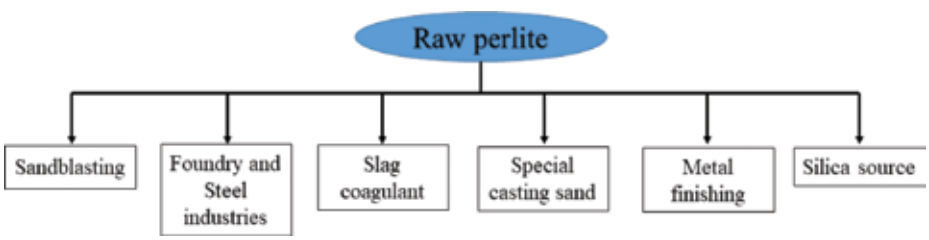

Figure 5. Uses and applications of raw perlite.

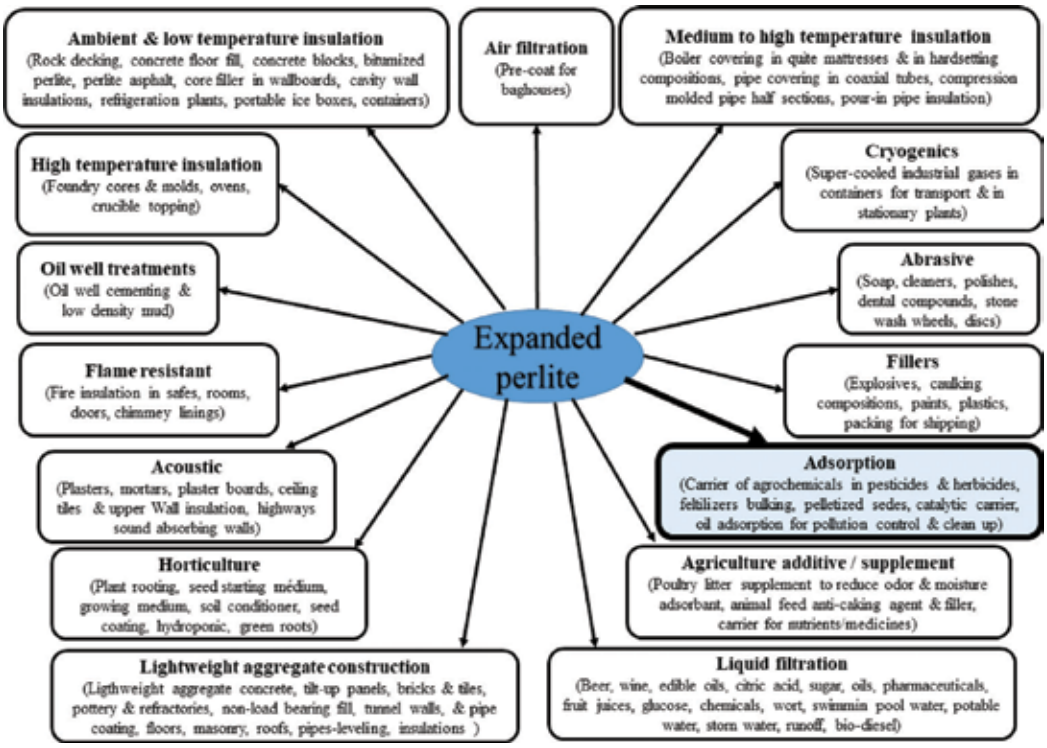

Figure 6. Uses and applications of expanded perlite.

5. Volcanic glass as adsorbent

The adsorption capacity of perlite is attributed to the presence of hydroxyl groups on its surface [19, 20]. Thus, silicon atoms tend to maintain their coordination at room temperature by attachment to the monovalent hydroxyl groups, forming silanol groups as follows (**Figure 7**):

while the hydrous oxide surface groups in alumina (**Figure 8**) are given by:

5.1. Adsorption of cations/anions

Heavy metals are among the most common pollutants that harm the aqueous environment and damage the health of human, animals, and plants [21]. Domestic and industrial wastewaters containing toxic metal ions are increasingly discharged into the environment, especially in developing countries. These metal ions are of significant importance as they are not biodegradable and cannot be metabolized by the environment but tend to accumulate in living organisms, causing various diseases and disorders. Also, they can only be diluted or transformed, not destroyed [22]. These heavy metal ions pose serious health implications to the vital organs of human beings and animals when consumed above certain threshold concentrations. There are various techniques for the removal of these toxic metal ions such as chemical precipitation, solvent extraction, ion exchange, reverse osmosis, and nanofiltration. Among these techniques, adsorption is considered effective and economic due to

http://dx.doi.org/10.5772/intechopen.75063

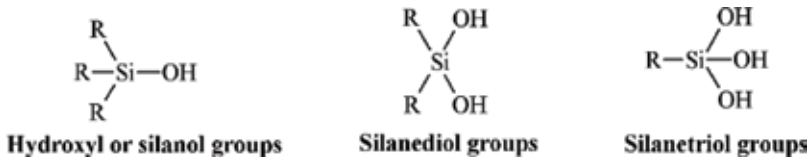

Figure 7. Hydroxyl groups in silica species.

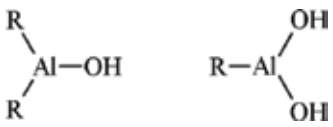

Figure 8. Hydroxyl groups in aluminum species.

its high efficiency, low-cost possibilities, easy handling, and the availability of different adsorbents. In this sense, perlite is a material with high potential due to its low cost and high availability.

Table 2 reports the adsorption capacity of perlite in various cations [19, 23–39]. From these data, it can be observed how the thermal treatment to expand the perlite does not improve the adsorption capacity due to the thermal treatment causes the dehydroxylation of the -OH groups so the possible cationic exchange H^+ by M^{n+} is disfavored [24]. On the other hand, these authors have pointed out that the adsorption follows a pseudo-second reaction and the maximum adsorption capacity takes place at pH = 5–6.5.

Several authors have established that the perlite can improve its adsorption capacity by a thermal treatment to expand the perlite structure, and then, this material has been coated by chitosan. This polymer has been increasingly studied as an adsorbent for the removal of M^{n+} ions from aqueous solutions because the amino and hydroxyl groups on the chitosan chain act as a chelation or reaction sites for the substances to be removed [28, 29, 32, 36] (**Figure 9**).

Other authors have pointed that expanded perlite can host certain oxides, which adsorb certain cations with high selectivity. Thus, it has been proposed in the literature that the incorporation of Fe_2O_3 or MnO_2 into the macrochannels of perlite, favoring the selective adsorption of harmful cations, such as As (III), Cr(VI) or Sb(V) [37–39] (**Figure 10**).

Perlite can also act as a barrier to isolate radioactive wastes [35, 40, 41]. Thus, Akkaya has carried out several studies where polyacrylamide or poly-2-hydroxyethylmethacrylate is incorporated (**Figure 11**) onto the expanded perlite to favor a selective adsorption of Th^{4+} and UO_2^{2+} species from aqueous solutions (**Table 3**) [40, 41]. The adsorption data revealed that Th^{4+} is more susceptible to be adsorbed and that the poly-acrylamide-expanded perlite composite is more efficient adsorbent than poly-2-hydroxyethylmethacrylate-expanded perlite probably due to the cations that show higher affinity by the amine groups of the acrylamide species. In the same way, Akkaya evaluated several adsorption parameters onto polyacrylamide-expanded perlite in five radio nuclides of the U- and Th- series (Tl^+, Ra^{2+}, Bi^{3+}, Ac^{3+}, and Pb^{2+} in a leaching solution), obtaining the following trend: ^{208}Tl (0.4 MBq kg^{-1}) > ^{212}Pb and ^{212}Bi (0.3 MBq kg^{-1}) > ^{228}Ac and (0.1 MBq kg^{-1}) > ^{226}Ra (0.04 MBq kg^{-1}) [42].

Material	Adsorbed (mg g^{-1})	Reference
Cu^{2+}		
Expanded perlite	8.62	[23]
Expanded perlite	0.51	[24]
Unexpanded perlite	1.01	[24]
Unexpanded perlite	10.87	[25]
Unexpanded perlite	0.70	[26]
Expanded perlite	1.95	[27]
Chitosan-coated perlite	62	[28]
Chitosan-coated perlite	325	[29]
Expanded perlite	0.09	[30]
Ni^{2+}		
Expanded perlite	0.06	[30]
Expanded perlite	2.24	[31]
Cd^{2+}		
Unexpanded perlite	6.23	[25]
Expanded perlite	0.03	[30]
Expanded perlite	1.79	[31]
Unexpanded perlite	0.42	[19]
Chitosan-coated perlite	178	[32]
Pb^{2+}		
Unexpanded perlite	9.52	[25]
Expanded perlite	0.13	[30]
Expanded perlite	6.27	[33]
Unexpanded perlite	8.91	[34]
Zn^{2+}		
Unexpanded perlite	4.46	[25]
Unexpanded perlite	0.07	[35]
Cr^{6+}		
Chitosan-coated perlite	452	[36]
γ-Fe_2O_3-perlite	8.64	[37]
α-MnO_2-perlite	7.60	[37]
$Cr_2O_7^{2-}$		
Unexpanded perlite	0.002	[35]
As^{5+}		
γ-Fe_2O_3-perlite	8.64	[38]
α-MnO_2-perlite	7.60	[38]

Material	Adsorbed (mg g^{-1})	Reference
AsO_4^{2-}		
Unexpanded perlite	0.003	[35]
Sb^{3+}		
α-MnO_2-perlite	7.64	[39]

Table 2. Cations adsorption onto perlite reported in the literature.

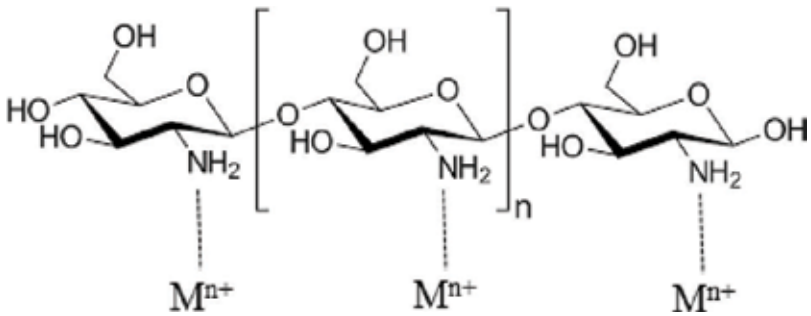

Figure 9. Chemical interaction between chitosan and the cations in solution.

Perlite has also been used as a sorbent to retain F^- or NO_3^- from aqueous solutions since NO_3^- is found frequently in fertilizers, while F^- species are added in a controlled way in the water supply; however, an excess of F^- can cause severe damages to health. Thus, Vijaya et al. used a chitosan-coated perlite to adsorb fluoride species, obtaining the highest value of 64.4 mg g^{-1} [43]. This process takes place by electrostatic interactions between F^- species and -NH_2 species of the chitosan. In the case of the NO_3^- species, expanded perlite was used to support γ-Fe_2O_3, which interacts directly with the NO_3^- species, reaching an adsorption of 32.6 mg g^{-1} [44].

5.2. Adsorption of dyes/surfactants

Dyes and pigments are highly used organic compounds as colorants in a wide variety of products. These processes generate wastes that are often released together with wastewater. The treatment of these wastewaters is one of the main environmental issues since these residues are very dangerous for the environment and harmful to health. Wastewater from the textile industry is processed in biological treatment plants. These processes are not very efficient so it is necessary to use complementary or alternative processes to eliminate these organic compounds from the water. Several processes such as precipitation, flocculation, coagulation, ion exchange, reverse osmosis, ozonization or adsorption have emerged as processes to remedy these emissions of dyes and pigments. Adsorption is one of the processes mostly used to remove organic compounds from wastewater. Active carbon is the adsorbent that has shown the greatest adsorption capacity; however, this adsorbent is synthesized from various physical and chemical processes, which raises the price of the process in comparison with the natural adsorbent that are inexpensive and highly available,

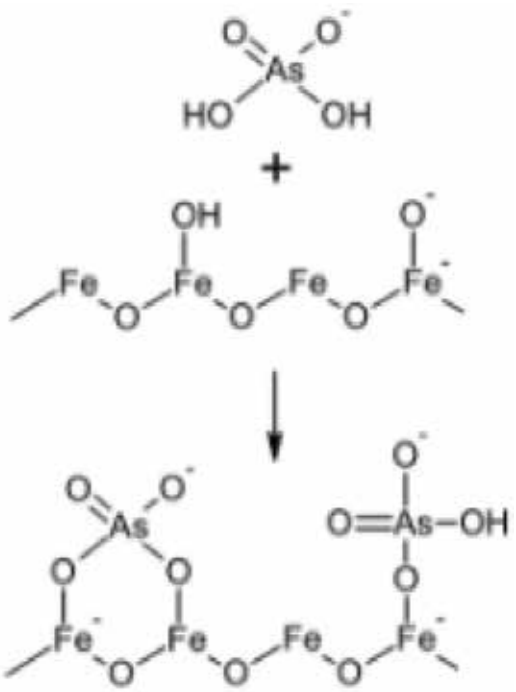

Figure 10. Chemical adsorption of As(V) in γ-Fe_2O_3 species.

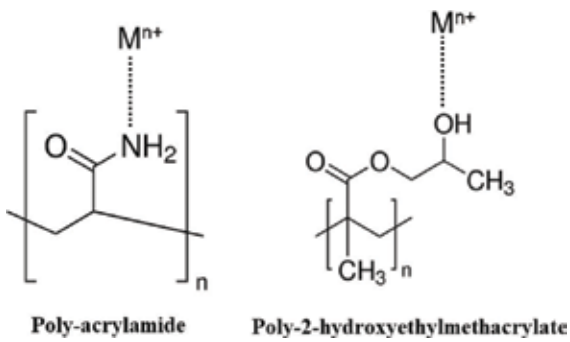

Figure 11. Interaction of polyacrylamide and poly-2-hydroxyethylmethacrylate with cations.

although its adsorption capacity is lower. Among these adsorbents, perlite is a low-cost material with great potential to adsorb pigments and dyes. Thus, several studies have been carried out for the adsorption of cationic dyes as methylene blue [20], methyl violet [45, 46], C.I. basic blue 41 [47], rhodamine B [48], maxilon blue G5 [49], or rhodamine B [50] (**Figure 12** and **Table 4**).

In all cases, the adsorption process is favored under basic conditions since perlite (negatively charged) interacts with the dye (positively charged) as indicates the following reactions::

Material	Adsorbed (mol kg^{-1})	Reference
UO_2^{2+}		
Unexpanded perlite	1.59	[35]
poly-acrylamide-expanded perlite	0.66	[40]
poly-2-hydroxyethylmethacrylate-expanded perlite	0.29	[41]
Th^{4+}		
Unexpanded perlite	4.63	[35]
poly-acrylamide-expanded perlite	0.74	[40]
poly-2-hydroxyethylmethacrylate-expanded perlite	0.44	[41]

Table 3. Radioactive cations adsorption onto perlite reported in the literature.

$$-M-OH+OH^- \rightarrow -M-O^- + H_2O$$

$$-M-O^- + Dye^+ \rightarrow -M-O-Dye$$

In the same way, anionic dyes have been adsorbed in expanded and unexpanded perlite as well as chitosan, orthophenanthroline or γ-Fe_2O_3 coated-perlite (**Figure 13** and **Table 5**).

The adsorption processes are favored under slightly acid conditions since the electrostatic interactions increase, as indicated in the following scheme.

$$-M-OH+H^+ \rightarrow -M-OH_2^+$$

$$-M-OH_2^+ + Dye^- \rightarrow -M-OH_2^+ Dye^-$$

Surfactants are among the most versatile of the products of the chemical industry, being used as detergent, in pharmaceuticals, in prospecting for petroleum. However, the application of surfactants can also produce environmental pollution and raises a series of problems for wastewater treatment plants. One of the characteristic features of surfactants is their tendency to adsorb at interfaces in an oriented fashion. Similarly to the dyes, the surfactants can be classified into cationic and anionic so the adsorbent-surfactant interactions should be similar; however, the long hydrocarbon chains give rise to a polar section and another nonpolar in the surfactant, so nonelectrostatic interactions appear.

Considering this premises, an inexpensive adsorbed as perlite has been used to adsorb a cationic surfactant such as cetyltrimethylammonium bromide (CTAB), obtaining a maximum adsorption value of 0.04 mmol g^{-1} for unexpanded perlite and 0.11 mmol g^{-1} for expanded perlite [55]. As takes places in cationic dyes, the adsorption is favored in basic conditions since the negatively charged surface of the perlite interacts with the cationic surfactant. The

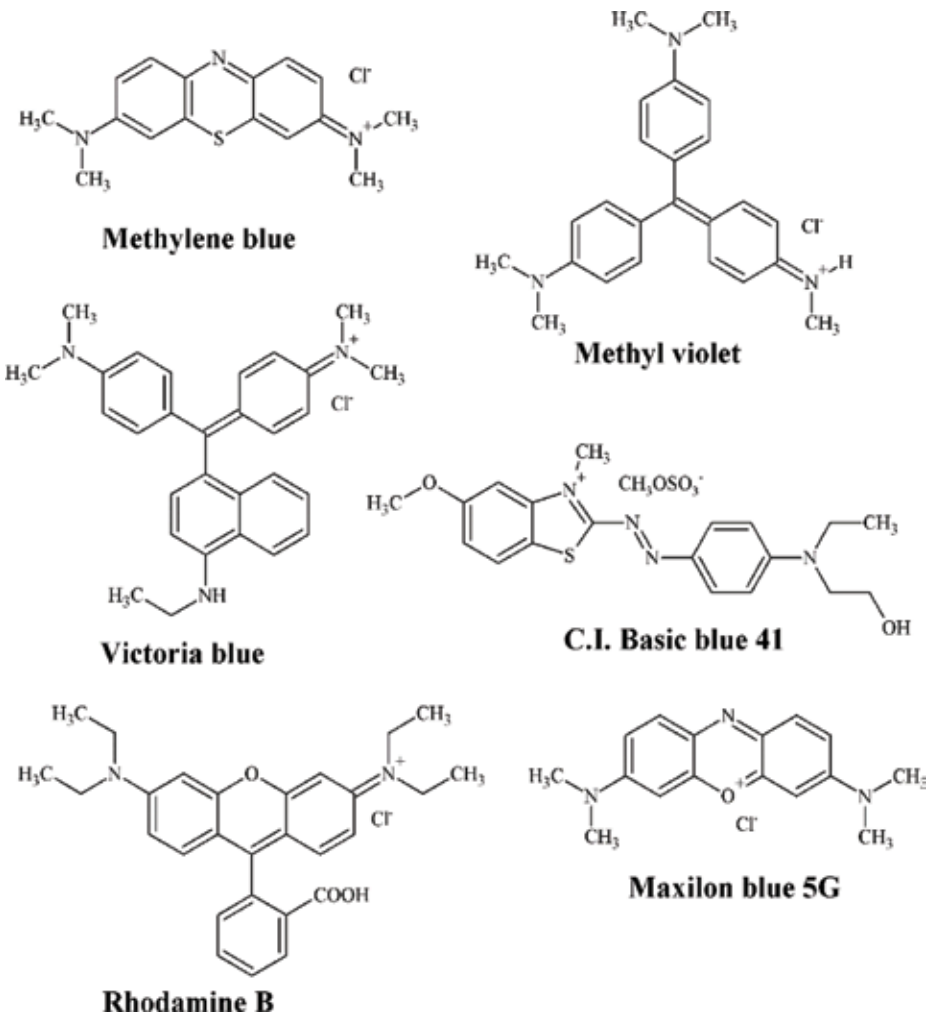

Figure 12. Cationic dyes adsorbed onto perlite.

Material	Cationic dye	Adsorbed (mmol g^{-1})	Reference
Unexpanded perlite	Methylene blue	0.71	[20]
Expanded perlite		0.08	
Expanded perlite	Methyl violet	0.02	[45]
Unexpanded perlite	C.I. Basic blue 41	$1.79 \cdot 10^{-3}$	[47]
Expanded perlite		$2.69 \cdot 10^{-3}$	
Unexpanded perlite	Rhodamine B	0.14	[48]
Expanded perlite	Maxilon blue 5G	0.05	[49]
Expanded perlite	Rhodamine B	$1.02 \cdot 10^{-3}$	[50]

Table 4. Adsorption of cationic dyes onto perlite reported in the literature.

http://dx.doi.org/10.5772/intechopen.75063

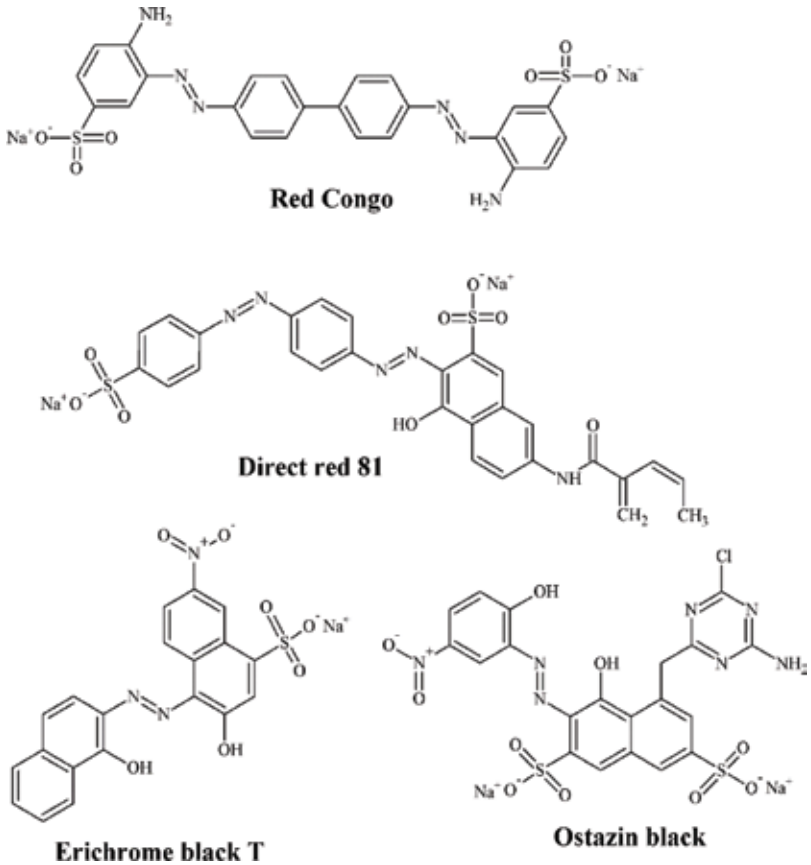

Figure 13. Anionic dyes adsorbed onto perlite.

Material	Cationic dye	Adsorbed (mmol g^{-1})	Reference
Unexpanded perlite	Congo Red	0.05	[51]
γ-Fe_2O_3-perlite	Direct red 81	0.61	[52]
Orthophenanthroline-perlite	Eriochrome black T	0.03	[53]
Chitosan-coated perlite	Ostazin black	0.03	[54]

Table 5. Adsorption of anionic dyes onto perlite reported in the literature.

amount of the cation is another key factor due to CTA^+ which can adopt different morphologies depending on the proportions (**Figure 14**).

In the same way, the adsorption capacity of the expanded perlite was evaluated in anionic surfactant using sodium dodecylbenzenesulfonate (**Figure 15**) as target molecule [56], reaching an adsorption value of 0.08 mmol g^{-1}. Similarly to the CTA^+, the anionic surfactant must adopt different morphologies as a function of its concentration.

5.3. Adsorption of biomolecules

The expansion that shows the structure of the perlite after a thermal treatment about 850°C (**Figures 3** and **4**) allows to host large molecules such as proteins and enzymes, which has great potential in the field of enzymatic catalysts and biosensors as well as the diagnosis of diseases. Thus, Rodríguez et al. have immobilized α-amylase onto expanded perlite [57], while Demirbas et al. have immobilized casein [58]. Pezzella et al. have adsorbed laccase on expanded perlite to adsorb dyes [59]. This process takes place by H-bond interactions. In addition, considering that perlite can also be used as lightweight aggregate concrete, this material has also been used to the adsorption of an antibiotic as cefixime [60] or even the immobilization of bacteria [61].

5.4. Adsorption of aromatic compounds and hydrocarbons

Phenolic compounds are generally considered to be one of the most important organic pollutants discharged into the environment causing serious damage to health, unpleasant taste and odor. The major sources of phenol pollution in the aquatic environment are wasterwaters from the paint, pesticide, coal conversion, polymeric resin, petroleum, and petrochemicals industries. Degradation of these substances produces phenol and its derivatives in the environment. The chlorination of natural waters for disinfection produces chlorinated phenols. A variety of techniques, such as ozonolysis, photolysis, and photocatalytic decomposition, have been implemented to purify water contaminated by phenols. Traditionally, biological treatment, activated carbon adsorption, reverse osmosis, ion exchange, and solvent extraction are the most widely used techniques for removing phenols and related organic substances. Adsorption of phenols onto solid supports such as activated carbons allows for their removal from water without the addition of chemicals [62].

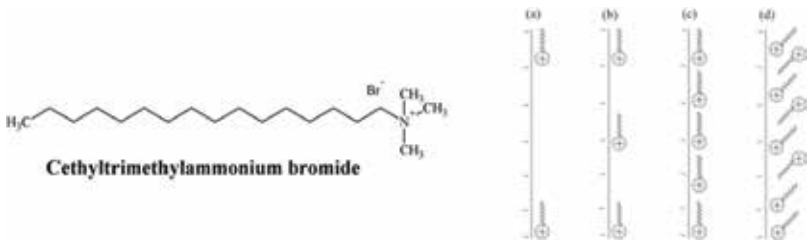

Figure 14. Interaction between a cationic surfactant and perlite in basic conditions.

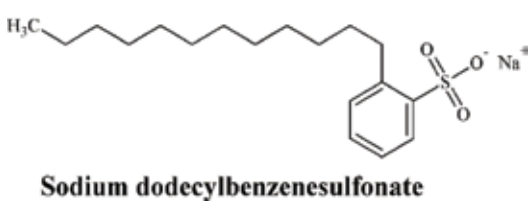

Figure 15. Chemical structure of sodium dodecylbenzenesulfonate.

Unexpanded perlite has shown to be an efficient material to adsorb 4-chlorophenol (**Table 6**), although its adsorption capacity is lower than bentonite [63]. In a later study, an expanded perlite was coated with chitosan to carry out a comparative study with phenol and chlorophenols [64]. The adsorption data reveal higher adsorption values than those shown for unexpanded perlite [63, 64]. The maximum adsorption capacity takes place at neutral pH through hydrogen bonds and van der Waals forces. The use of basic pHs causes a decrease of the adsorption capacity due to repulsive forces between adsorbate-adsorbent. On the other hand, Rostami et al. carried out an experiment where perlite was used to filtrate phenolic compounds from cigarette smoke, obtaining the highest adsorption values for phenol and cresols [65]. The expanded perlite was treated with basic solution to adsorb benzene (**Table 6**) [66]. According to the authors, the basic treatment generates a surface Si-O^-, which favors the interaction with the benzene. Björklund et al. evaluated the sorption of several hydrophobic organic pollutants onto perlite [67], obtaining an adsorption of 95% of alkylphenols, while the adsorbed polyaromatic hydrocarbons was about 80%.

Bisphenol A (BPA) is an aromatic monomer used in the industrial production for polycarbonate polymers and epoxy resins. This compound is used as linings for food and beverage packaging, as dental sealants, and as an additive to other consumer products. BPA can mimic estrogen and leads to negative health effects on animals and human beings so it is considered a potential toxic food contaminant because it could migrate from the containers into a variety of foods and beverage. Thus, expanded perlite immobilized ionic liquids to retain BPA (**Table 6**), where the adsorption takes place between the π-electrons of the BPA with the π-electrons of the imidazolic ring of the ionic liquid and H-bonds between the -OH groups of the ionic-liquid/expanded perlite and BPA [68].

Methyl *tert*-butyl ether (MTBE) is another compound used by society since it is an additive gasoline. MTBE is highly soluble in water and its biodegradability is very low. Thus, the presence of low amounts of MTBE is harmful to the nervous system, genotoxic, and eye irritant. Various techniques including air stripping, adsorption, advanced oxidation processes, and biological treatment have been used for the removal of MTBE from aqueous systems. Among techniques, the adsorption process due to its simplicity, moderate operational conditions, and economic feasibility has been used as an effective method for the removal of MTBE from

Material	Organic compound	Adsorbed (mmol g^{-1})	Reference
Unexpanded perlite	4-chlorophenol	0.04	[63]
Chitosan-coated perlite	Phenol	2.04	[64]
	2-chlorophenol	2.04	
	4-chlorophenol	2.50	
Expanded perlite/NaOH	Benzene	0.25	[66]
Ionic liquid-immobilized expanded perlite	Bisphenol A	0.01	[68]
Perlite/diatomite	Methyl *tert*-butyl ether	1.51	[69]

Table 6. Adsorption of aromatic compounds and hydrocarbons onto perlite reported in the literature.

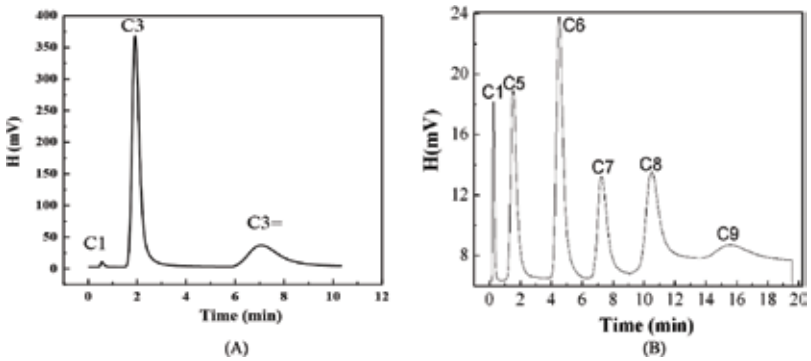

Figure 16. Chromatogram of propane (C3)-propylene (C3=) mixture (A) and C5-C9 mixture (B).

aqueous solutions. The adsorption of MTBE onto perlite was in the same range than diatomite or dolomite (**Table 6**). These authors proposed that the adsorption process occurs by the water ionization ($MTBE \rightarrow MTBE^{+} + OH^{-}$). Then, $MTBE^{+}$ interacts with a surface negatively charged in basic conditions by electrostatic interactions [69].

As indicated above, volcanic glass has an amorphous structure, so these aluminosilicates could be considered as zeolites without a clear hierarchy. Thus, it has been proposed the use of the volcanic glass as molecular sieve to separate hydrocarbons with similar physicochemical properties. Fernández-Hechevarría et al. have adsorbed and separated similar compounds as propane and propylene due to specific interactions of the double bond of the propylene (**Figure 16A**) [70]. The same authors have separated olefins C5-C9 using these materials by inverse chromatography, demonstrating that these materials are excellent molecular sieves (**Figure 16B**) [71].

6. Conclusions

In summary, volcanic glass is an igneous rock obtained by the rapid cooling of magma giving rise to an aluminosilicate without a defined order. The cooling of the rhyolitic magma forms a volcanic glass with excellent properties since the heating of these volcanic glass generates a macroporous structure with a wide range of applications as insulation in a wide range of temperatures, oil well treatment, flame resistant, acoustic insulation, filtration, adsorbent, agriculture and horticulture, lightweight aggregate construction, among other applications.

Focusing on its use as an adsorbent, perlite can be used to adsorb both cations and anions. The adsorption capacity can be improved by the incorporation of several organic or inorganic structures onto the expanded perlite to favor a specific adsorption. In addition, the expanded perlite can be used to retain bulkier molecules such as aromatic compounds, dyes or biomolecules so these materials can play an important role in the water purification. Recently, volcanic glass has been used as molecular sieve to adsorb and separate short hydrocarbons such as propane/propylene or the separation of short olefins (C5–C9). Considering these premises, the volcanic glass is a material with high potential to the selective adsorption of different biomolecules. In addition, as expanded perlite has the ability to host molecules with variable behavior and dimensions.

Author details

Juan Antonio Cecilia[1], Miguel Armando Autie-Pérez[1,2], Juan Manuel Labadie-Suarez[2], Enrique Rodríguez Castellón[1]* and Antonia Infantes Molina[1]

*Address all correspondence to: castellon@uma.es

1 Departamento de Química Inorgánica, Cristalografía y Mineralogía, Facultad de Ciencias, Universidad de Málaga, Spain

2 Facultad de Ingeniería Química, Universidad Tecnológica de la Habana José Antonio Echevarría, La Habana, Cuba

References

[1] Huang PM, Li Y, Sumner ME, editors. Handbook of Soil Sciences: Properties and Processes (Second Edition). Boca Raton: CRC Press; 2012. pp. 20-24. ISBN: 978-1-4398-0306-6

[2] Kenlab A, Normanclan M, Hutcheon D, Stolper M. Assimilation of seawater derived components in an oceanic volcano: Evidence from matrix glasses and glass inclusions from Loihi seamount, Hawaii. Chemical Geology. 1999;**156**:299-319

[3] Staudigel H, Furnes H, McLoughlin N, Banerie R, Connell LB, Templeton A. 3.5 billion years of glass bioalteration: Volcanic rocks as a basis for microbial life? Earth-Science Reviews. 2008;**89**:156-176

[4] Knoche R, Dingwell DB. Temperature dependent in thermal expansivities of silicate melts: The system anorthite-diopside. Geochimica et Cosmochimica Acta. 1992;**56**:689-699

[5] Knoche R, Dingwell DB, Well SL. Non-linear temperature dependence of liquid volumes in the system albite-anorthite-diopside. Contributions to Mineralogy and Petrology. 1992;**111**:61-73

[6] Melson WG, O'Hearn T, Jarosewich E. A data brief on the Smithsonian abyssal volcanic glass data file. Geochemistry, Geophysics, Geosystems. 2002;**3**:1-11

[7] Webb S. Silicate melts: Relaxation, rheology, and the glass transition. Reviews of Geophysics. 1997;**35**:191-218

[8] Stevenson RJ, Dingwell DB, Webb SL, Bagdassarov NS. The equivalence of enthalpy and shear stress relaxation in rhyolitic obsidians and quantification of the liquid-glass transition in volcanic processes. Journal of Volcanology and Geothermal Research. 1995;**68**:297-306

[9] Friedman I, Long W. Volcanic glasses, their origins and alteration processes. Journal of Non-Crystalline Solids. 1984;**67**:127-133

[10] Aiuppa A, Moretti R, Federico C, Giudice G, Gurrieri S, Liuzzo M, Papale P, Shinohara H, Valenza M. Forecasting Etna eruptions by real-time observation of volcanic gas composition. Geology. 2007;**35**:1115-1118

[11] Zhang Y. H_2O in rhyolitic glasses and melts: Measurement, speciation, solubility, and diffusion. Reviews of Geophysics. 1999;**37**:493-516

[12] Ross CS, Smith RL. Ash-flow tuffs: Their origin, geologic relations, and identification. 1961;**366**:81

[13] Venezia AM, Floriano MA, Deganello G, Rossi A. Structure of pumice: An XPS and 27Al MAS NMR study. Surface and Interface Analysis. 1992;**18**:532-538

[14] Mrazova S, Gadas P. Obsidian balls (marekanite) from Cerro Tijerina, Central Nicaragua: Petrographic investigations: J. Geoscience. 2011;**56**:43-49

[15] Cas RAF, Wright JV. Volcanic Successions Modern and Ancient: A Geological Approach to Processes, Products and Successions. United Kingdom: Chapman & Hall; 1988

[16] http://www.obsidianlab.com/

[17] Perlite—Mineral Deposit Profiles. B.C. Geological Survey. Retrieved November 20, 2007

[18] Maxim LD, Niebo R, McConnell EE. Perlite toxicology and epidemiology—A review. Inhalation Toxicology. 2014;**26**:259-270

[19] Mathialagan T, Viraraghavan T. Adsorption of cadmium from aqueous solutions by perlite. Journal of Hazardous Materials. 2002;**94**:291-303

[20] Dogan M, Alkan M, Onganer Y. Adsorption of methylene blue from aqueous solution onto perlite. Water, Air, and Soil Pollution. 2000;**120**:229-248

[21] Liu G, Jiang Y, Liao Y, Wang W. Preparation and characterization of a novel metal affinity adsorption PVDF membrane. Advances in Information Sciences and Service Sciences. 2013;**5**(13):110

[22] Fu F, Wang Q. Removal of heavy metal ions from wastewaters: A review. Journal of Environmental Management. 2011;**92**:407-418

[23] Sarı A, Tuzen M, Cıtak D, Soylak M. Adsorption characteristics of Cu(II) and Pb(II) onto expanded perlite from aqueous solution. Journal of Hazardous Materials. 2007;**148**:387-394

[24] Alkan M, Dogan M. Adsorption of copper(II) onto perlite. Journal of Colloid and Interface Science. 2001;**243**:280-291

[25] Sekomo CB, Rousseau DPL, Lens PNL. Use of Gisenyi volcanic rock for adsorptive removal of Cd(II), Cu(II), Pb(II), and Zn(II) from wastewater. Water, Air, & Soil Pollution. 2012;**223**:533-547

[26] Ortega-Hernández L, Fernández-Hechevarría HM, López-Cordero R, Autie-Pérez MA, Infantes-Molina A, Rodríguez-Castellón E. Cu^{2+} removal from aqueous solution with a Cuban volcanic glass mineral. International Journal of Plant, Animal and Environmental Sciences. 2015;**6**:174-183

[27] Ghassabzadeh H, Mohadespour A, Torab-Mostaedi M, Zaheri P, Maragheh MG, Taheri H. Adsorption of Ag, Cu and Hg from aqueous solutions using expanded perlite. Journal of Hazardous Materials. 2010;**177**:950-955

[28] Jeon C, Holl WH. Application of the surface complexation model to heavy metal sorption equilibria on to aminated chitosan. Hydrometallurgy. 2004;**71**:421-428

[29] Swayampakula K, Boddu VM, Nadavala SK, Abburi K. Competitive adsorption of Cu(II), Co(II) and Ni(II) from their binary and tertiary aqueous solutions using chitosan-coated perlite beads as biosorbent. Journal of Hazardous Materials. 2009; **170**:680-689

[30] Hasan S, Ghosh TK, Viswanath DS, Boddu VM. Dispersion of chitosan on perlite for enhancement of copper(II) adsorption capacity. Journal of Hazardous Materials. 2008;**152**: 826-837

[31] Torab-Mostaedi M, Ghassabzadeh H, Ghannadi-Maragheh M, Ahmadi SJ, Taheri H. Removal of cadmium and nickel from aqueous solution using expanded perlite. Brazilian Journal of Chemical Engineering. 2010;**27**:299-308

[32] Hasan S, Krishnaiah A, Ghosh TK, Viswanath DS, Boddu VM, Smith ED. Adsorption of divalent cadmium (Cd(II)) from aqueous solutions onto chitosan-coated perlite beads. Industrial and Engineering Chemistry Research. 2006;**45**:5066-5077

[33] Ghassabzadeh H, Torab-Mostaedi M, Mohaddespour A, Maragheh MG, Ahmadi SJ, Zaheri P. Characterizations of Co(II) and Pb(II) removal process from aqueous solutions using expanded perlite. Desalination. 2010;**261**:73-79

[34] Irani M, Amjadi M, Mousavian MA. Comparative study of lead sorption onto natural perlite, dolomite and diatomite. Chemical Engineering Journal. 2011;**178**:317-323

[35] Steinhauser G, Bichler M. Adsorption of ions onto high silica volcanic glass. Applied Radiation and Isotopes. 2008;**66**:1-8

[36] Hasan S, Krishnaiah A, Ghosh TK, Viswanath DS, Boddu VM. Adsorption of chromium (VI) on chitosan-coated perlite. Separation Science and Technology. 2003;**38**:3775-3793

[37] Edebali S. Alternative composite nanosorbents based on Turkish perlite for the removal of Cr(VI) from aqueous solution. Journal of Nanomaterials. 2015:697026

[38] Thanh DN, Singh M, Ulbrich P, Strnadova N, Štěpánek F. Perlite incorporating γ-Fe_2O_3 and α-MnO_2 nanomaterials: Preparation and evaluation of a new adsorbent for As(V) removal. Separation and Purification Technology. 2011;**82**:93-101

[39] Sarı A, Şahinoğlu G, Tüzen M. Antimony(III) adsorption from aqueous solution using raw perlite and Mn-modified perlite: Equilibrium, thermodynamic, and kinetic studies. Industrial and Engineering Chemistry Research. 2012;**51**:6877-6886

[40] Akkaya R. Removal of radioactive elements from aqueous solutions by adsorption onto polyacrylamide–expanded perlite: Equilibrium, kinetic, and thermodynamic study. Desalination. 2013;**321**:3-8

[41] Akkaya R, Akkaya B. Adsorption isotherms, kinetics, thermodynamics and desorption studies for uranium and thorium ions from aqueous solution by novel microporous composite P(HEMA-EP). Journal of Nuclear Materials. 2013;**434**:328-333

[42] Akkaya R. Removal of radio nuclides of the U- and Th-series from aqueous solutions by adsorption onto polyacrylamide-expanded perlite: Effects of pH, concentration and temperature. Research Section A: Accelerators, Spectrometers, Detectors and Associated Equipment. 2012;**688**:80-83

[43] Vijaya Y, Vekata M, Subbaiah ASR, Krishnaiah A. Equilibrium and kinetic studies of fluoride adsorption by chitosan coated perlite. Desalination and Water Treatment. 2010;**20**:272-280

[44] Khani A, Nemati A. Modeling of nitrate removal by nanosized iron oxide immobilized on perlite using artificial neutral network. Asian Journal of Chemistry. 2013;**25**:4340-4346

[45] Doğan M, Alkan M. Adsorption kinetics of methyl violet onto perlite. Chemosphere. 2003; **50**:517-528

[46] Dogan M, Alkan M. Removal of methyl violet from aqueous solution by perlite. Journal of Colloid and Interface Science. 2003;**267**:32-41

[47] Roulia M, Vassiliadis AA. Sorption characterization of a cationic dye retained by clays and perlite. Microporous and Mesoporous Materials. 2008;**116**:732-740

[48] Vijayakumar G, Tamilarasan R, Dharmendirakumar M. Adsorption, kinetic, equilibrium and thermodynamic studies on the removal of basic dye Rhodamine-B from aqueous solution by the use of natural adsorbent perlite. Journal of Materials and Environmental Science. 2012;**3**:157-170

[49] Demirbaş Ö, Alkan M. Adsorption kinetics of a cationic dye from wastewater. Desalination and Water Treatment. 2015;**53**:3623-3631

[50] Damiyine B, Guenbour A, Boussen R. Adsorption of rhodamine B dye onto expanded perlite from aqueous solution: Kinetics, equilibrium and thermodynamics. Journal of Materials and Environmental Science. 2017;**8**:345-355

[51] Vijayakumar G, Dharmendirakumar M, Renganathan S, Sivanesan S, Baskar G, Elango KP. Removal of Congo red from aqueous solutions by perlite. CLEAN – Soil, Air, Water. 2009;**37**:355-364

[52] Shirkhodaie M, Hossein Beyki M, Shemirani F. Biogenic synthesis of magnetic perlite@ iron oxide composite: Application as a green support for dye removal. Desalination and Water Treatment. 2016;**57**:11859-11871

[53] Almeida JMF, Oliveira ES, Silva IN, de Souza SPMC, Fernandes NS. Adsorption of Eriochrome black T from aqueous solution onto expanded perlite modified with orthophenanthroline. Revista Virtual de Química. 2017;**9**:502-513

[54] Sahbaza DA, Acikgoz C. Adsorption of a textile dye Ostazin black NH from aqueous solution onto chitosan-coated perlite beads. Desalination and Water Treatment. 2017;**67**:332-338

[55] Alkan M, Karadas M, Dogan M, Demirbas Ö. Adsorption of CTAB onto perlite samples from aqueous solutions. Journal of Colloid and Interface Science. 2005;**291**:309-318

[56] Acikgoz C, Sahbaz DA, Balbay S. Determination of anionic surfactant adsorption capacity of expanded perlite from aqueous solutions. Fresenius Environmental Bulletin. 2016; **25**:3447-3453

[57] Rodríguez J, Soria F, Geronazzo H, Destefanis H. Modification and characterization of natural aluminosilicates, expanded perlite, and its application to immobilise α—Amylase from *A. oryzae*. Journal of Molecular Catalysis B: Enzymatic. 2016;**133**:S259-S270

[58] Demirbas Ö, Alkan M, Demirbas A. Adsorption of casein onto some oxide minerals and electrokinetic properties of these particles. Microporous and Mesoporous Materials. 2015; **204**:197-203

[59] Pezzella C, Russo ME, Marzocchella A, Salatino P, Sannia G. Immobilization of a *Pleurotus ostreatus* Laccase mixture on perlite and its application to dye decolourisation. BioMed Research International. 2014:308613

[60] Rasoulifard MH, Khanmohammadi S, Heidari A. Adsorption of cefixime from aqueous solutions using modified hardened paste of Portland cement by perlite; optimization by Taguchi method. Water Science and Technology. 2016;**74**:1069-1078

[61] Zhang J, Liu Y, Feng T, Zhou M, Zhao L, Zhou A, Li Z. Immobilizing bacteria in expanded perlite for the crack self-healing in concrete. Construction and Building Materials. 2017;**148**:610-617

[62] Ahmaruzzaman M. Adsorption of phenolic compounds on low-cost adsorbents: A review. Advances in Colloid and Interface Science. 2008;**143**:48-67

[63] Koumanova B, Peeva-Antova P. Adsorption of p-chlorophenol from aqueous solutions on bentonite and perlite. Journal of Hazardous Materials. 2002;**90**:229-234

[64] Kumar NS, Sugura M, Subbaiah MV, Reddy AS, Kumar NP, Krishnaiah A. Adsorption of phenolic compounds from aqueous solutions onto chitosan-coated perlite beads as biosorbent. Industrial and Engineering Chemistry Research. 2010;**49**:9238-9247

[65] Rostami F, Robati GM, Naghizadesh F, Hosseini S, Chaichi MJ. Perlite filtration of phenolic compounds from cigarette smoke. Combinational Chemistry & High Throughput Screening. 2013;**16**:73-77

[66] Appiah-Ntiamoah R, Mai TX, Momade FWV, Kim H. Adsorption of benzene from aqueous solution using base modified expanded perlite. Advances in Materials Research. 2013;**622**:1779-1783

[67] Björklund K, Li L. Evaluation of low-cost materials for sorption of hydrophobic organic pollutants in stormwater. Journal of Environmental Management. 2015;**159**:106-114

[68] Liu J, Zhu X. Ionic liquid immobilized expanded perlite solid-phase extraction for separation/analysis of bisphenol A in food packaging material. Food Analytical Methods. 2016;**9**:605-613

[69] Sherkhaoleslami NSN, Irani M, Gholamian R, Alabadi M. Removal of MTBE from aqueous solution using natural nanoclays of Iran. Desalination and Water Treatment. 2016;**57**:27259-27268

[70] Fernandez-Hechevarría HM, Labadie Suarez JM, Santamaría-Gonzalez J, Infantes-Molina A, Autie-Castro G, Cavalcante Jr CL, Rodríguez-Castellon E, Autie-Perez M. Adsorption and separation of propane and propylene by Cuban natural volcanic glass. Materials Chemistry and Physics. 2015;**168**:132-137

[71] Autie-Pérez M, Infantes-Molina A, Cecilia JA, Labadie-Suárez JM, Rodríguez-Castellón E. Separation of light liquid paraffin C5–C9 with Cuban volcanic glass previously used in copper elimination from water solutions. Applied Science. 2018;**8**:295

Section 5

Impact of Volcanoes on the Human Health

Chapter 12

Health Impact of Volcanic Emissions

Martha Patricia Sierra-Vargas,
Claudia Vargas-Domínguez,
Karen Bobadilla-Lozoya and
Octavio Gamaliel Aztatzi-Aguilar

Additional information is available at the end of the chapter

http://dx.doi.org/10.5772/intechopen.73283

Abstract

Volcanoes form along the edges of tectonic plates. Although it is true that volcanic eruptions are destructive, these eruptions also have benefits. Volcanic eruptions provide minerals to the surrounding soil, and these minerals are beneficial to agriculture and can be used as building materials. Exposure to volcanic emissions can threaten the health of inhabitants in many ways; dermal and ocular irritation, cardiopulmonary exacerbations in people who suffer from chronic diseases, and even cancer have been linked with exposure to volcanic emissions. When rainwater passes through volcanic ashes deposited on land surfaces, the leaching of metals leads to significant changes in the chemistry of the surface water, increasing the risk of drinking water and land contamination. In addition to the health effects, volcanic eruptions are known to lead to surface cooling at the regional and global scales because of the emission of fine ash particles; however, these emissions, being a source of sulfates, contribute to acid rain formation. Because volcanic ash is highly abrasive, this ash can lower visibility and cause considerable damage to the engines of transportation systems. To avoid fatalities, it is important to closely monitor volcanic activity and promote a culture of prevention at all levels of society.

Keywords: volcanic emissions, health impact, cardiopulmonary disease, environmental impact, public policies

1. Introduction

Volcanoes form along the edges of tectonic plates, making up a cluster known as the Ring of Fire (**Figure 1**). Currently, there are about 100 active volcanoes all over the world, and more than a 100 million people are potentially exposed to volcanic emissions, which pose a threat to

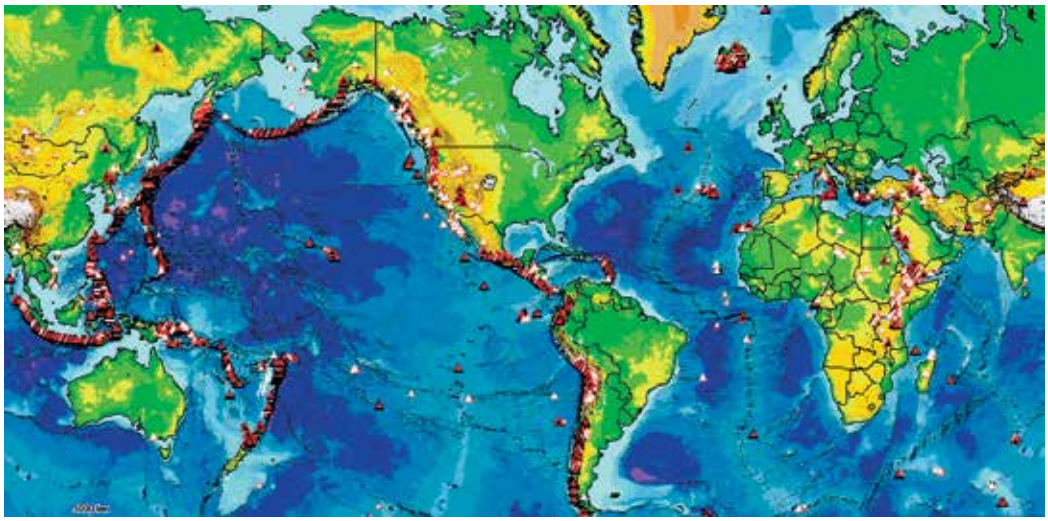

Figure 1. Ring of fire (red triangles) covers an area of 40,000 km (25,000 mi) located in the basin of the Pacific Ocean. It comprises about 75% of all active volcanoes on the earth, and approximately 90% of all earthquakes occur along the ring of fire. It is also known as circum-Pacific belt. http://nmnh-arcgis02.si.edu/thisdynamicplanet/.

the health of those exposed [1]. As a consequence of an eruptive event, a diversity of volcanic material rises to the surface (**Figure 2**). As shown in **Table 1**, the emission of volcanic material threatens the safety of populations in two different ways. In addition, volcanic emissions are a global concern due to the impact of these emissions on health, property and climate [2]. A volcanic plume is a mixture of liquid and solid particles produced during the eruptive event; volcanic plumes can reach the stratosphere depending on the intensity of the eruption, which is measured as the volcanic explosivity index (VEI). The chemical reactions within the plume are intense, and aerosol particles formed by nucleation remain in the plume and are transported by the wind across long distances (**Figures 3** and **4**) [3, 4].

Humans experience multiple types of exposure (respiratory and gastrointestinal tract, skin contact) to volcanic emissions. The respiratory system is the most susceptible because of the large quantities of air we breathe (20 m^3/day). Moreover, the impact of such exposure depends on different factors; essentially, the physical and chemical characteristics of the toxic substances (e.g., heavy metals, salts, metal oxides, inorganic carbons, silicates, plastics or organics) are in question. In addition, the age, sex, respiratory pattern and health status of the exposed person are also determinant factors. Among the physical characteristics, the size of the ash particles emitted by volcanoes, which can be less than 2 mm (**Figures 5**–**7**), and the number, concentration and density of the particles as well as the dynamics of the gas flow in the airways will determine the region where the ash particles will be deposited and will determine the local adverse effects [5]. The health effects of the volcanic emissions depend on the physical and chemical characteristics of the emissions and on the corresponding toxicological properties. The health effects are a consequence of the inhalation of particles directly emitted from active volcanoes or of resuspension of the soil ashes during the cleanup after the eruption. The effects that such exposure has on human health can be classified as acute or chronic. **Figure 8**

http://dx.doi.org/10.5772/intechopen.73283

shows the interaction of some components of volcanic emissions within the respiratory tract and the possible effects caused by these components coming in contact with segments of the respiratory tract.

Acute effects include eye and throat irritation, cough, dyspnea, wheezing, chronic obstructive pulmonary disease (COPD), cardiovascular events, psychological stress, reversible changes in healthy lung function, and acute exacerbations of previously existing respiratory conditions such as asthma [6, 7]. As the lung is not a closed system, tiny particles (<0.1 μm) called ultrafine particles (UFPs) can translocate to other organs, where these particles can have adverse effects [5]. In addition, components of the ash particles can be dissolved in the

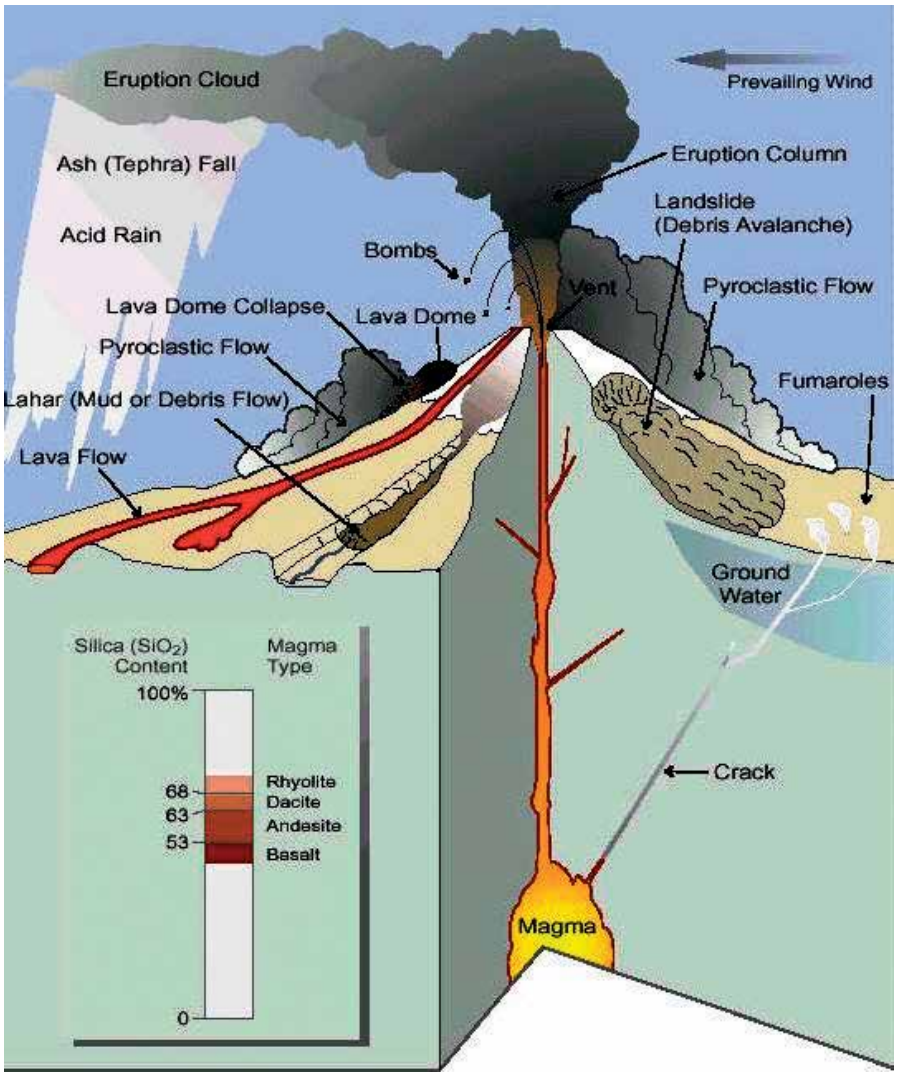

Figure 2. Material emitted during volcanic emissions, extracted from https://pubs.usgs.gov/fs/fs002-97/.

Hazard type	Kind of material emitted	Consequence
Primary hazards	Lava flows	Can cause massive damage to land, property and trigger fires
	Tephra (lava bombs)	Can damage buildings and start secondary fires.
	Pyroclastic flow	Can travel at speeds up to 500 km/h and incinerate anything in their path.
	Ash cloud	Can alter visibility, increase the air concentration of some pollutants, contribute to the acid rain, and contaminate water and land when the ash falls to ground.
	Poisonous gases	Can be toxic to animals and humans, if inhaled in large quantities can cause death.
Secondary hazards	Lahar	Volcano ash and/or lava can mix with snow or with river/rainwater. These flows are powerful enough to remove everything in their path.
	Acid rain	Sulfur dioxide emitted during the eruption can mix with water vapor in the atmosphere. Can damage buildings. Soils and lakes in contact are more acid, threatening plant and animal's life.
	Climate change	Ash released into the atmosphere can absorb or reflect incoming solar radiation and reduce global temperatures. Volcanic emissions are also a source of greenhouse gases.
	Fires	Are produced by tephra and lava flows once they are in contact with the buildings and land.

Table 1. Types of hazards from volcanic emissions.

lung-lining fluid and can pass through the alveolar-capillary membrane; this interaction explains, at least in part, the relationship between particle exposure, cardiovascular disease and some neurological alterations [8]. Chronic effects are related to increased mortality rate for cardiopulmonary disease [6], increased medication use (e.g., asthma medication, analgesics) [9], and increased prevalence of some types of cancer (e.g., lip, oral cavity, pharynx and female breast cancers) [10]. Moreover, neurodegenerative diseases such as Alzheimer's disease have also been linked to chronic exposure to volcanic emissions [11]. Animal models have reported that volcanic emissions are associated with impairment of spermatogenesis [12].

Toxicological studies have suggested that exposure to volcanic ash could also have a negative impact on immunological defense and could increase the occurrence of biological redox reactions [13], which could lead to more frequent infections and to organic damage [14] (**Table 2**). In addition to the inherent physical and emotional disruptions caused by eruptive events, the economic impact of these events has severe consequences at a regional level because the people most impacted are those who belong to low-income groups. In this chapter, we summarize the toxicological aspects of volcanic emissions and the impact that a potential multimedia exposure has on health, with emphasis on inhalation exposure.

2. Volcanic emissions

The type and physicochemical characteristics of volcanic emissions vary depending on the volcano. In fact, these characteristics and types depend on the volcanic morphology and the

http://dx.doi.org/10.5772/intechopen.73283

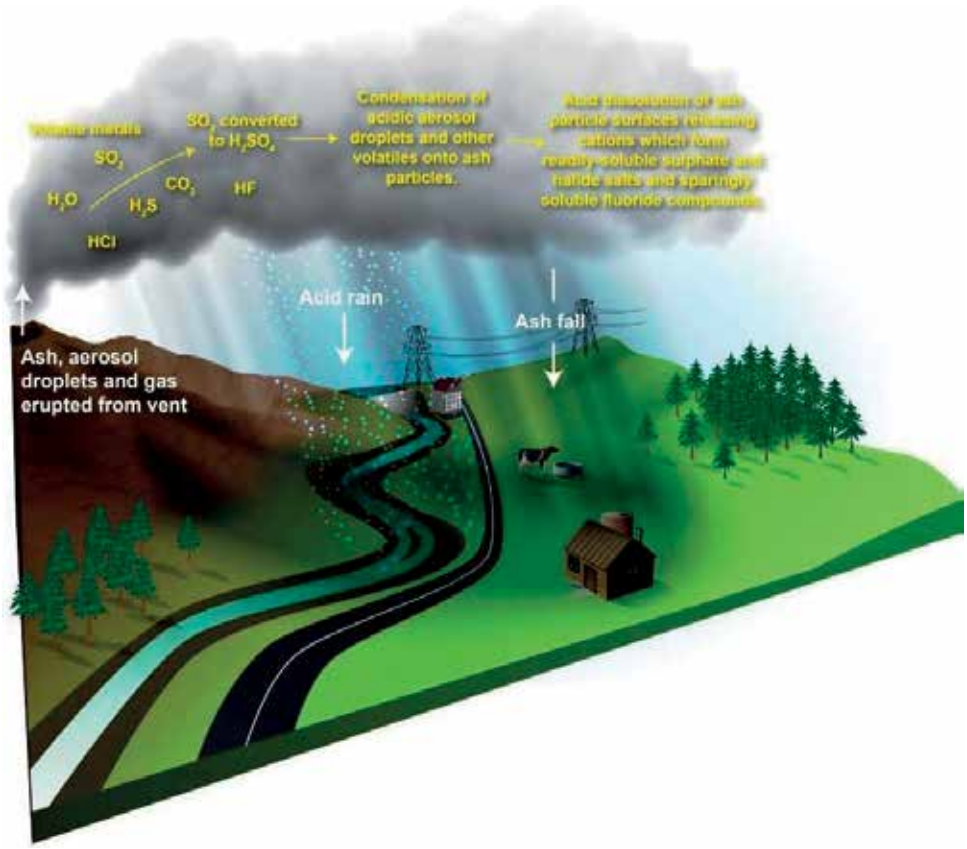

Figure 3. Dynamics of volcanic emissions. Sulfur dioxide emitted during volcanic eruption can reach the stratosphere altering the chemistry of the atmosphere. https://volcanoes.usgs.gov/volcanic_ash/gases_aerosols.html.

Figure 4. Volcanic plume dispersion from Popocatépetl, México. NASA image courtesy Jeff schmaltz, LANCE MODIS rapid response and Robert Simmon. Caption by Michon Scott. Mexico's Popocatépetl volcano released a plume on March 8, 2013. The ash plume reached roughly 1500 m (4900 feet) above the volcano crater, or about 7 km (4 miles) above sea level. The plume blew eastward away from the volcanic summit. https://earthobservatory.nasa.gov/NaturalHazards/view.php?id=80621.

Figure 5. A sample of tephra erupted by Mount St. Helens on May 18, 1980. The tephra was collected between about 40 and 60 km downwind from the volcano. USGS image, D.E. Wieprecht. http://volcanoes.usgs.gov/Imgs/Jpg/Tephra/30410914_075_caption.html.

geological features of the region where the volcano is located. Generally, volcanic ashes are composed of magmatic fragments, consisting of both glass and minerals.

The mineralogical composition of volcanic ash consists of approximately 45–75 wt% silica (SiO_2) [15], making SiO_2 content useful as a classification parameter (**Figure 9**). There are also other major components in volcanic emissions, such as water vapor, hydrogen peroxide (H_2O_2), carbon dioxide (CO_2), sulfur dioxide (SO_2) (the dominant sulfur component), hydrogen sulfide

Figure 6. Ballistic tephra fragment from Popocatépetl volcano (May 14, 2013). CENAPRED image. http://www.cenapred.unam.mx/popo/2015/mar/p03041510.png.png.

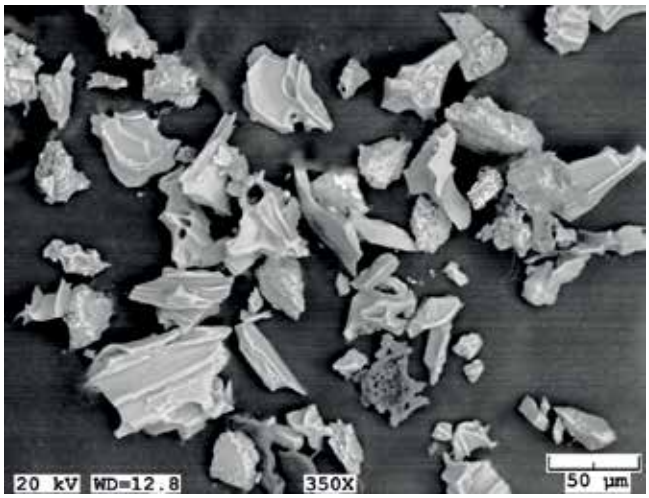

Figure 7. Scanning electron microscope image of resuspended volcanic ash from the 1912 Novarupta-Katmai deposits in the Katmai region picked up during high winds on November 1, 2015, and carried to Larsen Bay on Kodiak Island, AK. Sample collected by Sherry Harmes of Larsen Bay. Credit: Kristi Wallace, Alaska volcano observatory, US geological survey. https://www.usgs.gov/media/images/scanning-electron-microscope-image-volcanic-ash.

Cause	Effect
Innate immunity	
Decreases in C3 and C4 complement	Reduce phagocytosis processes and cellular activation
Impairs autophagy in human alveolar macrophages	Impairs bacterial killing, increase susceptibility to bacterial infections
Decrease activation of JNK and ERK pathways	Promote inflammation
Inhibitory effect of antimicrobial peptides and defensins 1 and 2	Decrease bactericidal capacity
Induce cytokines TNF-α, IL-8, IL-1β	Promotes inflammation
Adaptive immunity	
Reduction in T-cell response	Impairs T-cell response, impairs antigenic presentation
Reduction in T-cell proliferation	Impairs T-cell response
Humoral immunity	
Decreases immunoglobulines (IgG)	Immunity humoral altered, unknown

Table 2. Effects of volcanic ash exposure on immune system responses.

(H_2S) (the second most important S species, converted to SO_2 in the atmosphere), sulfates (SO_4^{-2}), and carbonyl sulfide (COS) and its precursor carbon disulfide (CS_2).

COS has a residence time of several years in the atmosphere and is an important source of sulfate aerosols. The main halogen component of volcanic ash is hydrogen chloride (HCl), which is highly soluble and is rapidly washed out from the atmosphere. Hydrogen fluoride

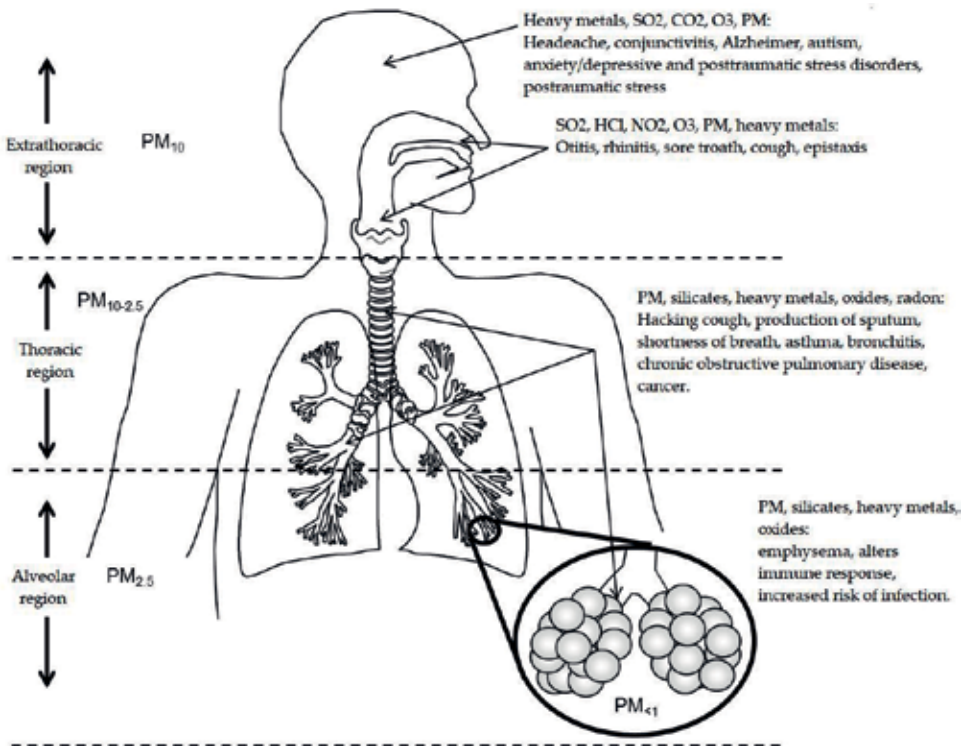

Figure 8. Airway impact of volcanic emissions (courtesy: Dr. Mario Vargas, modified by Dra. Patricia sierra).

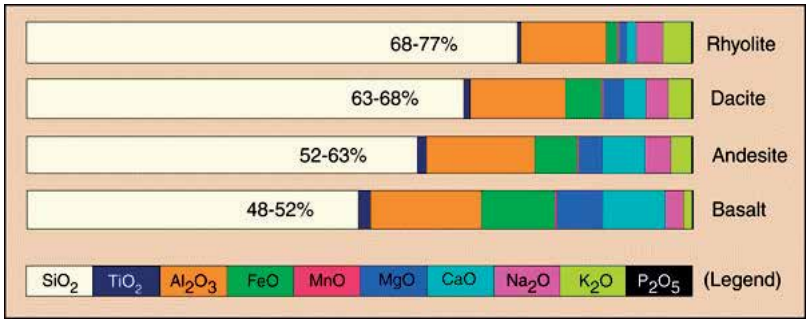

Figure 9. Igneous rocks and magma major chemical elements http://scienceviews.com/geology/igneoustypes.html.

(HF), which is another ash component, may be dangerous because it is introduced into the alimentary chain mainly through contaminated water, not to mention that fluoride is an emergent toxicant affecting smooth organs (e.g., lungs and kidney) [16]. Volcanic ash is a source of helium (He), radon (Rn), mercury (Hg), magnesium (Mg), manganese (Mn) and bromide (Br), increasing the risk for people who have difficulty in absorbing essential elements such as Ca, Fe and Zn and retaining other elements such as Cd and Mn [17].

http://dx.doi.org/10.5772/intechopen.73283

3. Epidemiological impact of volcanoes

The effects of exposure to volcanic emissions depend on the summit elevation and topographic features and on the intensity and duration of volcanic activity as well as the population density near volcanoes. This last parameter determines the difference between volcanic eruptions being a spectacle or a natural disaster. It has been reported that 4.7 million people have been affected by volcanoes all over the world and a total of 14,726 injuries (range 11,549–17,917) and 91,834 deaths (range: 85,169–102,372) result from volcanic eruptions between 1900 and 2009 [18]. In this context, exposure to CO_2 emissions was responsible for 30 and 1700 deaths at Monoun and Nyos lakes, respectively [19, 20]. In Mexico, the Popocatepetl volcano is part of the trans-Mexican volcanic belt and represents a high-risk zone because of the human settlements that surround the volcano, which include the states of Mexico, Morelos and Puebla, which are 65, 41 and 45 km away, respectively, from the volcanic crater. The Popocatepetl volcano reawakened on December 21, 1994, after a dormancy period of 70 years; the volcano remains active, with a VEI of 3–4 being registered in January 2001. In addition to the impact that a Popocatepetl eruption could have on crops and wildlife, the 2010 population census indicated that there are 173,928 people living approximately 30 km from the crater of Popocatepetl [21] who could potentially be directly affected by the eruption. Furthermore, the ashes produced by a major eruption could affect an area containing more than 20 million people and have a large economic impact [22, 23].

4. Impact on morbidity

During volcanic eruptions, there are multiple interactions that occur between the sets of chemical products emitted into the atmosphere. These chemicals are commonly referred to as "vog," a term that is a combination of the words "volcanic" and "fog" and is frequently used by volcanologists. Vog is composed of sulfuric acid (H_2SO_4); ammonium bisulfate (NH_4HSO_4) and ammonium sulfate $(NH_4)_2SO_4$; and solid material, less than 2.5 μm in size ($PM_{2.5}$), that is rich in sodium sulfate, ammonium sulfate and sulfuric acid aerosols.

The impact of volcanic emissions on morbidity and mortality has been described by several authors; however, some effects cannot be fully explained by vog exposure. For example, Michaud et al. [24] found a close relationship between emergency department visits in Hilo, Hawai'i and at the Kilauea volcano from January 1997 to May 2001 and occurrences of asthma/COPD, cardiac conditions, flu, cold and pneumonia. However, after adjusting for day of the week and month of the year, only visits for asthma/COPD remained associated with air quality, which was measured as SO_2 and PM_1 levels. Furthermore, the association with SO_2 levels was stronger with a 3-day lag and that with PM_1 levels was stronger with a one-day lag. In another study, it was reported that 3 weeks after the eruption of the Guagua Pichincha volcano in Quito (Ecuador), the emergency room visits increased due to acute pediatric respiratory infection and asthma, mainly in children under 5 years old [25].

In Hawai'i, Shinkura et al. [26] determined a relative risk of 2.2 for neonatal mortality associated with the average monthly SO_2 concentrations. Volcanic emissions greatly contribute to

the environmental SO_2 concentrations in some cities, such as Miyakejima (Japan). In this regard, it is worth mentioning the results from the Yorifuji study [27], where the odds ratio of having a baby with low birth weight was 1.71 if there had been SO_2 exposure during the entire pregnancy period, including exposure to SO_2 derived from volcanic emissions.

These highly irritant species are associated not only with respiratory effects but also with ocular effects. Kimura et al. [28] evaluated the effects of volcanic ash on the ocular symptoms of 10,380 children aged 6–15 years who lived near Mount Sakurajima (Japan). The study was carried out from 1994 to 2003. The authors concluded that ocular symptoms, such as redness, discharge, foreign-body sensation and itching, were influenced by volcanic eruptions, and stronger correlation was found with those who lived 4 km away from the volcanic crater.

Camara and Lagunzad [29] also evaluated the negative impact on residents of the island of O'ahu in Hawai'i who were exposed to volcanic emissions from Mount Kilauea for at least 7 years. The authors found a combination of toxic and allergic reactions, characterized by signs and symptoms such as conjunctival injection, papillary reaction, clear mucous discharge, pulmonary edema, lid swelling, chemosis, itchiness, foreign-body sensation, tearing and burning sensation. Some of these symptoms were present in 100% of the people studied. The authors introduced the term "vog-induced conjunctivitis (VIC)" and recommended that physicians refer patients to an eye specialist when the patients exhibit the aforementioned signs and symptoms.

Cardiovascular effects have also been observed in people exposed to volcanic emissions; nonmedicated, nonsmoking and nonobese participants had significantly faster mean pulse rates, as did those aged ≥65 and having a body mass index < 25 kg/m^2, and a higher mean systolic blood pressure was observed in nonobese participants. Interestingly, indoor concentrations of volcanic air pollution were higher than the exposure limits recommended by the World Health Organization (20 $\mu g/m^3$, ~7.5 ppb, 24-h mean for SO_2) [7]. As mentioned earlier, volcanic emissions include metals, and some of these metals are essential for life and participate in a wide range of biochemical reactions.

In addition, toxic heavy metals are also released and deposited in the airways and hair and can be retained in tissues, increasing the inflammatory, oxidative stress, DNA damage response and, ultimately, the carcinogenic response [10, 12, 30].

Adults and children living in active-volcanic areas of Azores (Portugal) and Etna (Italy) have shown significant increase in scalp hair concentrations of metals and metalloids such as Cd, Cu, Pb, Rb, Zn, V, U and, to a lesser extent, As and Mn [31, 32], and the risk of chronic bronchitis for the people living in the volcanically active area was much higher (males RR = 3.99; females RR = 10.74) than that for those living in volcanically inactive areas [10].

The literature reports two cases of lung damage associated with the inhalation of fresh volcanic ash [33, 34]. In both cases, the medical conditions improved, and the patients were allowed to go home. In the first case, the authors did not follow up, but in the second case, the patient returned to the hospital 6 months later with the shortness of breath and worsening chest pain; the authors associated the lung symptoms with a kind of silicosis.

http://dx.doi.org/10.5772/intechopen.73283

5. Impact on the respiratory system

Volcanic gases affect people even after they return to their homes. This is the case with the citizens of Miyakejima who returned to the island four-and-a-half years after the eruption of the Mount Oyama in Japan. The volcanic emissions were mainly composed of SO_2, the levels of which reached 80,000 tons/day during the peak period. Although emission rates of SO_2 decreased after the initial eruption, the levels remained high compared to those at Sakurajima in Japan, Kilauea in Hawai'i, and Stromboli and Etna in Italy [35–38]. Before the residents of Miyakejima returned to the island, the Tokyo Metropolitan Government established the Scientific Committee for the Assessment of Health Risks and Volcanic Activity. Iwasawa et al. [39] and Kochi et al. [40] started a follow-up study and evaluated the impact on the respiratory health of the residents. The authors found that the mean SO_2 concentration in the air ranged from 6.64 to 12.6 ppb with a maximum concentration between 1580 and 1880 ppb from November 2006 to 2011. The authors observed clear dose-response relationships with symptoms of irritation and established a threshold concentration of approximately 70 ppb in adults. In addition, in children aged 6–18 years, the authors observed a clear exposure-dependent increase in respiratory symptoms such as throat and eye irritation and/or pain, and the threshold concentration was established to be 30 ppb for this group.

Longo et al. [41] found a statistically significant positive association between chronic exposure to SO_2 and fine sulfate particles ($PM_{2.5}$) emitted from the Kilauea volcano (Hawai'i) and increased prevalence of cough, phlegm, rhinorrhea, sore/dry throat, sinus congestion, wheezing, eye irritation and bronchitis. The chronic exposure to volcanic SO_2 emissions increased the risk of acute bronchitis in children aged 0–14 years, with a cumulative incidence ratio of 6.56 [41]. However, Tam et al. [42] found that chronic exposure to respirable acidic particulates is associated with a reduction in the FEV1/FVC ratio; however, this effect was not statistically significant. The authors did not find any association with the diagnosis of asthma or with persistent wheezing or bronchitis in the last 12 months in the group studied.

Rojas-Ramos et al. [43, 44], in a 7-month prospective study of 80 nonsmoking farmers exposed for 1- to 5-day periods to volcanic ash from the Popocatépetl volcano, found an increase in the occurrence of respiratory symptoms such as sore throat, cough, expectoration and dyspnea. Of the 80 exposed people, 44 showed a restrictive spirometric pattern and two showed an obstructive pattern; the proportions of these symptoms were considered to be higher than those observed in persons exposed to tobacco and wood smoke. After 7 months of exposure, the lung function returned to normal values.

In contrast, Benítez et al. [45] did not observe significant differences in spirometric parameters before and after volcanic eruption in Bariloche, Argentina. The data obtained before and after the event did not correspond to the same individual, which could lead to an underestimation of the effect.

6. Toxicological effects

In vitro and in vivo toxicological studies of volcanic emissions have been performed and have focused on cytotoxicity, immunological response, production of reactive oxygen species and pulmonary response.

The physicochemical characterization of ash particles from different volcanoes is important in toxicological studies. Volcanic ash particles have a wide distribution in size and composition. Due the high content of SiO_2 in volcanic ash, many investigators have been interested in the fibrotic effects.

It is well known that particles less than 10 μm (PM_{10}) in size, which are found in volcanic ash, can enter the respiratory tract, including the alveolar region with a deposit of 10% of the ash particles; the tracheobronchial region with a range of 1–4.5% of ash deposit; and the head airways with a deposit of 15–60%, increasing the risk of in situ lung damage (**Figure 8**) [46]. Furthermore, the deposition of ash particles along the respiratory system could cause systemic alterations because the smallest particles can translocate from airway tissues to other organs via the blood stream and to the brain via the axon extensions in the nose [47, 48].

Studies in mice exposed to volcanic emissions have provided evidence of increased alveolar damage (decrease in alveolar space and perimeter, increase in alveolar septal thickness, inflammation and particle deposits) compared to mice exposed to environmental pollutants [49]. Inflammatory lung reactions were noted in lymph nodes after 13 weeks of exposure to volcanic ash, and the reaction lasted until 49 weeks after exposure [50].

One single instillation of ash from Mount St. Helens (40 mg) was performed in female fisher rats that were then killed at 109 days; the exposure induced an inflammatory response, leading to increased lung and lymph node weight. A mononuclear cell inflammatory reaction, cell necrosis, hyperplasia of type-II pneumocytes and evident damage of type-I epithelial cells were observed in the lungs. Microgranulomas were observed in rats exposed to volcanic ash, and a significant increase in fibrosis was observed. These responses suggest that the toxicity of ash is associated with the levels of crystalline silica. The toxicity of ash from Mount St. Helens on lungs has been extensively studied and reviewed by Martin et al. [51]. Discordant results have also been obtained by several authors. For example, THP-1 macrophages exposed to volcanic ash from Mount St. Helens had low levels of LDH release, minimal suppression of cellular metabolism, and negligible apoptosis and necrosis as well as IL-1β production [52, 53]. The last result was not consistent with the reported cristobalite toxicity and concentration in the ash from Mount St. Helens.

Since macrophages in the lung constitute the first line of defense to foreign substances and materials, and the mineral content of volcanic ash particles determines the bioreactivity and the intensity of immunological response, these results could indicate a gradual change from an acute to a chronic inflammatory process that involves the biochemical and biomolecular modification (e.g., proteins or lipids) of the lung-lining fluid, altering the protective effects of this fluid [54]. The bactericidal capacity of macrophages is also impaired, which could be related to the type and levels of metals that can affect the activity of antimicrobial peptides

present in the lung-lining fluid [55, 56]. Dodson et al. [57] reported an electron-microscopic analysis of interaction of ash with human macrophages from smokers and nonsmokers, and these authors did not observe morphological changes associated with cytotoxic effects of the eruption of Mount St. Helens.

The exact mechanism by which volcanic ash could damage lung tissue is not clear, and the literature shows contradictory results. One of the proposed mechanisms involves the generation of reactive oxygen and nitrogen species, especially hydroxyl radicals ($HO^{\bullet}$) [58], related to interactions with some metals, both essential and nonessential to biochemical and physiological functions [59], that are present in volcanic ash [60]. Horwell et al. demonstrated that the production of hydroxyl radicals from volcanic ash was independent of the iron content of basaltic volcanic ash, but the production was associated with the uncoordinated iron ions exposed at the surface of the ash [38].

Volcanic ashes from Eyjafjallajökull and Grímsvötn were not oxidative and had low acute cytotoxicity (20–30%) in human alveolar type-1-like epithelial cells (TT1) after a 24-h exposure to 50–1000 μg/ml, and a pro-inflammatory response was observed, with increased levels of Il-6, Il-8 and MCP1 after acute exposure when evaluated at 24 and 96 h [61].

The cytotoxic effect of Monserrat volcanic ash was tested in the A549 cell line via the evaluation of the mitochondrial reduction of tetrazolium salts (MTT assay). The authors reported a reduction in cell viability (20–30% with respect to cell controls) of the cell line exposed to 500 μg/ml for 24 h [62].

We have not found reports of in vitro cytotoxicity studies with the ashes of Popocatepetl. Experiments that are ongoing in our laboratory on the cell viability of the A549 cell line exposed for 48 h to ash collected in 2013 from Popocatepetl showed, by using the MTT assay, elevated, concentration-dependent cytotoxic effects (**Figure 10**) (Aztatzi-Aguilar et al., in preparation). The cytotoxic effect of ash from Popocatepetl could be attributable to the high fluoride content reported by Armienta et al. in ash leachates from the Popocatepetl volcano (5–513 mg/kg)

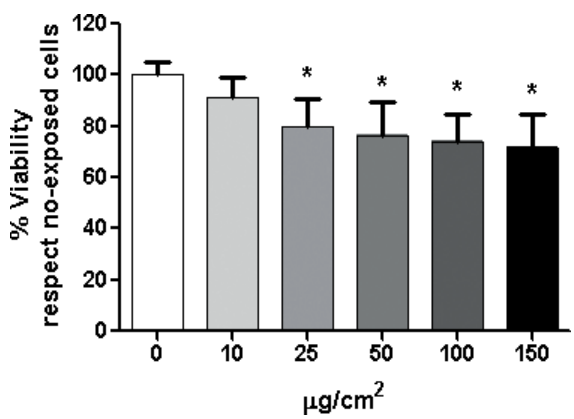

Figure 10. Cytotoxic effect of Popocatépetl's ash on A549 cell line. Exposure of A549 cell line to volcanic ash showed an increase in cell death in a dose-dependent manner (MTT assay).

and by D'Addabbo et al. in ash from Mount Etna (10 mg/L) [63, 64]. Rodents exposed to ash from Popocatepetl at 10 mg/m^3 for 60 days (4 h/day) showed reduced body weight and changes in differential blood count, with increased lymphocyte counts and reduced neutrophil counts [65]. D'Addabbo et al. did not observe any toxicity of Popocatepetl ash leachates on *Xenopus laevis* embryos; however, the authors observed a 40% increase in larval malformation [64].

Volcanic ashes from Mt. Vesuvius led to decreased lung antioxidant defenses, had low acute cytotoxicity in human alveolar type-1-like epithelial cells and had a chronic pro-inflammatory response [61]. This effect could lead to an increase in alveolar-capillary permeability, which correlates with lung injury and with impaired gas exchange [66]. People living near volcanoes are also exposed to anthropogenic pollutants; the exposure to volcanic ash from the Soufrière Hills volcano mixed with diesel exhaust particles (DEP) increased the pro-inflammatory response of cellular culture, as determined by the enhanced release of TNF-α, IL-8 and IL-1β [67]. Discordant results have also been obtained by several authors. For example, THP-1 macrophages exposed to volcanic ash from Mount St. Helens had low levels of LDH release, minimal suppression of cellular metabolism, and negligible apoptosis and necrosis as well as IL-1β production [52, 53]. The last result was not consistent with the reported cristobalite toxicity and concentration in the ash from Mount St. Helens.

7. Geotourism

In 2002, the Travel Industry Association of America introduced the term geotourism, which is increasing in popularity and represents a new trend in travel. Unfortunately, this kind of travel carries the risk of injuries ranging from mild cuts and abrasions to thermal burns, broken bones, hypothermia and altitude sickness, which are life-threatening conditions [68–70]. Lung emphysema associated with exposure to high concentrations of SO_2 or CO has been reported as a cause of death in some tourists [71, 72].

In addition to geotourism, such fatalities have also been reported in workers during winter months, when snow can block volcanic vents, making them nonvisible. Moreover, snow can trap toxic fumes and form dangerous, gas-filled pits [73].

8. Environmental effects

The effects of volcanic emissions are not limited to living organisms. There is plausible information regarding stratospheric ozone depletion related to the emission of hydrochloric acid from major explosive eruptions [74], where volcanic ash can play the role of a temporary atmospheric reservoir of chloride salts that may generate reactive chlorine species, contributing to catalytic O_3 destruction [75]. Furthermore, the reactivity and activation of volcanic ashes are influenced by the mineralogical and chemical composition of the ashes [76]. Additionally, it is important to note that the acidification of surface waters caused by ash precipitation can

increase the leaching of toxic elements such as fluoride and arsenic, leading to the poisoning of aqueous environments and increasing the risk of fluorosis [63, 77, 78].

9. Conclusions

There is no doubt that people will continue to live near volcanic flanks, and this is for many reasons:

1. Because of poor urban planning.
2. Because governments and stakeholders fail to provide alternatives.
3. Because citizens cannot afford a safer place to live in.
4. Because of the influence of religion on people's behavior and risk perception.

Whatever the cause, governments must work together with residents to identify the hazards in the environment and the vulnerabilities of the communities in order to improve public policies to lower the risk from volcanic exposure or other natural disasters.

Acknowledgements

This work was supported by National Council of Science and Technology (CONACYT) grant FOSISS-SALUD-220014-01-233950 and CÁTEDRA-CONACYT-280. The authors wish to thank Drs. Ana Lillian Martín Del Pozzo and Hugo Delgado Granados from the Department of Volcanology of the Institute of Geophysics, National Autonomous University of Mexico (UNAM), for supplying the ash samples.

Conflict of interest

The authors declare that they have no competing interests.

Author details

Martha Patricia Sierra-Vargas[1]*, Claudia Vargas-Domínguez[1], Karen Bobadilla-Lozoya[1] and Octavio Gamaliel Aztatzi-Aguilar[1,2]

*Address all correspondence to: mpsierra@iner.gob.mx

1 National Institute for Respiratory Diseases Ismael Cosío Villegas, Mexico City, Mexico

2 National Council of Science and Technology (CONACYT), Mexico

References

[1] Carn SA, Fioletov VE, McLinden CA, Li C, Krotkov NA. A decade of global volcanic SO_2 emissions measured from space. Scientific Reports. 2017;**7**:44095-44106. DOI: 10.1038/srep44095

[2] Loughlin SC, Vye-Brown C, Sparks RSJ, Brown SK, Barclay J, Calder E, Cottrell E, Jolly G, Komorowski JC, Mandeville C, Newhall C, Palma J, Potter S, Valentine G. An introduction to global volcanic hazard and risk. In: Loughlin S, Sparks S, Brown S, Jenkins S, Vye-Brown C, editors. Global Volcanic Hazards and Risk. Cambridge: Cambridge University Press; 2015. pp. 1-80. DOI: 10.1017/CBO9781316276273.003

[3] Mather TA. Volcanism and the atmosphere: The potential role of the atmosphere in unlocking the reactivity of volcanic emissions. Philosophical Transactions A Mathematical Physical and Engineering Science. 2008;**366**(1885):4581-4595. DOI: 10.1098/rsta.2008.0152

[4] Delmelle P, Stix J, Baxter P, Garcia-Alvarez J, Barquero J. Atmospheric dispersion, environmental effects and potential health hazard associated with the low-altitude gas plume of Masaya volcano, Nicaragua. Bulletin of Volcanology. 2002;**64**(6):423-434. DOI: 10.1007/s00445-002-0221-6

[5] Lippmann M, Yeates DB, Albert RE. Deposition, retention, and clearance of inhaled particles. British Journal of Industrial Medicine. 1980;**37**(4):337-362

[6] Hansell A, Oppenheimer C. Health hazards from volcanic gases: A systematic literature review. Archives of Environmental Health. 2004;**59**(12):628-639. DOI: 10.1080/00039890409602947

[7] Longo BM, Rossignol A, Green JB: Cardiorespiratory health effects associated with sulphurous volcanic air pollution. Public Health 2008;**122**(8):809-820. DOI: 10.1016/j.puhe.2007.09.017

[8] Terzano C, Di Stefano F, Conti V, Graziani E, Petroianni A. Air pollution ultrafine particles: Toxicity beyond the lung. European Review for Medical and Pharmacological Sciences. 2010;**14**(10):809-821

[9] Hlodversdottir H, Petursdottir G, Carlsen HK, Gislason T, Hauksdottir A. Long-term health effects of the Eyjafjallajökull volcanic eruption: A prospective cohort study in 2010 and 2013. BMJ Open. 2016;**6**(9):e011444. DOI: 10.1136/bmjopen-2016-011444

[10] Amaral A, Rodrigues V, Oliveira J, Pinto C, Carneiro V, Sanbento R, Cunha R, Rodrigues A. Chronic exposure to volcanic environments and cancer incidence in the Azores, Portugal. Science of the Total Environment. 2006;**367**(1):123-128. DOI: 10.1016/j.scitotenv.2006.01.024

[11] Giacoppo S, Galuppo M, Calabrò RS, D'Aleo G, Marra A, Sessa E, Bua DG, Potortì AG, Dugo G, Bramanti P, Mazzon E. Heavy metals and neurodegenerative diseases: An observational study. Biological Trace Element Research. 2014;**161**(2):151-160. DOI: 10.1007/s12011-014-0094-5

[12] Ferreira AF, Garcia PV, Camarinho R, Rodrigues Ados S. Volcanogenic pollution and testicular damage in wild mice. Chemosphere. 2015;**132**:135-141. DOI: 10.1016/j.chemosphere.2015.03.017

[13] Olenchock SA, Mull JC, Mentnech MS, Lewis DM, Bernstein RS. Changes in humoral immunologic parameters after exposure to volcanic ash. Journal of Toxicology and Environmental Health. 1983;**11**:395-404. DOI: 10.1080/15287398309530353

[14] Convit J, Ulrich M, Castillo J, De Lima H, Pérez M, Caballero N, Hung J, Arana B, Pérez P. Inorganic particles in the skin of inhabitants of volcanic areas of central America: Their possible immunomodulatory influence in leishmaniasis and leprosy. Transactions of the Royal Society of Tropical Medicine and Hygiene. 2006;**100**(8):734-739. DOI: 10.1016/j.trstmh.2005.09.012

[15] Heiken G. Morphology and petrography of volcanic ashes. GSA Bulletin. 1972;**83**(7):1961-1988 doi.org/10.1130/0016-7606(1972)83[1961:MAPOVA]2.0.CO;2

[16] Bellomo S, Aiuppa A, D'Alessandro W, Parello F. Environmental impact of magmatic fluorine emission in the Mt. Etna area. Journal of Volcanology and Geothermal Research. 2007;**165**:87-101. DOI: 10.1016/j.jvolgeores.2007.04.013

[17] Heikens A, Widianarko B, Dewi IC, de Boer JL, Seinen W, van Leeuwen K: The impact of the hyperacid Ijen crater Lake. Part II: A total diet study. Environmental Geochemistry and Health 2005;**27**(5–6):475-483. DOI: 10.1007/s10653-005-5229-3

[18] Doocy S, Daniels A, Dooling S, Gorokhovich Y. The human impact of volcanoes: A historical review of events 1900-2009 and systematic literature review. PLoS Currents. 2013;**5**. DOI: 10.1371/currents.dis.841859091a706efebf8a30f4ed7a1901

[19] Kling GW, Clark MA, Wagner GN, Compton HR, Humphrey AM, Devine JD, Evans WC, Lockwood JP, Tuttle ML, Koenigsberg EJ. The 1986 lake Nyos gas disaster in Cameroon, West Africa. Science. 1987;**236**(4798):169-175. DOI: 10.1126/science.236.4798.169

[20] Baxter PJ, Kapila M, Mfonfu D. Lake Nyos disaster, Cameroon, 1986: The medical effects of large scale emission of carbon dioxide? BMJ. 1989;**298**(6685):1437-1441

[21] The 2010 Population and Housing Census Instituto Nacional de Estadística y Geografía 2010, INEGI. Available from: http://www.beta.inegi.org.mx/proyectos/ccpv/2010/ [Accessed: 2017–12-04]

[22] De La Cruz-Reyna S, Siebe C. The giant Popocatépetl stirs. Nature. 1997;**388**:227. DOI: 10.1038/40749

[23] Macías JL, Siebe C. Popocatépetl crater filled to the brim: Significance for hazard evaluation. Journal of Volcanology and Geothermal Research. 2005;**141**:327-330. DOI: 10.1016/j.jvolgeores.2004.10.005

[24] Michaud JP, Grove JS, Krupitsky D. Emergency department visits and "vog"-related air quality in Hilo, Hawai'i. Environmental Research. 2004;**95**(1):11-19. DOI: 10.1016/S0013-9351(03)00122-1

[25] Naumova EN, Yepes H, Griffiths JK, Sempértegui F, Khurana G, Jagai JS, Játiva E, Estrella B. Emergency room visits for respiratory conditions in children increased after Guagua Pichincha volcanic eruptions in April 2000 in Quito, Ecuador observational study: Time series analysis. Environmental Health. 2007;**6**:21-31. DOI: 10.1186/1476-069X-6-21

[26] Shinkura R, Fujiyama C, Akiba S. Relationship between ambient sulfur dioxide levels and neonatal mortality near the Mt. Sakurajima volcano in Japan. Journal of Epidemiology. 1999;**9**(5):344-349. DOI: 10.2188/jea.9.344

[27] Yorifuji T, Kashima S, Doi H. Outdoor air pollution and term low birth weight in Japan. Environment International. 2015;**74**:106-111. DOI: 10.1016/j.envint.2014.09.003

[28] Kimura K, Sakamoto T, Miyazaki M, Uchino E, Kinukawa N, Isashiki M. Effects of volcanic ash on ocular symptoms: Results of a 10-year survey on schoolchildren. Ophthalmology. 2005;**112**(3):478-481. DOI: 10.1016/j.ophtha.2004.09.031

[29] Camara JG, Lagunzad JK. Ocular findings in volcanic fog induced conjunctivitis. Hawaii Medical Journal. 2011;**70**(12):262-265

[30] Rodrigues AS, Arruda MS, Garcia PV. Evidence of DNA damage in humans inhabiting a volcanically active environment: A useful tool for biomonitoring. Environment International. 2012;**49**:51-56. DOI: 10.1016/j.envint.2012.08.008

[31] Amaral AF, Arruda M, Cabral S, Rodrigues AS. Essential and non-essential trace metals in scalp hair of men chronically exposed to volcanogenic metals in the Azores, Portugal. Environment International. 2008;**34**(8):1104-1108. DOI: 10.1016/j.envint.2008.03.013

[32] Varrica D, Tamburo E, Dongarrà G, Sposito F. Trace elements in scalp hair of children chronically exposed to volcanic activity (Mt. Etna, Italy). Science of the Total Environment. 2014;**470-471**:117-126. DOI: 10.1016/j.scitotenv.2013.09.058

[33] Shojima J, Ikushima S, Ando T, Mochida A, Yanagawa T, Takemura T, Oritsu M. A case of volcanic ash lung: Report of a case.[article in Japanese]. Nihon Kokyūki Gakkai Zasshi. 2006;**44**(3):192-196

[34] Trisnawati I, Budiono E, Sumardi SA. Traumatic inhalation due to Merapi volcanic ash. Acta Medica Indonesiana. 2015;**47**(3):238-243

[35] Kazahaya K: Monitoring of Volcanic Gases at Miyakejima Volcano, Japan, 2007. Available from: http://staff.aist.go.jp/kazahaya-k/miyakegas/COSPEC.html [Accessed 15 November 2017]

[36] Uda H, Akiba S, Hatano H, Shinkura R. Asthma-like disease in the children living in the neighborhood of Mt. Sakurajima. Journal of Epidemiology. 1999;**9**(1):27-31. DOI: 10.2188/jea.9.27

[37] Mannino DM, Ruben S, Holschuh FC, Holschuh TC, Wilson MD, Holschuh T. Emergency department visits and hospitalizations for respiratory disease on the island of Hawaii, 1981 to 1991. Hawaii Medical Journal. 1996;**55**(3):48-54

[38] Durand M, Grattan J. Effects of volcanic air pollution on health. Lancet. 2001;**357**(9251):164. DOI: 10.1016/S0140-6736(00)03586-8

[39] Iwasawa S, Nakano M, Tsuboi T, Kochi T, Tanaka S, Katsunuma T, Morikawa A, Omae K. Effects of sulfur dioxide on the respiratory system of Miyakejima child residents 6 years after returning to the island. International Archives of Occupational and Environmental Health. 2015;**88**:1111-1118. DOI: 10.1007/s00420-015-1037-y

[40] Kochi T, Iwasawa S, Nakano M, Tsuboi T, Tanaka S, Kitamura H, Wilson DJ, Takebayashi T, Omae K. Influence of sulfur dioxide on the respiratory system of Miyakejima adult residents 6 years after returning to the island. Journal of Occupational Health. 2017;**59**(4): 313-326. DOI: 10.1539/joh.16-0256-OA

[41] Longo BM, Yang W. Acute bronchitis and volcanic air pollution: A community-based cohort study at Kilauea volcano, Hawai'i, USA. Journal of Toxicology and Environmental Health. Part A. 2008;**71**(24):1565-1571. DOI: 10.1080/15287390802414117

[42] Tam E, Miike R, Labrenz S, Sutton AJ, Elias T, Davis J, Chen YL, Tantisira K, Dockery D, Avol E. Volcanic air pollution over the island of Hawai'i: Emissions, dispersal, and composition. Association with respiratory symptoms and lung function in Hawai'i Island school children. Environment International. 2016;**92-93**:543-552. DOI: 10.1016/j.envint.2016.03.025

[43] Rojas M, Noa H, Pérez J, Villalba J. Efecto sobre la función pulmonar en personas expuestas a cenizas del volcán Popocatépetl. Diciembre 1994-1995. Revista del Instituto Nacional de Enfermedades. 1995;**8**:112-118

[44] Rojas M, Pérez J, Villalba J, Catlán M, Hernández E, Hernández P. San Nicolás de los Ranchos. ¿Un caso representativo de afecciones respiratorias por exposición a cenizas volcánicas? Revista del Instituto Nacional de Enfermedades. 1996;**9**:14-18

[45] Benítez S, Sobrino E, Calandrelli M, Gutiérrez L, Irazola V, Rubinstein A: Efectos de la ceniza volcánica sobre la función pulmonar en una cohorte de personas mayores de 45 años en Bariloche (Argentina). Revista americana de medicina respiratoria, 2014;**14**(4): 411-416. Available from: http://www.scielo.org.ar/scielo.php?script=sci_arttext&pid=S1852-236X2014000400009&lng=es&tlng=es [Accessed: 2017–12-04]

[46] Lähde A, Gudmundsdottir SS, Joutsensaari J, Tapper U, Ruusunen J, Ihalainen M, Karhunen T, Torvela T, Jokiniemi J, Järvinen K, Gíslason SR, Briem H, Gizurarson S. In vitro evaluation of pulmonary deposition of airborne volcanic ash. Atmospheric Environment. 2013;**70**:18-27. DOI: 10.1016/j.atmosenv.2012.12.048

[47] Elder A, Oberdörster G. Translocation and effects of ultrafine particles outside of the lung. Clinics in Occupational and Environmental Medicine. 2006;**5**(4):785-796. DOI: 10.1016/j.coem.2006.07.003

[48] Oberdörster G, Sharp Z, Atudorei V, Elder A, Gelein R, Kreyling W, Cox C. Translocation of inhaled ultrafine particles to the brain. Inhalation Toxicology. 2004;**16**(6–7):437-445. DOI: 10.1080/08958370490439597

[49] Camarinho R, Garcia PV, Rodrigues AS. Chronic exposure to volcanogenic air pollution as cause of lung injury. Environmental Pollution. 2013;**181**:24-30. DOI: 10.1016/j.envpol.2013.05.052

[50] Sang Hee L, Richards RJ. Montserrat volcanic ash induces lymph node granuloma and delayed lung inflammation. Toxicology. 2004;**195**(2–3):155-165. DOI: 10.1016/j.tox.2003.09.013

[51] Martin R, Wehner AP, Butler J. Pulmonary toxicity of Mt. St. Helens volcanic ash: A review of experimental studies. The American Review of Respiratory Disease. 1983; **128**(1):158-162. DOI: 10.1164/arrd.1983.128.1.158

[52] Huang YC, Li Z, Harder SD, Soukup JM. Apoptotic and inflammatory effects induced by different particles in human alveolar macrophages. Inhalation Toxicology. 2004;**16**(14): 863-878. DOI: 10.1080/08958370490519480

[53] Damby DE, Murphy FA, Horwell CJ, Raftis J, Donaldson K. The in vitro respiratory toxicity of cristobalite-bearing volcanic ash. Environmental Research. 2016;**145**:74-84. DOI: 10.1016/j.envres.2015.11.020

[54] Jones T, Bérubé K. The bioreactivity of the sub-10 μm component of volcanic ash: Soufrière Hills volcano, Montserrat. Journal of Hazardous Materials. 2011;**194**:128-134. DOI: 10.1016/j.jhazmat.2011.07.092

[55] Monick MM, Baltrusaitis J, Powers LS, Borcherding JA, Caraballo JC, Mudunkotuwa I, Peate DW, Walters K, Thompson JM, Grassian VH, Gudmundsson G, Comellas AP. Effects of Eyjafjallajökull volcanic ash on innate immune system responses and bacterial growth in vitro. Environmental Health Perspectives. 2013;**121**(6):691-698. DOI: 10.1289/ehp.1206004

[56] Roberts JR, Young SH, Castranova V, Antonini JM. The soluble nickel component of residual oil fly ash alters pulmonary host defense in rats. Journal of Immunotoxicology. 2009;**6**(1):49-61. DOI: 10.1080/15476910802630379

[57] Dodson RF, Martin RR, O'Sullivan MF, Hurst GA. In vitro response of human pulmonary macrophages with volcanic ash: A morphological study. Experimental and Molecular Pathology. 1982;**37**(3):406-412. DOI: 10.1016/0014-4800(82)90052-1

[58] Horwell CJ, Stannett GW, Andronico D, Bertagnini A, Fenoglio I, Fubini B, Le Blond JS, Williamson BJ. A physico-chemical assessment of the health hazard of Mt. Vesuvius volcanic ash. Journal of Volcanology and Geothermal Research. 2010;**191**(3–4):222-232. DOI: 10.1016/j.jvolgeores.2010.01.014

[59] WHO/FAO/IAEA. Trace Elements in Human Nutrition and Health. Report of a WHO Expert Committee. Geneva; 1996. 343 pp. (WHO Technical Report Series, No. 532)

[60] Bagnato E, Aiuppa A, Bertagnini A, Bonadonna C, Cioni R, Pistolesi M, Pedone M, Hoskuldsson A. Scavenging of sulphur, halogens and trace metals by volcanic ash: The 2010 Eyjafjallajökull eruption. Geochimica et Cosmochimica Acta. 2013;**103**:138-160. DOI: 10.1016/j.gca.2012.10.048

[61] Horwell CJ, Baxter PJ, Hillman SE, Calkins JA, Damby DE, Delmelle P, Donaldson K, Dunster C, Fubini B, Kelly FJ, Le Blond JS, Livi KJ, Murphy F, Nattrass C, Sweeney S, Tetley TD, Thordarson T, Tomatis M. Physico-chemical and toxicological profiling of ash from the 2010 and 2011 eruptions of Eyjafjallajökull and Grímsvötn volcanoes, Iceland using a rapid respiratory hazard assessment protocol. Environmental Research. 2013;**127**: 63-73. DOI: 10.1016/j.envres.2013.08.011

[62] Wilson MR, Stone V, Cullen RT, Searl A, Maynard RL, Donaldson K. In vitro toxicology of respirable Montserrat volcanic ash. Occupational and Environmental Medicine. 2000; **57**(11):727-733. DOI: 10.1136/oem.57.11.727

[63] Armienta MA, De la Cruz-Reyna S, Cruz O, Ceniceros N, Aguayo A, Marin M. Fluoride in ash leachates: Environmental implications at Popocatepetl volcano, central Mexico. Natural Hazards and Earth System Sciences. 2011;**11**:1949-1956. DOI: 10.5194/nhess-11-1949-2011

[64] D'Addabbo M, Sulpizio R, Guidi M, Capitani G, Mantecca P, Zanchetta G. Ash leachates from some recent eruptions of Mount Etna (Italy) and Popocatépetl (Mexico) volcanoes and their impact on amphibian living freshwater organisms. Biogeosciences. 2015;**12**(23):7087-7106

[65] Rivera A, Cedillo L, Giono S, Cuautle L, Milflores L, Yanez A. Lung damage in rats following inhalation exposure of the Popocatepetl volcano ash. Research Journal of Biological Sciences. 2009;**4**(10):1104-1109

[66] Delaval M, Boland S, Solhonne B, Nicola MA, Mornet S, Baeza-Squiban A, Sallenave JM, Garcia-Verdugo I. Acute exposure to silica nanoparticles enhances mortality and increases lung permeability in a mouse model of Pseudomonas Aeruginosa pneumonia. Particle and Fibre Toxicology. 2015;**12**:1-13. DOI: 10.1186/s12989-014-0078-9

[67] Tomašek I, Horwell CJ, Damby DE, Barošová H, Geers C, Petri-Fink A, Rothen-Rutishauser B, Clift MJ. Combined exposure of diesel exhaust particles and respirable Soufrière Hills volcanic ash causes a (pro-)inflammatory response in an in vitro multicellular epithelial tissue barrier model. Particle and Fibre Toxicology. 2016;**13**(1):67-80

[68] Heggie TW, Heggie TM. Viewing lava safely: An epidemiology of hiker injury and illness in Hawaii volcanoes National Park. Wilderness & Environmental Medicine. 2004;**15**(2):77-81. DOI: 10.1580/1080-6032(2004)015[0077:VLSAEO]2.0.CO;2

[69] Heggie TW. Reported fatal and non-fatal incidents involving tourists in Hawaii volcanoes National Park, 1992-2002. Travel Medicine and Infectious Disease. 2005;**3**(3):123-131. DOI: 10.1016/j.tmaid.2004.09.004

[70] Gregory M, Sprowl MD. Hazards of Hawai'i volcanoes National Park Hawaii. Journal of Medicine and Public Health. 2014;**73**(11 Suppl 2):17-20

[71] Ng'walali PM, Koreeda A, Kibayashi K, Tsunenari S. Fatalities by inhalation of volcanic gas at Mt. Aso crater in Kumamoto, Japan. Legal Medicine (Tokyo). 1999;**1**(3):180-184. DOI: 10.1016/S1344-6223(99)80034-0

[72] Hill PM. Possible asphyxiation from carbon dioxide of a cross-country skier in eastern California: A deadly volcanic hazard. Wilderness & Environmental Medicine. 2000;**11**(3): 192-195. DOI: 10.1580/1080-6032(2000)011[0192:PAFCDO]2.3.CO;2

[73] Cantrell L, Young M. Fatal fall into a volcanic fumarole. Wilderness & Environmental Medicine. 2009;**20**(1):77-79. DOI: 10.1580/08-WEME-CR-199.1

[74] Gutiérrez X, Schiavi F, Keppler H. The adsorption of HCl on volcanic ash. Earth and Planetary Science Letters. 2016;**438**:66-74. DOI: 10.1016/j.epsl.2016.01.019

[75] Ayris PM, Delmelle P, Cimarelli C, Maters EC, Suzuki YJ, Dingwell DB. HCl uptake by volcanic ash in the high temperature eruption plume: Mechanistic insights. Geochimica et Cosmochimica Acta. 2014;**144**:188-201. DOI: 10.1016/j.gca.2014.08.028

[76] Lemougna PN, Chinje Melo UF, Delplancke MP, Rahier H. Influence of the chemical and mineralogical composition on the reactivity of volcanic ashes during alkali activation. Ceramic International. 2014;**40**(1 part A):811-820. DOI: 10.1016/j.ceramint.2013.06.072

[77] Jones MT, Gislason SR. Rapid releases of metal salts and nutrients following the deposition of volcanic ash into aqueous environments. Geochimica et Cosmochimica Acta. 2008;**72**(15):3661-3680. DOI: 10.1016/j.gca.2008.05.030

[78] López DL, Bundschuh J, Birkle P, Armienta MA, Cumbal L, Sracek O, Cornejo L, Ormachea M. Arsenic in volcanic geothermal fluids of Latin America. Science of the Total Environment. 2012;**429**:57-75. DOI: 10.1016/j.scitotenv.2011.08.043

Edited by Gemma Aiello

This book contains 12 chapters dealing with the studies on volcanoes, their geological and geophysical setting, the theoretical aspects and the numerical modeling on volcanoes, the applications of volcanoes to the industry, and the impact of volcanoes on the human health, in different geological settings and using several techniques and methods, including the volcanology, the seismology, the statistical methods to assess the correlation between seismic and volcanic activity (modified Ripley's K-function to regional seismicity), the field geological survey of volcanic successions, the analytical methods of petrologic analysis, the petrography of the volcanic rocks with the individuation of the modal compositions of volcanic rocks and their comparison with major elements and trace elements in variation diagrams, and the argon isotopic measurements performed through the peak height comparison (unspiked) method. The oceanographic methods have also been applied to case studies of submarine volcanic edifices located in the Canary Islands (Atlantic Ocean), including the sampling of the water column with a conductivity-temperature-depth (CTD) sensor rosette with 24 Niskin bottles, in order to determinate key physical and chemical parameters, such as the total-scale pH, the total dissolved inorganic carbon (C), the total alkalinity (A), the temperature, the salinity, and the dissolved oxygen. Problems of volcanic risk mitigation have also been treated, regarding the eruption disasters in Indonesia, a country where a high number of people live next to the volcanoes, and characterized by the lack of public awareness of the eruption disasters. Petrographic methods have been successfully applied to the study of the Cretaceous magmatism of the layered gabbroids of the Chukotka region (Pekulney Ridge, Russia), and geodynamic implications have been successfully established through geological and petrographic studies. The relationships among the mantle wedge, the convective heat and mass transfer, the infiltration metasomatism, the zoning, and the mathematical models have been applied to the comprehension of complex volcanic areas through the theoretical aspects of volcanic studies on magmatic chambers coupled with numerical modeling, including finite element models (FEMs) in the individuation of volcanic deformations.

Published in London, UK

IntechOpen

ISBN 978-1-83881-290-4